Respiratory Motion Compensation in 3D Positron Emission Tomography

Submitted by

Jianfeng He

M. Sc., B. Sc

A thesis submitted in total fulfilment of

the requirement for the degree of

Doctor of Philosophy

School of Medical Sciences

Science, Engineering and Technology Portfolio

RMIT University

Bundoora, Melbourne Victoria 3001

Australia

September 2008

Declaration

I certify that except where due acknowledgement has been made, the work is that of the author alone; the work has not been submitted previously, in whole or in part, to quality for any academic award; the content of the thesis is the result of work which has been carried out since the official commencement date of the approved research program; and, any editorial work, paid or unpaid, carried out by a third party is acknowledged.

Name: Jianfeng He

Signature:

Date: 15th September 2008

Acknowledgements

First of all, I would like to express my great thanks to my supervisors Dr Graeme O'Keefe and A/Prof Moshi Geso. I am grateful to Dr Graeme O'Keefe for his guidance, support, wise advice, encouragement and insightful comments throughout my candidature. I am indebted to A/Prof Moshi Geso for his guidance, assistance and encouragement.

I wish to thank Tim Saunder for his assistance in image processing and computer system support during my research. I would also like to acknowledge Gareth Jones for his assistance in initial installation and utilisation of simulation software packages. My gratitude goes to Shayne Cox for computer system support for my thesis writing and Jason Bradley for assistance in collecting clinical data for my research. I wish to acknowledge director of Centre for PET, Professor Andrew Scott for making the PET facility available. Also thanks are extended to other staff for all their support during my time at the Department of Nuclear Medicine and Centre for PET, Austin Hospital.

My special thanks must go to Dr. Sylvia J Gong for her friendship, encouragement and substantial spiritual for the pursuit for my doctoral studies, also for her assistance in the phantom measurements, continuous support during my study, and reading some chapters of my thesis.

My deep thanks go to Trevor Ackerly for all his assistance in thesis proofreading and encouragement. I am grateful for his kindness and generosity in sparing his busy time to proofread my thesis carefully and provide many helpful suggestions, which is much appreciated.

My sincere thanks go to Wanxian Zhu for his heart-warming assistance in my first year study at RMIT, also many thanks are extended to Changfa He for his spiritual support.

I am grateful for Ralph Brinks, Philips Research Division, Aachen, Germany for his valuable communications.

I also wish to thank the sponsorships of the Australian Postgraduate Awards and RMIT University Postgraduate Research Scholarship for my study and living, without the financial support, I cannot complete this research.

I would like to thank my beloved mum, sister and brother, for their devoted love, emotional and spiritual support, for their comforts during my difficult time, and for encouragements to pursue my doctoral degree.

Finally, my profound gratitude goes to my beloved wife, although far away from here, for visiting me each year and sharing with me the agony and joy of this scholastic pursuit, for all her loving care, understanding, spiritual and emotional support, and encouragement along this journey.

DECLARATION ..... **II**

ACKNOWELEDGE ..... **III**

LIST OF FIGURES ..... **VII**

LIST OF TABLES ..... **XII**

LIST OF ABBREVIATIONS ..... **XIII**

SUMMARY ..... **XIV**

1 INTRODUCTION **1**

1.1 POSITRON EMISSION TOMOGRAPHY 1
1.1.1 History 1
1.1.2 Basic Principle 5
1.2 PROBLEM STATEMENT 6
1.3 HYPOTHESIS 8
1.4 OBJECTIVES 15
1.5 THESIS STRUCTURE 16

2 LITERATURE REVIEW **17**

2.1 MOTION GATING TECHNIQUES 20
2.1.1 External Monitor Systems Methods 20
2.1.2 Data-Driven Methods 25
2.1.2.1 Sinogram Based Gating Methods 26
2.1.2.2 List-mode Data Based Gating Methods 30
2.1.2.3 Image Based Gating Methods 33
2.2 MOTION CORRECTION TECHNIQUES 36
2.2.1 List- mode Data Based Correction Methods 37
2.2.2 Sinogram-Based Correction Methods 39
2.2.3 Reconstruction-Based Correction Methods 41
2.2.4 Image-Based Correction Methods 42
2.3 SUMMARY 45

3 MATERIALS AND METHODS **47**

3.1 INTRODUCTION 48
3.2 SIMULATION OF PET ACQUISITION DATA 48
3.2.1 Coordinate System 50
3.2.2 PET Imaging Relevant to the Monte Carlo Simulation 51
3.2.2.1 PET Scanner Parameters 52
3.2.2.2 Hardware Event Processing 54
3.2.3 Simulation Software 57
3.2.3.1 GATE 57
3.2.3.1.1 Structure and Digitiser Optimisation 57
3.2.3.1.2 Simulation Steps 59
3.2.3.1.3 Geometric and Voxelised Phantom 61
3.2.3.2 NCAT Digital Phantom 64
3.2.3.3 Validation for GATE 66
3.2.3.4 Computational Issues 70
3.3 SORT LIST-MODE DATA 72
3.3.1 Simulation List-mode Data 72
3.3.2 Clinical List-mode Data 73
3.4 MOTION GATING METHOD 75
3.5 MOTION CORRECTION METHOD 80
3.6 RECONSTRUCTION IMAGE 86
3.7 IMAGE ANALYSIS 86
3.8 SUMMARY 89

4 SIMULATIONS AND VALIDATIONS **91**

4.1 GEOMETRIC PHANTOM SIMULATION 92
4.1.1 Introduction 92

4.1.2 Simulation Procedure ... 93
4.1.2.1 Motion Phantom and Sources Generated by GATE ... 93
4.1.2.2 Oscillation Equation ... 94
4.1.2.3 Sort List-Mode Data ... 95
4.1.2.4 Motion Gating and Correction ... 95
4.1.3 Results and Discussion ... 96
4.1.3.1 Event Rate versus Frame Evaluation ... 96
4.1.3.2 Motion Gating ... 102
4.1.3.3 Motion Correction ... 110
4.1.4 Summary ... 123
4.2 VOXELISED SIMULATION ... 124
4.2.1 Introduction ... 124
4.2.2 Simulation Procedure ... 124
4.2.2.1 Phantom Generated by NCAT ... 124
4.2.2.2 Phantom Imported into GATE ... 127
4.2.2.3 Sort List-Mode Data ... 127
4.2.2.4 Motion Gating and Correction ... 129
4.2.3 Results and Discussion ... 129
4.2.3.1 Frame Events and Lung Volume Curves ... 129
4.2.3.2 Motion Gating with and without Attenuation Modeling ... 133
4.2.3.3 Motion Correction ... 139
4.2.4 Summary ... 140
4.3 CLINICAL VALIDATION ... 144
4.3.1 Introduction ... 144
4.3.2 Validation Procedure ... 144
4.3.2.1 Patient Scanned with and without-Tumor ... 144
4.3.2.2 Sorted List-Mode Data ... 145
4.3.2.3 Filter Noise in List-Mode Data ... 146
4.3.2.4 Motion Gating and Correction ... 147
4.3.3 Results and Discussion ... 147
4.3.3.1 Frame Events in Time Domain ... 147
4.3.3.2 Frame Events in Frequency Domain ... 149
4.3.3.3 Filtered Frame Events ... 151
4.3.3.4 Motion Gating ... 154
4.3.3.5 Motion Correction ... 156
4.3.4 Summary ... 160

5 DISCUSSION AND CONCLUSION ... 162

5.1 GEOMETRIC SENSITIVITY GATING ... 163
5.2 GEOMETRIC SENSITIVITY CORRECTION ... 165
5.3 STUDY LIMITATIONS AND FUTURE RESEARCH ... 167
5.3.1 Limitations of the methods ... 167
5.3.2 Further Research ... 172
5.4 CONCLUSION ... 172
5.5 MAIN CONTRIBUTIONS AND PUBLICATIONS ... 173

APPENDICES ... 175

APPENDIX A GATE MACROS OF PHILLIPS ALLEGRO PET SCANNER SIMULATION ... 176
APPENDIX B GATE MACROS OF GEOMETRIC PHANTOM AND SOURCE MOTION ... 180
APPENDIX C GATE MACROS OF VOXELISED PHANTOM AND SOURCE ... 182
APPENDIX D NCAT PHANTOM GENERATION PARAMETERS ... 184
APPENDIX E PUBLICATION IN IEEE TRANSACTIONS ON NUCLEAR SCIENCE (IN PRESS) ... 191

REFERENCES ... 192

List of Figures

Figure No. Page No.

Chapter 1

1.1. PET imaging system overview 1

1.2. Comparison between 2D and 3D geometric acquisition modality 3

1.3. PET/CT imaging system 4

1.4. Schematic representation of the principles of PET imaging 6

1.5. Demonstrating artifacts at the level of the diaphragm as a result of respiration motion 7

1.6. Comparison of the geometric sensitivity between 2D and 3D mode by Michellogram 10

1.7. One point source at offset position in 3D PET cylindrical scanner 12

1.8. The geometric sensitivity with Allegro PET Scanner parameters 13

1.9. The change of breathing volume and diaphragm motion within one breathing cycle 13

Chapter 2

2.1 Techniques implementation of respiratory motion compensation 19

2.2 Respiratory motion gating 21

2.3 Optical lased motion tracking system 23

2.4 Sinogram and projection of PET acquisition 27

2.5 Comparison of the sinogram maps between exhale and inhale breathing 27

2.6 LORs out of the scanner field of view 31

2.7 List-mode data format 31

2.8 Comparison of the images between exhale and inhale breathing 33

2.9 Respiratory motion correction 36

2.10 Explanation for transformation matrix 37

2.11 A LOR transformed to another position 38

Chapter 3

3.1 Coordinate system 50

3.2 Image direction at transverse, sagittal and coronal views 51

3.3 Allegro PET scanner crystal orientation 53

3.4 Photo-Multiplier tubes in Allegro PET scanner 53

3.5 The field of view of Allegro PET scanner 54

3.6 Flood maps illustrates covering process for distortions correction 56

3.7 Two line of response events are converted into sinogram with 2D or 3D mode 57

3.8 Structure of GATE 58

3.9 GATE digitiser chain 58

3.10 GATE simulation architecture 60

3.11 A geometric phantom generated by GATE 62

3.12 Voxelised phantom with uniform voxels 63

3.13 Translation of intensity in voxelised phantom to source activities 64

3.14 3D renderings of the NCAT phantom 65

3.15 The procedure of simulation validation for GATE 67

3.16 Comparison of simulation result of Jaszczack phantom by GATE with measurement by Allegro PET Scanner 68

3.17 Comparison of simulation result of Hoffman phantom by GATE with measurement by Allegro PET Scanner 69

3.18 List-mode format of Allegro PET acquisition 74

3.19 Simulated geometric sensitivity of Allegro/Gemini by GATE with 2D and 3D plot 75

3.20 Geometric sensitivity value of three sphere activity sources varies along z axis 76

3.21 Geometric sensitivity gating method 77

3.22 The steps for implementing geometric sensitivity gating (GSG) 79

3.23 Geometric sensitivity correction method 80

3.24 Assuming scattered frame events could reflect motion displacements 82

3.25 The line of response translation within the scanner field of view 85

3.26 The steps of implementing geometric sensitivity correction (GSC) 85

3.27 The gradient of the edge of static image and the motion image 89

3.28 The summary of implementation GSG and GSC 90

Chapter 4

4.1.1 A cylindrical phantom centred at the FOV to do oscillation 94

4.1.2 List-mode data sorting of geometric simulation 95

4.1.3 Variation of frame events of static phantom simulation 97

4.1.4 Variation of frame events of phantom oscillation simulation with 10 cm amplitude 98

4.1.5 Variation of frame events of phantom oscillation simulation with 5 cm amplitude 98

4.1.6 Variation of frame events of phantom oscillation simulation with 2 cm amplitude 99

4.1.7 Variation of frame events of phantom oscillation simulation with 1 cm amplitude 99

4.1.8 The Power Spectral Distribution of frame event rate for 2 cm motion amplitude 100

4.1.9 The Power Spectral Distribution of frame event rate for 1 cm motion amplitude 100

4.1.10 Butterworth filter for phantom motion of 2 cm and 1 cm with low band-pass 101

4.1.11 Band pass filter of frame events for phantom motion of 2 cm amplitude 101

4.1.12 Band pass filter of frame events for phantom motion of 1 cm amplitude 102

4.1.13 Motion amplitude = 10 cm, simulated sinusoidal oscillation was gated by GSG 104

4.1.14 Motion amplitude = 5 cm, simulated sinusoidal oscillation was gated by GSG 104

4.1.15 Motion amplitude = 2 cm, simulated sinusoidal oscillation was gated by GSG 104

4.1.16 Motion amplitude = 1 cm, simulated sinusoidal oscillation was gated by GSG 104

4.1.17 Comparison of line profiles of the gated image for amplitude= 10 cm 105

4.1.18 Comparison of line profiles of the gated image for amplitude= 5 cm 105

4.1.19 Comparison of line profiles of the gated image for amplitude= 2 cm 106

4.1.20 Comparison of line profiles of the gated image for amplitude= 1 cm 106

4.1.21 ROI is masked by yellow boxes for EMR evaluation for gating improvement 107

4.1.22 Comparison of EMR value ratio of the gated image for amplitude= 10 cm 108

4.1.23 Comparison of EMR value ratio of the gated image for amplitude= 5 cm 108

4.1.24 Comparison of EMR value ratio of the gated image for amplitude= 2 cm 109

4.1.25 Comparison of EMR value ratio of the gated image for amplitude= 1 cm 109

4.1.26 Variation of frame events of oscillation with maximum and minimum frames 110

4.1.27 Frame event curve shows 14 frames being corrected to the reference frame 112

4.1.28 One hundred frames simulation with 5cm motion amplitude corrected by GSC 113

4.1.29 First 14 frames motion were corrected by GSC 113

4.1.30 Comparison of line profiles of the motion and the 14 frames corrected-GSC image 114

4.1.31 Motion amplitude = 10 cm, simulated sinusoidal oscillation was corrected by GSC 115

4.1.32 Motion amplitude = 5 cm, simulated sinusoidal oscillation was corrected by GSC 115

4.1.33 Motion amplitude = 2 cm, simulated sinusoidal oscillation was corrected by GSC 116

4.1.34 Motion amplitude = 1 cm, simulated sinusoidal oscillation was corrected by GSC 116

4.1.35 Comparison of line profiles of the corrected image for amplitude= 10 cm 117

4.1.36 Comparison of line profiles of the corrected image for amplitude= 5 cm 117

4.1.37 Comparison of line profiles of the corrected image for amplitude= 2 cm 118

4.1.38 Comparison of line profiles of the corrected image for amplitude= 1 cm 118

4.1.39 Comparison of EMR value ratio of the corrected image for amplitude= 10 cm 120

4.1.40 Comparison of EMR value ratio of the corrected image for amplitude= 5 cm 120

4.1.41 Comparison of EMR value ratio of the corrected image for amplitude= 2 cm 121

4.1.42 Comparison of EMR value ratio of the corrected image for amplitude= 1 cm 121

4.1.43 Geometrical phantom motion amplitude estimated by COM 122

4.2.1 Voxelised phantom was centred in the 18 cm axial FOV of the scanner 128

4.2.2 Sort of list-mode data of voxelised phantom into the sequence of frames 128

4.2.3 Variation of NCAT lung volume during four breathing cycles 130

4.2.4 NCAT lung volume variation curves of during four breathing cycles are overlapped 130

4.2.5 Variation of frame events of phantom 64x64x64 matrix with non-attenuation modelling 131

4.2.6 Variation of frame events of phantom 128x128x55 with non-attenuation modelling 132

4.2.7 Variation of frame events of phantom 128x128x55 matrix with attenuation modelling 132

4.2.8 Comparison of the summed and the gated images for non-attenuation modeling 134

4.2.9 Comparison of line profile images for the summed and the gated image 135

4.2.10 Comparison of the normalized EMR values for the static, the summed and the gated 135

4.2.11 Motion gating with a lesion and with non-attenuation modelling 136

4.2.12 Comparison of line profile images for the images with a lesion 137

4.2.13 Comparison of the EMR values from the static, the summed and the corrected 137

4.2.14 Motion gating with attenuation modeling and a lesion 138

4.2.15 Comparison of the static, the summed and the corrected for NCAT phantom 141

4.2.16 Comparison of line profile images for the images with a lesion for NCAT phantom 142

4.2.17 Comparison of the EMR values for the static, the summed and the corrected for NCAT 143

4.2.18 NCAT phantom motion amplitude estimated by COM 143

4.3.1 Sort of list-mode data of Allegro or Gemini PET/CT into the sequence of frames 146

4.3.2 Variation of frame events of patient numbered P1 148

4.3.3 Variation of frame events of patient numbered P2 148

4.3.4 The Power Spectral Distribution of frame events for patient P1 150

4.3.5 Butterworth filter for patient P1 with band-pass 0.1Hz-0.3Hz 150

4.3.6 Power Spectral Distribution of frame events for patient P2 151

4.3.7 The filtered curve of frame events for P1 152

4.3.8 The filtered curve of frame events shows fits well the non-filtered for P1 152

4.3.9 The filtered curve of frame events for P2 153

4.3.10 The filtered curve of frame events shows fits well the non-filtered for P2 153

4.3.11 Comparison of the summed and the gated image for P1 by GSG 154

4.3.12 Comparison of line profile image from the summed and the gated for P1 155

4.2.13 Comparison of the EMR values for the summed and the gated for P1 155

4.3.14 Comparison of the summed and the corrected images for P1 157

4.3.15 Comparison of line profile image from the summed and the corrected for P1 157

4.2.16 Comparison of the EMR values for the summed and the corrected for P1 158

4.3.17 The reconstructed corrected 296 frames by GSC for patient P2 158

4.3.18 The reconstructed corrected 360 frames at coronal for P2 by GSC 159

4.3.19 Comparison of line profile form the summed and the corrected images for P2 159

4.2.20 Comparison of the EMR values for the summed and the corrected for P2 160

Chapter 5

5.1 Variation of geometric sensitivity along axial position in 2D, 3D mode PET Scanner 168

5.2 Limitations of the methods in conditions of a balanced radioactivity distribution 168

5.3 Variation of the sum of sensitivity value in different motion or radioactivity states 170

List of Tables

1.1 2D mode PET scanner versus 3D mode PET scanner 3

1.2 Positron range 5

3.1 Features of Allegro/Gemini PET Scanner 52

3.2 A summary of validation for the GATE simulations 71

4.1 Comparison of FWHM of the static, the motion and the gated images 107

4.2 Comparison of FWHM of the static, the motion and the corrected images 119

4.3 Simulation Activity in the NCAT phantom with 64x64x64 matrix 125

4.4 Lesions in lung generated in the NCAT phantom with 128x128x55 matrix 125

4.5 Simulation Activity in the NCAT phantom with 128x128x55 matrix 126

4.6 Comparison of FWHM of the static, the motion, and GSC correction images 142

List of Abbreviations

AIR	Automated Image Registration
COM	Centre of Mass
CT	Computed Tomography
ECG	Electrocardiogram
EMR	Edge Magnitudes Range
FFT	Fast Fourier Transform
^{18}F-FDG	^{18}F-Fluoro-2-Deoxy-Glucose
FOV	Field of View
GATE	Geant4 Application for Tomographic Emission
GSC	Geometric Sensitivity Correction
GSG	Geometric Sensitivity Gating
GTV	Gross Tumor Volume
LOR	Line of Response
MAF	Multiple Acquisition Frame
ML-EM	Maximum Likelihood Expectation Maximisation
MRI	Magnetic Resonance Imaging
NEMA	National Electrical Manufactures Association
NURBs	Non Uniform Rational B-Splines
NCAT	NURBs-Based Cardiac Torso
OPL-EM	One-pass List Mode ML-EM
PET	Positron Emission Tomography
PSD	Power Spectral Distribution
RAMLA	Row Action Maximum Likelihood Algorithm
ROI	Region of Interest
SUV	Standard Uptake Value
SPECT	Single Photon Emission Tomography
SPM	Statistical Parametric Mapping
UGM	Ulrike Gerhard Mueller
VOI	Volume of Interest

Summary

Image degradation caused by respiratory motion is an issue of concern in clinical positron emission tomography (PET) imaging. Compensation for respiratory motion requires an accurate motion sensor or a complicated data driven method. This thesis describes two new methods for respiratory motion gating and correction that relies upon information from the list mode data stream. The methods are based on a proposed hypothesis that geometric sensitivity varies along the z axis of a 3D PET scanner and can be used to compensate for respiratory motion. This hypothesis was developed into two directions: Geometric Sensitivity Gating (GSG) for respiratory motion gating and Geometric Sensitivity Correction (GSC) for respiratory motion correction.

To test the proposed hypothesis, two steps have been undertaken in this thesis: simulation and clinical validation. Simulations were implemented by the use of Geant4 Application for Tomographic Emission (GATE) and NURBs-Based Cardiac Torso (NCAT) software packages to simulate the Phillips Allegro/Gemini PET Scanner and respiratory motion respectively. Patient data with both tumour and non-tumour cases were collected and clinical validation was performed on it. All data was collected in list-mode data format, which can be sorted into a sequence of frames. Then the proposed specific hypothesises GSG and GSC was applied to the sorted frames respectively.

Simulation validations consist of geometric phantom and voxelised phantom validation. The geometric validation was implemented using a cylindrical phantom with a known sinusoidal oscillation. This oscillation was used as a representation of simple respiratory motion. When GSG and GSC were applied to the sorted list-mode data, they were shown to be able to gate and correct for the motion. For a more realistic simulation of respiratory motion, voxelised phantoms generated by NCAT were imported into GATE and employed to validate GSG and GSC, and gave encouraging indications for the application of respiratory motion gating and correction. Finally, when applied to the clinical patient data, it was demonstrated that the artifacts caused by respiratory motion were significantly reduced using GSG and GSC. Additional benefits of these two methods include:

- No additional hardware device is required;
- They only use list-mode data and are non-invasive;
- There is no acquisition burden;
- There is no additional patient preparation required;
- There is no additional time required for clinical setup;

This thesis demonstrates the proposed hypothesis of using the geometric sensitivity properties of a 3D PET scanner for respiratory motion compensation and proves this hypothesis using results from simulated and clinical studies.

CHAPTER 1
INTRODUCTION

1 Introduction

1.1 POSITRON EMISSION TOMOGRAPHY 1

1.1.1 History 1

1.1.2 Basic Principle 5

1.2 PROBLEM STATEMENT 6

1.3 HYPOTHESIS 8

1.4 OBJECTIVES 15

1.5 THESIS STRUCTURE 16

1.1 Positron Emission Tomography

1.1.1 History

Positron Emission Tomography (PET) is one of several non-invasive diagnostic examination imaging techniques as shown in Fig 1.1. PET involves the acquisition of functional images based on the detection of radiation due to the emission of positrons from an injected radiopharmaceutical. There has been a tremendous increase in the use of PET as both a clinical and research imaging modality in the past 15 years[1]. PET imaging today has value in the care of patients with suspected or known cancer, for establishing the diagnosis in detecting early stage of cancer, for treatment planning and monitoring therapy treatment [2], and for fundamental research on drug uptake and brain function.

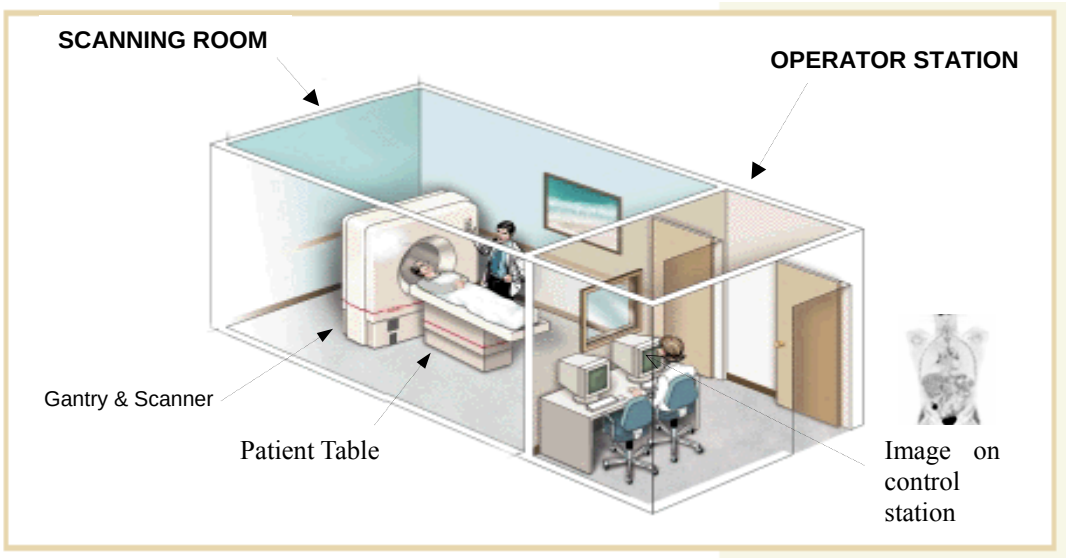

Fig 1.1 PET imaging system overview for scanning and operation rooms.

In 1933, Thibaud[3] and Joliot[4] discovered positron emission from radioactive nuclei, which led eventually to the first images from coincidence imaging of positrons for localization of brain tumors in 1951 by a research group, Wrenn *et a*l, at the Massachusetts General Hospital[5]. Subsequently, several research groups around the world began the application of coincidence

imaging of positrons for lung studies in 1951 [6] and for cardiac studies in 1961 [7] respectively. However, scanning techniques preceded the development of the mathematical and computational techniques required for reconstruction of tomographic images by more than a decade.

Tomography has been one of the pillars of radiological diagnostics since the availability of minicomputers and the application of the transverse axial scanning method enabled Hounsfield and Cormack to invent the modality of CT in 1972[8]. To improve the quality of the reconstruction image, in 1973 Chesler applied the x-ray tomography algorithm to the data collected from a positron camera to produce transaxial tomographic reconstructions[9].

In the early stage of PET development a 2D scanner was the conventional mode of scanner. Septa were placed between the transaxial planes in order to reduce the scattered coincidences and shield detectors from out-of-plane annihilation γ-rays as shown in Fig 1.2. At the end of the 1970s, the recording of scattered coincidences and random events were minimized by using parallel delayed coincidence circuits technique[6], and recording transmission scans with ring source to provide accurate corrections for tissue attenuation[10], which meant quantifiable tomographic physiological data was improved. In addition, the 2D mode scan also results in sensitivity reductions as shown in Fig 1.2. To increase sensitivity, 3D PET was proposed in the mid-1980s, which involved withdrawing the septa and recording all possible coincidences, thereby increasing the basic sensitivity [11] as shown in Fig 1.2. Many different PET scanners including whole body scanners had been developed at that time, especially for studies of the brain[12]. A wide range of clinical applications and research studies using PET modality developed in the 1990s due to the improved detector design and spatial resolution[1].

In a conventional 2D mode scan, septa were placed between the transaxial planes in order to reduce the scattered coincidences and shield detectors from out-of-plane annihilation γ-rays, however it also results in the sensitivity reductions as shown in Fig 1.2. To increase sensitivity, 3D PET was designed in the mid-1980s which involves withdrawing the septa and recording all

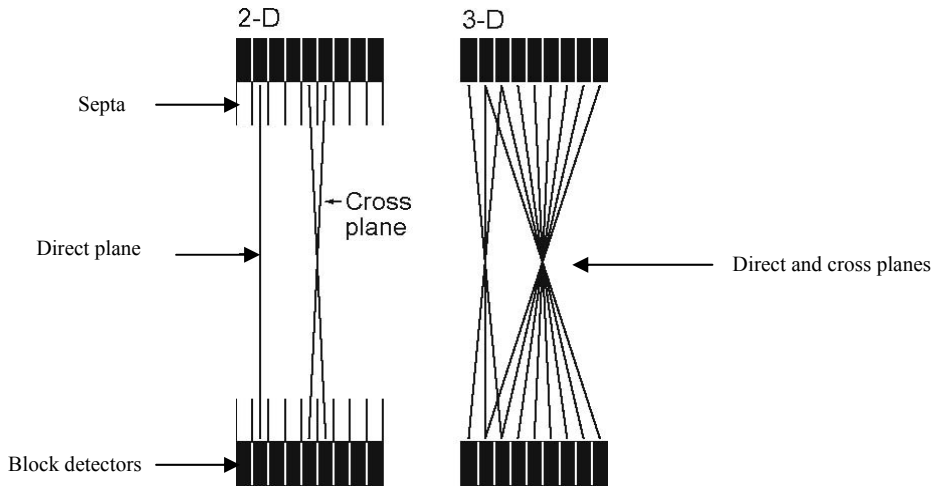

Fig. 1.2. Comparison between 2D and 3D acquisition modalities. Removal of septa used to shield of detectors from out-of-plane events significantly increases sensitivity to radioactive sources near centre of thFOV.

possible coincidences, thereby increasing the basic sensitivity[11] as shown in Fig 1.2. A brief performance comparison of 2D mode versus 3D mode is listed in Table 1.1. Many different PET scanners including whole body 3D mode scanners had been developed at that time, especially for studies of the brain[12]. A wide range of clinical applications and research studies using PET were developed in the 1990s due to the improved detector design and spatial resolution, 3D mode then became mainstream in the late 1990s[1].

Table. 1.1
2D mode PET scanner versus 3D mode PET scanner

Performance	**BGO**		**GSO**	**NaI(TI)**
	2D	**3D**	**3D**	**3D**
Scatter fraction (%)	17	37	32	28
Sensitivity (cps/Ba/ml)	5.7	30.4	24	12.7
NEMA-NU-94: Peak NEC (kcps)	84	110	180	58

Computed tomography (CT) and magnetic resonance imaging (MRI) are used to provide anatomical information within the body, while PET reveals regional function activity about biological processes. PET makes it possible to measure the temporal and spatial variations of

these molecular processes in a living being. However, accurate anatomic localization of functional abnormalities seen on PET scans is well known to be challenging because of the lack of detailed, high-resolution anatomy. With the combination of advantages of structural and functional imaging, the evolution of the technology ultimately joining CT and PET into a hybrid system that provides intrinsic image co-registration in early 2000 is shown in Fig 1.3[13]. It helps to minimize the uncertainty of co-registering anatomical information with functional information. In addition, attenuation measurements can be significantly shortened by utilising the CT scan, but that introduces problems such as respiratory motion artefacts due to CT transmission mismatch with emission acquisition.

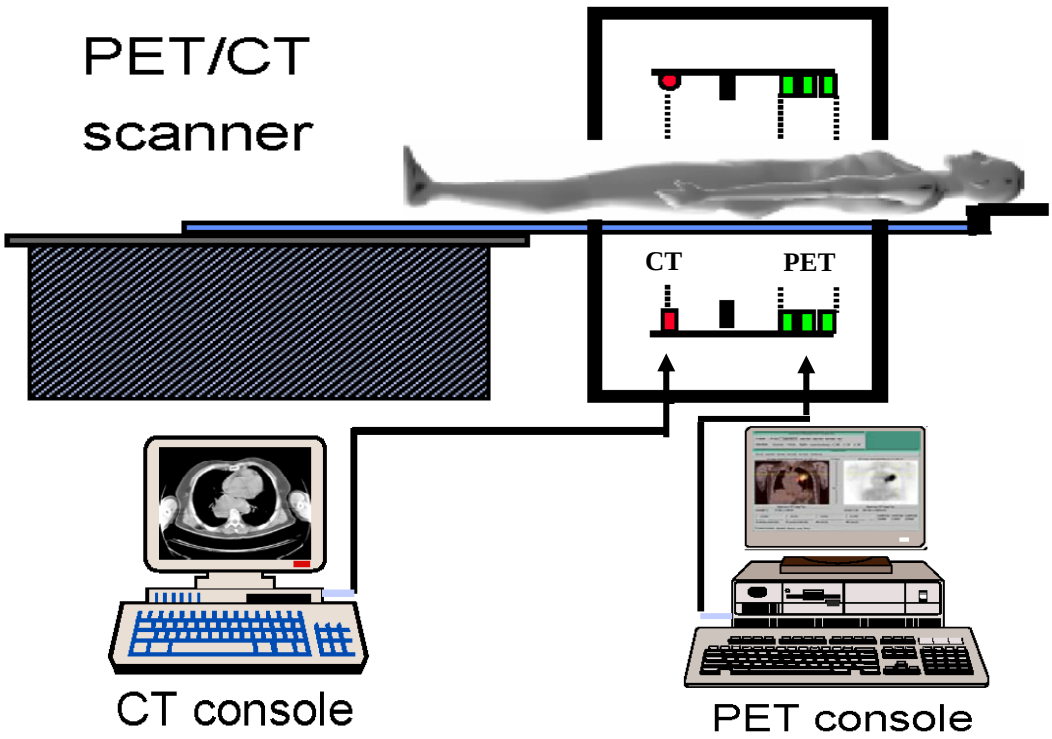

Fig. 1.3. PET/CT imaging system, CT image registered with PET image for diagnosis.

PET imaging is currently applied in therapy planning and monitoring[14] [15]. The most important aspect of radiation therapy is locating the target in the required position accurately at the time of treatment. There is already a loss of accuracy from not knowing the precise physical extent of the active tumor within the planned radiation field[16]. The combination of PET/CT is able to define the gross tumor volume (GTV) with greater accuracy than is possible with the CT

modality alone[17].

1.1.2 Basic Principle

The process of positron emission decay and detection as show in Fig 1.2, a positron emission isotope radiotracer is injected into the human or animal by intravenous injection. After an appropriate uptake period, the concentration of tracer in tissue is measured by the scanner. During its decay process, the radionuclide emits a positron which travels a short distance (positron range) in tissue as illustrated in Table 1.2, then the positron will combine with an electron from the surrounding environment, and the two particles will undergo an annihilation resulting in the emission, in opposite directions, of two gamma photons of 511 keV as illustrated in Fig. 1.4. The positron range is one of the inherent performance limitations of PET. In addition, the non-colinearity of gamma rays and Compton scatter also impose physical limits on the resolution of PET.

The image acquisition is based on the external detection of the coincidence of the annihilation gamma photons. A valid annihilation event requires a coincidence between two detectors within a designed coincidence time window, typically 6-12 nsec. For accepted coincidences within the coincidence time window, lines of response (LOR) connecting the coincidence detectors are drawn through the object. The LORs are used in the reconstruction of the images.

Table. 1.2: Positron Range

Max β^+ Energy		**Average Range**	**Maximum Range**
(Mev)		**(mm)**	**(mm)**
F-18	0.64	0.64	2.3
C-11	0.96	1.03	3.9
N-13	1.19	1.32	5.1
O-15	1.72	2.01	8.0
Rb-82	3.35	4.29	16.5

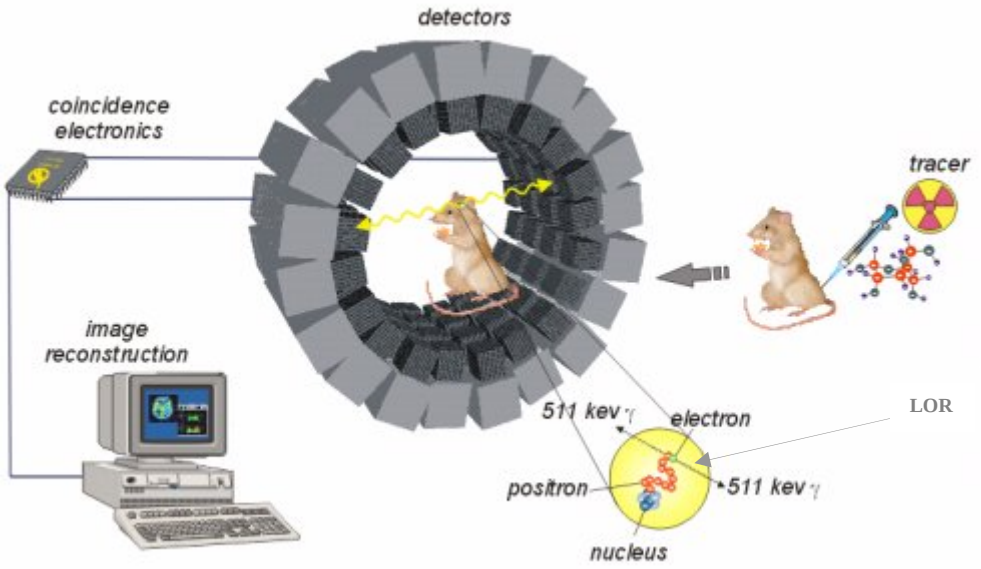

Fig. 1.4. Schematic representation of the principles of PET imaging.

PET imaging in oncology already has an important role in staging of cancer and the investigation of disease recurrence. PET has shown many advantages over x-ray CT imaging[17, 18]. However, PET still has some challenging tasks such as the compensation of respiratory motion artefact. In the thoracic-abdominal region, parts of the lung, liver, and other organs move appreciably due to breathing, which degrades the accuracy of imaging, treatment planning and delivery.

1.2 Problem Statement

The PET data are acquired over an elongated period of time (typically 3-5 min/bed position) and, thus, represent the sum of information gained over the whole period of acquisition. As the patients are continuously breathing during the procedure, there is unavoidable lung movement which affects image quality. Breathing results in the displacement of organs in the thorax such as lungs, heart, ribs etc. Respiratory motion affects mainly organs of the thorax and abdomen, particularly in the diaphragmatic area as illustrated in Fig. 1.5[19] which gives rise to attenuation correction artifacts and mis-localization of the lesion [20-22].

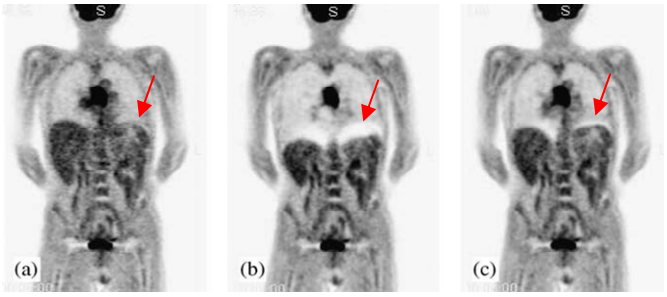

Fig. 1.5. Whole-body PET images demonstrating artifacts at the level of the diaphragm as a result of respiratory motion differences between emission and transmission maps used for attenuation correction; use of (a) CT acquired at normal breathing, (b) CT acquired at breath-hold (end inspiration), (c) CT acquired at breath-hold (end expiration).

Attenuation correction is the method for correcting the PET data for the effects of different types of tissues the photons pass through on their way to the detectors. Attenuation correction can be performed by measuring transmission of radiation from a single photon emitter such as Cs-137 or CT scan. In PET/CT scans[22], as the CT images are acquired much faster (typically 0.5 sec per slice) than PET images and moreover in breath hold technique, they represent a static view of the breathing cycle in contrast to the PET image which is acquired over several minutes per bed position. Therefore, a part of the PET data will mismatch the attenuation distribution (e.g., activity from heart may be attenuated with lung density, etc.) and only that part of the PET data which corresponds to the CT position in the breathing cycle will be correctly attenuated. Incorrect attenuation correction will result in the incorrect determination of reconstruction isotope density[23] [24] [25].

Evidence of artifacts caused by respiratory motion has been observed[20]. The motion of lungs during the PET acquisition may lead to incorrect staging of tumours[26]. A study [27] of 42 patients showed that in 98% of the cases, artifacts due to respiratory motion were present on the images. Again, studies showed that imaging lesions near the lung base, which has the most pronounced motion due to breathing, might involve significant motion artifacts[28] .Another study[29] showed that 84% of patients had respiratory motion induced artifacts in the right lung, including 2% classified as “severe” and 84% had the same in the left lung including 10% classified as “severe” respiratory motion artifacts. Major affects result from respiratory motion along the cranial-caudal direction, in which direction an average amplitude of the tumour motion of 12±2mm in the lower lobes of the liver[21]and diaphragm motion of up to 15-25mm[30] have

been observed during scanning.

Motion distortion is a major problem degrading resolution when imaging lungs[29]. A number of existing techniques for respiratory motion compensation have improved PET imaging such as gating techniques and registration techniques. However, robustness and an intrinsic nature have still been demanded for improving existing techniques in clinical application[31, 32]. For example, monitoring systems for respiratory motion gating need to integrate the signal of external devices into the emission data of PET acquisition, which may cause extra cost. In addition, most existing techniques for respiratory motion compensation involve implementing the algorithms of motion correction in the image domain which can be time-consuming. Therefore, the aim of this research study is to investigate an effective method for the respiratory motion gating and correction by using the intrinsic features of the geometric sensitivity in 3D PET imaging.

1.3 Hypothesis

In PET imaging, system sensitivity is a key factor in obtaining high-quality images[33] [34] [35]. System sensitivity can be defined as the number of events (in counts per second) detected per unit of radioactive concentration (cps/Bq/ml) in a specific phantom. The system sensitivity (η) is a product of several factors, which include intrinsic efficiency (δ) and geometric efficiency. The intrinsic efficiency involves detector efficiency, crystal materials and photopeak efficiency. The geometric efficiency (ε) is related to the overall solid angle (Ω) coverage of the detectors with respect to the source location and the packing fraction (φ) that is the ratio of the detector element area to the total surface area. The overall system sensitivity is given by [36].

$$\eta = 100 \times \frac{\delta^2 \varepsilon}{4\pi} = 100 \times \frac{\delta^2 \varphi \Omega}{4\pi} \quad (1)$$

In this thesis, the feature of geometric efficiency will be the main focus and will be utilised to compensate respiratory motion. “Geometric efficiency” and “geometric sensitivity” have the same meaning in this thesis.

The 3D acquisition mode as shown in Table 1.1 provides a dramatic improvement in sensitivity compared to 2D acquisition by removing the tungsten septa as illustrated in Fig 1.2[37]. As a result of recording all possible coincidences of direct and cross planes, higher sensitivity can be achieved in 3D mode as shown in Michellograms maps in Fig 1.6[38]. The axial sensitivity drops off linearly at the edge of the axial FOV because no additional cross-plane combinations can be added to the planes at the axial extremes. When acquiring in 2D and 3D mode, one may limit the geometric range of allowable coincidences. The axial extent of the coincidences allowable in 3D PET is characterised by "maximum ring difference" (RD or nspan) as displayed in Fig 1.6. 3D Scanner retracts the septa allows coincidences from any detector ring with any other detector ring. The advantage of not using septa is that the sensitivity of the scanner is substantially improved. However, disadvantages are the increase in the amount of scatter (from 10%- 15% to 30%- 40%), the increase in the random coincidences from activity that is out of the field of view, which result in the 3D datasets being in some senses incomplete. In 3D PET, an analogous situation would occur if the scanner had the geometry of a sphere which all possible projection angles would be measured. However, PET scanners generally have a cylindrical geometry and the limited axial length of the scanner results in projections that are truncated in the axial direction. As the ring difference is increased, the truncation because more severe. An accurate reconstruction requires that this truncation be removed for the "maximum ring difference" that are to be included to improve the signal-to-noise of the reconstructed image. Planes in the centre of the gantry have the highest plane sensitivity whereas the planes on the axial periphery have the lowest. Plane sensitivity is a function of axial position or plane number as shown in Fig 1.2. In all cases, the plane sensitivity ramps up to a maximum value toward the axial centre of the gantry and eventually ramps down.[39].

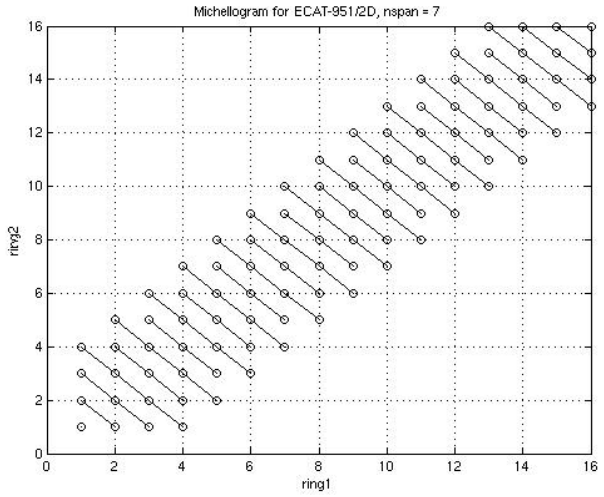

(a). 2D Michellogram with ring difference = 7 for a 16 ring detector

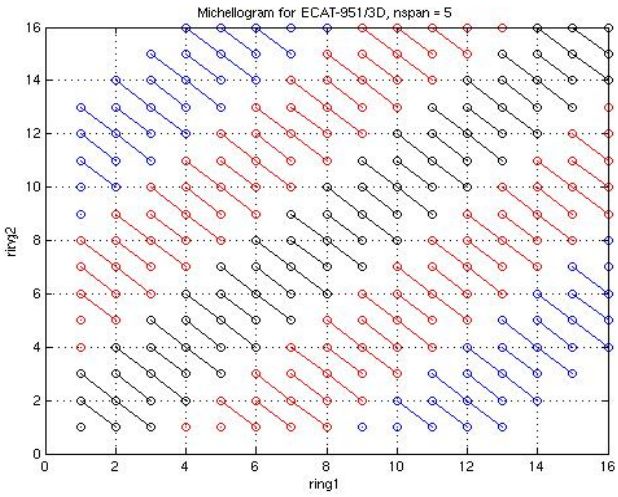

(b). 3D Michellogram with ring difference = 5 for a 16 ring detector. Colour Coding indicates all possible acceptable LORs in the ring difference 5 is allowed from ring 1 to ring 16.

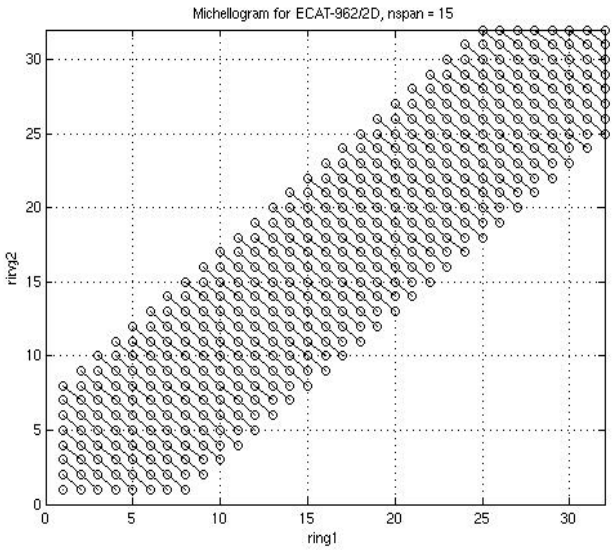

(c). 2D Michellogram with ring difference = 15 for a 30 ring detector.

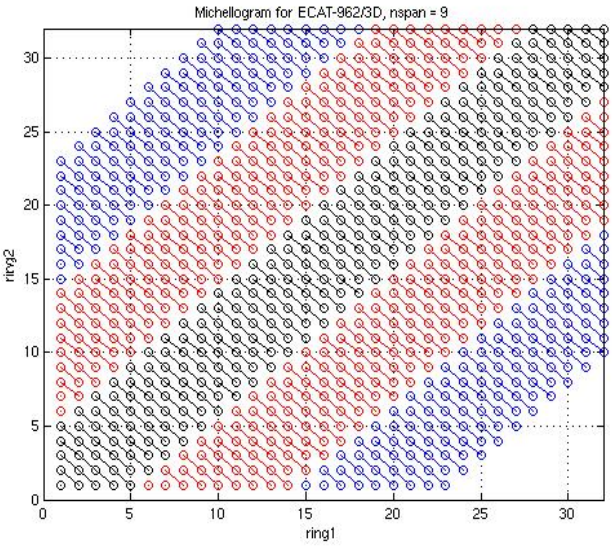

(d). 3D Michellogram with ring difference = 9 for a 30 ring detector. Colour Coding indicates all possible acceptable LORs in the ring difference 9 is allowed from ring 1 to ring 32.

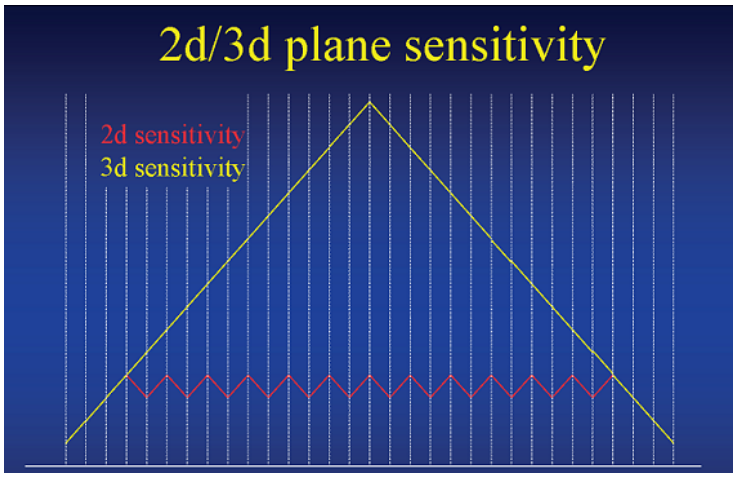

(e). 2D and 3D geometric sensitivity

Fig 1.6. Comparison of the geometric sensitivity and the coincidences allowable in 2D and 3D mode by Michellogram maps, they show 3D mode covers more 90% of ring-ring combinations for the coincidences collection in (b) and (d).

Specifically, for a 3D septaless PET system as illustrated in Fig. 1.7, *Z* is the offset of the point source P from the centre of the FOV, *A* is the axial length and *D* is the detector ring diameter. For example, for the Philips Allegro PET scanner, the variation of geometric sensitivity value along axial direction was plotted as shown in Fig 1.8. It can be seen that the geometric sensitivity is not uniform across the axial direction. The geometric sensitivity decreases linearly with increasing axial separation from the centre of the scanner with a maximum sensitivity at the centre of the scanner. That is, due to the cylindrical geometry of the PET scanner, the probability of detection of annihilation at a certain position depends on the location of the decay. As an organ moves through the axial FOV, the sensitivity to detected LOR events will vary as displayed in Fig. 1.7, which may associate with organ motion position. For example, LOR events were collected from an organ dynamic frame scan. By nominally binning acquired LOR events into 200msec frames, a change in the number of LOR events in a frame, 'frame events' will indicate a change in axial position with respect to the previous frame.

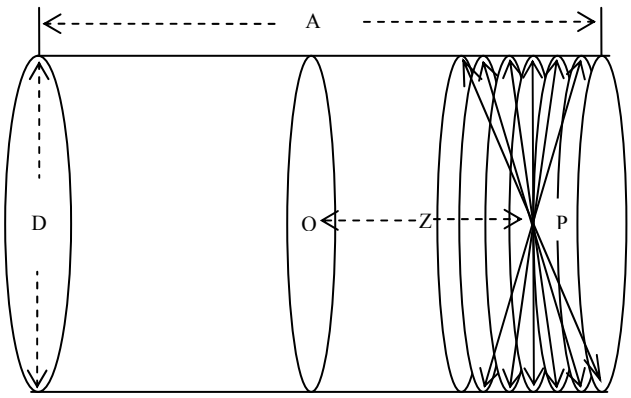

Fig. 1.7. The geometrical sensitivity of 3D PET cylindrical scanner determined by Z the axial distance from O the centre of the FOV to P the point source position. Sensitivity is highest at the centre than offset positions. Note: A and D are not to the same scale.

Specifically, for a 3D septaless PET system as illustrated in Fig. 1.7, Z is the offset of the point source P from the centre of the FOV, *A* is the axial length and *D* is the detector ring diameter. The geometric sensitivity (ε) can be calculated by formula (2). For example, for the Philips Allegro PET scanner, the variation of geometric sensitivity value along axial direction was plotted as shown in Fig 1.7 according to formula (2). It can be seen that the geometric sensitivity is not uniform across the axial direction. The geometric sensitivity decreases linearly with increasing axial separation from the centre of the scanner with a maximum sensitivity at the centre of the scanner. That is, due to the cylindrical geometry of the PET scanner, the probability of detection of annihilation at a certain position depends on the location of the decay along the axis. As an organ moves through the axial FOV, the sensitivity to detected LOR events will vary as displayed in Fig. 1.8, the changes in counts rate then be used to determine organ motion position. For example, by binning acquired LOR events into nominally 200msec frames, a change in the number of LOR events in a frame, 'frame events', will indicate a change in axial position with respect to the previous frame.

$$\varepsilon(Z) = \frac{A - 2Z}{\sqrt{(D^2 + (A + 2Z)^2}} \qquad (2)$$

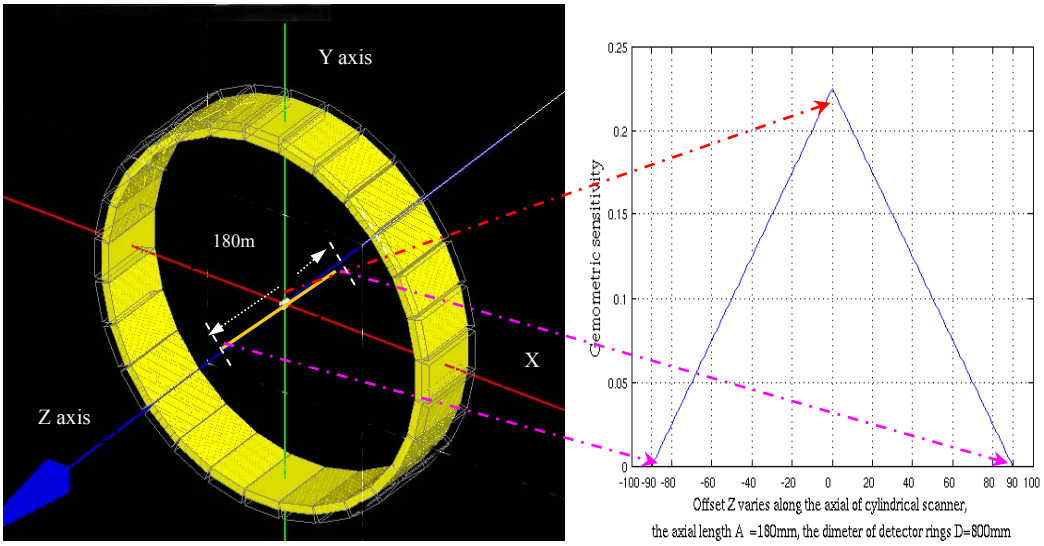

(a). Simulation of Philps Allegro/Gemini PET

(b). Geometric sensitive calculated by formula (2).

Fig. 1.8. For the Philips Allegro Scanner, the geometrical sensitivity of 3D PET cylindrical scanner varies with the axial position. The sensitivity value is the highest at the centre of FOV while the sensitivity value at the edge of FOV is close zero.

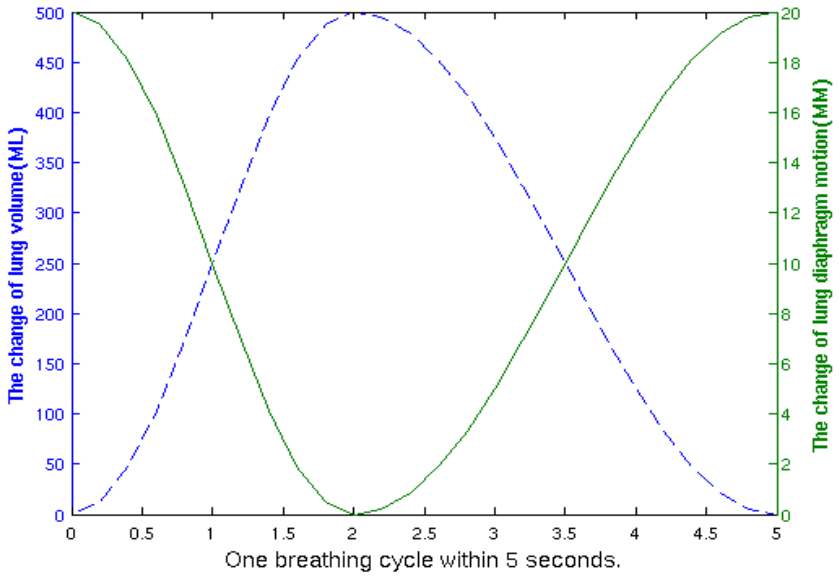

Fig. 1.9. The change of breathing volume and diaphragm motion within one breathing cycle including inhale and exhale.

Respiratory motion results from the diaphragmatic expansion/contraction cycle of the lung cavity.

The change on respiratory volume and diaphragm motion within one breathing cycle [40, 41]

have been determined and are illustrated in Fig. 1.9. The respiratory motion is not one-dimensional, but a combination of movement in all three dimensions, motion along cranial-caudal direction for tidal breathing has been observed to be the most significant component in diaphragm at 17±3mm [42]. For tumour motion due to tidal breathing an amplitude of 12±2mm has been observed, especially in unfixed lower-lobe tumours[21].

As a result, organs in the thoracic volume will undergo displacement during the respiratory cycle and will occupy different axial positions within the scanner of the PET scanner. In terms of the properties of geometric sensitivity of a 3D PET scanner, since the geometric sensitivity of a 3D PET cylindrical scanner varies along the axial position as illustrated in Fig. 1.7, the event rate detected by the scanner from given organs will be subject to the axial position of the organs. If each axial position of the organs can be regarded as one respiratory motion phase within one motion cycle, the respiratory phase can then be determined from event rates changes. The event rate of for a particular organ reaches a maximum when respiration moves it to the centre of the FOV and a minimum when moves to the FOV edge. Therefore, with different events rate from breathing cycles, it is possible to extract the respiratory phase of interest such as the maximum or minimum phase for motion gating. This hypothesis for respiratory motion gating is called Geometric Sensitivity Gating (GSG).

Respiratory gating of only a single respiratory phase results in a reconstructed image with increased noise. To reduce the noise, a correction technique is developed to utilize all phases for motion correction. According to the variation of the geometric sensitivity along the axial direction within scanner, each phase of breathing cycle has a movement displacement offset position along the axial direction, each displacement then corresponds to some events rate collected. The relationship between the displacement and the events rate may be assumed to be correlated with the lung volume change and the diaphragm motion change as shown in Fig 1.9. As a result of the relation of displacement and events rate, a transformation displacement may be determined for correcting the respiratory phases to a reference phase for motion correction. This hypothesis for respiratory motion correction is called Geometric Sensitivity Correction (GSC).

Therefore, based on the unifying hypothesis that the properties of geometric sensitivity of 3D PET scanner would be employed to indicate the characteristics of respiratory motion, the specified hypothesises may be divided into two categories: respiratory motion gating and respiratory motion correction could be implemented by the GSG method and the GSC method respectively.

The proposed methods, GSG and GSC are novel ideas. Both methods have several advantages over existing techniques:

- No additional hardware device is required;
- They only use list-mode data stream and are non-invasive;
- There is no acquisition burden;
- There is no additional patient preparation required;
- There is no additional time required for clinical setup;

1.4 Objectives

The aim of the research presented in this thesis is to investigate an effective technique for respiratory motion compensation by the use of the geometric sensitivity properties of a 3D PET scanner. The proposed hypothesises will be validated by using simulation studies and clinical studies. The following specific objectives for this work are:

1. The GSG method and the GSC method are tested in a simulated geometric phantom both without attenuation and with attenuation modelling. These simulations for the GSG method were performed for one dimensional motion along the Z axis and three dimensional motion along X, Y and Z axis, but simulations for GSC were purely a one dimensional motion test along the Z axis.
2. The GSG method and the GSC method are evaluated for a simulated voxelised phantom both without attenuation and with attenuation modelling. This evaluation involves 3D non-rigid motion along X, Y and Z dimensions.
3. Finally, the GSG method and the GSC method are validated against clinical studies.

1.5 Thesis Structure

The work undertaken to meet the objectives in this thesis is presented in five chapters as follows;

- Chapter 1 outlines the background of the study including the problem statement and hypothesis.
- Chapter 2 reviews the existing techniques to address respiratory motion compensation, specifically motion gating and motion correction.
- Chapter 3 provides methodology for hypothesises testing in the simulation and clinical data.
- Chapter 4 details the results of the simulation with geometric and voxelised phantoms. Important practical considerations in implementing the proposed approach with clinical data are also described.
- Chapter 5 summarises the results of the previous chapters and draws conclusions on the presented the research work, and also discusses the limitations and future development of this work.

CHAPTER 2
LITERATURE REVIEW

2 Literature Review

2.1 MOTION GATING TECHNIQUES 20

2.1.1 External Monitor Systems Methods 20

2.1.2 Data-Driven Methods 25

2.1.2.1 Sinogram Based Gating Methods 26

2.1.2.2 List-mode Data Based Gating Methods 30

2.1.2.3 Image Based Gating Methods 33

2.2 MOTION CORRECTION TECHNIQUES 36

2.2.1 List- mode Data Based Correction Methods 37

2.2.2 Sinogram-Based Correction Methods 39

2.2.3 Reconstruction-Based Correction Methods 41

2.2.4 Image-Based Correction Methods 42

2.3 SUMMARY 45

Artifacts and image degradation caused by respiratory induced motion may lead to misinterpretation of images and quantitative errors. Various methods for respiratory motion compensation, such as gating techniques, have been developed. These techniques may be divided into two stages: the first is respiratory motion gating, which involves the use of respiratory synchronized indicators to estimate motion parameters for gating respiratory acquisitions by external tracking systems or an intrinsic data-driven method; the second stage is motion correction, which registers the gated data with motion information, such as the motion transformation parameters, to the reference respiratory phase.

A number of techniques for respiratory motion gating and correction currently exist [19, 31, 43]. To review those techniques easily and logically, this chapter will sort the techniques into different classifications, in terms of which stage of the PET imaging procedure they modify, as illustrated in Fig 2.1. Although the exact procedure of PET imaging involves many stages, for the purpose of classification within the review, it may be divided into three steps as illustrated in Fig 2.1. In the first step, the PET scanner acquires line of response (LOR) events as raw data, so that the acquisition data (LORs) are sorted into sinogram space (refer to Chapter 2.1.2.1) with angle and distance as projections data or list-mode format (refer to in Chapter 2.1.2.2). In the second step, a reconstruction algorithm is chosen to reconstruct the image. In the third and final step the reconstructed image is obtained.

All existing techniques for respiratory motion compensation can be classified as modifying one or more of these basic three steps of PET imaging. As shown in Fig. 2.1, compensation techniques for respiratory motion consist of two stages: Stage 1, motion gating, generally involves acquisition of gating data from tracking devices. Stage 2, motion correction, applies the acquired gating data and can be performed at any of the list-mode, sinogram, reconstruction or tomographic images stages of PET imaging.

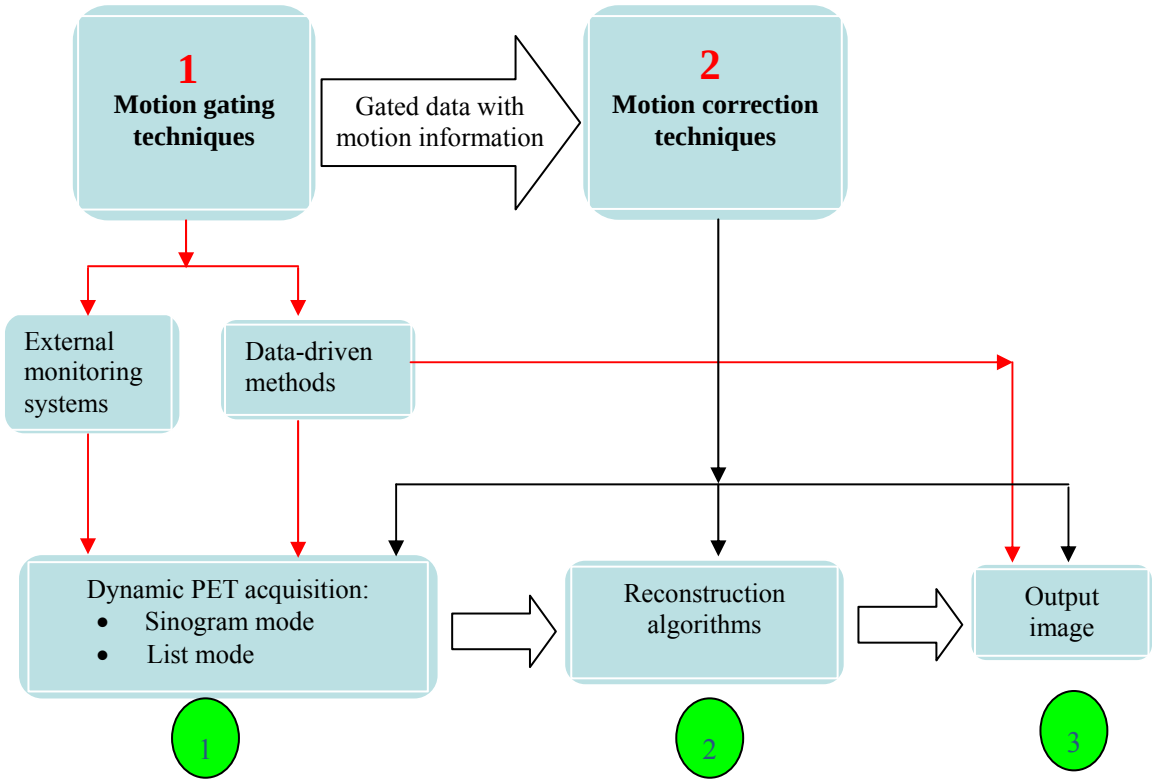

Fig. 2.1. Motion compensation may be divided into 2 stages, gating and correction. The process of PET imaging may be simply divided into 3 steps, PET data acquisition with sinogram or list-mode, image reconstruction algorithm chosen and output reconstructed image. Respiratory motion gating or correction techniques may be implemented on one of 3 steps.

2.1 Motion Gating Techniques

Motion gating techniques separate breathing cycles into discrete phases of the respiratory cycle by recording a signal that is a surrogate for the respiratory motion. The procedure of motion gating is shown schematically in Fig. 2.2, for two cycles of the respiratory motion. Each cycle is separated into 8 motion phases each with a different colour bar. The same colour bar represents that respiratory phase within the second cycle. Thus colour bars 1 and 9, belonging to the same phase, will be summed together to represent the first gated phase. The temporal resolution (t_1, t_2, t_3, …t_n) needs to be selected so that the range of motion within a single temporal phase is commensurate with the spatial resolution, which means if sufficient respiratory phases are used, each gated phase may be approximately considered as respiratory motion free. Existing techniques used for motion gating can be classified into two types; external monitoring and data driven. The external monitoring systems method involves tracking motion position information using external monitoring devices. The data-driven method (internal method) uses the data itself to estimate the phase of respiratory motion. External monitoring techniques can detect the object motion for a surface measurement in all directions, but internal motion of the object may not correlate directly with the external monitoring. In contrast, data-driven methods can accurately reflect internal motion by analysing data-driven triggering for motion compensation. Data-driven methods for respiratory motion gating are the primary emphasis of this review as they are pertinent to the proposed hypothesises in this thesis.

2.1.1 External Monitor Systems Methods

A large number of studies have been devoted to the development of respiratory motion gating by external tracking systems for PET imaging including electromagnetic, mechanical, optical, infrared, spirometric, air flow and temperature sensors. It is essential to synchronize the measurement of the respiratory motion by the external tracking system with the emission data of the PET camera. For this purpose all current clinical PET camera systems have an interface port (mostly to support cardiac gating) to which a gating signal can be applied to determine into which

phase the emission data should be summed at that instant. The required input is often an analogue voltage or current but the number of available phases is usually limited to no more than sixteen. All respiratory data from the external tracking system, regardless of whether it relates to translation or rotation may be tracked and converted into the electronic signals such as the current or voltage to be applied on respiratory gated acquisitions or for the motion correction stage.

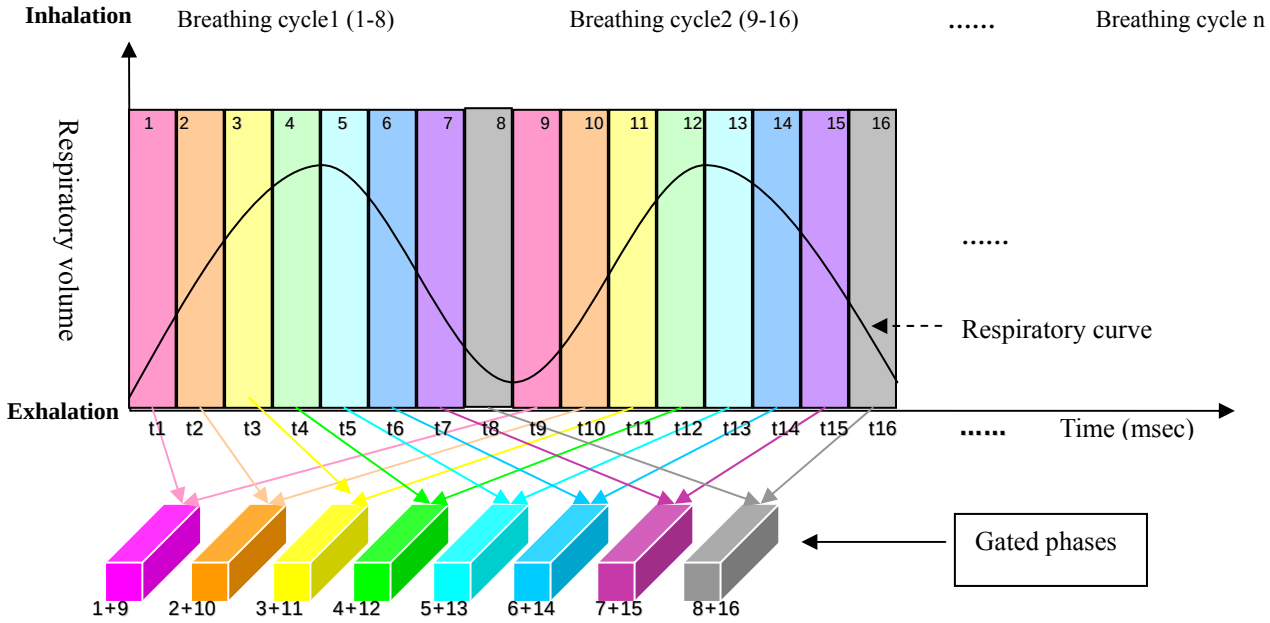

Fig. 2.2. Two breathing cycles for gating procedure with 16 phases, each bar represents one phase of breathing, same color bars in two breathing cycles mean at the same phase of breathing cycles. These two breathing cycles can be gated by 8 phases.

Electromagnetic motion tracking systems were reported first for detecting head motion[44-46]. Such systems can be applied to respiratory motion tracking as well[46]. The tracking process consists of a reference field that induces currents in orthogonal coils fixed to the patient. The induced currents can be converted to positional information via calibration data. This technique is suitable for the tracking of flexible endoscopes or other instruments within the body, particular in image-guided surgery and therapy. For example, the NDI Aurora (Northern Digital Inc., Waterloo, Ontario) system, with the sensor diameter being 0.55 mm at a length of 8.0 mm for 5 degrees of freedom (5DOF) emits AC magnetic fields at 45 Hz, temporal resolution of 70 ms, and a relative positional error of 0.96 ± 0.68 mm for a given distance of 50 mm. The relative rotation error was

found to be 0.51°[46]. However, it suffers from eddy currents induced by the metal in the PET gantry, which seriously compromises the accuracy of the motion measurement[45]. Although it has since been reported that electromagnetic tracking systems have been improved in their accuracy and reliability[46], the ferromagnetic materials placed close to sensors of electromagnetic tracking systems still may distort the reference field and affect the accuracy of the tracker.

Optical devices are currently in wide clinical application, with similar performance to electromagnetic tracking systems. Optical devices have none of the drawbacks of the electromagnetic systems while retaining all the necessary accuracy and reliability. As an example the Polaris IR tracking system (Northern Digital Inc., Waterloo, Ontario) has a positional 0.35 mm (RMS) accuracy and a sampling rate of 60 Hz [47]. Optical tracking utilises a motion tracking sensor to detect reference markers affixed to a tool or patient as illustrated in Fig 2.3[48]. The motion tracking sensor calculates the position and orientation of the tool based on the information the position sensor receives from those reference markers. There are two types of markers: actively emitting markers with an infrared-emitting signal to the tracking sensor, and passively reflecting markers which reflect infrared light, emitted by the tracking sensor, back to the camera sensors. From the detected position of multiple markers, the optical system can determine the position and orientation information of the reference markers in the tracking coordinate system. The tracking system coordinates are then transformed into the PET scanner coordinate system using the fixed spatial relationship between the tracking coordinate system and the PET coordinate system[49-54] [48, 55-58]. For example, Nehmeh et al [59] uses a camera-based respiratory gating system, real time position management(RPM Varian Medical Systems, Inc., Palo Alto) to monitor the respiratory cycle. The tracking system provides a trigger to the PET scanner to initiate the gating cycle. Each respiratory cycle is divided into discrete bins triggering, in this case, preselected to be relative to the end of expiration within the patient's breathing motion. The PET acquired data within the time bins correspond to different respiratory motion phases within the breathing cycle. The very nature of the system, relying on markers fixed on the patient, makes it of limited use for tracking of flexible endoscopes or internal motions of the body and generally prohibits its wider application.

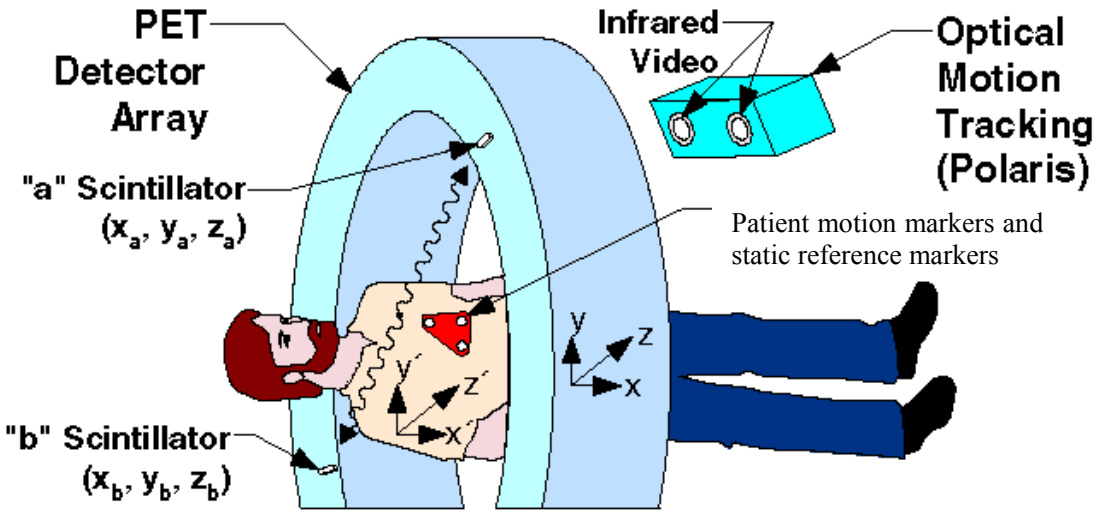

Fig. 2.3. Optical motion tracking for PET. Shown are the PET detector rings with a patient attached a referenced marker on the chest. The Polaris device tracks the reference marker for movement. The xyz coordinate system defines the PET coordinate system. The x'y'z' coordinate system is fixed to reference marker. Scintillator crystals "a" and "b" are the detectors that make up a coincidence LOR.

Another method used to detect respiratory motion incorporates the use of a strain measurement with an elasticised belt. An elasticised belt can be also used to measure expansion and contraction of the patient's chest as a surrogate for respiratory motion[60]. The tension of the belt changes with the respiratory motion. A transducer converts this tension to an electronic signal proportional to the expansion of the chest belt. The signal measured by the strain sensor generates a timing signal which is input to the PET scanner online acquisition system gating interface, so that the different signal amplitudes indicate different phases of the breathing cycle. Typically the lower signal amplitude corresponds to the maximum exhalation and highest amplitude corresponds to the maximum inhalation[60-62]. For example, RespiTrace R250 Studley Data system has approximately 15 Hz (15 readings per second) for inhalation signals and is related to the degree of chest movement and excellent for tracking of the peaks and valleys[62]. The elasticised belt tracking system is inexpensive, readily available, requiring almost no warm-up and calibration. But some signals of the belt tracking system have low signal-to-noise ratio due to the minimal

chest expansion of patients with weak respiration. Another issue is that incorrect set-up of the belt on the patient.

The spirometer is designed to measure lung capacity by measuring the volume of air passing through the airway during respiration[62]. The gating mechanism is therefore volume based rather than temporal based. Regardless of the types of spirometers, they all have the same objectives of plotting of expired flow (liters/sec) versus time (sec); which can be integrated to show expired volume in litres versus time. For example, Medgraphics CPFS/D USB Spirometer, a full function spirometry system for testing flow-volume, has a flow rang of ± 18 L/second (± 1080 L/min) and with a resolution of 8.64 ml/sec. Spirometer-based monitoring is notably most suitable for deep inspiration breath-hold but less important for free breathing gating techniques, however, signal drift issues during measurement may affect its accuracy and reliability[63].

Temperature sensors such as a thermistor have been used to measure the extreme respiration states of respiratory motion[62, 64]. The signal amplitude corresponds to the room temperature when inhaling and the lung temperature when exhaling. A sensitive thermistor is connected to a discriminator, producing a trigger signal such as 3 times per second to indentify the maximum inhalation[62]. The temperature signal at the beginning of inspiration is regarded as a referenced level. The exhaled temperature above the selected reference level is monitored as a varible resistance (ohms). It allows the thermistor temperature to be adjusted to the subject's exhaled air and regulates the respiratory pulse emission with the variable-resistance dial to modify temperature threshold necessary to give a signal. Temperature sensors can track the respiratory positions of the peaks and the valleys, and are inexpensive. However, drifting ambient temperature can disrupt the monitoring of the respiratory gating signal, and minor adjustments of the variable-resistance setting occasionally are necessary during acquisition.

In the external motion tracking systems reviewed above, PET data are acquired into discrete bins using a synchronized signal from motion tracking sensors monitoring a surrogate of respiratory motion. A number of possible sensors whose signal is dependent on the state of respiration are available. The main difference between these external monitor system techniques lies in the type

of sensors used for position and orientation measurement. All of these tracking systems have different characteristics that make them suited to particular clinical applications and all of them have found use in applications other than motion correction for PET imaging. With regard to their application to PET imaging, some limitations should be noted. External sensors need to be placed on the patient which takes additional time and might increase the discomfort of patient. Most important for correction algorithms, all sensors deliver information about movement of the thorax only rather than information corresponding to movement of internal organs as there is a phase shift between internal organs and thoracic and abdominal surface motion[65]. Motion tracking systems complicate the scan acquisition procedure by adding another signal to be acquired and integrated with the emission data. Tracking motion information requires an accurate motion sensor. The signal from the sensor needs to be converted into a digital signal and imported into PET imaging system, but interfacing the signal to a PET acquisition system is often challenging, requiring extra hardware and calibration procedures. In addition, existing techniques for respiratory gating have advantages and disadvantages in clinical studies, and these have not yet been fully explored, to the extent that it is still uncertain which method will be proven to be more adequate for patient and technologist acceptance, and be the most robust clinically.

To overcome the disadvantages of external tracking monitors, it was decided to investigate the development of a data-driven method. Such a method does not involve any external hardware or data calibration procedure. Motion parameters can be estimated from the acquired data by using algorithms or motion detection based on signal / image processing of the PET acquired data.

2.1.2 Data-Driven Methods

The majority of the external monitoring systems provide a respiratory signal through the measurement of the displacement at a particular respiratory phase, while a respiratory motion indicator corresponding to respiratory characteristics such as respiratory phase are also recorded or mixed in the PET acquisition data. The purpose of data-driven methods is to estimate the respiratory motion indicator from intrinsic properties of the data by using a mathematical algorithm or signal / image processing techniques. Various data-driven methods for respiratory

motion gating have been developed. They may be separated into different categories according to the stage of PET imaging at which they are implementated [19] as illustrated in Fig. 2.1. From Fig 2.1, several stages are available for the development of data-driven methods from the initial sinogram mode raw data or list-mode raw data to the post-acquisition reconstructed image respectively.

2.1.2.1 Sinogram Based Gating Methods

Conventionally, PET coincidence events are recorded in a histogram in 'sinogram-space' and then reconstructed into 'image-space'. In a sinogram as illustrated in Fig. 2.4 [39]**,** a memory location is assigned to each possible LOR, and each time a valid prompt coincidence event is detected in that LOR, the value stored in that memory location is incremented. This provides the integrated number of events detected in each LOR and is frequently the most efficient manner to store the data[39]. However, in a sinogram, the events are integrated over a time interval that define a 'frame' that must be specified prior to or at the time of data acquisition. The LOR reflects a line integral of source activity through the body as illustrated in Fig 2.4 (A). It is characterised by the angle of orientation of the LOR and the shortest distance between the LOR and the centre of the gantry. If all of the activity is concentrated at a single point in the patient and we plot a planar greyscale map of the integrated number of events in each LOR, using the shortest distance between the LOR and the centre of the gantry as the abscissa, and the angle of orientation as the ordinate, the resulting graph appears as a rotated half period sine curve as shown in Fig 2.4 (B). This graph is appropriately referred to as a "sinogram." Each pixel value along the row of sinogram is the sum of all of the events acquired along the corresponding LOR. Such a collection of LOR sums is referred to as a "projection" as illustrated in Fig 2.4 (C).

There are some motion detection approaches such as the Centre Of Mass (COM)[19] and the cross-correlation method[66] that utilise sinogram space data. For example, features of respiratory motion can be reflected in Philips Allegro UGM (Ulrike Gerhard Mueller) sinogram space as illustrated in Fig 2.5[67], it can be used for motion detection by the COM or the cross-correlation method. However, sinogram storage is not efficient for respiratory gating and list-mode format

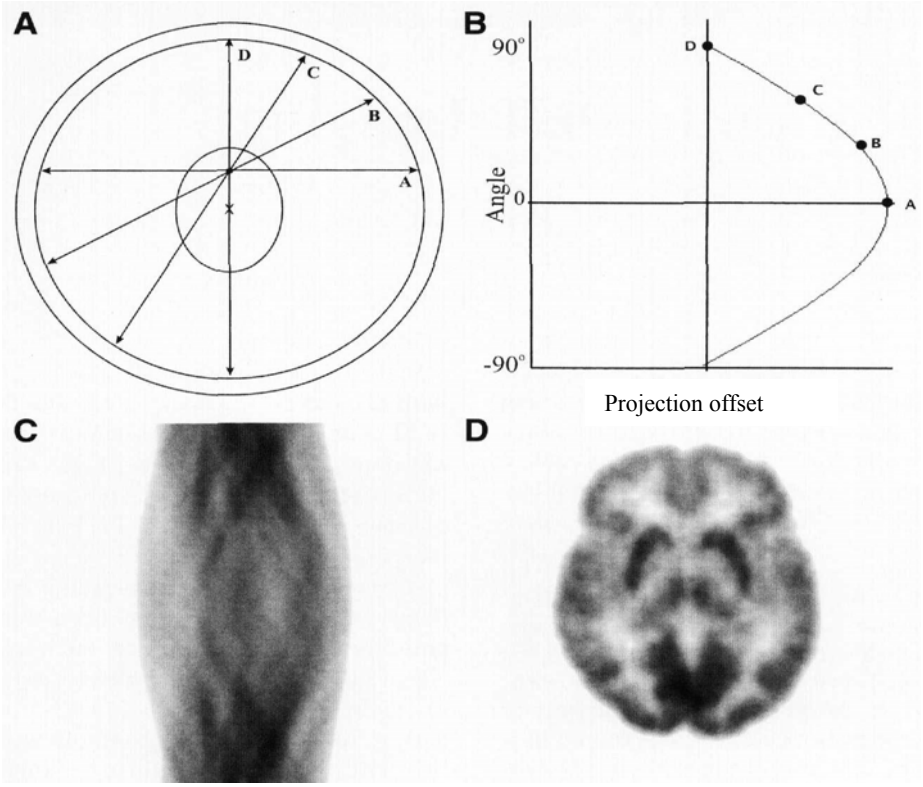

Fig. 2.4. Sinogram and projections. The sinusoid curve of LORs is referred to as "sinogram." with angular orientation and shortest distance from centre of gantry. (A) Cross (X) marks to the Centre of FOV. Four events passing through a tumour labelled as A, B, C and D. (B) These four LORs are plotted on this sinogram with angular orientation and distance from X. If all possible LORs passing through this point are plotted as half of sine wave turned on its side here. "projection." is defined by plotting of LOR sums from series of parallel LORs at particular angle (C) Sinogram of brain scan shown is composed of many overlapping sine waves. (D) Reconstructed image associated with sinogram & projections.

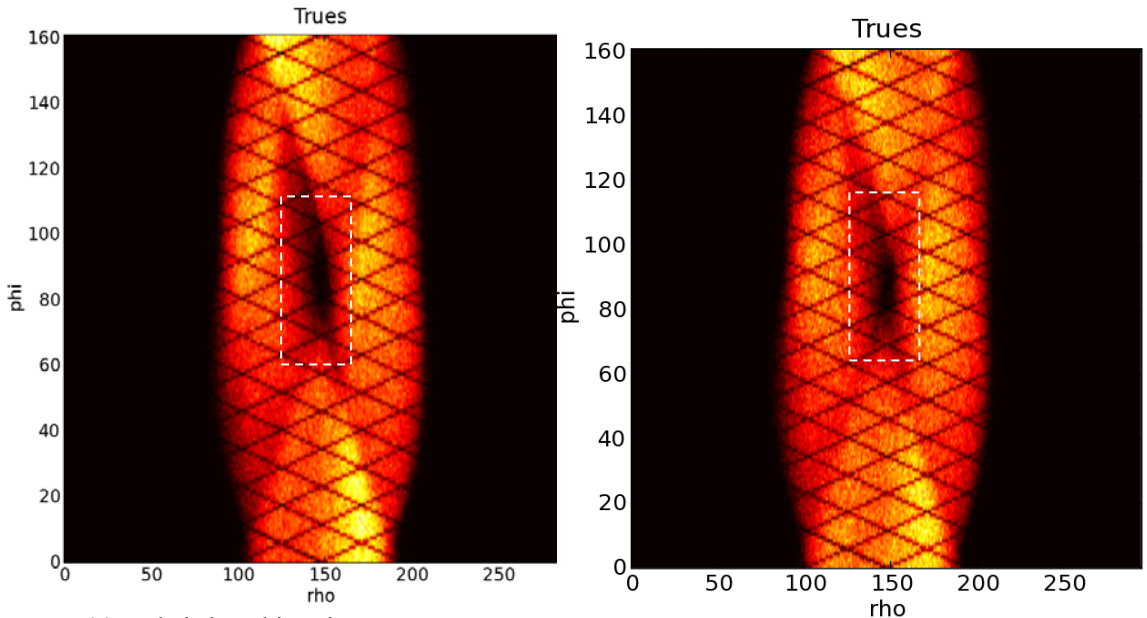

(a). Exhale breathing sinogram

(b). Inhale breathing sinogram

Fig. 2.5. Comparison of the Allegro PET UGM sinogram maps between (a) exhale breathing and (b) inhale breathing, it is clear that sinograms are different in positions such as the dash rectangle region due to respiratory motion. Motion detection can be performed by sinogram based method.

stream data is the preferred mode of storage (see next section 2.1.2.2).

The definition of the centre of mass of a system of particles is a specific point at which the system's mass behaves as if it were concentrated. It is defined as the average of their positions r_i weighted by their masses m_i;

$$COM = \frac{1}{M}\sum m_i r_i = \frac{\sum m_i r_i}{\sum m_i} \tag{2.1}$$

where *M* is the total mass of the system, equal to the sum of the particle masses[68]. In the case of a rigid body, the position of its COM is fixed in relation to the object. COM can be utilised as a measure of the respiratory motion; if the Equation 2.1 is applied to each respiratory phase in sinogram space, the COM along the z axis for any projection can be determined by using the Equation 2.2 [69](for SPECT):

$$COM(\theta,t) = \frac{\sum_{i}^{K} i \sum_{j}^{L} A(\theta,t,i,j)}{\sum_{i}^{K} \sum_{j}^{L} A(\theta,t,i,j)} \tag{2.2}$$

Where *K* and *L* are the height and width of projections respectively, and $A(\theta,t,i,j)$ is the activity in pixel (i,j) in the projection acquired at angle θ for time frame *t*, which is for SPECT scanner COM calculation. If for PET scanner, equation 2.2 COM calculation will be changed as COM(t), not COM(θ, t). The COM method works satisfactorily if count rates are high enough. However, COM algorithm calculates the axial position for tomography LORs events is unsatisfactory as the 3D mode geometry shown in Fig 2.6. In addition, if the count rate is too low or the organ motion is not adequately sampled temporally, then the COM method does not adequately define respiratory motion [70].

For example, in the 1970s , Schmidlin, Oppenheim and Hoffer *et al* [71, 72] used the COM method to adjust the y axis signal, to compensate for longitudinal motion of the liver in planar scintigraphy. In 2001, Klein et al [73] reported that the COM method can be applied as a respiratory signal in sinogram space in PET for gating. They compared the COM method with the

ECG monitor and respiratory bellows monitoring tracking system around a patient's chest, finding that the COM calculation waveform agreed well with the measurement of the monitoring system. Klein *et al* thought that COM may provide a considerably more accurate indicator than the external tracking system particularly in cases such as minor patient movement, soft tissue compression or bulk patient motion. However, the accuracy of COM may be affected by background activity. For example, organs like lung and liver around the heart may move partially in and out of the FOV with each breathing cycle, which causes some LORs that are measured in one stage of a motion cycle will be un-measured in another stage of the motion cycle as shown in Fig 2.6. It will result in an inaccurate COM calculation due to the event lost during LOR rebinning. Solving this problem, Klein *et al* suggested using masking techniques selecting a volume of interest (VOI) around the heart, and then projecting the VOI into sinogram space. However, the accuracy of the COM calculation is still challenging when the target movement has large amplitude. In 2007, Bundschuh et al[74] applied COM method techniques on 10 patients with lesions in the lung or upper abdominal organs to evaluate Klein's method, and pointed out a disadvantage of the COM to be the time consumed in processing to define the VOI. To address this problem, Bruyant et al [69] constructed projections thresholded before estimation of COM positions in order to minimize activity stemming from low-activity and static organs. This gives rise to a trade-off between a maximal elimination of activity stemming from organs and the better counting statistics for noisy projections.

Another technique, the cross-correlation method is a measure of similarity of two signals, commonly used to find features in an unknown signal by comparing it to a known one[75]. Cross-Correlation techniques can be used in the sinogram space and respiratory phase may be determined by calculating the cross-correlation function in sinogram planes. In 1987, Eisner et al [66] detected in-plane translational motion in cardiac PET by using the cross-correlation function. Evidence of motion can be observed as abrupt peaks in the frame-to-frame correlation. However, this algorithm did not work well for small amplitude motion of the target[66]. In 2002, Lu and Mackie [76] proposed an improved algorithm in which respiratory motion was modelled as a time-varying scaling along two directions based on some fiducial traces in the sinogram. This algorithm can detect minor movement in sinogram space by estimating the expected trace from

distorted sine curves of high contrast traces. However, the limitation of the algorithm is that it only models intra-scanning motion as in-plane scaling, not general 3D motion. Kyme et al [77] investigated a method to detect motion parameters by comparison of acquired data with the forward projections. To identify groups of projections corresponding to discrete locations of the brain, a partial reconstruction should be used in preference to the full reconstruction to provide better estimates of motion. In the dual-scan approach of Passalaqua et al [78], inter-scan translational motion can be determined from an initial fast scan and a subsequent slow scan by cross-correlation. In 2001, Pellot-Barakat et al [79]used cross-correlation of partial sinograms to detect motion. However this technique was limited to the detection of fast, discrete motion and had low sensitivity. In addition, Wallis et al. [12] described a motion detection method based on a selective sinogram in which consecutive columns represented consecutive projection angles. This method is useful for revealing axial motion in an acquisition. Cooper et al[80] found that visual detection, cross-correlation, and two-dimensional fit most accurately detected axial motion and that cross-correlation was most accurate in detecting lateral motion. In general, the disadvantage of cross-correlation techniques is that frame-to-frame effects such as object asymmetry, and gantry motion inconsistencies can hamper precise quantification using such cross-correlation measures[79].

2.1.2.2 List-mode Data Based Gating Methods

The list mode data stream consists of LOR coincidence events combined with a timing tag word with a typical time resolution of a millisecond. Data in this stream are stored directly in a disk, event-by-event as displayed in Fig 2.7, rather than combining them into sinograms as shown in Fig 2.4. List-mode based methods are common in research studies as an important aspect of the list mode acquisition scheme is that it allows retrospective analysis of data acquired during arbitrary time frames of a study. Also, they are much more data-storage efficient for rapid dynamic scanning.

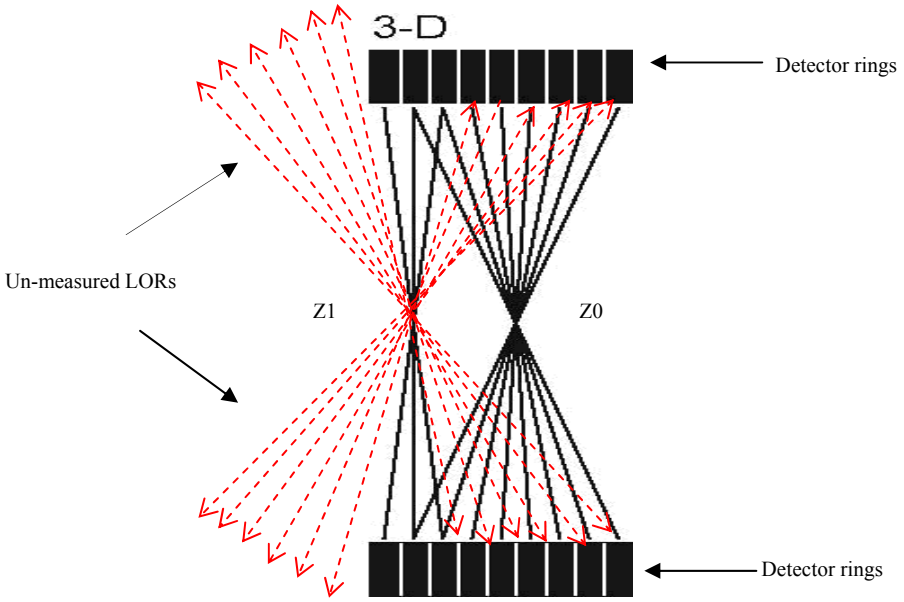

Fig. 2.6. Point activity source at Z0 may move to Z1 the edge of the FOV along Z axis, some oblique LORs like the red lines escape from the FOV, which will result in an inaccurate COM calculation or potential correction artifacts.

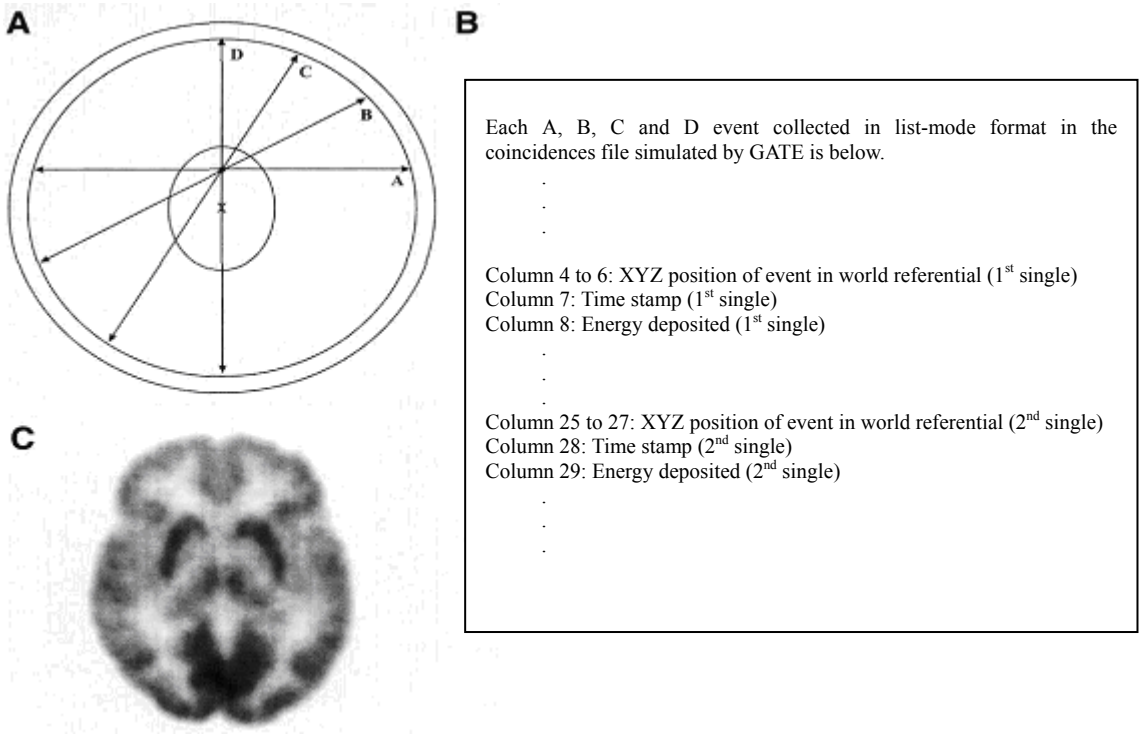

Fig. 2.7. List-mode data format. The sinusoid curve of LORs is referred to as a "sinogram." with angular orientation and shortest distance from centre of gantry. (A) Cross (X) marks to the Centre of FOV. Four events passing through a tumour are labelled as A, B, C and D. (B) These four LORs are stored in list-mode format with the information about position, time stamp, energy, etc., al (C) Reconstructed image associated with list-mode stream.

Some respiratory motion gating techniques have been developed based on list-mode data[69, 74, 81, 82]. For example, Schleyer (2003) [81] described a respiratory motion gating approach based on the use of frequency spectrum analysis to determine respiratory motion phase. The main idea is that a pixel which lies on the edge of a feature or organ subject to motion will contain different temporal frequency components to that of a pixel which lies in a non-moving region or in a homogeneous moving region. Images with the same frequency component of pixels are then placed into bins which contain equal phase within respiratory cycles. This approach can observe pixel frequency magnitude peaks corresponding to liver spleen motion. However, it requires many steps to process the raw data which could affect final image quality and image processing is more time consuming, also the results were obtained under 2D SPECT acquisition system rather than 3D PET. In 2004, Visvikis et al [82]proposed another similar method for respiratory motion gating in PET scanning. The principle of the technique is based on the assumption that although the amplitude of the motion may vary from pixel to pixel inside the same organ, the frequency of the periodic motion is the same in each pixel. Simulated list-mode data were binned into different frame duration time schemes for image reconstruction. Subsequently, a ROI was placed at the organs of interest, such that during part of the motion cycle the organ of interest is inside the ROI, while during the other part of the cycle, it is outside the ROI. The fourier transform of the different time activity curve of the ROI is used to estimate the frequency of respiratory motion. This method presented the frequency of respiratory motion based on simulated data. However, the choice of ROI placement needs to be correct because the determination of the frequency is dependent on the region of interest considered. The time activity curve of different ROIs shows readily apparently differences. In addition, the choice and calculation of ROI is performed in image space, and therefore requires operator intervention and gives rise to a lengthy process. This method also requires further validation in clinical studies.

To avoid the occurrence of the above mentioned problems in the list mode data, the Geometric Sensitivity Gating (GSG) method has been proposed in this thesis. The GSG technique estimates

the respiratory phase purely on list mode data and potentially requires no operator intervention. As a result, the gating procedure is simple and less time consuming compared with conventional techniques. Details are presented in Chapter 3.4.

2.1.2.3 Image Based Gating Methods

Image based gating methods are post-image reconstruction process methods in which respiratory motion gating is carried out on the image volumes. PET images are obtained by reconstructing sinogram or list-mode data, artifacts caused by respiratory motion can be easily observed on the sequence of images. The aim of an image based method is to detect respiratory motion through those obtained images. Each individual image in the sequence of images is different from other images, it represents a phase of respiratory motion as illustrated in Fig 2.8[67]. Estimation of the respiratory phase for gating can be performed by image based methods such as image registration software packages, markers, breath-hold, PET/CT and the calculation of COM or cross-correlation.

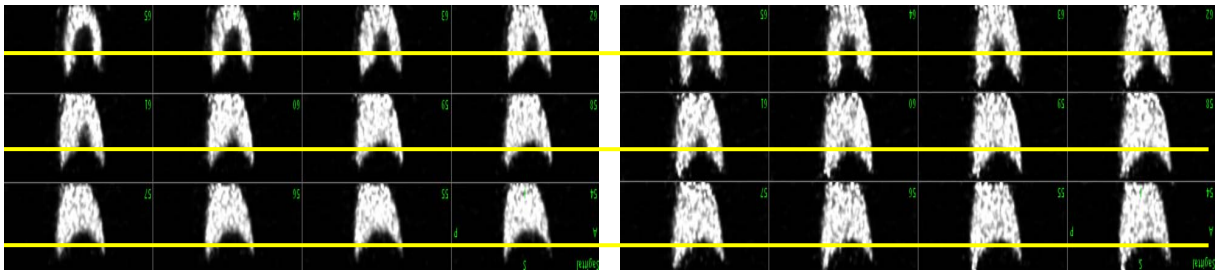

(a). Exhale breathing images at sagittal view (b). Inhale breathing images at sagittal view

Fig. 2.8. Comparison of the reconstructed images at exhale (a) and inhale (b) phases of breathing. Respiratory motion was simulated by NCAT phantom. It is clear that images are different in position and volume indicated by yellow lines marking due to respiratory motion. Motion detection can be implemented by image based method.

Motion displacements can be measured in reconstructed images by some software packages such as Automated Image Registration (AIR) and Statistical Parametric Mapping (SPM) used for coregistration in gating, but such packages are limited to measuring rigid body motion [83] [84]. Software Packages detect motion by matching the two images datasets. These methods don't

require any special device, the results however, depend on the level of noise in the images and the distribution of the radioisotope. Moreover, software packages can't correct for any motion which occurred during scanning[85]. An alternative method is the use of registration algorithms to derive respiratory phase or motion transformation fields. For example, Lamare *et al* (2007)[86] estimated respiratory motion according to an affine registration algorithm which was based on maximizing the normalized mutual information to determine transformation matrix. In addition, B-spline basis functions were employed by Lamare et al (2007) [32] to derive transformation parameters accounting for the respiratory motion using the NCAT dynamic CT images.

External radioactive markers can be used as a method to detect respiratory motion directly in the images. In 2003, Nehmeh et al [57, 76], Lu et al 2002 [76]tracked the respiratory motion using an external source marker. A point source attached on the patient's abdomen is extended into the camera field of view at the level of the lesion. Respiratory motion through the consecutive dynamic frames can then be tracked by the point source within the breathing cycles. However, this method needs to reconstruct each frame for tracking the source marker motion, it is inevitably time consuming. Another disadvantage is that the time resolution is only 1 second. In addition, in the registration of the thoracic and abdominal area, the placement and accuracy of external fiducial markers could be problematic because of soft-tissue deformations of internal organs such as the lungs that give rise to non-rigid motion effects.

With PET/CT scanning, it may be feasible to use the respiratory motion synchronized CT datasets to derive the transformation parameters to be applied in the corresponding gated PET datasets Nehmeh *et al* 2004[52], Lamare *et al* 2004[87], Qiao *et al* 2006[88]. In the clinical case, the magnitude of the displacement at the level of the thorax due to respiration may be assessed by the use of the internal anatomy through the acquisition of a corresponding dynamic CT series.

Some studies have been based on asking a patient to hold their breath for a deep inspiration breath-hold and the gated acquisition takes place only during this period. Kim *et al* (2001) presented four different parts of the breathing cycle for breath-hold[89]. Della Biancia *et al* (2003)[90] showed improved normal lung sparing at end inspiration compared with end

expiration. Barnes *et al* (2001)[91] pointed out an extraordinary range of breath-hold periods of up to 52 seconds and Mah *et al* (2000) [92]showed this locked the tumour position to the corresponding planning position to better than 2 mm for a large number of patients. However, this method demands a high level of patient cooperation during acquisition, it will be problematic for some patients such as unconscious or patients with psychological problems. It is a common affliction of lung cancer patients to be frequently coughing and unable to breath hold for any significant period of time.

The COM technique can also be used in image space to determine respiratory phase according to equation 2.1. For example, Feng *et al* (2006) [93]proposed a COM method to detect rigid-body motion from a series of reconstructed images. The limitation of the method is that in image space, each state of motion must be available as a 3D image to calculate COM points.

In conclusion, all techniques reviewed above for respiratory motion gating are able to improve image quality in reducing image artifacts. However, the gated respiratory data associated with one temporal frame corresponds to only 10-15% of the overall data available throughout a respiratory averaged emission acquisition. The reduced statistics associated with individual gated frames lead to poor signal-to-noise ratio reconstructed images[19]. Therefore, there is a need for the development of correction methodologies which will allow the use of all available data throughout a respiratory average emission acquisition. This suggests that gated acquisitions are only the first step towards a viable solution to respiratory motion effects in PET.

2.2 Motion Correction Techniques

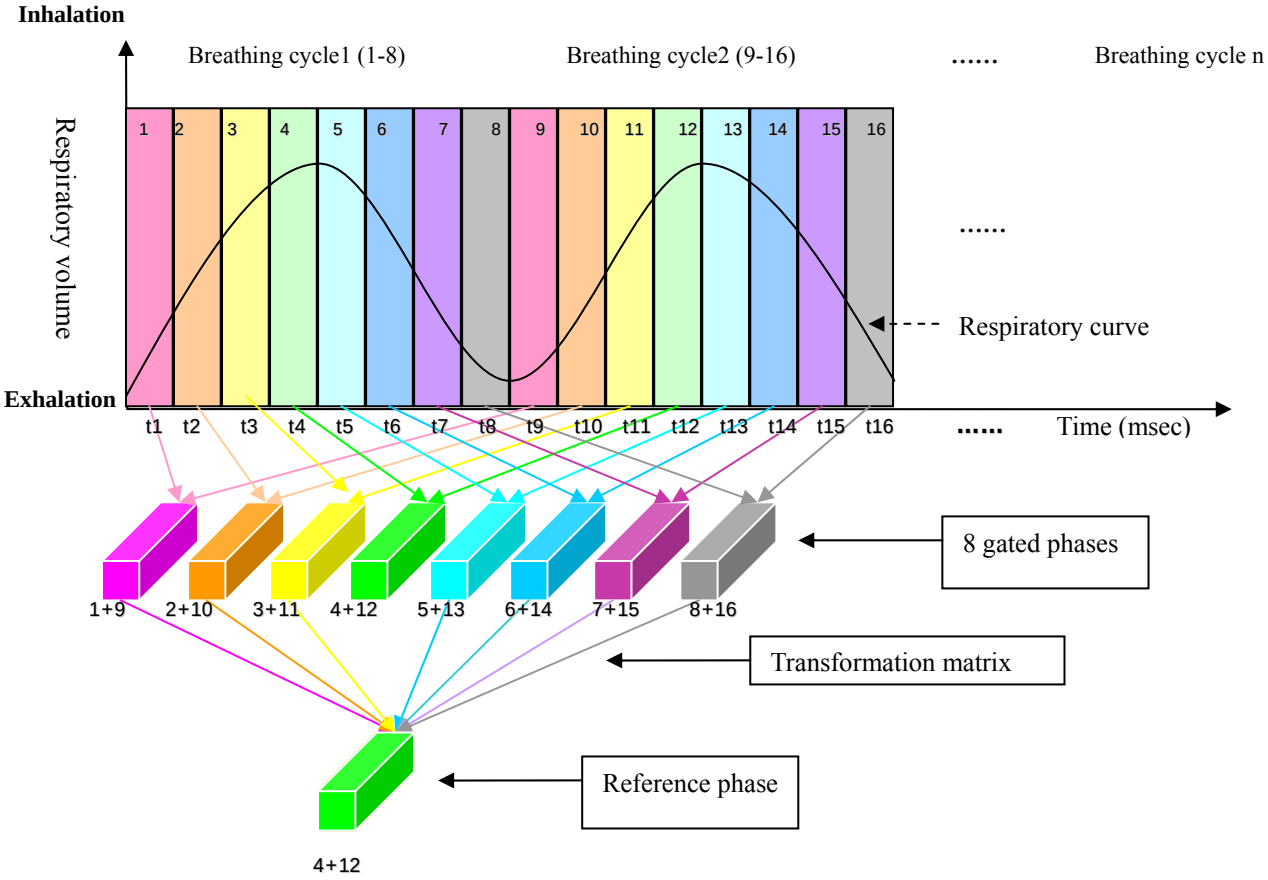

Fig. 2.9. Two breathing cycles gated into 8 breathing phases, respiratory motion correction based on 8 gated phases by transformation matrix. Each bar represents one phase of breathing, bars of the same colour in different breathing cycles represent the same relative phase of breathing.

In order to make use of all available emission data acquired throughout the respiratory cycle, respiratory motion gated data by using either external monitor systems or data-driven methods will be applied to the motion correction stage. Based on the gated breathing phases obtained with an example of 8 gated phases illustrated in Fig. 2.9, the aim of respiratory motion correction here is to transform each gated phase to the reference phase so as to make the corrected image with maximum possible signal to improve the signal to noise ratio rather than discarding the information in phases. The reference phase can be any one respiratory position corresponding to one specific gate such as the gated phase of '4+12' as shown in Fig 2.9. The transformation matrix may be derived through the use of image registration algorithms estimating transformation

parameters on the reconstructed images of individual gated phases. It defines the spatial relationship between the two images as shown in Fig 2.10. Transformations are described by a number of parameters (often referred to as degrees of freedom). For instance, the displacement parameter of the reference phase '4+12' in the transformation matrix is 0 since other gated phases are transformed into the reference phase position, while the reference phase "4+12' is not moved**.**

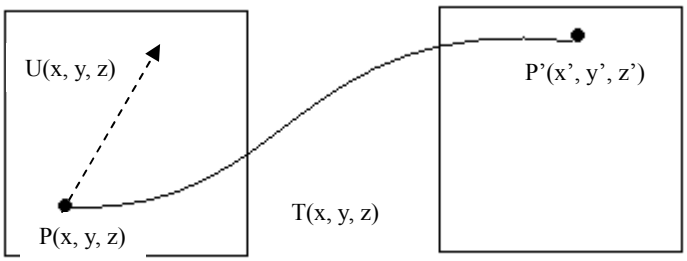

(a). Image A (b). Image B

Fig. 2.10. Transformation between two (a) images A and (b) Image B. For example, one point source moves from position P(x, y, z) in A to P'(x', y', z') in B, then transformation matrix T: (x, y, z) → (x', y', z') which defines the spatial relationship between the two points P and P' as: (x', y', z') = T(x, y, z) = (x, y, z) + U(x, y, z), where U(x, y, z) may be translation, rotation, affine, shear, scale. etc.

Respiratory motion correction techniques can be broadly classified according to which of the four phases of PET acquisition/imaging the transformation of gated phases occurs, as shown in Fig 2.1 These are list-mode based methods or dynamic sinogram based methods, reconstruction based motion correction methods and image volume based motion correction methods. The list-mode based methods will be primarily concentrated upon because they are the basis for the specified hypothesis (GSC) for respiratory motion correction developed in this thesis.

2.2.1 List- mode Data Based Correction Methods

Correction methods utilising list-mode acquired data involve transforming the corresponding emission list mode datasets to the reference frame prior to reconstruction; Bruyant et al 2002, [69] Livieratos et al[61], and Lamare et al 2007,2004[86, 87]. The advantage of list-mode acquired data lies in the time stamp available with each detected coincidence event, allowing the formation of dynamic datasets with interval times that can be specified post-acquisition. The list-mode data

stream firstly needs to be sorted into temporal interval frames representing respiratory motion phases. List-mode methods are based on application of a determined / calculated realignment to the lines of response (LORs) formed by coincidences which belong to the same phase in the respiratory cycle. In order to perform the transformation of LORs, it is necessary to determine the information in the transformation matrix related to the displacement to be applied. The required displacement can be obtained through the use of external monitoring systems, or data-driven methods. For each temporal interval the LORs are subsequently shifted to the position where they would have been if there was no motion involved. Using a geometric model of the scanner, the location of the new LORs can be determined through the identification of the new pair of detector elements in coincidence as shown in Fig 2.11.

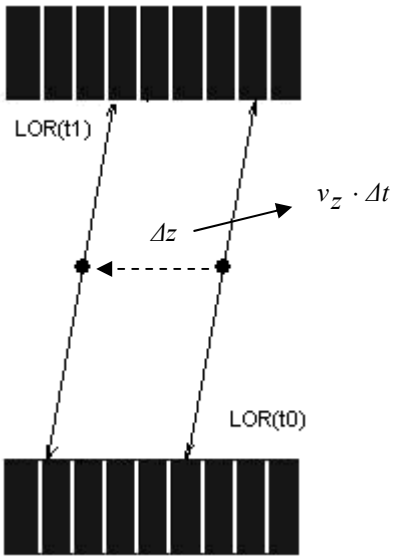

Fig. 2.11. In a 3D mode scanner, a LOR(t_0) transformed to another position LOR(t_1) along z axis due to motion, which means LOR(t_0) = LOR(t_1) + Δz.

For example, Livieratos *et al* 2004 [61] designed a method for the respiratory motion correction of cardiac PET data. An inductive respiration monitor with an elasticised belt at patient's chest was employed to detect respiratory motion phases. Data are retrospectively sorted into separate respiratory gates. The transformation matrix corresponding to the gated images was determined by means of image registration. Then the list-mode data were translated into the reference frame in terms of the transformation to obtain a single motion-corrected dataset. The transformation in the method involved the use of a rotation and a translation to correct the detected LORs in list-mode data. This method has been extended by Lamare *et al* [86, 87] to an affine

transformation including rotation, translation and one more scaling factor in 3D to correct the detected LORs for the respiratory motion, considering the whole of the thoracic field of view. The disadvantage of such a methodology is the application of a global set of transformations for the complete scanner's field of view, which is not appropriate considering the elastic nature of organ deformation produced as a result of respiratory motion. Results have demonstrated that such a method can be used to accurately correct for respiratory motion associated with single organs (liver or lungs) but cannot correct for all of the organs in the FOV around the diaphragmatic zone[86, 87]. Also, both methods presented by Livieratos et al and Lamare et al have a limitation that some spatially transformed LORs may fall outside the FOV after the translation of LORs to the reference frame as shown in Fig 2.6, which is associated with an entry of single-photon count rates. In order to maintain quantitative accuracy and avoid potential artefacts, Livieratos et al(2005) [61]proposed the normalization factor to compensate the un-measured LORs before spatial transformations were applied to the list-mode data.

In addition, list-mode based motion correction results provided by Lamare et al 2007[86] demonstrated that the application of the spatial transformation in the list-mode data domain prior to reconstruction leads to superior contrast in comparison to the application of the spatial transformation in the image space, which simply adds all reconstructed images together after all gated frames are first reconstructed and then transformed in image space.

The specific method developed in this thesis is the Geometric Sensitivity Correction (GSC) as mentioned in Chapter 1.3. It utilises the intrinsic geometric sensitivity properties of the 3D PET scanner to determine the transformation matrix of the corrections applied in the LOR domain, and also translates all LORs directly to a reference co-ordinate frame rather than based on the translation of the gated frames, further details are given in Chapter 3.5.

2.2.2 Sinogram-Based Correction Methods

In sinogram-based methods, transformation of the gated respiratory motion phases for motion correction is executed in the sinogram space prior to reconstruction. Breathing acquisition data is

separated into a sequence of sinogram frames. The displacing transformation of projections in sinogram space is determined by image registration algorithms such as the COM and cross-correlation between successive image projections in a scan. After alignment of sinogram frames to the reference frame, the corrected data are reconstructed and summed with the reference frame data to produce a motion corrected image.

For example, Eisner *et al* (1987)[66] presented a motion correction method in terms of cross-correlation of summed horizontal and vertical profiles of successive projections. However, the motion correction is clearly limited by the dependence of lateral motion on the radius of rotation for objects which are off centre. Geckle *et al* (1988)[94] described an algorithm for tracking the centre of the heart in successive projections and correcting its motion according to realignment of that centre to a fixed point in space. Germano *et al* (1993)[95] also used a similar approach to enhance the accuracy using a point source. The axial and transaxial dimension translation were found to be more accurate. O'Connor *et al*(1998)[96] showed that simple manual shifting of projection data was effective in correcting small, continuous and sinusoidal motions translations in a cardiac SPECT phantom study. Although it has been developed for SPECT cardiac study, it definitely has the potential to be used in respiratory motion compensation in PET studies.

Respiratory motion correction by tracking of the COM can determine the transformation component of the transformation matrix. Klein *et al* (1999)[97] and Bruyant *et al*(2002b) [69] suggested that the COM should vary with over the time of image acquisition. This property has been used to apply the calculation of COM of the sinogram to track respiratory motion. The motion correction was performed by shifting the projections axially up or down relative to the reference frame. However, the disadvantage of COM method is that if the amplitude of motion is too big, then some motion positions are beyond the FOV, and so not detectable, which results in the loss of LORs detected by scanner, the insufficient LORs inevitably generates an error to the calculation of COM, and consequently leads to an incorrect result to motion correction[73].

2.2.3 Reconstruction-Based Correction Methods

Reconstruction-Based motion correction methods involve motion correction with the gated motion phases and the transformation matrix is performed in the image reconstruction stage as shown in Fig 2.1. Respiratory motion information about motion phase displacement or elastic terms may be detected by external monitoring systems, or data-driven methods. Generally, algorithms for reconstruction-Based methods are derived from the ML-EM iterative reconstruction algorithm. The advantage of that method is that the algorithm incorporating the use of a system matrix that has been modified to incorporate motion information and account for motion directly.

For example, image reconstruction was performed in a 4D-MAP/penalized likelihood framework, whereby a temporal prior/penalty term was used to enforce the consistency of image frames in the temporal dimension by Lalush *et al* 1996[98], Gilland et al 2002[99], Cao et al 2003[100], Gilland *et al* 2005[101], Gravier and Yang 2005 [102]. In such approaches, the parameter associated with the prior/penalty term often plays an important role in the final reconstruction result and hence needs to be selected with careful consideration; in practice it is often determined on a trial-and-error basis. In order to overcome this disadvantage, another approach was employed by Qi and Huesman (2002) [103] which incorporated the motion information into the system model of photon detection probabilities without the need of prior parameters, which implicitly compensates for the undetectable LORs due to the phantom motion. However, this approach was limited to rigid-body motion only. With a similar approach, Jacobson and Fessler 2003, 2006[104, 105]developed an approach that allowed non-rigid motion. Based on Jacobson and Fessler ‘s work, Qiao et al 2006[88] provided a more practical implementation and performed a validation test in 3D space using a physical phantom. However, neither photon attenuation nor detector response was modeled in the reconstruction algorithm. Incorporating the elastic transformations into reconstruction algorithms have been lately proposed for respiratory motion compensation by Lamare et al 2005[106] and Qian et al 2005[88]. The method is based on shifting the contributions of each emission LOR individual voxels during the reconstruction process. The applied shift is based on displacement matrices derived through the use of an elastic registration of 4D CT images corresponding to the same phases of the respiratory cycle as the gated emission

datasets. In addition, Lamare et al 2006[107], 2007[32] investigated a method to incorporate elastic transformations in the system matrix. The one-pass list mode EM (OPL-EM) algorithm was modified to integrate the elastic transformation accounting for event displacement and voxel shape deformation in the system matrix. However, the very limited work that has been performed in the domain is largely validated with simulated datasets. There is therefore an obvious need for clinical validation studies. An alternative approach reported by Rahmim et al 2004[108] is that of a modified EM algorithm and was addressed by including motion-compensated sensitivity correction factors with system matrix modeling and time-weighted sensitivity motion factors in histogram-mode and list-mode reconstructions. However, a scatter correction is yet to be incorporated into the proposed algorithm.

The advantages of reconstruction-based methods are: First the final image is generated in a single optimisation process with regard to both the acquired data and the motion information. The possibility of different a priori information, such as noise component, attenuation or characteristics of detector non-uniformity may be incorporated for more accurate image reconstruction. Second; all acquisition data in an image sequence are considered when generating the final image, thereby allowing the total emission statistics to contribute to the final image quality.

However, it must be pointed out that the method requires a precise model of the moving structures and an accurate tracking scheme for each type of potential motion. Any variations in the motion from the model lead to errors in the image. Inclusion of additional parameters means increase in processing times.

2.2.4 Image-Based Correction Methods

Image-Based motion correction methods are conducted in the image space where breathing acquisition data has already been reconstructed into a sequence of images or already sorted into gated images. The aim of image-based methods is to align gated images or sequence of images to the reference image, which involves registration of multiple images using motion displacement parameters derived from registration algorithms. Different registration algorithms for the

transformation matrix estimation results in different application of image-based methods on motion correction such as optical flow and COM.

One such registration algorithm called "optical flow" Klein *et al* (2001)[109] uses the gated respiratory emission acquisition to correct reconstructed respiratory images. It is achieved by a 12-parameter affine motion model for registration of different respiratory gates to form a composite sum of a motion-compensated image, which results in only marginal improvement at the spatial resolution of a PET scanner. This type of algorithm is well adapted to non-rigid motion and can therefore be appropriate for the effects of respiratory motion. This method sums all images together corresponding to individual temporal bins in the registration. Although emission images of gated frames have shown encouraging results with similar optical flow method, clinical studies need to be validated further. In addition, attenuation correction was not addressed in this method Dawood *et al* (2005)[110]. He et al (1993)[111] proposed an elastic deformed registration method that is essentially similar to a global optical flow method. This method used four conditions of intensity similarity, incremental transformation, smoothness and error minimisation to perform the deformable registration. However, this method is prone to noise as are other similar optic flow methods. Another method applied motion parameters from an external tracking system to respiratory-gated images to correct the motion of the lung. It defined an objective function consisting of both the degree of similarity between a reference image and a deformed image in the algorithm. Ue *et al*(2006)[50] demonstrated encouraging results in phantom and clinical studies.

Ledesma-Carbayo *et al* (2005)[112] reported an alternative elastic registration algorithm that has demonstrated encouraging correction results. The algorithm was developed by using a spatio-temporal B splines basis functions algorithm which was validated with CT and emission sysnchronized datasets of the phantom. Similarly, B-spline basis functions were employed by Lamare et al (2007) [32] to derive transformation parameters accounting for the respiratory motion using the NCAT dynamic CT images. In addition, Lamare *et al* (2007)[86] estimated respiratory motion according to an affine registration algorithm which was based on maximising the normalised mutual information to derive respiratory phase or motion transformation fields.

Bundschuh et al(2007)[74] applied the COM technique on 10 patients with lung lesions to detect the cranial-caudal motion of respiration. The z axis component of the COM over the time were analysed and compared with respiration curves obtained using a pressure-sensitive belt. Pressure belt motion detection agreed well with COM motion detection. However, a disadvantage of this data-driven method is the long computing time. On a dual-processor workstation, with a 10-min list-mode dataset with a sampling time of 500 ms, the result takes about 2.5 h of processing time for rebinning and 15 h for reconstructing.

Alternative methodologies have focused on the development of methodologies adapted for combined PET/CT images. In this case, a respiratory averaged emission image and a CT scan at breath-hold are used in combination with a registration algorithm[113-115] . Such approaches may be useful in minimizing the problems associated with the mismatch between PET and CT images for the use of CT in the attenuation correction of the emission data. However, repeated breath-hold imaging requires significant patient cooperation. In addition, the volume at which the breath is held may not be consistent over time.

On the other hand, registration image software package such as AIR and SPM were used for coregistration in image analyses. They are used mostly as a tool to identify functional regions of interest and estimate translation matrix on reconstruction images. The images are then realigned so that patient image motion is corrected[116, 117]. However, they have limited-dimension deformation models, and as a result are limited in accuracy for non-rigid motion correction. Wu *et al* (2005)[118] found that the fully deformable model with voxel-level refinement consistently produces a more accurate structural segmentation and a more reliable signal localization than does AIR or SPM.

There are some significant issues associated with the use of image registration for the compensation of respiratory motion. If gated emission frames result in noisy images, the result of the registration will be affected. Computational time and the need for operator intervention is also an issue, as image based correction operates in image space and reconstruction of each frame is necessary due to the motion vector having to be estimated from the reconstructed images. In

addition, registration of respiratory images is a more complex problem with non-rigid motion than brain image registration with rigid motion. It remains a challenge in clinical application[119].

2.3 Summary

As discussed previously, existing respiratory motion compensation techniques including motion gating and motion correction are implemented at different stages of the PET imaging procedure as shown in Fig 2.1. The respiratory motion gating techniques implemented by external monitor systems and data-driven methods have been demonstrated by several groups showing that more accurate tumour quantification is provided. Although external devices for gating motion can perform in real-time, the requirement of extra hardware and data calibration limits its popularity in clinical application. Existing intrinsic data-driven methods do not employ any hardware; they often however, involve complicated algorithms or operating in image space, and add significant additional time to the imaging 'chain'.

Because gating and reconstruction at a single respiratory phase produce such noisy images, many efforts have been made to develop methods of aligning all phases to the reference phase to improve the statistics. The majority of the available techniques that utilise a transformation matrix derived for motion correction are limited by the use of complicated registration algorithms to estimate motion parameters on reconstructed images which present some limitations in the practical application of these techniques.

Despite most of techniques reviewed here for gating and correction providing promising results for respiratory motion compensation, their validation was mostly performed with simulated dataset. There is, therefore a need to further determine the accuracy and robustness of the methods and their applicability as a practical clinical tool in routine use. The requirement for clinical utility provided the motivation for the development of a new method for the compensation of respiratory motion using a data-driven method. The GSG & GSC methods developed within thesis and described in the following chapters utilise list-mode data and are potentially applicable within the

acquisition / image-reconstruction chain.

CHAPTER 3
MATERIALS AND METHODS

3 Materials and Methods

3.1 INTRODUCTION 48

3.2 SIMULATION OF PET ACQUISITION DATA 48

3.2.1 Coordinate System 50

3.2.2 PET Imaging Relevant to the Monte Carlo Simulation 51

3.2.2.1 PET Scanner Parameters 52

3.2.2.2 Hardware Event Processing 54

3.2.3 Simulation Software 57

3.2.3.1 GATE 57

3.2.3.1.1 Structure and Digitiser Optimisation 57

3.2.3.1.2 Simulation Steps 59

3.2.3.1.3 Geometric and Voxelised Phantom 61

3.2.3.2 NCAT Digital Phantom 64

3.2.3.3 Validation for GATE 66

3.2.3.4 Computational Issues 70

3.3 SORT LIST-MODE DATA 72

3.3.1 Simulation List-mode Data 72

3.3.2 Clinical List-mode Data 73

3.4 MOTION GATING METHOD 75

3.5 MOTION CORRECTION METHOD 80

3.6 RECONSTRUCTION IMAGE 86

3.7 IMAGE ANALYSIS 86

3.8 SUMMARY 89

3.1 Introduction

It is proposed to exploit the geometric sensitivity properties of 3D PET to effectively compensate for respiratory motion in PET imaging. Event rate changes due to non-uniform geometric sensitivity will be used as a surrogate for respiratory motion. By this method, respiratory motion phases or axial displacements due to respiratory motion can be determined from the change in number of frame events if acquisition data is sorted into dynamic frames. Based on this hypothesis, two specific methods of respiratory motion gating and correction were proposed: Geometric Sensitivity Gating (GSG) and Geometric Sensitivity Correction (GSC) respectively.

Two steps have been undertaken to test the proposed hypotheses: Firstly simulation software packages were used to validate and test the hypothesis before clinical studies are considered. The second and subsequent step, after encouraging results from the simulation testing, was the clinical validation of the simulation outcome.

All data for both simulations and clinical studies are acquired and processed in list-mode format. The formalism defined in Chapter 2.1.2.2 and Chapter 3.3 for GSG and GSC are list-mode data driven techniques. The practical clinical implication of this is that neither GSG nor GSC is possible if the PET acquisition is not performed in list-mode.

3.2 Simulation of PET acquisition data

Simulation plays an increasingly important role in imaging research studies. It has become a significant and indispensable tool that complements theoretical derivations, experimental methods, and clinical studies in medical imaging research and development. An essential aspect of simulation is to have a realistic phantom or model of the subject's anatomy and physiological functions, and subject's imaging data can then be generated using an accurate physical model of the camera system or phantom. The advantage of using a phantom, the source geometry, detection process and camera geometry in simulation studies is that all simulated modelling is constructed according to the exact known anatomy and physiological functions, or chemical and physical

processes. Thus simulation provides a gold standard or 'truth' which can be employed to investigate new techniques such as imaging devices, data acquisition, image processing and reconstruction algorithms. As a result of the inherent complexity of such phantoms, the computational time for an analytical method is too long for them to be used. Monte Carlo simulations compute a statistical estimate of the answer for complex phantoms using currently availably computing power. Monte Carlo simulations have become an essential evaluation tool for emission tomography developments[120]. Generally Monte Carlo techniques are used, where a solution is determined by pseudo random sampling of the interaction probabilities of individual quantum particles, until a statistical estimate of the answer is obtained with a small enough confidence interval.

In this research, respiratory motion was investigated by Monte Carlo simulation using GATE (Geant4 Application Tomographic Emission) and NCAT (NURBs [Non Uniform Rational B-Splines] Cardiac Torso) software packages. GATE is a toolkit designed for PET and SPECT Monte Carlo simulation in nuclear medicine [121]. NCAT was developed to provide a realistic and flexible model of human anatomy and physiology for use in nuclear medicine imaging research[41]. It provides the option to specify the data in different respiratory phases. The combination of GATE & 4D NCAT allows many configurations to be investigated for respiratory motion gating and correction prior to validation with clinical measurement[67] [32].

3.2.1 Coordinate System

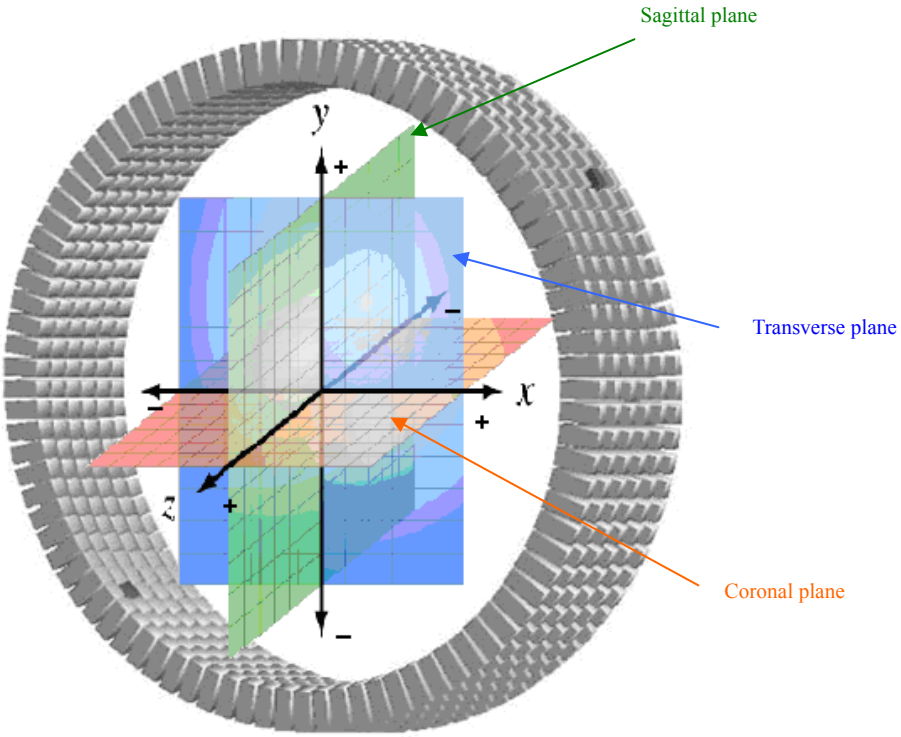

Fig. 3.1 Simulation and patient coordinate system in the geometry of PET scanner.

In this research, the Cartesian coordinate system was used for the phantom studies and clinical studies. The centre of the coordinate system is located at the centre of the PET scanner as specified in Fig. 3.1. Observed from the patient support couch of the PET scanner, the x axis increases from the right to the left, the y axis increases from down to up, and the z axis increases with distance from the observer. An example of the reconstructed images on Allegro PET for different plane views within the field of view (FOV) is given in Fig 3.2.

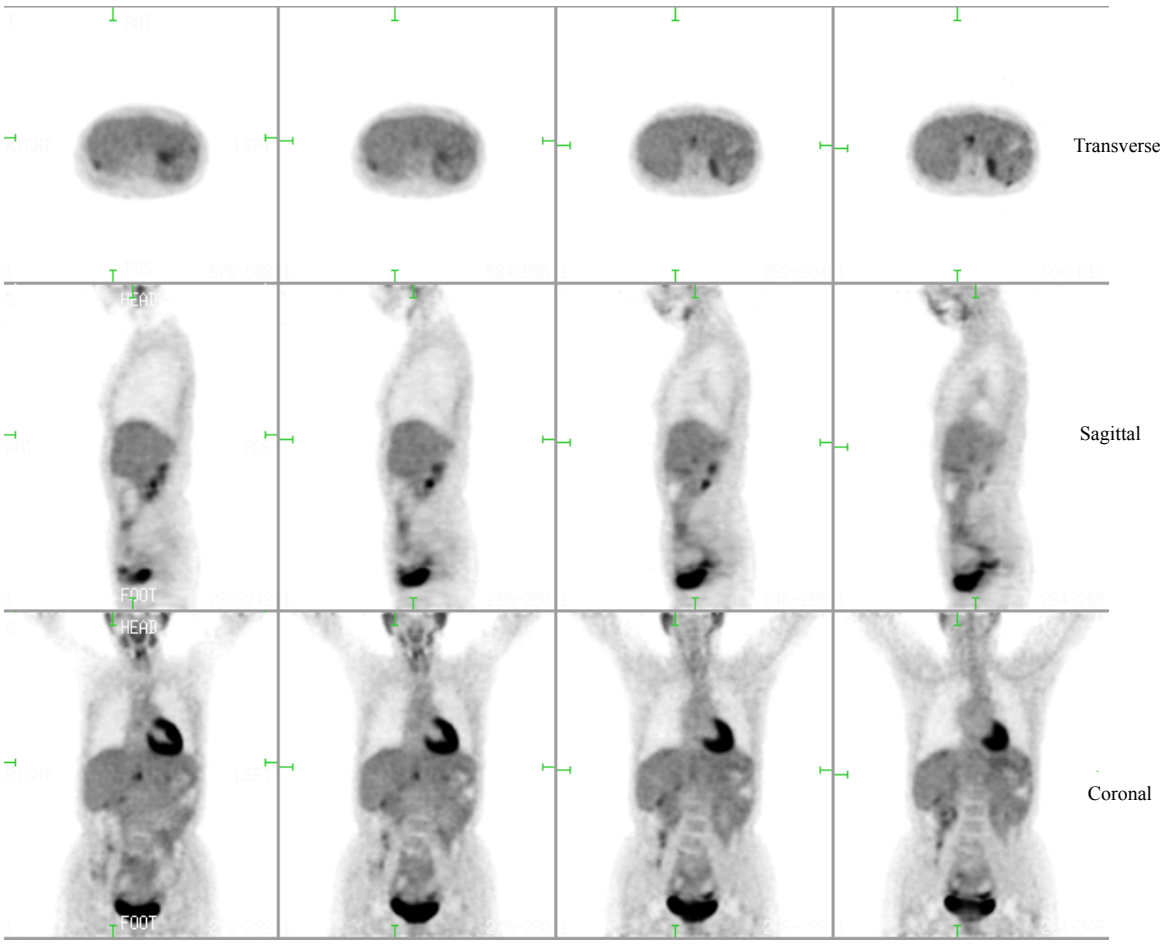

Fig. 3.2 Reconstructed image from Allegro PET in transverse, sagittal, and coronal views respectively from top to bottom. Graphic taken from Allegro User/ Service Manual, courtesy of Philips Medical System.

3.2.2 PET Imaging Relevant to the Monte Carlo Simulation

In order to investigate the potential of GATE for the simulation of a fully three-dimensional (3D) clinical PET system, GATE must be configured with the physical characteristics of the clinical PET scanner that it is to simulate. The PET scanner used in clinical respiratory motion measurements is the Philips Allegro/Gemini. It is a whole body PET Scanner and for the purpose of simulation it can be described in terms of the following physical characteristics, which are dominant the parameters affecting system's performance as illustrated in Table 3.1[122]:

Table 3.1 Features of Allegro/Gemini

Detectors				
Module	Thickness (X)	Radial (Y)	Axial (Z)	Crystal number
Pixels	1	22	29	636
Crystal size (mm)	20	4	6	
GAP	0	0.3	0.3	
Ring size (mm)	20	94.6	182.7	
Module number	PMTs	Detector number	PMTs zones	17864
28	420	6	56	
Detector Material		GSO		
Detector Ring (mm)				
Inner	Outer	Middle crystal	Ring diameter	Patient port
432.05	452.05	442.05	860	565
Energy (Ke V)			**Imaging**	
Resolution	Low threshold	Upper threshold	Acquisition mode	Sinogram
0.15	434.35	587.65	3D	UGM
			Axial FOV	Transverse FOV
Time (ns)			576 mm	180 mm
Dead time	Coincidence time window	Time Resolution	Number of image planes	Slice thickness
100	8	3	90	2 mm
Scatter shielding (mm)				
High	25	Extension	170	

3.2.2.1 PET Scanner Parameters

The detector ring consists of 28 modules as shown in Fig 3.3 and Fig 3.4[122]. The 28 modules are grouped into 6 virtual detectors. Each module is made up of an array of 22 tangential by 29 axial Gadolinium Orthosilicate (GSO) crystals (638 crystals per module), totaling 17,864 crystals for the whole PET scanner. The modules are arranged around the patient port with the GSO crystals facing the patient. The system utilises 420 Photo-Multiplier Tubes (PMTs) which are grouped into seven signal pre-amplifier circuit boards (PAC60) as shown in Fig 3.3. The 420 PMTs are mounted on the side furtherest from the centre of the 28 modules and collect light from the scintillating crystals. Each crystal element has a surface area of 4 (axial) x 6 (transverse) mm^2 and has a depth of 20 mm. The detector arrangement results in an axial FOV of 180mm as shown in Fig 3.5(a), with a ring diameter of 864 mm at the surface of the detectors and a radial FOV (patient port) of 576 mm for whole body scanning as shown in Fig 3.5(b)[122]. The lead shielding

(28.6 mm in thickness) placed on either side of the detector ring to minimize the effects of activity from outside the FOV and the scanning bed must also be included in the model. Surrounding the patient with 28 position-sensitive modules, data can be acquired simultaneously along any parallel line and at right angle[122]. By using reconstruction algorithms, the internal distribution of radioactivity can be determined. Allegro / Gemini's parameters can be seen in Table 3.1[122].

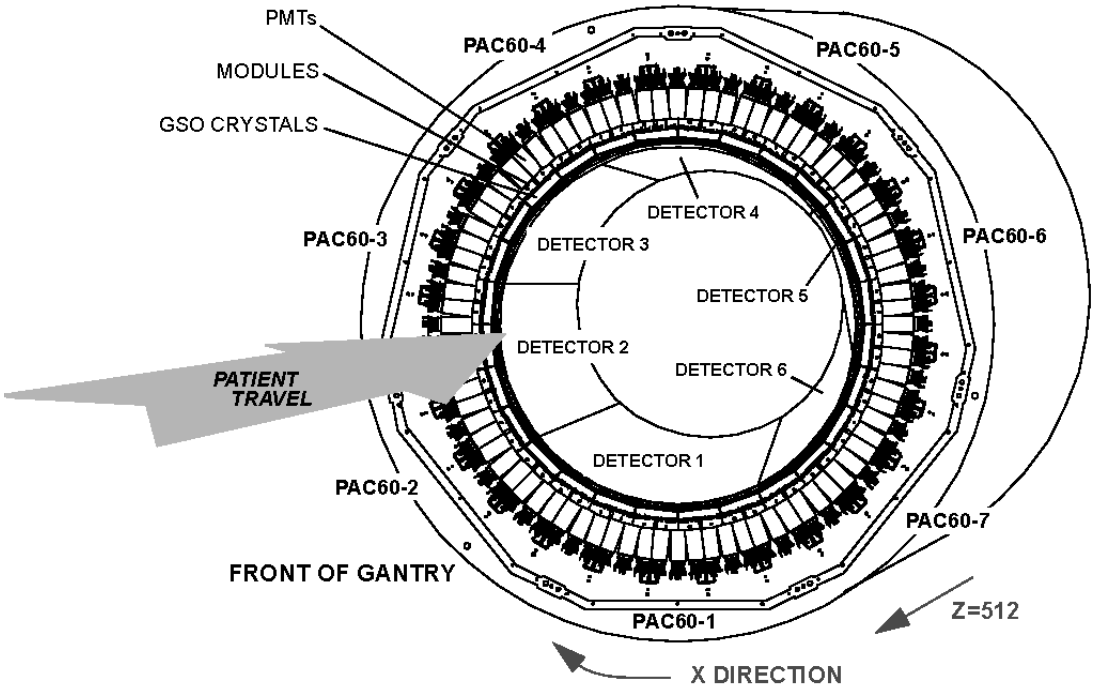

Fig. 3.3 Allegro PET scanner crystal orientation. Graphic from Allegro User / Service Manual, courtesy of Philips Medical System.

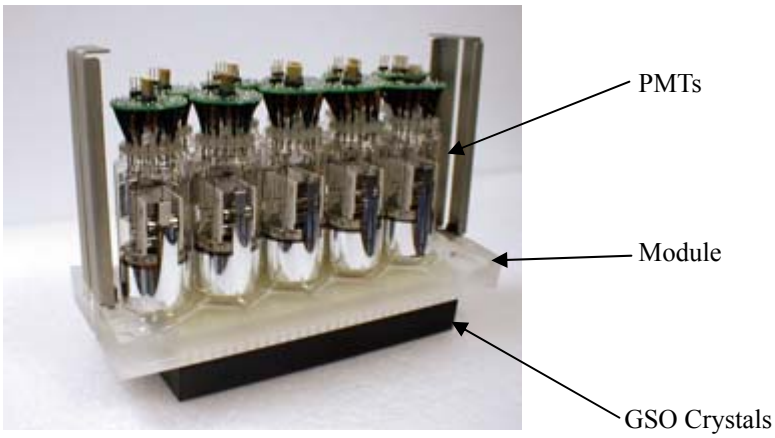

Fig. 3.4 Photo-Multiplier Tubes in Allegro PET Configuration. Graphic from Allegro User/ Service Manual, courtesy of Philips Medical System.

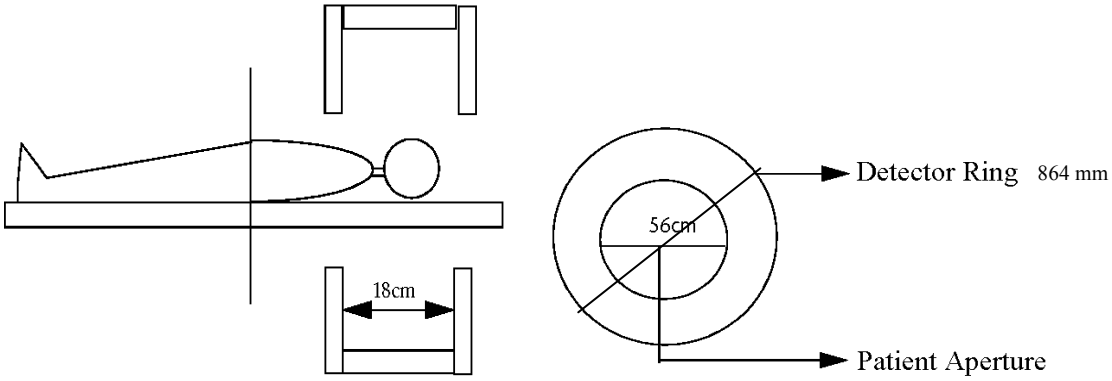

(a). Axial FOV is 180mm (b). Transverse FOV is 576 mm

Fig. 3.5 The FOV of Allegro PET Scanner in axis and transverse. Graphic from Allegro User/ Service Manual, courtesy of Philips Medical System.

3.2.2.2 Hardware Event Processing

An emission collection measures the distribution of activity in the FOV. During an emission collection, all hardware events processing are performed as below.

The pulses from GSO have a dominant decay time of about 60 nsec, approximately 200 nsec would be needed until most of the pulse is integrated. PET scanners rely on the detection of individual coincidence photons within a set 'coincidence' window. When this does not occur, and two consecutive pulses are not resolved in the coincidence resolving and more than one photon contributes to the pulse, this is termed pulse pileup. The Allegro scanner uses pulse shaping to shorten the pulse to approximately 100 nsec, thereby allowing a larger number of events to be processed without increasing the probability of pulse pileup.

The complete detector ring is subdivided into 28 trigger modules (channels), which logically overlap with each other. The total light output from each trigger channel is summed and represents the total energy deposited by the gamma-ray hitting the area associated with each trigger channel. This signal is processed by a constant fraction discriminator to give a logic signal. The discriminator also performs a lower level energy discrimination set to roughly 400 keV. The exact

level of the energy discriminator is set to avoid dead spaces between the trigger channels and to avoid a large amount of double triggering. Double triggers between two adjacent channels indicate that the event took place between two trigger channels and these events are accepted.

A coincidence between the allowed trigger channels determines which PMTs must be read out and used for the position calculation. Groupings of PMTs used for position determination are called zones. There are a total of 56 zones in the system. These zones again define logically overlapping groups of PMT's. Currently there are a total of 28 trigger channels grouped into 6 virtual detectors. Detectors 1 and 4 include 6 trigger channels, while detectors 2, 3, 5, and 6 include 4 trigger channels each. If only one trigger channel fires during an event, the zone centred over that trigger channel is read out. If two adjacent trigger channels fire, the zone between these two trigger channels is read out creating more zones than trigger channels.

After a valid coincidence event has been detected, the waveform from the PMTs – which are continuously digitized every 20 nsec - are integrated for 120 nsec. The PMT signals associated with the two zones identified during the coincidence are transferred to the position calculator. The position calculator first normalizes the PMT amplitudes by looking up a corrected amplitude from a calibration table, then it determines the PMT with the highest signal and calculates a local centroid using the PMTs in the direct vicinity of that peak PMT. In this way, signals on PMTs which may receive light from some other event are excluded from the position calculation.

As in other single crystal position-sensitive detectors, the calculated positions do not correspond exactly to the point at which the scintillation occurred. Therefore, the system analyzes a flood image and creates a mapping from calculated positions to crystal coordinates. To remove systematic errors the system adds position offsets to the calculated values. These position offsets are derived from previous calibration measurements as shown in Fig 3.6[38]. At the energy determination in the event processing, the exact energy of each event is known. Energy discrimination is performed by applying upper and lower energy thresholds. At this point in the event processing, the exact energy of the two events is known. A second energy discrimination is now performed by first correcting the energy signal for local spatial variation in amplitude and then applying upper and lower energy thresholds. This energy window is usually set with tighter

energy limits to reduce scatter, a lower energy level of 450 keV is typical. These energy thresholds are set in the acquisition program but are rarely changed.

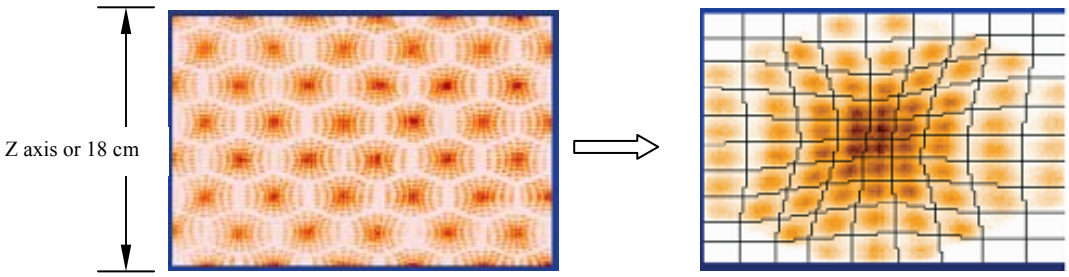

(a). Flood maps (b). Scanner calibration

Fig. 3.6. Flood maps illustrates process to define scanner geometric distortions correction. (a) Allegro PET 2D flood image with continuous positioning, no block detectors. (b) Scanner distortions correction.

At the rebinning stage of the event processing the detector coordinate pair is converted to 4D projection coordinates (i.e. sinogram coordinates) or list data. For each event a single element in a Line of Response sinogram is incremented as shown in Fig 3.7 and Fig 2.4. The coordinates are the rotational angle in the transverse plane (ϕ) the radius in the transverse plane (ρ), and the axial location on each detector (Z). The axial acceptance angle can be selected by the user; by selecting a very narrow axial acceptance angle, the scanner can be operated effectively in 2-D mode with a large resulting loss of sensitivity. This feature may be of interest if the user wishes to investigate the effects of the 3-D mode of operation**.** However, in this '2-D mode' the scatter fraction would still be 40% compared to 10% for 2D septa system[122].

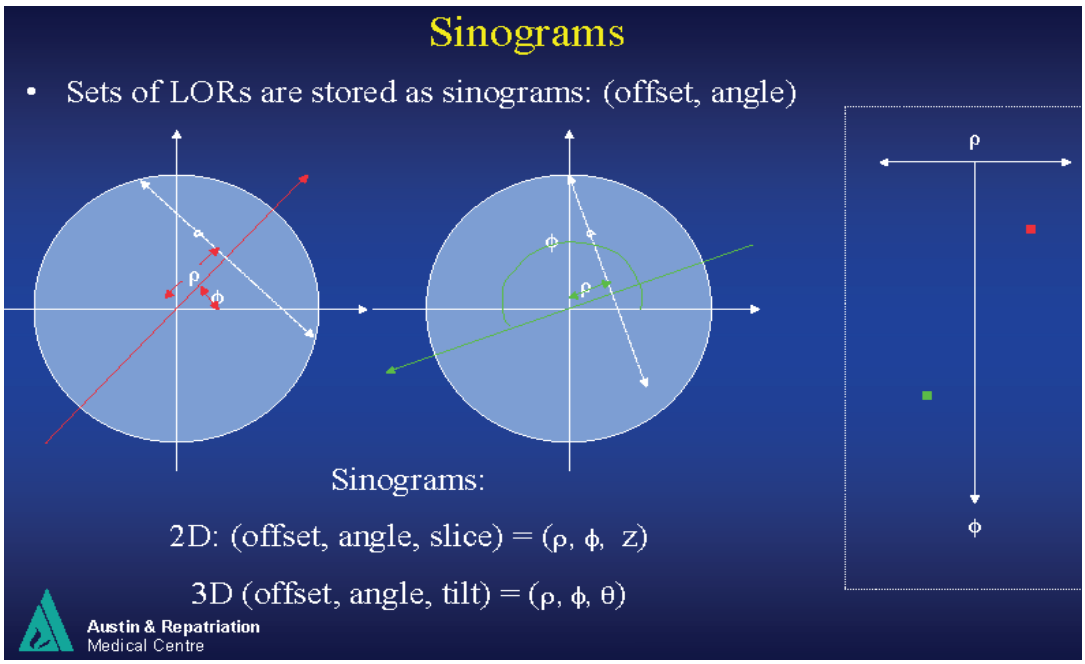

Fig. 3.7. Two line of response events are converted into sinogram with 2D or 3D mode.

3.2.3 Simulation Software

3.2.3.1 GATE

It has been demonstrated that GATE is able to effectively simulate the Allegro PET Scanner[123, 124]. The use of GATE for simulation of respiratory motion requires understanding of the structure of GATE, the simulation steps and how to generate a Geometric phantom and a voxelised phantom.

3.2.3.1.1 Structure and Digitiser Optimisation

GATE is a PET/SPECT camera simulator which is Open Source and developed on Geant4 as illustrated in Fig. 3.8[121]. The core layer defines the basic mechanisms available in GATE for geometry definition, time management, source definition, detector electronics modelling, data output and very importantly the physical processes involved in photon interactions with matter, such as Photoelectric absorption, Compton scattering and Rayleigh scattering. The application layer is composed of the base classes derived from the core layer to model specific objects or processes. In the user layer, GATE provides mechanisms for running simulations either interactively or batch-wise using scripts. The use of GATE does not require low level

programming, such as C++. It provides a high level interface made of a dedicated scripting mechanism, referred to as the macro script language and is available to facilitate simulations. GATE is able to synchronise all time-dependent components in order to allow a coherent description of the acquisition process [123, 125].

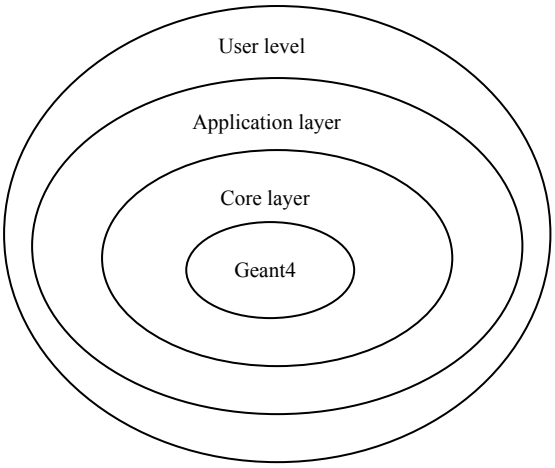

Fig. 3.8 Structure of GATE containing 4 levels: Geant4, core, application, user.

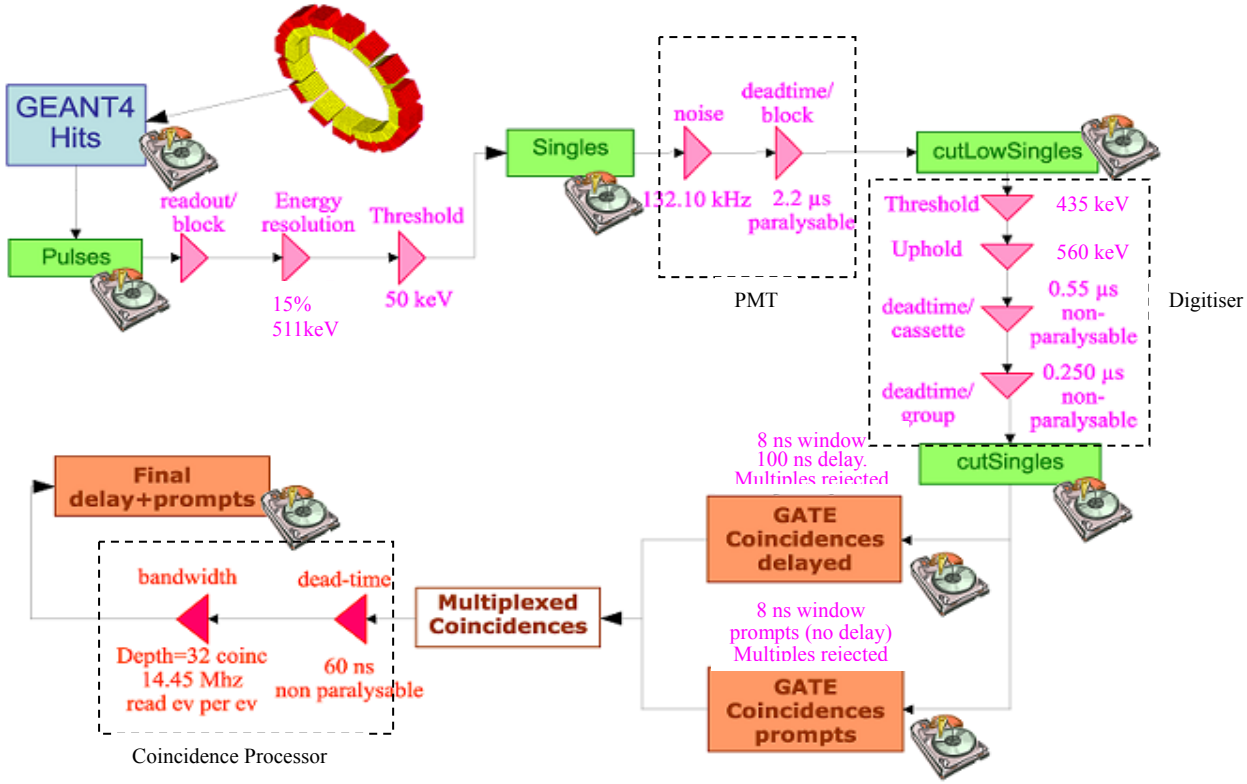

Fig. 3.9. GATE digitiser chain, the disk icons represents the data written to the GATE output files.

In addition, GATE provides digitiser optimisation to simulate the procedure of line of response (LOR) event processing in PET. Primary particles are generated by the source manager, and then propagated through the attenuating geometry before generating hits in the detectors, which feed into the digitiser chain as illustrated in Fig 3.9[121].

3.2.3.1.2 Simulation Steps

GATE simulations are based on the execution of scripted commands defined in a GATE macro file. A simulation is generally divided into 7 steps as illustrated in Fig 3.10[121]:

1. Verbosity and Visualization: One can set a verbosity level between 0 and 2 to trace information returned on the screen during simulation by GATE. The on-line visualisation tools allow one to visually check of the scanner geometry and also source geometry necessary for debagging.
2. Geometry: The world volume must be created for the scanner and the phantom. Next the PET scanner system is chosen to attach all the scanner elements. A phantom is defined with a geometric or voxelised volume.
3. Digitiser: The digitiser pre-processes the hits to build singles with the time stamps on them and stored them in the events history. The coincidence window width, dead time and the detection parameters are set at the digitiser lever.
4. Physics: This comprises broadly aspects such as the definition of which physical processes will be simulated, whether the standard or low energy electromagnetic processes package will be used, enabling photoelectric effect, Compton effect, Rayleigh … etc, and the cut-off to define tracking energy steps.
5. Source: A source is defined by its isotope definition, activity, geometry and movement. ^{18}F is the specified radioactive isotope of which all sources are composed for all of the simulations in this research.
6. Data outputs: The result of simulation can be outputted as two types of format file which can be set up in macros file of GATE. One is standard outputs: ASCII and Root. Another is system dependent outputs: List-Mode Format (LMF), sinogram, ecat7 and Interfile.

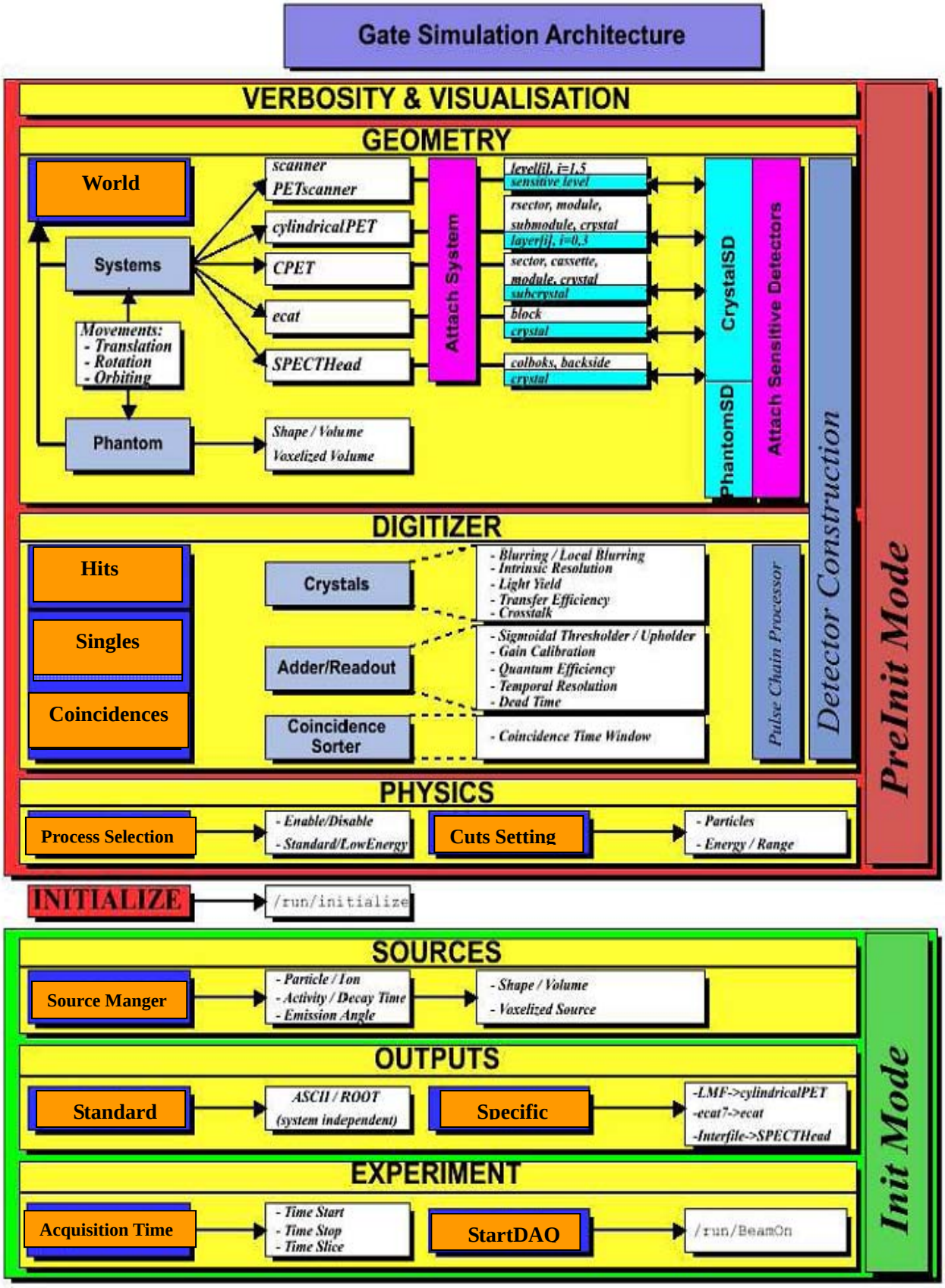

Fig. 3.10. GATE simulation architecture.

7. Experiments: Setting up the duration of the simulated acquisition by defining the beginning and the end of the simulation. This provides the possibility to take into account the movement of the sources or the detectors by subdividing a run in time slices characterised by different snapshots of time dependent geometry.

Following the above 7 steps, GATE is configured with the scripted macros command in terms of Allegro scanner geometry and signal processing flow to simulate respiratory motion acquisition. Specifically, retrieved parameters of the Allegro Scanner /Gemini in macro file involve three aspects: geometry, such as the size and number of detector and module; digitiser such as energy resolution and dead time; and physics such as selection of electromagnetic process. The detailed scripted macro command file following the above steps can be seen in the Appendix C. All simulations were performed using GATE software package version 2.2.

3.2.3.1.3 Geometric and Voxelised Phantom

Two classes of simulations were performed, one series of geometric phantom for rapid evaluation and the another using a series of voxelised phantom for more detailed, realistic simulation.

In GATE, a phantom for respiratory motion simulation can be generated with a geometric phantom and voxelised phantom[67]. A geometric phantom may be composed of a simple combination of geometric objects such as cylinders and spheres. Boundaries of shapes can be represented by mathematical equations, such as spheres, cylinders, parallelepipeds, etc. and these can be used to approximate irregularly-shaped regions. The principle advantage of the geometric phantom approach is its speed of generation and simulation. However the geometric phantom modeled cannot simulate complex objects. The geometric phantom was generated by the GATE software itself as shown in Fig 3.11.

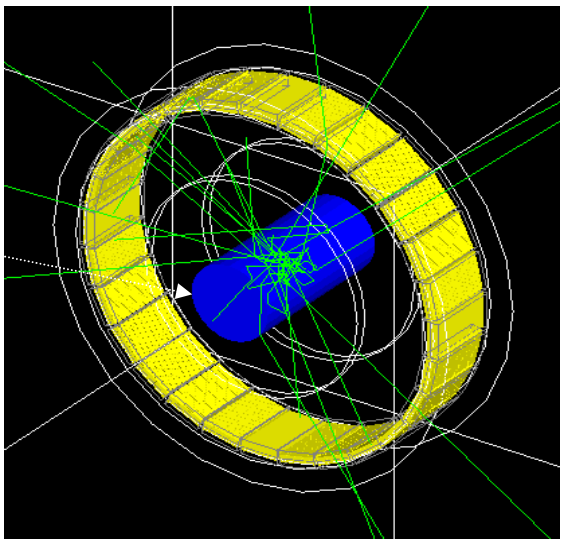

Fig. 3.11. A geometric phantom (cylindrical shape) and LORs were generated by using GATE within the FOV simulating Allegro PET Scanner.

GATE is able to simulate simple respiratory motion with the geometric phantom[125, 126]. One of the distinctive features of GATE is the management of time-dependent phenomena. The synchronization of the source kinetics with the movement of geometry thus allows for the simulation of realistic acquisition conditions including patient movement, respiratory and cardiac motion, scanner rotation or changes in activity distribution with time. GATE is able to manage the temporal dependence of: (a) the movements associated with the physical volume that describe the detector and phantom; (b) radioactivity sources and (c) the start and stop times of the acquisition.

One motion cycle, representing a single complete respiratory cycle, was defined by a number of sub phases, each with a corresponding frame describing the geometry. The time interval for which each frame was relevant was defined by a "setTimeSlice" command in the macro file of GATE. The number of respiratory cycles simulated was then specified implicitly using the "setTimeStart" and "setTimeStop" command in the same macro file. Sample geometric phantom script macro files for GATE are given in Appendix A and Appendix B. The results obtained from these preliminary investigations are described in section 4.1 of this thesis.

With respect to a voxelised phantom, GATE cannot generate a voxelised phantom by itself, but GATE provides an interface to import external phantoms as voxelised phantoms for simulation. A

voxelised phantom is a discrete representation of a continuous distribution. By subdividing an object into a set of discrete cubes (voxels) as shown in Fig 3.12 of sufficient size (typically, ½ to ¼ the spatial resolution of the scanner) where each voxel takes on the average value of the modelling continuous distribution at the voxel location, the object is represented in a form suitable for numerical integration and sampling by GATE. An object is thus represented by a union of voxels of the same size. A new family of phantoms was constructed from human CT and MRI data. The digital human phantoms more accurately represent the location and shape of the organs, in particular the hard bone and bone marrow. With the advantage of the more accurate representation of the anatomy from CT and MRI images comes the disadvantage of increased calculation time that results from the increased complexity of the phantom[127]. The result obtained from voxelised phantom investigations are described in section 4.2 of this thesis.

There are two supported file formats within GATE to allow import of voxelised phantoms or sources: ASCII file and InterFile format. For an ASCII file, the numbers in the file represents the source activities in each of these voxels which converted to source activities using range translation table. An example of an entry in the range translation table to convert numbers to source activities is given here, “10 50 100”. This is specifies that a number associated with a voxel in the range of 10-50 indicates an activity within that voxel of 100 Bq as displayed in Fig 3.13. The resulting voxelised source thus has assigned to its voxels only discrete activity values selected from the range lookup table.

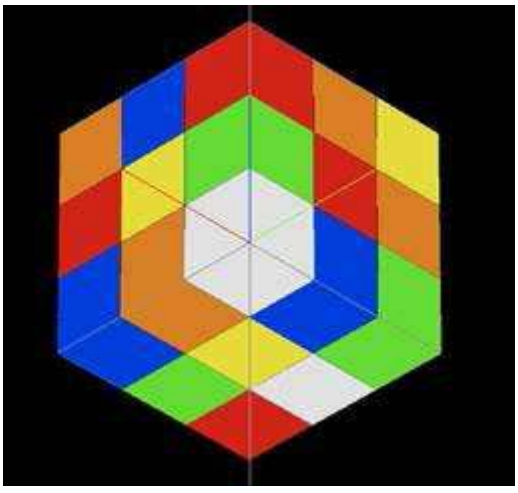

Fig. 3.12. A simple voxelised phantom with uniform voxels.

The method used in this thesis was to import images in InterFile format. The greyscale values of the image are then converted into activity values by the range translator. The images were generated for respiratory motion by the NCAT software packages. The NCAT generated frames each corresponded to a sub phase of the respiratory motion cycle. The script macros files of GATE for this can be seen in Appendix C.

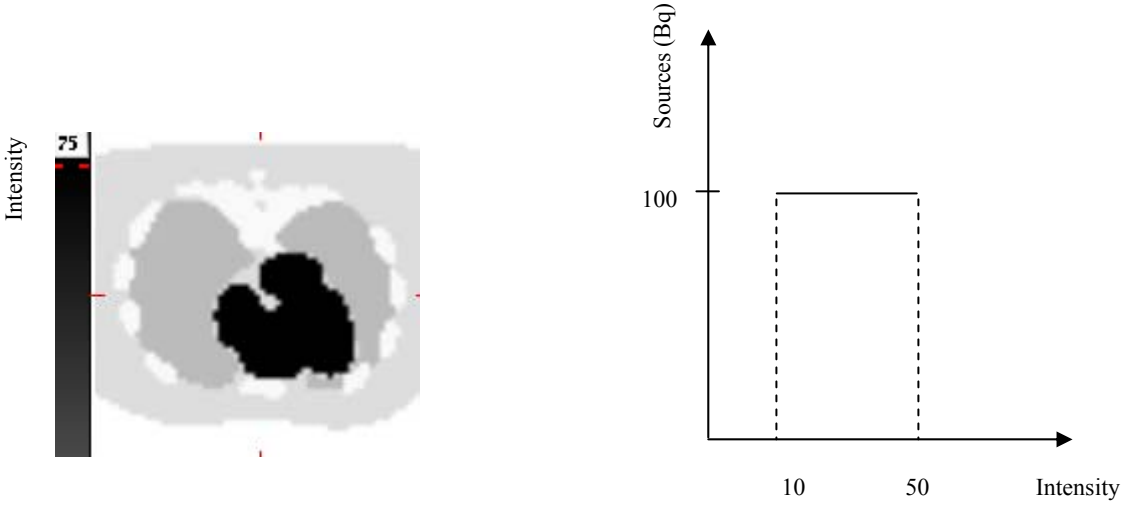

(a). Intensity value = 10 ~ 50 in the voxelised phantom

(b). Intensity value = 10 ~ 50 converted to source activity = 100 Bq

Fig. 3.13 Translation of intensity in voxelised phantom to source activities

3.2.3.2 NCAT Digital Phantom

To simulate a more realistic respiratory motion, the 4D-NCAT voxelised phantom was imported into the GATE environment. The NCAT phantom was developed by Segars [41] using MRI data and high-resolution respiratory-gated CT data to create the 3D surfaces for the torso structures. An example is shown in Fig 3.14[128]. A model of the heart beating using 4D cubic NURBS (Non Uniform Rational B-Splines) was incorporated. Respiratory motion was included in the phantom which modeled organ motion of normal quiet or tidal breathing. During inspiration, the abdominal organs move downward and outward, increasing the volume of the thorax. The ribcage moves upward and outward, further increasing the thoracic volume and is characterised by a non-rigid motion. There are compressible motions of lung, liver and heart. The volume of the lungs changes with the volume of thorax and the heart moves downward and upward with the

diaphragm. Compared with the geometric phantom, which just simulates oscillation along the z-axis direction, the NCAT phantom can simulate 3D respiratory motion.

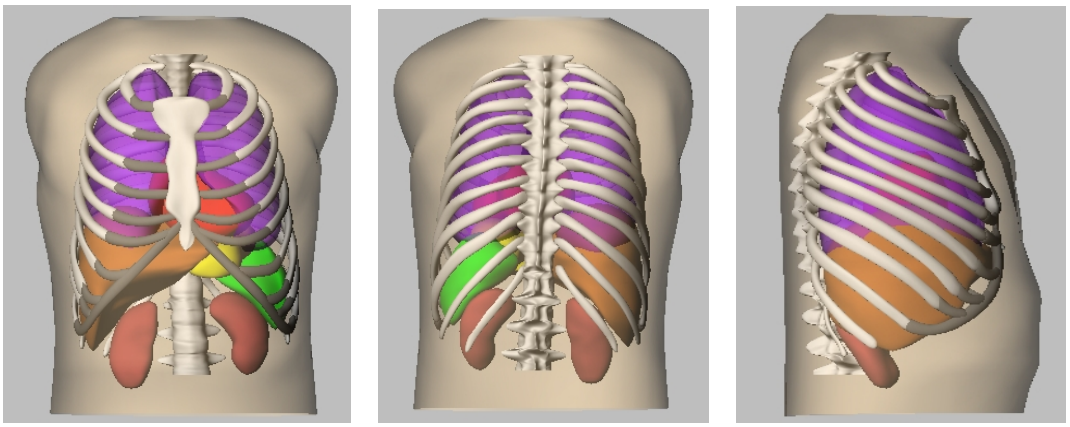

(a). Anterior view (b). Posterior view (c). Right lateral view

Fig. 3.14. 3D renderings of the NCAT phantom at anterior posterior and right lateral views.

The period of tidal breathing is approximately 5 seconds[40]. For a cycle of this duration, the inspiration phase takes 2 seconds, and the expiration phase lasts 3 seconds[40][41].

NCAT version 2.0 provides very flexible suite of programs for a wide range purposes, only two of which were used to generate phantoms and model lesions in the lungs in this research. One is "dncat_bin", the main phantom program, and the other is "resp_lesn_bin", the generator lesion program. Each program has a sample parameters text file containing numerous parameters to define the phantoms produced by the program. This includes parameters to define voxel size, patient motion, variations in anatomy, radionuclide uptake ratios for the activity phantoms, photon energy to define attenuation coefficients, etc. See these text files for more information on the types of parameters that are available in Appendix D.

The NCAT phantoms were generated as raw binary image frames and attenuation coefficient image frames. All image frames can be imported into GATE as voxelised phantoms by converting the binary format into Interfile format. The gray scale in the Interfile image is then converted to

material definitions in the phantom using the range translator command line in the script macros file of GATE.

3.2.3.3 Validation for GATE

The structure and working principles of GATE as a Monto Carlo software simulation of a PET camera has been introduced in section 3.2.31. In this research, the PET camera to be simulated by GATE is the Allegro / Gemini, we therefore need to investigate and validate whether GATE is able to effectively simulate the Allegro PET Scanner. This validation involves comparing the GATE simulation using the geometric phantom and voxelised phantom with the measurement of the Allegro PET scanner, which the evidence briefly presented here would be characterised as visual confirmation of the spatial resolution of the simulation, because computation time prevented a number of validations and more meaningful quantitative validation of simulation of Allegro/Gemini Scanner has been done by Lamare et al [123] and can be cited.

The simulation processing pipeline involves four steps [67]as shown in Fig. 3.15: first, setting up GATE in terms of the Allegro PET as shown in TABLE 3.1 and phantom parameters; second, running GATE to obtain the phantom projection data as list-mode data; next, converting the list-mode data to Allegro UGM sinogram format; last, obtaining a reconstructed image from UGM sinogram data. All simulations were running with a total of 37 MBq ^{18}F source activity in the phantom. For GATE simulation of the Allegro scanner, geometric phantoms and voxelised phantom are selected to simulate Allegro acquisition data. The geometric phantoms simulated are Jaszczsak and cylindrical[67]. The voxelised phantoms are defined by Hoffman and NCAT phantoms. For NCAT simulation of respiratory motion, voxelised phantoms are generated for a 5 second breathing cycle with 25 frames at 200 ms per frame. Each frame is then imported to GATE as a voxelised phantom to simulate different phases of breathing. The 1st and 12th frames are selected as representative of full inspiration and expiration respectively and imported into GATE as voxelised sources and μ-maps to simulate respectively, full inspiration and full expiration.

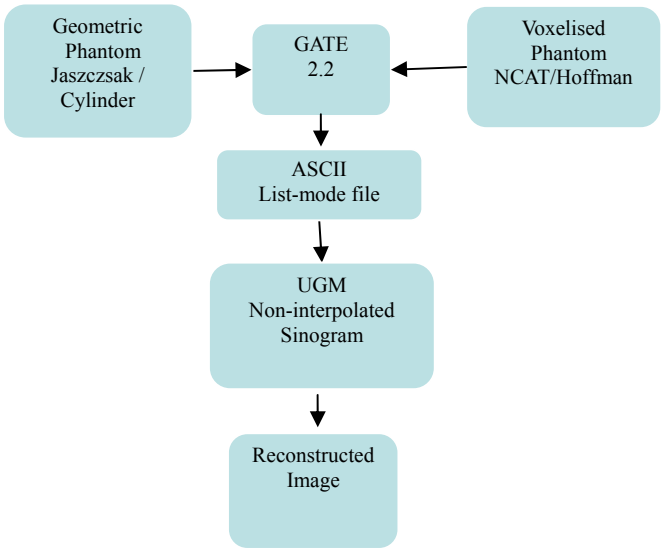

Fig. 3.15. The procedure of simulation validation for GATE

Two examples of validation by the geometric phantom and voxelised phantom are shown in Fig 3.16 and Fig 3.17 respectively. In comparisons of the Jaszczack simulation by GATE with direct measurement by Allegro, although the number of LOR events collected by GATE are far less than from the Allegro measurement, the reconstructed image of the GATE simulated five spheres source activity in Fig 3.16(d) visually compares favourably with the Allegro measured five sphere phantom in Fig. 3.16(b) In addition, the UGM sinogram map (Fig 3.16(c)) of GATE list-mode data reflects the distribution of LOR events in the scanner geometry. Also for cylindrical phantom simulation, the image profile of the simulated non-attenuation-modelled source gives a uniform distribution of activity as displayed in Fig. 3.16(e). In contrast, the image profile of Fig. 3.16(f) clearly shows the effects of attenuation in the reconstructed attenuation-modelled source.

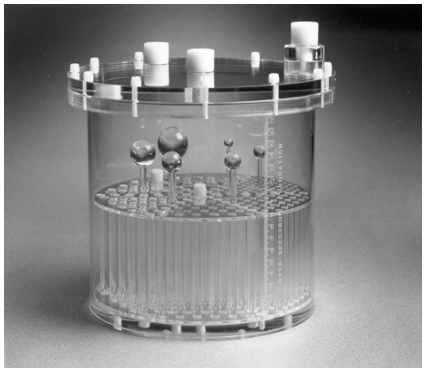

(a). Jaszczack phantom

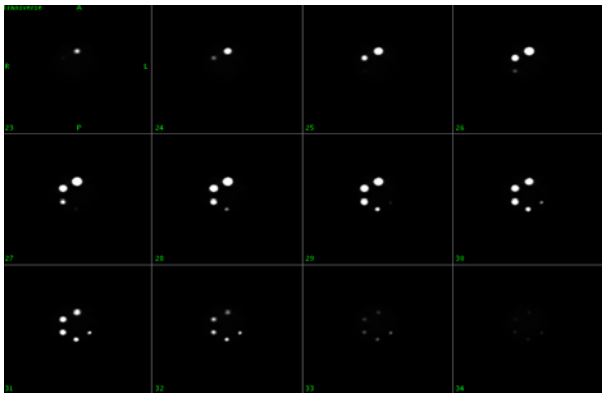

(b). Measurement reconstructed image by Allegro, with 300 million LOR events

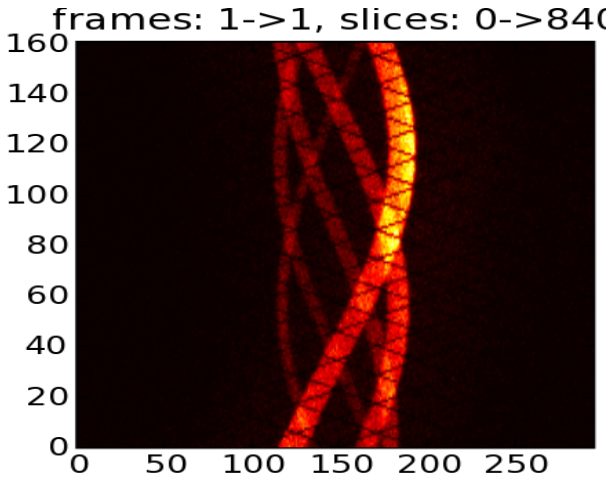

(c). UGM sinogram from GATE projection data

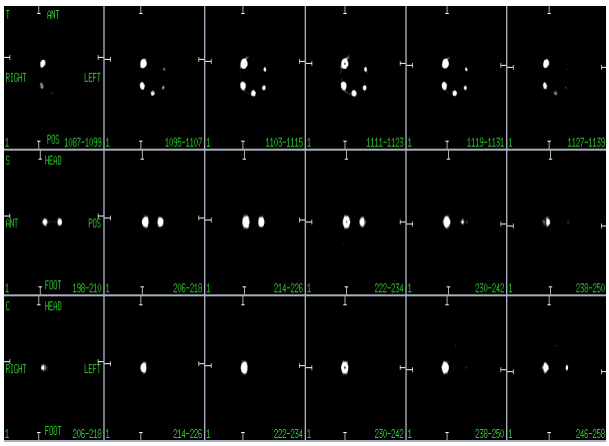

(d). Simulation reconstructed image by GATE with 3 million LOR events

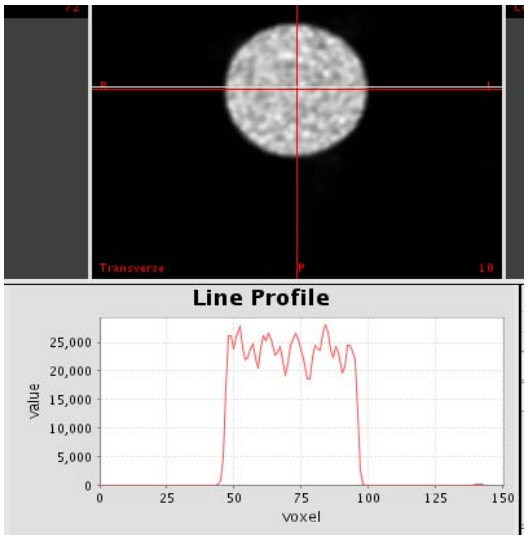

(e). Cylindrical phantom simulated non-attenuation modelled by GATE with 3.4 million LOR events

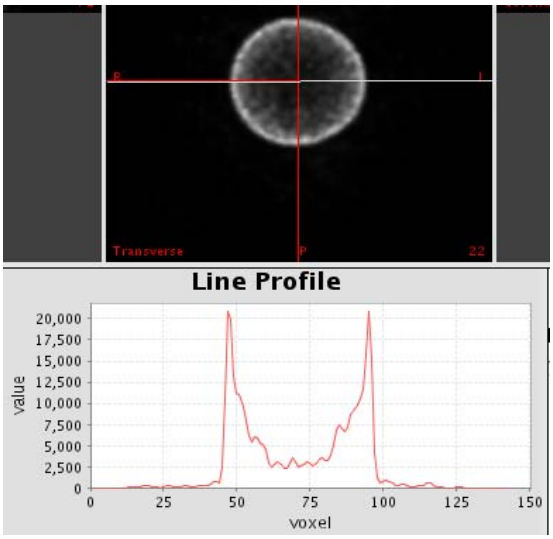

(f). Cylindrical phantom simulated attenuation modelled by GATE with 3.4 million LOR events

.Fig. 3.16. Comparison of simulation result of Jaszczack phantom by GATE with measurement by Allegro. And simulated with and without attenuation modelled.

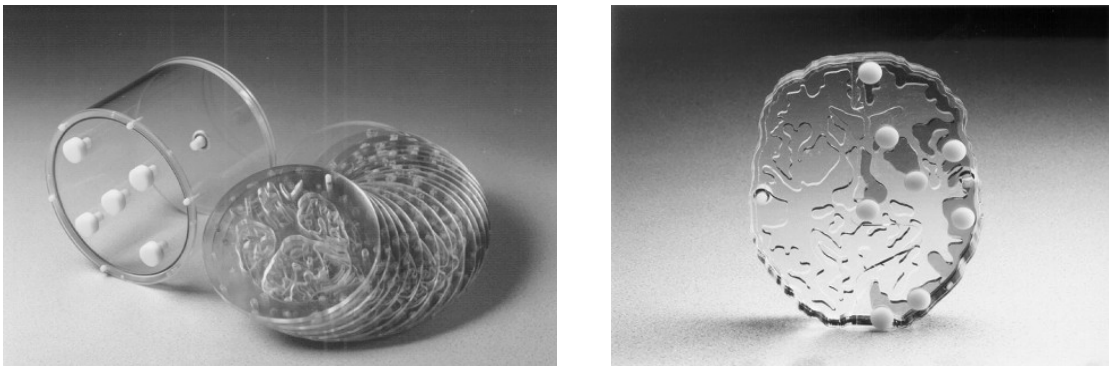

(a). Hoffman phantom

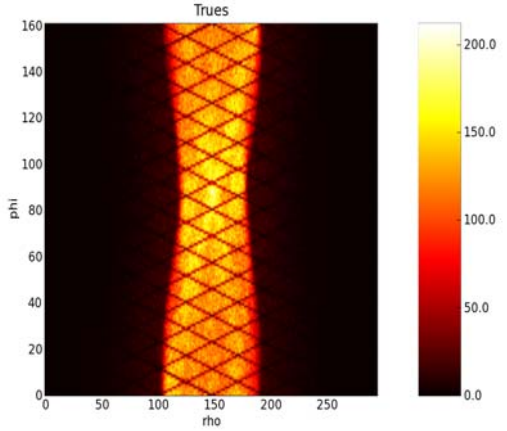

(b). UGM sinogram from GATE projection data

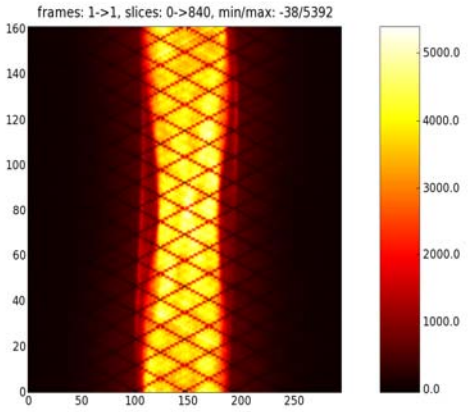

(c). UGM sinogram from the measurement by Allegro

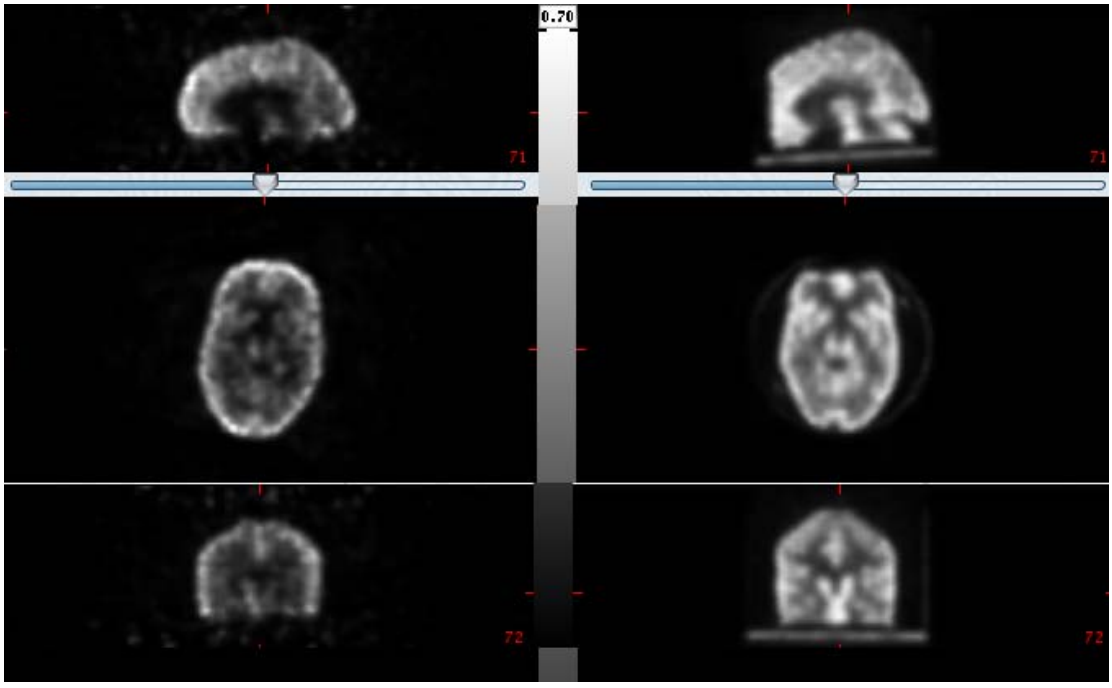

(d). Simulation reconstructed image by GATE with 1.6 million LOR events

(e). Measurement reconstructed image by Allegro, with 51 million LOR events

.Fig. 3.17. Comparison of simulation result of Hoffman phantom by GATE with measurement by Allegro.

The some validation results obtained[67] demonstrate that GATE is able to simulate the Allegro with both geometric and voxelised phantom. Also Lamare et al (2006)[123] demonstrated that GATE is able to simulate the Allegro / Gemini PET system through the comparison of simulated and measured results obtained with the Allegro / Gemini PET system for a number of the National Electrical Manufactures Association (NEMA) NU2-2001 performance protocols including spatial resolution, sensitivity and scatter fraction. they reported a good agreement between simulated and measured results. For example, an agreement of < 3% was obtained in scatter fraction, and the spatial resolution values was obtained using the simulated model are within 11- 18% of measured results. In addition, the simulated sensitivity is < 10% higher than the measured sensitivity.

3.2.3.4 Computational Issues

GATE performs a Monte Carlo simulation to simulate the interaction and transport of photons resulting in the accumulation of LORs by the PET camera. These procedural steps involved in simulation by GATE of the geometric and voxelised phantom are illustrated in Table 3.2. All simulations below were implemented on an Intel Pentium 4 2.28 MHz PC running Linux RedHat 8.2.

The GATE simulation is extremely time-consuming, particularly in the simulation of the attenuation modelling. For example, a voxelised NCAT phantom simulating a frame of respiratory motion with the attenuation modelling takes as much as 24 days for 1 million LOR events to be collected. This is an unmanageable amount of time to run one simulation for the study because the breathing cycles need to be separated into a sequence of frames to investigate each frame. For example, the simulation of 50 seconds of breathing acquisition time, at 5 seconds per breathing cycle with 200 msec per frame, requires 250 separate frames that need to be simulated both with and without attenuation modelling. For the non-attenuation modelling case, the total simulation time would be of the order of 500 hours (250 frames × 2 hrs) which demonstrates that this computational task is beyond what can be achieved with one computer.

Table 3.2 A summary of real-time and LOR events for the GATE simulations of the geometric and voxelised phantom and sources

Summary of simulations			**Computational / Measurement Times**		
Classifica-tion	phantoms	Simulations / Measurements	Measured	compute	LOR events
Geometric phantom & source	Jaszczsak	Measurement with attenuation	30 minutes	n/a	Non Attenuation: 1 million / 4 hrs Attenuation: 1 million / 5 days
		Simulation with attenuation	5.8 sec	4.4 days	
	Cylinder	Simulation without attenuation	3.2 sec	1 day	
		Simulation with attenuation	6.1 sec	3 days	
Voxelised phantom & source	Hoffman	Measurement with attenuation	30 sec	n/a	Non Attenuation: 1 million / 4hrs Attenuation: 1 million / 8 days
		Simulation without attenuation	6.1 sec	10 hrs	
		Simulation with attenuation	6.1 sec	12 days	
	NCAT	Measurement with attenuation	5 minutes	n/a	Non Attenuation: 1 million / 5 hrs Attenuation: 1 million / 24 days
		1st frame simulation without attenuation	4.4 sec	2 days	
		12th frame simulation without attenuation	2.9 sec	2 days	
		Average frame simulation without attenuation	3.7 sec	2 days	
		1st frame simulation with a lesion	12 sec	2 days	

To solve this computational issue, super cluster computers were employed to implement the designed simulations for this research in the Victorian Partnership for Advanced Computing (VPAC). The VPAC supercomputing systems provide many parallel processors working for users, but the number of processors for each user is still limited due to many users working on the systems. For our simulations, each frame simulation running needs to take one processor. So a 250 frame simulation needs 250 processors. However, the VPAC systems usually just assign around 18 processors to each user; users must wait for free processors to do more simulations in the waiting pool. Despite saving huge amounts of time by using the VPAC systems for simulations in this research, the total stimulation time is still extremely time-consuming as our

simulations involve several hundreds frames with attenuation and without attenuation modeling of geometric and voxelised phantom, which is described in Chapter 4.

3.3 Sort List-Mode Data

The purpose of sorting list-mode data is to determine respiratory motion phases. Acquisition data for respiratory motion is obtained in list-mode data format that can be sorted into retrospective dynamic frames. One cycle of respiratory motion consists can be broken down into a finite number of temporally exclusive and contiguous sub phases of motion. As a result, one phase of respiratory motion can be regarded as one frame from the list-mode data. Therefore, the sorted frames correlate to respiratory motion sub-phases in this research.

3.3.1 Simulation List-mode Data

After setting up a geometric phantom or a voxelised phantom for GATE, one can execute the macros of GATE for simulation. The output format can be either as ASCII file format or ROOT file format. In this research, all simulation results were saved in ROOT file format as it is advantageous for compression and will produce a much smaller size file, as a result it can enhance access speed compared to the ASCII file format [129].

The simulation output contains list-mode data, also named as coincidences in GATE where 42 variables are stored, including event position, time stamp and energy deposited, etc[121]. In order to sort the geometric phantom list-mode data of a simulation, we need to extract frames from the list-mode data, each comprised only of events corresponding to a particular time period. To achieve this, we search those coincidences with the same identification “runID” in list-mode data stream in the ROOT file to gather them as one frame corresponding to one sub phase in a particular breathing cycle (forward explanation referenced in Chapter 4.1.2.3). For the voxelised simulation list-mode data, a sort is not required since GATE simulates each NCAT voxelised phantom frame one by one, and we have only process each simulated frame in turn (forward explanation referenced in Chapter 4.2.2.3). In simulation, the ‘sort’ of ASCII & List-mode data

and then conversion of the sorted data to the format for reconstruction were implemented in Python & Geant C++ programming.

3.3.2 Clinical List-mode Data

The Philips Allegro scanner has been configured to allow operation in research mode which is able to obtain acquisition data in list-mode format. The particular format used in this research is the Compact List Mode with the magic number ASCII "LOR4"[130]. It consists of one 32-bit word with control words as illustrated in Fig. 3.18[131]. The control words contain timestamp information, table position, transmission ring position, gate input, singles trigger rate, prompt trigger rate, or delays trigger rate. All 7 control words are inserted with each timestamp.

In each event word the first 16 bits contains the distance and angle of the coincidence[130]. The next 6 bits uniquely identifies the A detector involved in the coincidence event. The next 6 bits uniquely identifies the B detector involved in the coincidence. The 29^{th} bit contains information about the delayed event or prompt event flag. The last two bits contain the identified flag of an event. LOR events are divided into prompt events and delayed events. The total number of events detected by the coincidence circuit in a PET scanner is referred to as prompt events. A delayed event may be a scattered, or random, or multiple event which has a degrading effect on the measurement and need to be corrected to produce an image that represents as closely as possible the true radioactivity concentration. The event format is shown below:

Event format:

Bits 0 .. 15 contain the R(radius of the event) and Phi

Bits 16 ..21 contain the zPosA

Bits 22 ..27 contain the zPosB

Bit 29 contains the delayed event flag

Bits 30 ..31 must be set to 0 (this identifies an event)

Control world:

Bits 30.. 31 must be set to 2 (control word 1) or 3 (control world 2)

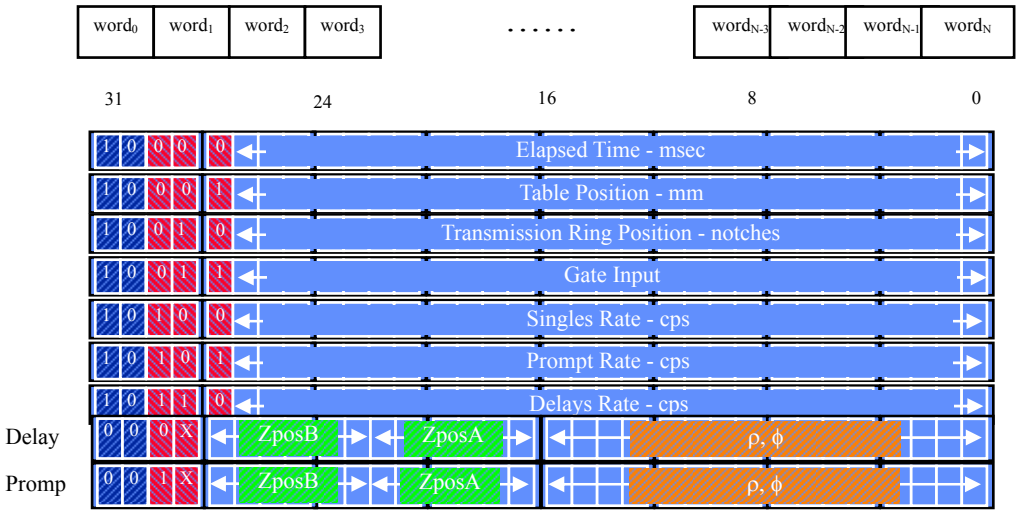

Fig. 3.18. List-mode format for Allegro PET acquisition.

A list-mode file contains an 8192-byte header, followed by list-mode events. Timestamps are added to the stream of list-mode events to mark boundaries of acquisition buffers and to supply additional information about each buffer of events. A timestamp is the same size as a list-mode event, and timestamps are embedded in the stream of list-mode events [130].

In list-mode data, each event is individually written to a file, with information about the two locations at which the annihilation photons interacted at which the event occurred. List-mode data are advantageous for dynamic studies, as the events can be sorted into time "bins" after the completion of the acquisition study[36]. The list-mode data can be sorted into static (single frame) and / or dynamic (multiple frame). One can then reconstruct the output LOR sinogram(s) into an image. To achieve that purpose, the code was developed for the sort of clinical list-mode data into sequence of frames in Python, which uses by input list-mode data with frame interval time setting and outputs frames as phases of breathing cycles. With frames extracted from list-mode data, we can apply the proposed hypothesis for respiratory motion gating and correction (forward explanation referenced in section 4.3.2.2).

3.4 Motion Gating Method

The geometric sensitivity is non-uniform along the z axis in 3D PET scanners as simulated Allegro / Gemini scanner by GATE in Fig 3.19. If radioactivity distributed within the FOV moves along z axis, the measured event rate will change. If the motion is cyclic, such as that caused by respiratory motion, the change in the event rate events will be cyclic as well. As a result, the feature of geometric sensitivity could be utilised for respiratory motion gating and correction as described in the section 1.3. Fig 3.20 is a schematic example of how the sensitivity varies when three sphere sources are displaced rigidly along the z axis. In this section, the application of Geometric Sensitivity Gating (GSG) for respiratory motion gating is illustrated. Respiratory motion phases can be determined from event rate changes, which are determined to suitable temporal resolution from the list-mode data stream. Further explanation of GSG for respiratory motion gating is illustrated in Fig 3.21. The results of event rate versus frame number resemble a sinusoidal waveform representative of the cyclic respiratory pattern.

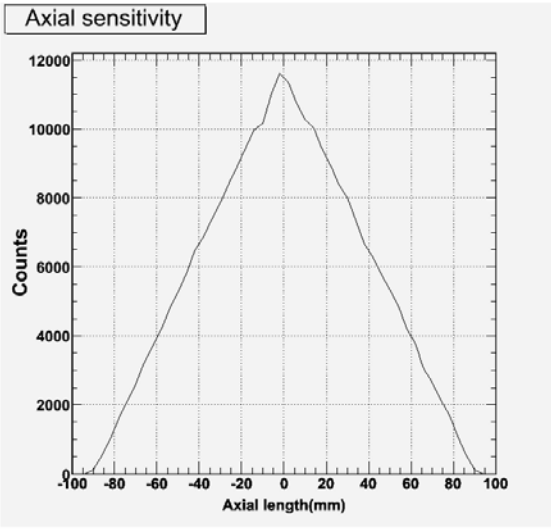

(a). 2D plot of the geometric sensitivity

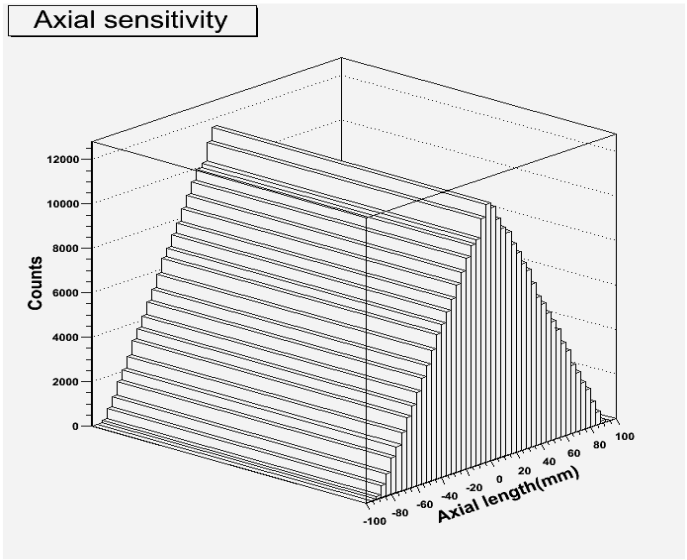

(b). 3D plot of the geometric sensitivity

Fig 3.19. Simulated geometric sensitivity of Allegro/Gemini by GATE with 2D and 3D plot

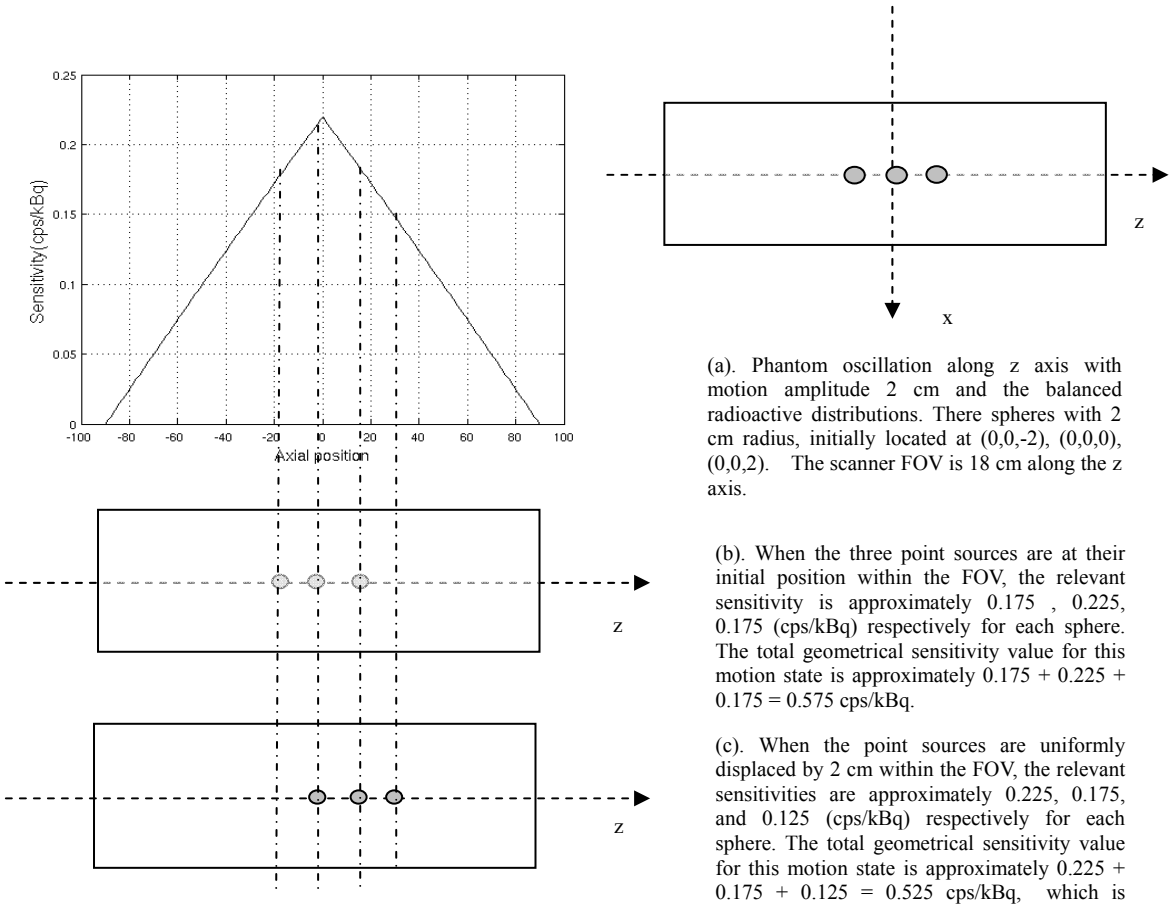

(a). Phantom oscillation along z axis with motion amplitude 2 cm and the balanced radioactive distributions. There spheres with 2 cm radius, initially located at (0,0,-2), (0,0,0), (0,0,2). The scanner FOV is 18 cm along the z axis.

(b). When the three point sources are at their initial position within the FOV, the relevant sensitivity is approximately 0.175 , 0.225, 0.175 (cps/kBq) respectively for each sphere. The total geometrical sensitivity value for this motion state is approximately 0.175 + 0.225 + 0.175 = 0.575 cps/kBq.

(c). When the point sources are uniformly displaced by 2 cm within the FOV, the relevant sensitivities are approximately 0.225, 0.175, and 0.125 (cps/kBq) respectively for each sphere. The total geometrical sensitivity value for this motion state is approximately 0.225 + 0.175 + 0.125 = 0.525 cps/kBq, which is smaller than the initial value (b).

Fig.3.20 Variation of sensitivity value of radioactivity distribution along z axis in 3D scanner. Comparison of motion states between (b) and (c), total sensitivity value in (b) is bigger than (c). Note that even though the radioactivity distribution is always at the centre of the transverse FOV, the total sensitivity value is different between two motion states. Thus the event rate will change., If the collection time of each frame is identical the number of LORs detected in the frames will be in the same proportion . GSG can be applied to this time varying distribution of radiation.

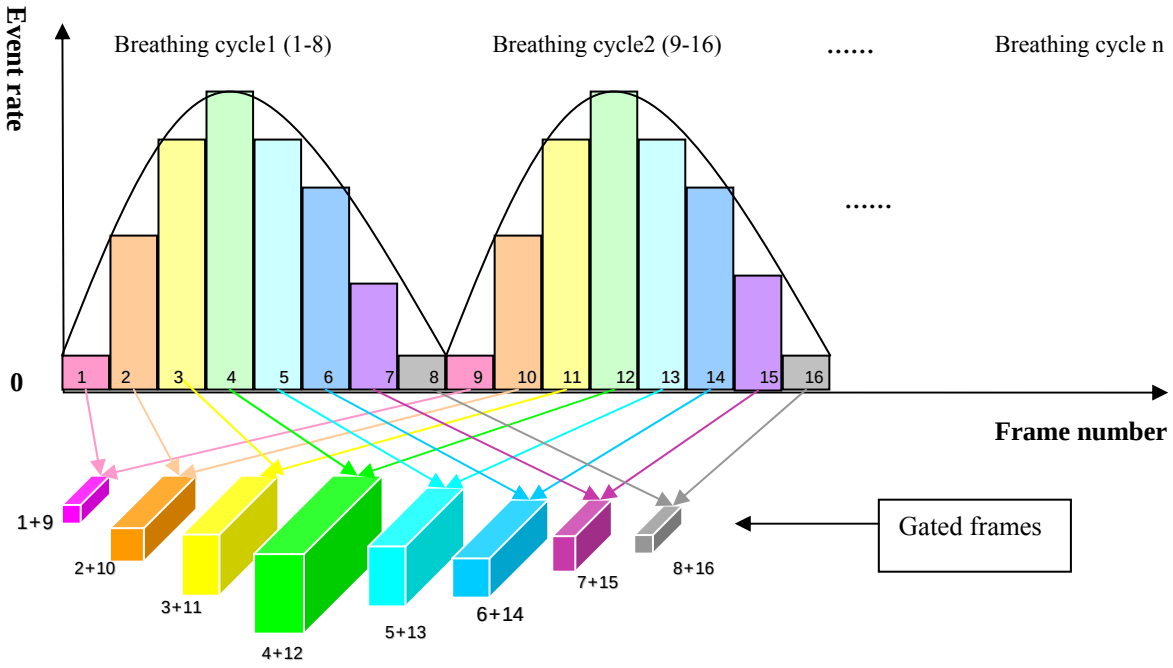

Fig. 3.21. The GSG method shows the cyclic change in event-rate with respect to frames illustrating the respiratory breathing cycle. The count-rate in two breathing cycles is used to determine gating-phases. Each cycle contains 8 respiratory motion sub phases of equal time length placed contiguously in order of time along the horizontal axis. The height of the bar represents the number of frame events, bars with of the same height with the same colour are from the same sub phase of breathing.

The procedure of GSG is depicted in Fig.3.21. A breathing acquisition consisting of many breathing cycles is sorted into a sequence of frames. For example, if each breathing cycle is broken down into 8 respiratory phases, two breathing cycles then contain 16 frames as shown in Fig 3.21. Each bar indicates a frame or one respiratory phase. The height of each bar represents the number of events in each frame. A higher bar indicates greater proximity to the centre of the FOV due to geometric sensitivity properties of 3D PET scanners as shown in Fig 3.19. In addition, bars of the same color and of the same height in different cycles represents the same respiratory phase with similar frame event rates. According to the GSG hypothesis, a change in frame event rate can be related to a change in axial position of the thoracic organs, relative to the centre of the FOV in the scanner. By detecting the periodicity in the frame event totals, a motion displacement or phase may be extracted for subsequent addition of identical respiratory phases from different cycles thereby giving rise to summed frames as a gated frame. For the purpose of the initial investigation of data-driven gating by utilising data from a single respiratory phase, this research uses frames corresponding to the peak count rate in a cycle for motion gating. For instance, the frame numbered 4 is the highest with the largest number events compared to others in the first cycle, and the frame numbered 12 in the second cycle is also the peak event rate with similar frame events as to frame 4, so the GSG method in this case will extract frames 4 and 12, and then sum them as a single frame called the gated frame, which is then reconstructed.

GSG is principally accomplished by the retrospective sorting of list mode data. The advantage of list- mode data acquisition is that retrospective analysis can be tailored optimally for a given clinical simulation. The specific proposed procedure steps are displayed in Fig. 3.22. List-mode events are sorted into dynamic frames; the total events in each frame are then calculated. The phase of each cycle is then determined based on the peak of frame events whereupon the frame corresponding to a phase of interest is extracted and summed to form a single gated-frame. The resultant gated-frame is then reconstructed.

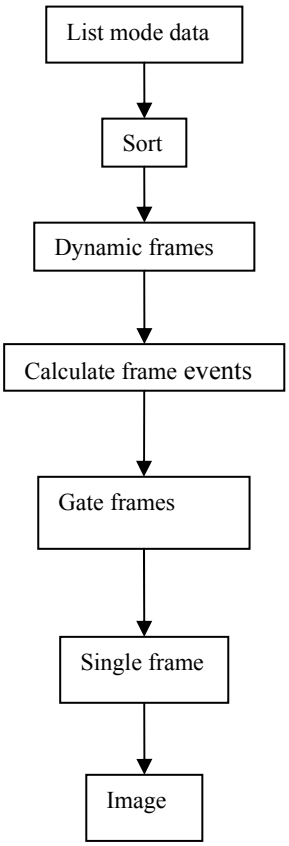

Fig. 3.22. The steps of implementing geometrical sensitivity gating

Respiratory gating can reduce the degrading effect of breathing motion on PET images. It allows a more complete recovery of the true counts within the lesion and a more accurate estimation of the lesion volume[51]. However, because detected counts of gamma rays are distributed into each phase, only one of which is used for reconstruction, if the acquisition time is not sufficient, then the detected counts for a frame / gate may become suboptimal; causing the reconstructed image to become noisy. To solve this problem, if all respiratory motion images are motion-corrected to a reference image and summed, the resultant image would have less motion blurring than an un-gated image and less noise than the gated image. To this end GSC is employed, as discussed in the next section.

3.5 Motion Correction Method

Conventionally, the respiratory-gated images at each phase are motion-corrected to the reference phase and summed to reduce noise. In the proposed motion correction method of GSC, based on the hypothesis outline in section 1.3, a transformation displacement matrix would be determined by the change in frame events in the breathing cycles. Motion correction was implemented by transforming all frames of sorted list mode data to the reference frame directly (before

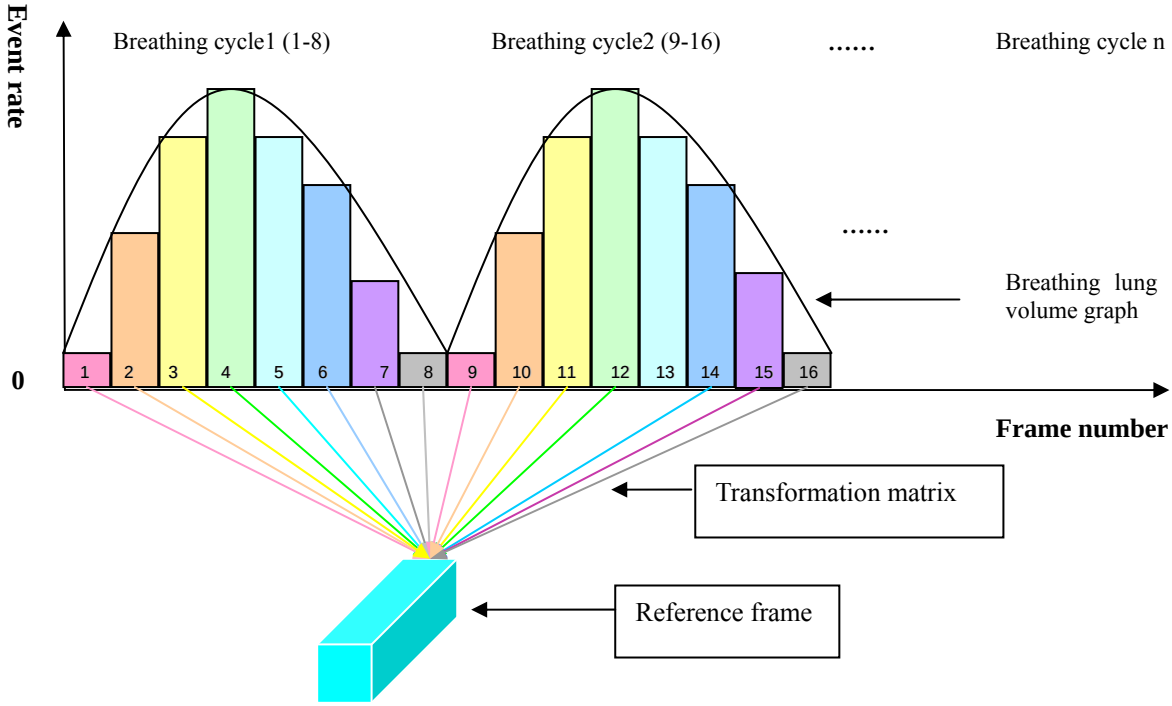

Fig. 3.23. GSC method shows the change in event-rate with respect to frames illustrating the respiratory motion displacements. The count-rate in two breathing cycles is used to determine transformation matrix. Each frame is directly moved to reference frame. Each cycle contains 8 frames motion along axis.

reconstruction) rather than moving gated frames to the reference frame. The procedure of GSC implementation is shown in Fig 3.23 where the graphical interpretation is consistent with that of Fig 3.21. For example, to correct two breathing cycles with 16 frames (1-8, 9-16), firstly, a reference frame needs to be determined such as the peak counts frame numbered 4 or 12; second all frames are directly translated into the frame 4 or 12 by transformation displacements. A fundamental issue in GSC is the method by which the transformation matrix is determined.

The transformation matrix contains the displacements for frames to move to the reference frame. The displacement is non zero only in the Z axis in this thesis. As discussed in section 1.3, respiratory motion is a 3D motion, but, the largest amplitude is along the Z axis. Therefore, it is anticipated that motion correction along the Z axis will be the most significant for respiratory motion compensation.

The scanner geometric sensitivity varies with the axial position as illustrated in Fig. 1.8 and Fig 3.19; From Fig 1.9, the change of lung volume and diaphragm motion follows sinusoidal curves. Following the hypothesis that the change of frame event rate can indicate the change of displacement, it is assumed the relationship between frame event rate and frame displacement is linear as shown in Fig 3.24.

If we assume that $f(i)\ (i = 1,2,3,.....n)$ is the frame event counts, *i* as the frame number; $f_{\max}$ as the maximum frame events, $f_{\min}$ as the minimum frame events, $D_z(i)\ (i = 1,2,3,.....n)$ is a displacement for a sorted frame $f(i)$. For the purpose of modelling simplified motion of geometric objects, we adopt a sinusoidal motion of the form:

$$D_z(i) = \frac{A}{2} * \sin(\frac{2\pi \cdot t_i}{T}) \tag{3.1}$$

where *A* is the amplitude of the respiratory motion, and set time zero to be in the middle of the maximum frame event reference frame, as well as the displacement of the reference frame to be zero. T is the time period of one breathing cycle. In addition, since the variation of $f(i)$ with time is sinusoidal, and we know that at time t=0 $f(i)$ is equal to $f_{\min}$, we have

$$f_{\max} - f(i) = \frac{1}{2} * (f_{\max} - f_{\min}) * \sin(\frac{2\pi \cdot t_i)}{T}) \qquad (i = 1,2,3,.....n) \tag{3.2}$$

From equation (3.1) and (3.2), we can determine

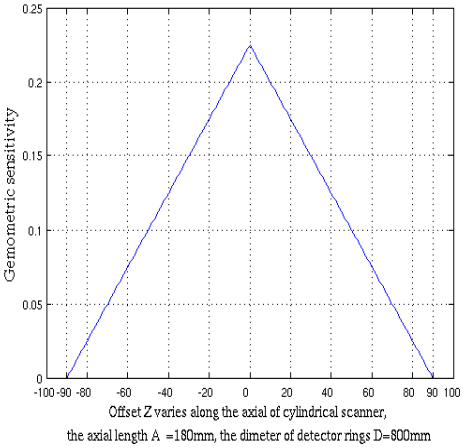

(a) Geometric sensitivity

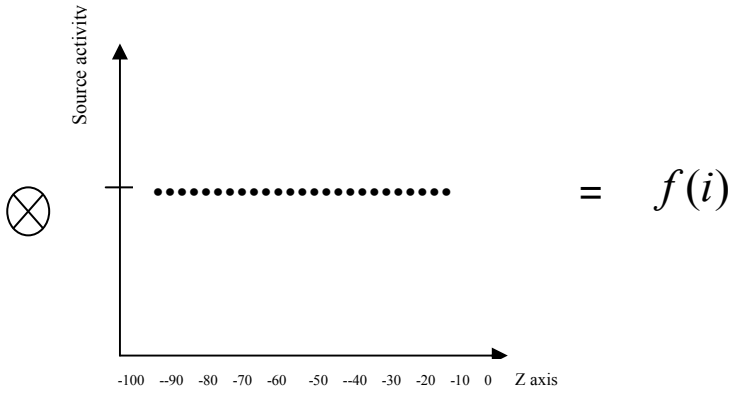

(b) A NCAT phantom (or point) source motion along z axis. One point position represents one motion frame (phase) in one motion cycle.

Frame event counts: $f(i)$

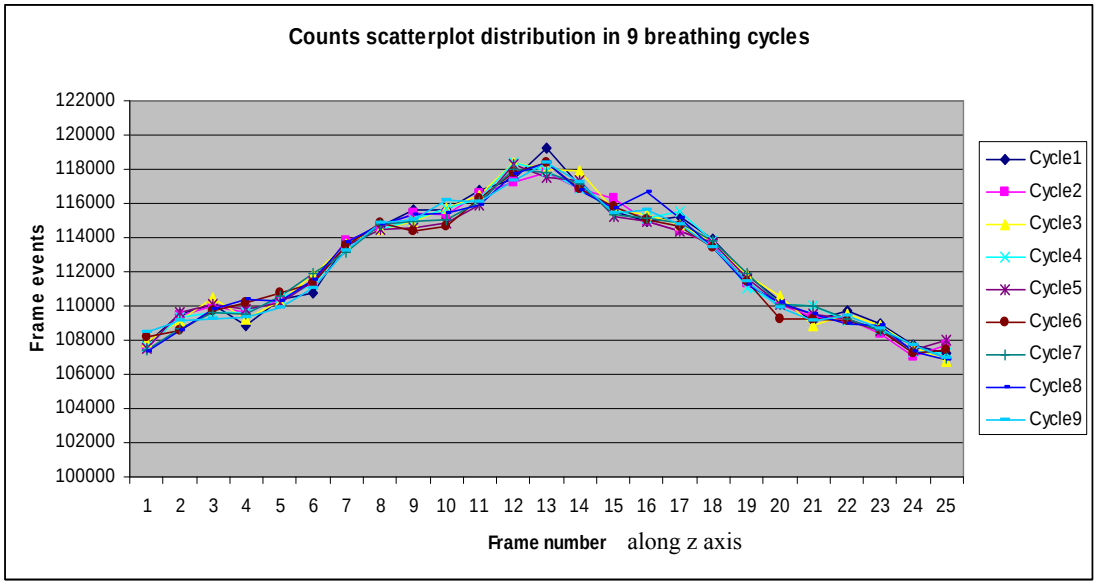

(c). Variation of frame counts overlapped in same position of nine breathing cycles simulated by GATE and NCAT. The shape of variation is similar with the change of lung volume as shown in Fig 1.9.

Fig. 3.24. A NCAT phantom (or point) source moves along z axis (b) with geometric sensitivity (a), the variations of frame event rate indicates an approximate sinusoidal graph (c), which we may assume that the relationship between frame event rate and frame displacement is linear.

$$D_z(i) = A * \frac{f_{\max} - f(i)}{f_{\max} - f_{\min}} \qquad (i = 1,2,3,.....n) \tag{3.3}$$

Where

$D_z(i)$: Translation element along z axis

i : Frame number

A : Maximum motion amplitude

$f_{\max}$: Maximum frame events

$f_{\min}$: Minimum frame events

$f(i)$: Each frame events

Equation 3.3 means that displacement transformation matrix element $D_z(i)$ can be estimated by changes in the frame events $f(i)$ and motion amplitude A. A is taken as a constant parameter of the motion. $D_z(i)$ depends on the change of $f(i)$. Analysing equation 3.3, we can know that $D_z(i) = 0$ when $f(i) = f_{\max}$ which means the motion frame at the centre of the FOV obtains maximum geometric sensitivity, but the displacement is zero; additionally $D_z(i) =$ A when $f(i) = f_{\min}$ which indicates the motion frame at the edge of the FOV receives minimum geometric sensitivity, but the displacement is maximum. In this research, motion amplitude can be determined by calculating the axial component of the sinogram's COM [69, 73, 74]. The COM for the two frames corresponding to the peak events frame and the minimum events frame are calculated, then difference between the two calculated Z moments is taken as the estimated motion amplitude. Although the translation calculated is only the axial motion in principle, x, y motions could be factored in as well.

The GSC is performed by translating the sorted frames to the reference frame by using the transformation matrix element which contains displacement transformation parameters for the frames translating to the reference frame. Each frame consists of lots of LORs. As a result,

correction of the frames to the reference frame can be implemented by translating each LOR event in the frame to the position of the reference frame in terms of the displacement in the transformation matrix [32, 86, 132] . In this research, the reference frame was defined by the peak count rate frame in the sorted frames. As an example of translating LORs to the reference position as specified in Fig 3.25, take two LOR events, LOR_a and LOR_b in a non reference frame. The transformation displacement for translating from the frame and the reference frame in the matrix can be calculated as $D_z(i)$ from Equation 3.3. As a result of the frame translation, LOR_a and LOR_b will be moved to the reference position $LOR_{a'}$ and $LOR_{b'}$ by Δz displacement along the z axis.

The steps of GSC implementation are depicted in Fig.3.26. List-mode event rate are sorted into dynamic frames. The total events in each frame are then calculated. The maximum and minimum frame events are also determined and then motion amplitude can be estimated by COM calculation. Transformation displacements accounting for respiratory motion can be calculated according to Equation 3.3. All LOR events in each frame are translated to the reference frame and summed to form a single frame. The reference frame is defined as the frame with most events. The resultant frame is then reconstructed into an image.

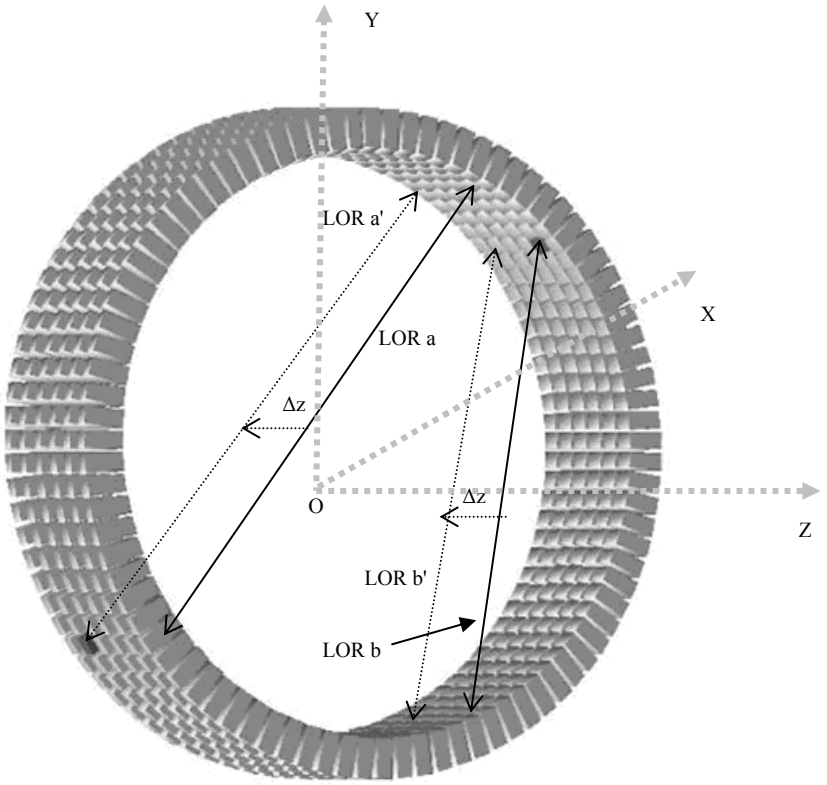

Fig. 3.25. The LORs transformed to the reference frame in the geometry of scanner. $D_{\min}$ and LOR_a became LOR_b and $LOR_{a'}$ after moving Δz displacement along z axis.

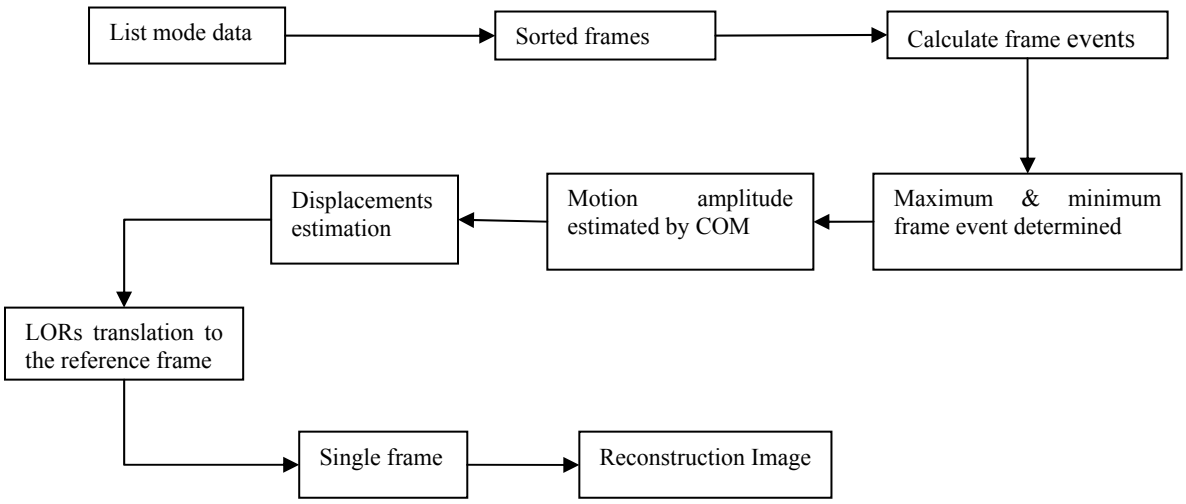

Fig. 3.26. The steps of implementing geometrical sensitivity correction (GSC)

3.6 Reconstruction image

In this research, all images were reconstructed by using the PURE software tool, which was developed by Philips Medical Systems Company. PURE software is a simple reconstruction software package [133] and is used as a simple LOR reconstructor for list-mode data in Philips format. It is an implementation of MLEM reconstruction image using Riddon's algorithm for LOR projection[134]. It contains basic functions to reconstruct the image without support for data correction of reconstruction such as scatter correction and random correction, Therefore, the quality of the reconstructed image is not as good as commercial reconstruction image software packages. However, its speed of reconstruction is fast due to its simple approach. The aim of this thesis is to demonstrate the feasibility of the use of data-driven GSG and GSC to gate and correct respiratory motion, and the software is adequate for this purpose. PURE also allows the algorithm of reconstruction to be specified, and in this work, the algorithm of reconstruction used for all images reconstructed by PURE is RAMLA (Row Action Maximum Likelihood Algorithm) with 5 iterations.

3.7 Image analysis

To validate the proposed methods and to quantify the level of improvement, three approaches were followed to evaluate the result of correction: visualization, image line profile and edge magnitudes ratio (EMR). The visualization approach means the efficacy of motion correction is evaluated subjectively by viewing the correct image and comparing it to the uncorrected image. Some images reconstructed with motion correction are readily seen to be different compared with the images that have no motion correction. Visualisation is thus only a qualitative evaluation of motion correction. For a quantitative evaluation of the improvement obtained by motion correction, then image line profiles can be used to inspect the difference of image intensity of corresponding voxels with and without motion correction, and the linear dimensions of image segments with and without motion correction. In addition, a further method to measure of image improvement is employed by the edge magnitude ratio (EMR) proposed by Schleyer [81]. The main idea of the EMR is that the gradient of the edge of static image will be steeper than the

gradient of an edge of motion image as shown in Fig 3.27. It is defined by

$$EMR = \frac{g(x,y)}{f(x,y)} \tag{3.4}$$

Where $f(x,y)$ is an image for the static, or the motion corrected image, $g(x,y)$ is the range of the edge magnitude values for an image providing an indication of the overall image edge strength. It can be determined by formula 3.5.

$$g(x,y) = f(x,y) * h(x,y) \tag{3.5}$$

Where $h(x,y)$ is an edge detector operator that includes a matrix to determine the loss of edge strength with 7 pixels in the y-direction and 3 pixels in the x-direction. The operator, $h(x,y)$ in this thesis is defined as,

$$h(x,y) = \begin{bmatrix} 1 & 1 & 1 \\ 2 & 2 & 2 \\ 3 & 3 & 3 \\ 0 & 0 & 0 \\ -3 & -3 & -3 \\ -2 & -2 & -2 \\ -1 & -1 & -1 \end{bmatrix} \tag{3.6}$$

$h(x,y)$ was designed to measure vertical edges only, and incorporated a smoothing effect on the edge data. If an object in an image has been blurred, then $g(x,y)$ can be expected to decrease. The EMR offers a measure of image quality improvement for motion gating and correction. As shown in Fig 3.27, the EMR ratio of the static (a) is higher than the motion (b) due to the steeper edge of the static than the motion.

For simulation studies and clinical studies in this research, some studies only use one or two of three approaches; some studies use the combination of three approaches to evaluate the improvement of motion correction.

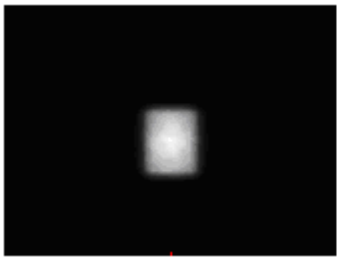

(a). Static image

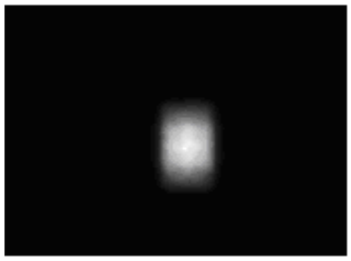

(b). Motion image with 1 cm amplitude

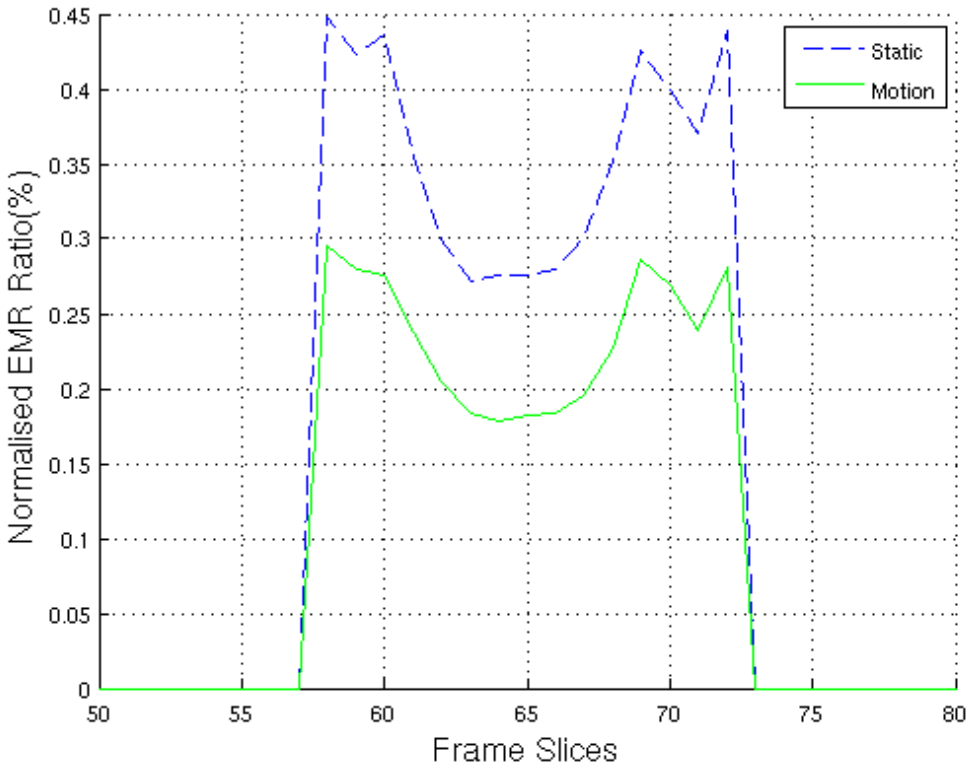

(c). Comparison EMR of the static image (a) between the motion image (b) in coronal view of frame slice from 57 to 78, it is clear that the EMR ratio of the static is higher than the motion due to the steeper edge of the static.

Fig. 3.27. The gradient of the edge of static image (a) is clearly steeper than the gradient of an edge of motion image (b) due to the motion 1 cm amplitude along z axis, which may be demonstrated by EMR ratio graphs (c).

3.8 Summary

As a brief overview of the methodology of GSG and GSC for respiratory motion used in this thesis, Fig 3.28 indicates the implementation steps of GSG and GSC in one diagram. As it shows, list-mode data which may be collected from either simulation results or clinical acquisition, is then sorted into dynamic frames and frame events are calculated. The next step focus to either GSG or GSC processing of the frame events as explained in sections 3.4 and 3.5 respectively. In the final common step, one summed frame corrected data-set can be reconstructed into an image.

In this research study, the fundamental idea of implementation of GSG and GSC is based on the geometric sensitivity properties of 3D PET. It is a simple method, but it will be demonstrated to be effective for compensating respiratory motion in the next chapter.

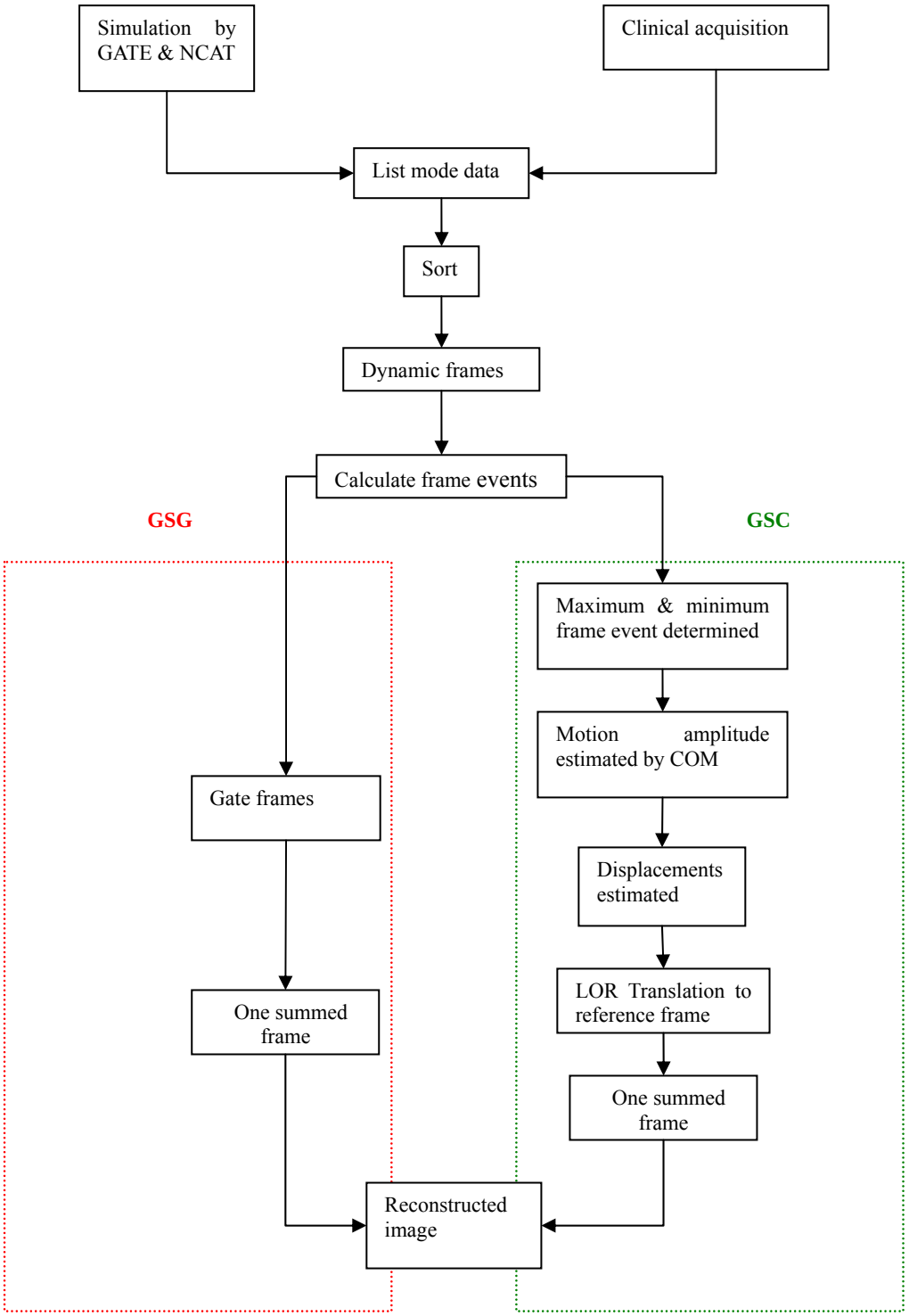

Fig. 3.28. The summary of implementing Geometrical Sensitivity Gating (GSG) and Geometrical Sensitivity Correction (GSC).

CHAPTER 4
SIMULATIONS AND VALIDATIONS

4 Simulations and Validations

4.1 GEOMETRIC PHANTOM SIMULATION 92
4.1.1 Introduction 92
4.1.2 Simulation Procedure 93
4.1.2.1 Motion Phantom and Sources Generated by GATE 93
4.1.2.2 Oscillation Equation 94
4.1.2.3 Sort List-Mode Data 95
4.1.2.4 Motion Gating and Correction 95
4.1.3 Results and Discussion 96
4.1.3.1 Event Rate versus Frame Evaluation 96
4.1.3.2 Motion Gating 102
4.1.3.3 Motion Correction 110
4.1.4 Summary 123
4.2 VOXELISED SIMULATION 124
4.2.1 Introduction 124
4.2.2 Simulation Procedure 124
4.2.2.1 Phantom Generated by NCAT 124
4.2.2.2 Phantom Imported into GATE 127
4.2.2.3 Sort List-Mode Data 127
4.2.2.4 Motion Gating and Correction 129
4.2.3 Results and Discussion 129
4.2.3.1 Frame Events and Lung Volume Curves 129
4.2.3.2 Motion Gating with and without Attenuation Modeling 133
4.2.3.3 Motion Correction 139
4.2.4 Summary 140
4.3 CLINICAL VALIDATION 144
4.3.1 Introduction 144
4.3.2 Validation Procedure 144
4.3.2.1 Patient Scanned with and without-Tumor 144
4.3.2.2 Sorted List-Mode Data 145
4.3.2.3 Filter Noise in List-Mode Data 146
4.3.2.4 Motion Gating and Correction 147
4.3.3 Results and Discussion 147
4.3.3.1 Frame Events in Time Domain 147
4.3.3.2 Frame Events in Frequency Domain 149
4.3.3.3 Filtered Frame Events 151
4.3.3.4 Motion Gating 154
4.3.3.5 Motion Correction 156
4.3.4 Summary 160

The hypothesis of GSG and GSC for respiratory motion gating and correction were tested by simulation studies and then used for validation of clinical studies. Simulation is one important step in the validation of respiratory motion compensation prior to clinical implementation. The configuration of simulation for the PET scanner was defined in terms of Philips Allegro configuration as specified in Chapter 3.2.2. The Allegro PET scanner construction and acquisition data procedure were simulated by the GATE software packages as described in Chapter 3.2.3.1. Phantom simulations consisting of two categories are discussed in this chapter. One is with geometric phantoms generated by using GATE for simple evaluation of GSG and GSC. The other was a voxelised phantom created by using the NCAT software packages for complicated and realistic simulations for respiratory motion to validate GSG and GSC. Finally, GSG and GSC will be applied to clinical studies.

Three sections for the simulations and validations in this chapter will be presented. Geometric phantom simulations will be firstly investigated followed by voxelised phantom simulations and then clinical validations will be discussed.

4.1 Geometric Phantom Simulation

4.1.1 Introduction

GATE is a software package that can be used to generate the geometric phantom and radioactivity sources. In addition, movement can be produced such as oscillation to simulate simple respiratory motion He *et al*(2006)[126]. The set up for geometric simulation specified by the script macros file of GATE can be seen in Appendix B. The oscillation can be determined by an equation provided by GATE itself. Simulated acquisition data collected in list-mode format were sorted into dynamic frames; GSG and GSC were then applied to those sorted frames.

The purpose of the geometric phantom simulations presented in this thesis is firstly to go through simple and effective simulations to test the hypothesis for GSG and GSC; secondly displaying the implementation of the principle of GSG and GSC. If the method of geometric simulations for

GSG and GSC are understood, both voxelised simulations and clinical validation are merely incremental developments because their methods are mostly the same as the geometric simulations.

4.1.2 Simulation Procedure

4.1.2.1 Motion Phantom and Sources Generated by GATE

In the geometric simulation, a cylindrical phantom was generated by GATE with a dimension of 2 cm radius and 5 cm length and so having a volume of $V_{cylinder}$ =62.8 mL. It was initially located at the centre of the FOV of the PET scanner as shown in Fig 4.1.1. The radioactivity source in the phantom was determined according to the clinical SUV defined by

$$SUV_{org} = \frac{\rho_{organ}}{\rho_{body}} = \frac{(\frac{A_{organ}}{V_{organ}})}{(\frac{A_{body}}{V_{body}})} \tag{4.1}$$

Where ρ_{organ} or ρ_{body} is the specific activity of organ or body. A_{organ} is activity sources concentred in the organ, V_{organ} is the volume of the organ. For example, a patient weighing 80 kg with V_{body} = 80000 mL is injected 370 MBq sources, the $\rho_{body} = {370000kBq}/{80000mL}$ = 4.5 kBq/mL. Typically, SUV_{lesion} is the range of 2 ~ 10, and then from the equation 4.1, $\rho_{lesion} \approx SUV_{lesion}$ * ρ_{body} = 9 ~ 45 kBq/mL. Therefore, to be consistent with the liver uptake of a clinical scan, an activity of 0.628 MBq ^{18}F-FDG (^{18}F-Fluoro-2-Deoxy-Glucose) was concentrated in the cylindrical phantom, so that its SUV is 628 kBq / 62.8 mL = 10 kBq/mL. In addition, this geometric oscillation simulation did not incorporate the effect of attenuation.

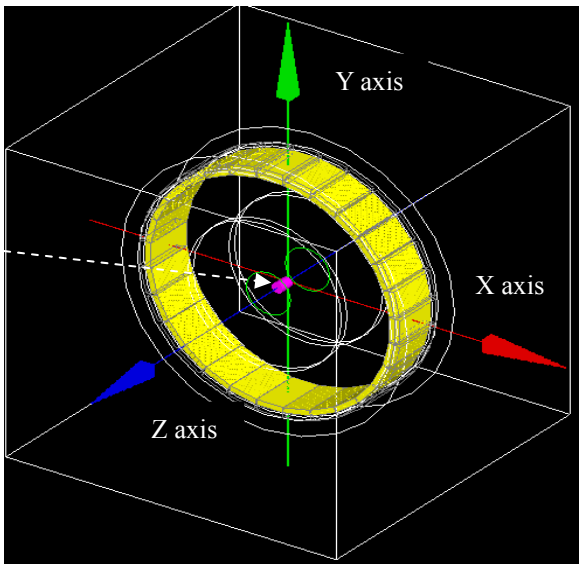

Fig. 4.1.1 A cylindrical phantom was centred at the FOV to do oscillation along z axis.

4.1.2.2 Oscillation Equation

In this geometric simulation, the cylindrical phantom oscillation along the z axis is defined by GATE with the following equation:

$$S(t) = \mathrm{A} * \sin\left(2\pi \frac{t}{T} + \theta\right) \qquad (t = 0,1,2,3,..... n) \tag{4.2}$$

Where $S(t)$ is the displacement at time t, A is the motion amplitude, T is the period of motion cycle, and θ is the phase at $t = 0$. For the simulation validation of GSG, the cylindrical phantom oscillation was set up with a 5 second period, motion phase $\theta = 90^0$, over 2 motion cycles with 100 dynamic frames, 0.1 second per frame time and 10 cm , 5 cm, 2 cm and 1 cm motion amplitude respectively. For GSC validation, all parameters of oscillation are set up the same as in the validation simulation of GSG. Tidal breathing normally has a period of approximately 5 seconds and around 2 cm amplitude of diaphragm motion [40]. The parameter of oscillation amplitude for validation of GSG and GSC was 10 cm and 5 cm respectively which are larger than normal respiratory diaphragm motion (around 2 cm) along the z axis but was chosen to highlight the effect of gating and correction. The amplitudes of 2 cm and 1 cm were included in the set as being representative of the amplitudes expected during motion gating and correction of tidal

breathing in the clinical context.

4.1.2.3 Sort List-Mode Data

The procedure for sorting geometric list-mode data is displayed in Fig 4.1.2. The geometric phantom oscillation simulation can be sorted into a sequence of 100 frames, 100 msec per frame from the list-mode data. Plots of frame events versus frame number were constructed to inspect the relationship between the changes in frame events.

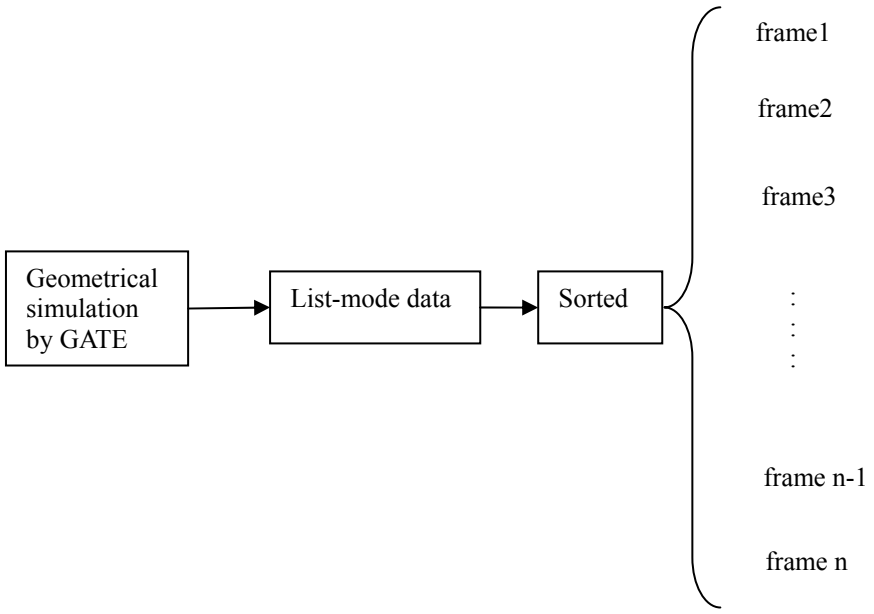

Fig. 4.1.2 Sort of list-mode data of geometric simulation into the sequence of frames. List-mode data was collected from GATE simulation result, which can be sorted into frames with same duration frame time.

4.1.2.4 Motion Gating and Correction

The geometric sensitivity gating (GSG) and the geometric sensitivity correction (GSC) will be applied to the sorted list-mode data. The specific implementation of GSG and GSC can be seen in Chapter 3.4 for GSG and Chapter 3.5 for GSC or summary Fig 3.29. The final gated or corrected

single frame will be reconstructed into an image. Image reconstruction of the geometric simulation was performed using the PURE software package which was developed by Philips company for list-mode data reconstruction[133]. All image reconstruction matrices are 128*128*55. The improvement in contrast is determined by inspection of image line profiles and the EMR method.

4.1.3 Results and Discussion

4.1.3.1 Event Rate versus Frame Evaluation

To evaluate the performance of the proposed methods, the total frame events are plotted versus frame number for the static-, motion-phantoms with 10 cm, 5 cm, 2 cm and 1 cm motion amplitude as shown in Figs 4.1.3 to Fig 4.1.7 respectively. In the simulation for the validation of GSG, 1.4 million events (Mevts) were collected for a static phantom and 0.5 Mevts, 1.0 Mevts, 1.38 Mevts and 1.38 Mevts for an oscillating phantom with 10 cm, 5 cm, 2 cm and 1 cm motion amplitudes in which 64%, 29%, 3.5% and 3.5% percent of events respectively were lost due to motion. The motion phantoms have less events compared with the static phantom due to motion of the source outside the axial FOV in extreme cases or due to the phantom in motion making excursions towards the edge region of the FOV where the sensitivity value is lower.

Comparing frame events versus frame number for the static phantom as shown in Fig. 4.1.3 and the oscillating phantom as shown in Fig. 4.1.4, the static phantom frame events are approximately constant to within 4% (Fig 4.1.3) which reflects the statistical uncertainty for the collection of events, while the oscillating phantom frame events have a clear sinusoidal character within amplitudes 96 % (Fig 4.1.4), 55% (Fig 4.1.5), 10% (Fig 4.1.6) and 7.5% (Fig 4.1.7), as a result of the frame events being collected from different positions along the z axis. The reason for the change in the number of frame events in Fig 4.1.4 (96 %) being larger than other figures is because of the larger motion amplitude. The larger motion amplitude will result in the phantom occupying the regions of the scanner with a lower average sensitivity, hence the lower events.

However, the plots of frame events obviously indicate the deviation from sinusoidal shape on 10 cm and 5 cm amplitudes and particularly the noise effect on 2 cm and 1 cm amplitudes, which results from the statistical random noise of events as shown in Fig 4.1.3. The noise is more clearly apparent on 2 cm and 1 cm amplitudes compared with 10 cm and 5 cm amplitudes because of the smaller amplitude motion. In order to reduce the noise, a Butterworth band-pass filter technique was utilised on equation 4.3 to filter the statistical noise in the sorted frames. First of all, the range of motion cycle in the Power Spectral Distribution (PSD) of frame events needs to be inspected as displayed in Fig 4.1.8 and Fig 4.1.9 in which the frequency component of motion is clearly evident; and then the band-pass of filter (0.3 Hz ~ 0.5 Hz) can be determined as shown in Fig 4.1.10. After the filtering, the plots of frame events shows the filtered frame events varying smoothly with frame number with less high frequency component as shown in Fig 4.1.11 and Fig 4.1.12.

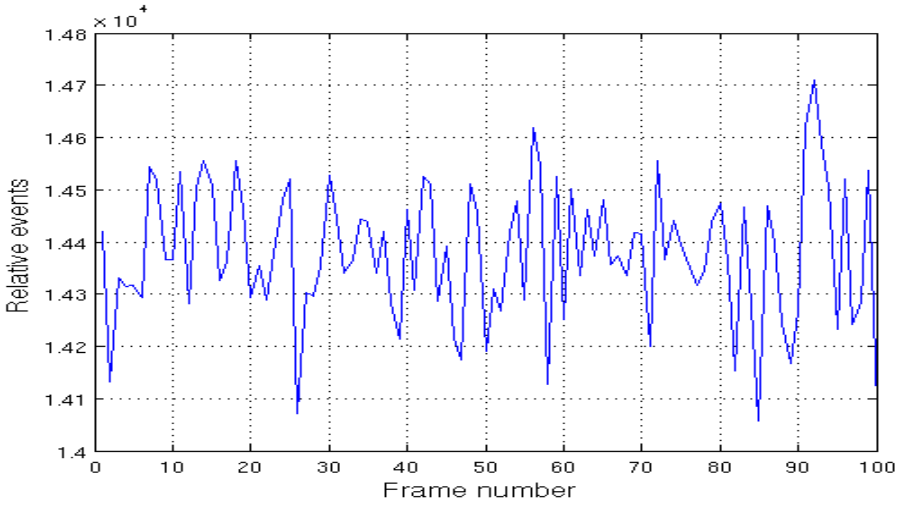

Fig. 4.1.3 Change in the number of frame events versus frame number. Static phantom simulation shows a less than 4 % variation in event-rate determined by peak-to-peak.

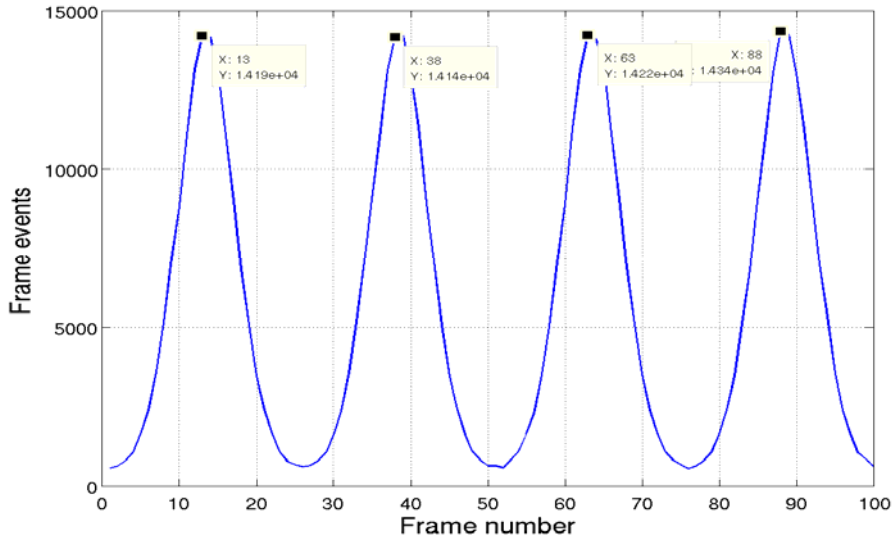

Fig. 4.1.4 Phantom motion amplitude **10 cm**, change in the number of frame events shows approximant sinusoid curve 96 % variation in event-rate determined by peak-to-peak.

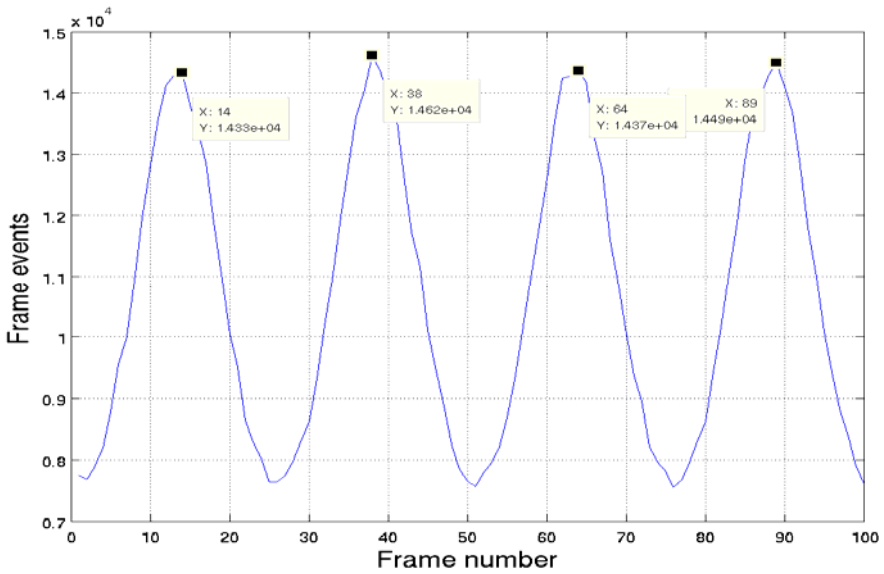

Fig. 4.1.5 Phantom motion amplitude **5 cm**, change in the number of frame events shows approximant sinusoid curve 55 % variation in event-rate determined by peak-to-peak.

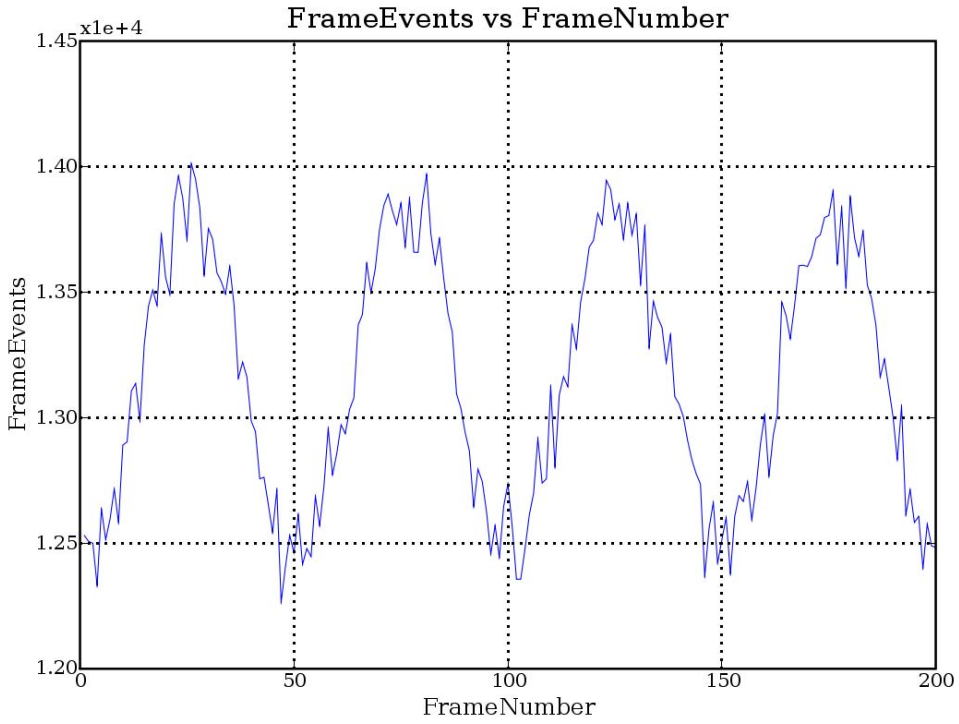

Fig. 4.1.6 Phantom motion amplitude of **2 cm** and 0.5s per frame, change in the number of frame events shows approximant sinusoid curve 10 % variation in event-rate determined by peak-to-peak.

.

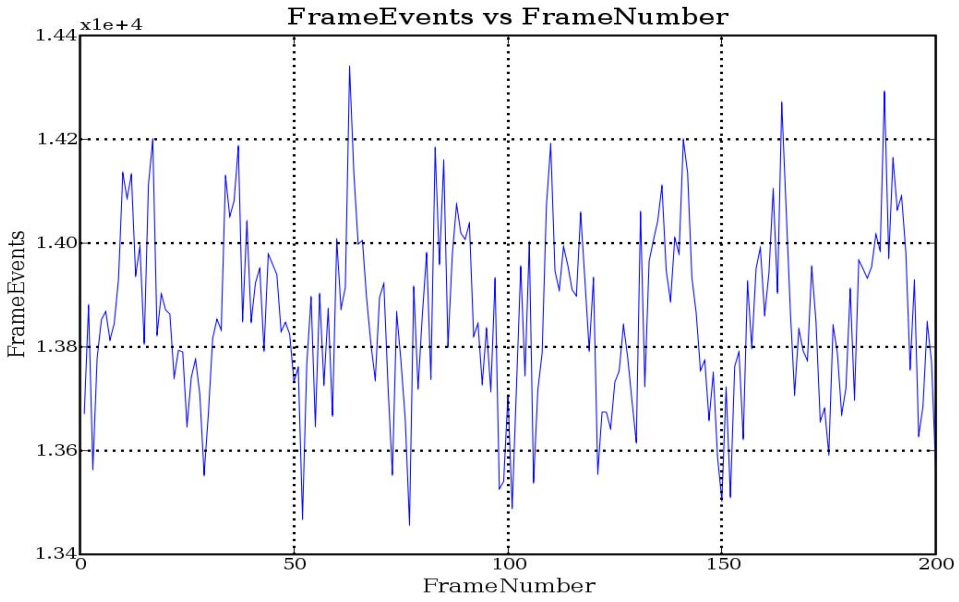

Fig. 4.1.7 Phantom motion amplitude of **1 cm**, and 4 motion cycles, change in the number of frame events shows the change of approximant sinusoid curve 7.5 % variation in event-rate determined by peak-to-peak.

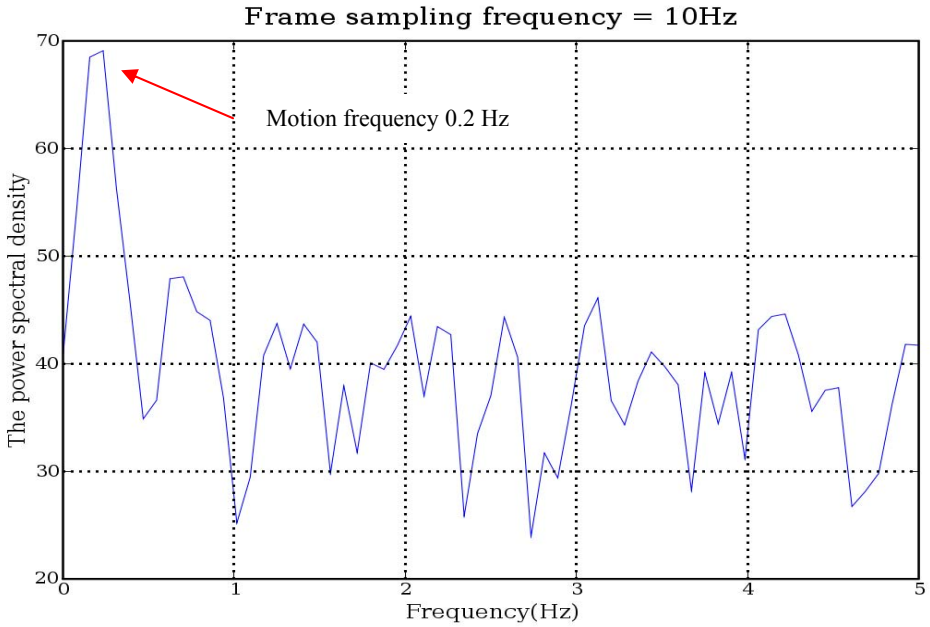

Fig. 4.1.8. The Power Spectral Distribution of frame event rate for **2 cm** motion amplitude for geometrical phantom, it demonstrates distinct frequency of motion by red arrow.

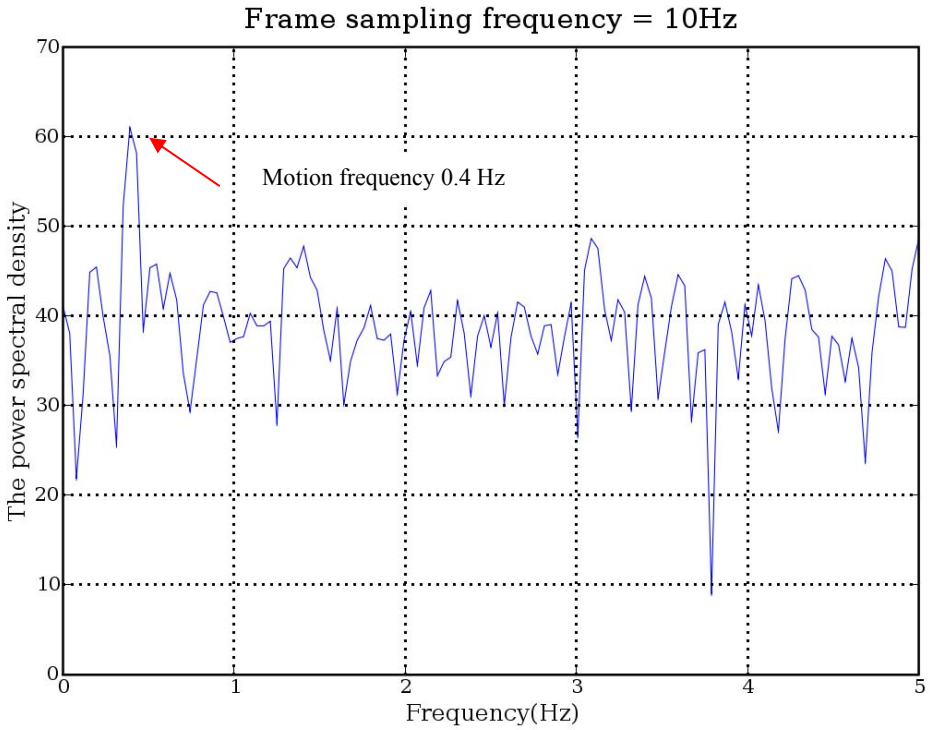

Fig. 4.1.9. The Power Spectral Distribution of frame event rate for motion amplitude of **1 cm** for geometrical phantom. It shows distinct frequency of motion by red arrow.

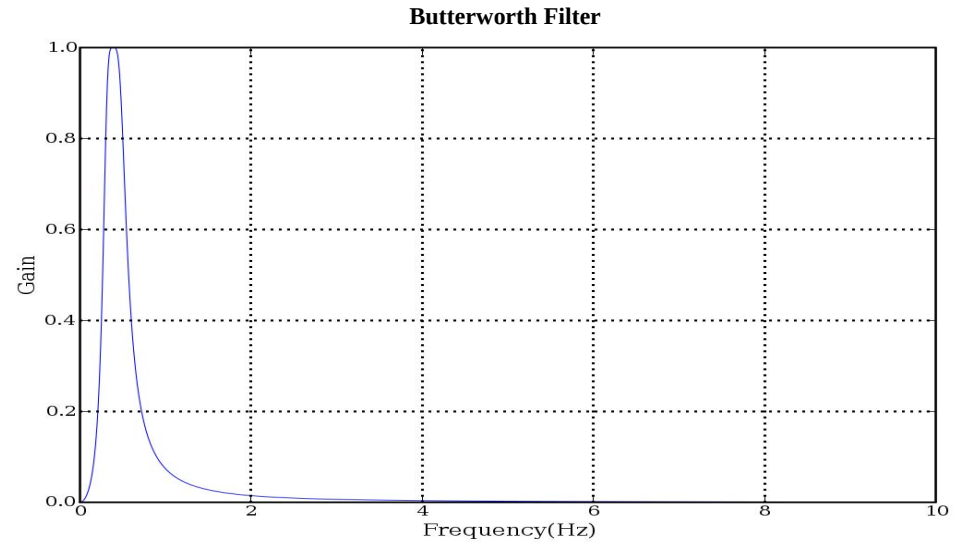

Fig. 4.1.10. Butterworth filter for phantom motion of 2 cm and 1 cm with low band-pass 0.3Hz ~ 0.5 Hz.

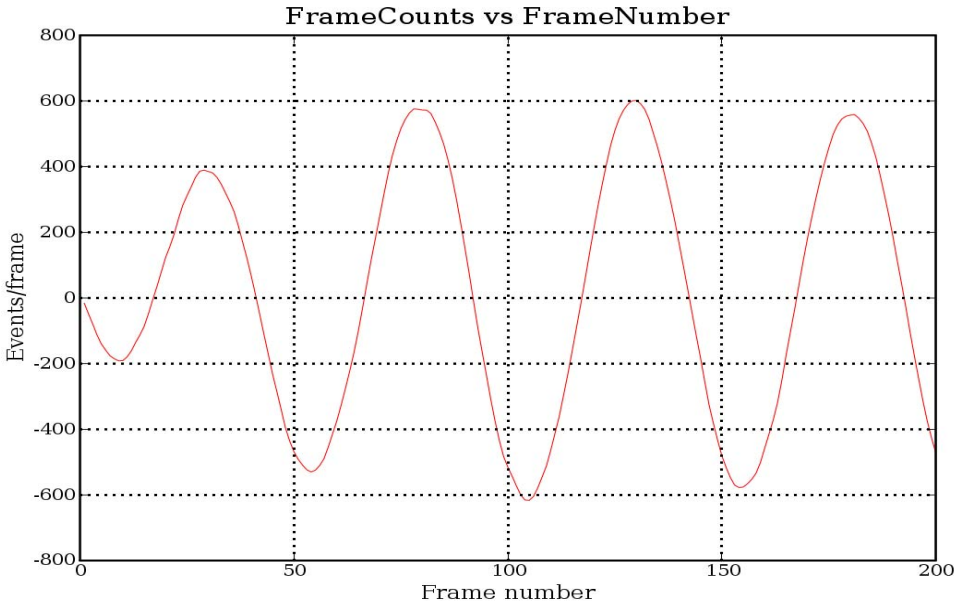

Fig. 4.1.11. Band pass filter of frame events for phantom motion of **2 cm** amplitude. The plot demonstrates the reduction of high frequency noise after filtering.

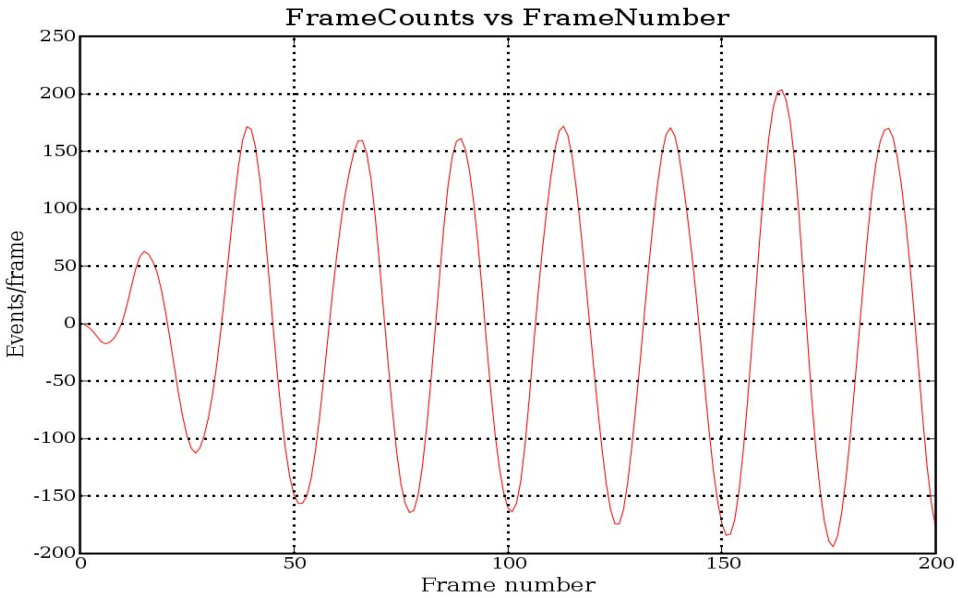

Fig. 4.1.12 Filtered curve for phantom motion amplitude of **1 cm**, shows clearly approximate sinusoid curve without high frequency noise.

4.1.3.2 Motion Gating

With the GSG method, the four peaks in frame-events as labelled in Fig. 4.1.4 correspond to the frames used for gating from a single phase of the oscillating. The resulting GSG gated frame contained 0.05 Mevts (5% of total events). A comparison of the reconstructed images generated from the static phantom (Fig. 4.1.13(a)), the oscillating phantom (Fig. 4.1.13(b)) and the proposed gating (Fig. 4.1.13(c)) clearly show that the edges of the simulated phantom (Fig. 4.1.13(b)) were largely blurred due to motion; while the image gated by the GSG method (Fig. 4.1.13(c)) reveals no such artifacts and has similar contrast to the static reconstruction (Fig. 4.1.13(a)). To compare the z-axis image line profiles of the three cases, images were normalized by the area under the curve as illustrated in Fig. 4.1.17. The static phantom profile has a full width at half maximum (FWHM) of 12 voxels, the non-gated motion phantom 22 voxels and the gated result 11 voxels as illustrated in Table 4.1. This table also provides further information about the value of the difference in FWHM between motion states. The difference between the static phantom FWHM and the GSG FWHM is only 1 voxel, while the difference to the ungated-motion is 10 voxels, which demonstrates that the phantom motion artefact was significantly reduced by the GSG method. In addition, the EMR was utilised to assess edge strength of interest in the image. For

example, the 10 cm motion amplitude case is illustrated in Fig 4.1.21 and Fig 4.1.22. The plots in Fig 4.1.22 clearly shows that from image slices 52 ~ 74 in the transverse section view, the plot positions for the static and the gated cases are close to each other, but are both much further from the plot of the motion case, which means the effect of the gating is to make the image of the edge of the phantom almost as sharp as in the static case. The motion case image has a small EMR ratio value around 0.1 which indicates a general degradation of spatial resolution of the motion image. The gated and the static images have large EMR ratio values around 0.3 and 0.4 respectively indicating that the spatial resolution of the gated case approaches that of the static case.

Similarly, the GSG applied to the 5 cm, 2 cm and 1 cm motion amplitudes as shown in Fig 4.1.14, Fig 4.1.15 and Fig 4.1.16 respectively. The evaluation of the gated image line profile for those amplitudes are displayed in Fig 4.1.18, Fig 4.1.19 and Fig 4.1.20. Comparison of FWHM parameters for motion amplitudes is listed in the Table 4.1, and indicates that not only for large amplitude motion values of 10 cm and 5 cm, but also for small values of 2 cm and 1 cm, the gated FWHM distances are within 1 voxel of the gated FWHM cases, which means the gated image spatial resolution is similar to that of the static phantom image. In addition, the evaluation for those motion amplitudes by the EMR ratios in Fig 4.1.23, Fig 4.1.24 and Fig 4.1.25 respectively shows that the effect of the gating does not reduce with the decrease of motion amplitude, on the contrary, the plots of the gated EMR values are close to the static ones.

However, the gated result shows more noise compared to the static phantom due to only utilizing fewer events for gating such as 5% of the total events for 10 cm motion amplitude case, therefore, it is necessary to investigate an effective method to use all frames for motion correction.

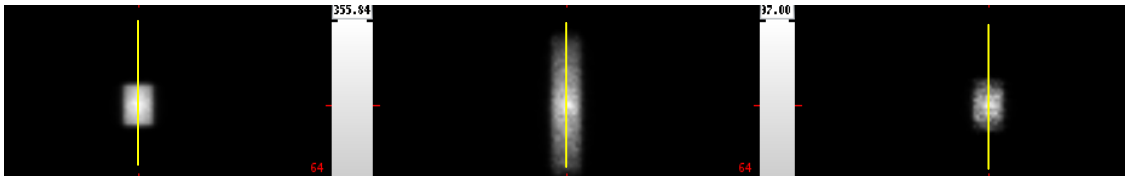

(a). Static (b). Summed (c). Gated

Fig. 4.1.13 Phantom motion amplitude = **10 cm**, simulated sinusoidal oscillation was gated by GSG.

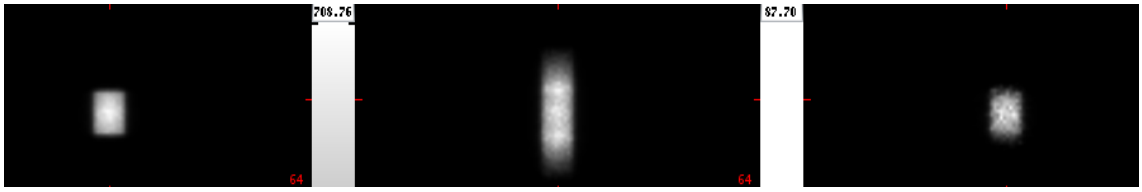

(a). Static (b). Summed (c). Gated

Fig. 4.1.14. Phantom motion amplitude = **5 cm**, simulated sinusoidal oscillation was gated by GSG.

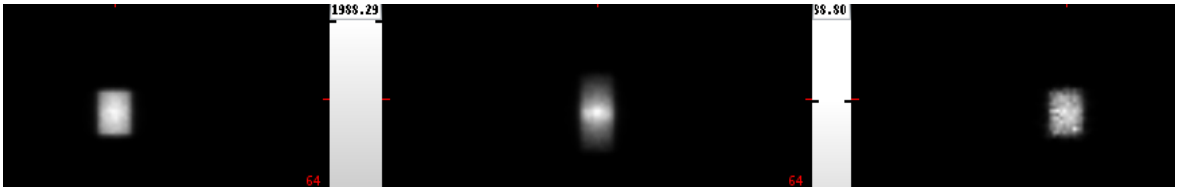

(a). Static (b). Summed (c). Gated

Fig. 4.1.15. Phantom motion amplitude = **2 cm**, simulated sinusoidal oscillation was gated by GSG.

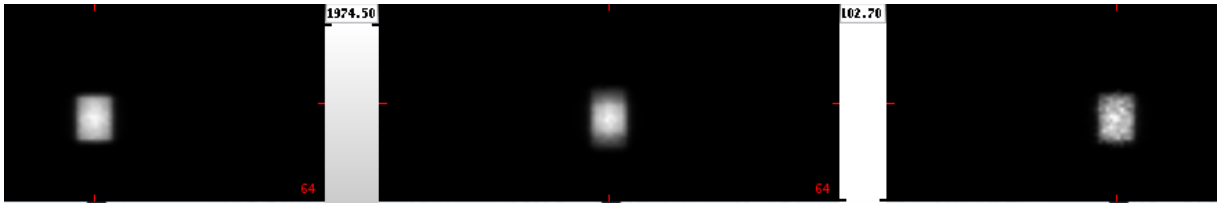

(a). Static (b). Summed (c). Gated

Fig. 4.1.16. Phantom motion amplitude = **1 cm**, simulated sinusoidal oscillation was gated by GSG.

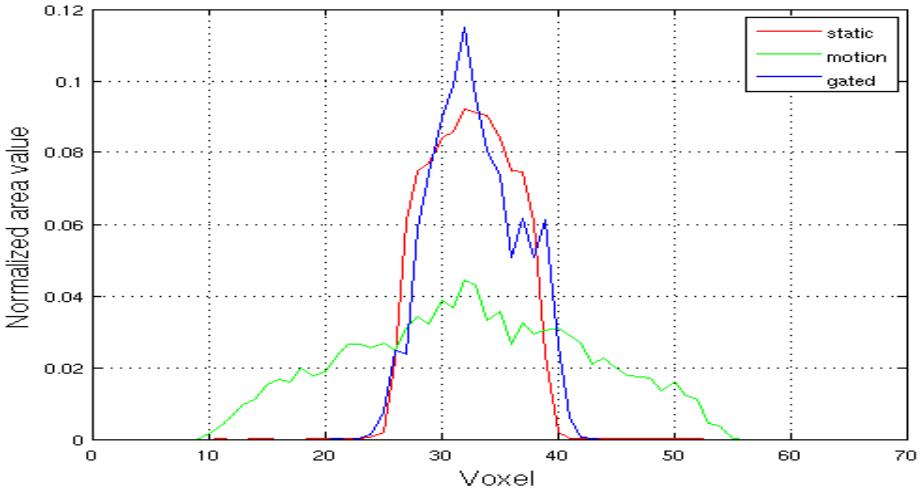

Fig. 4.1.17 Phantom motion amplitude = **10 cm** for Fig. 4.1.13, comparison of line profiles of static-, motion- and the gated images normalised by the area under curve. The line profile of the gated image demonstrated a spatial resolution similar to the static phantom image.

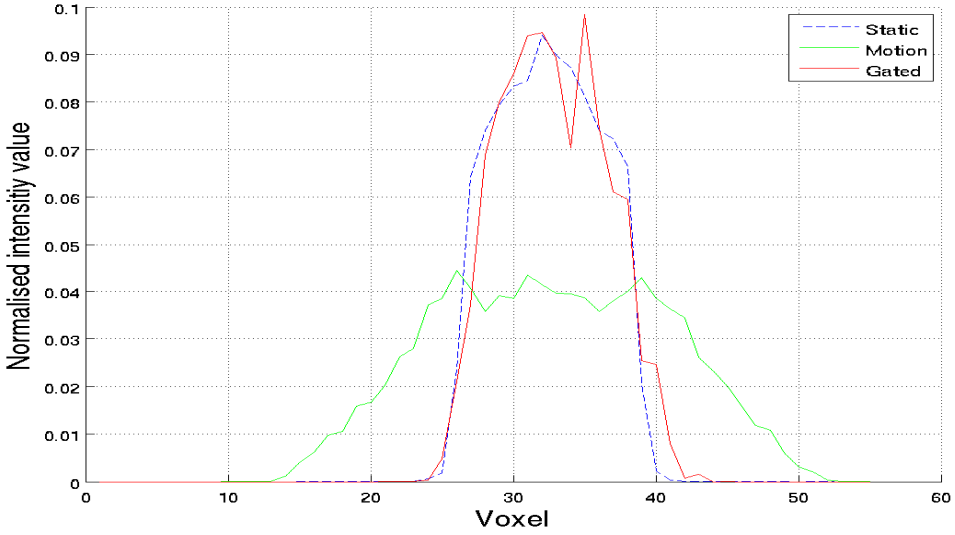

Fig. 4.1.18 Phantom motion amplitude = **5 cm** for Fig. 4.1.14, comparison of line profiles of static-, motion- and the gated images. The line profile of the gated image demonstrated a spatial resolution similar to the static phantom image.

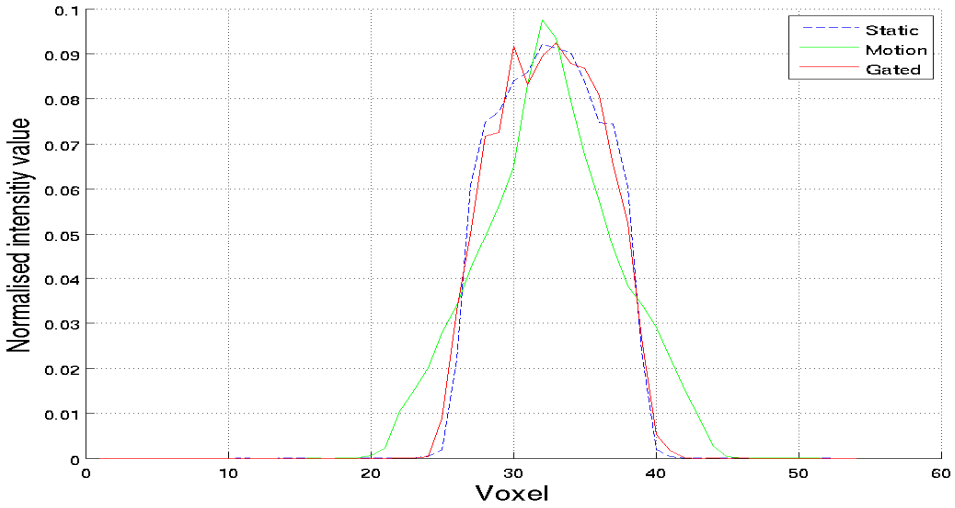

Fig. 4.1.19. Phantom motion amplitude = **2 cm** for Fig. 4.1.15, comparison of line profiles of static-, motion- and the gated images. The line profile of the gated image demonstrated a spatial resolution similar to the static phantom image.

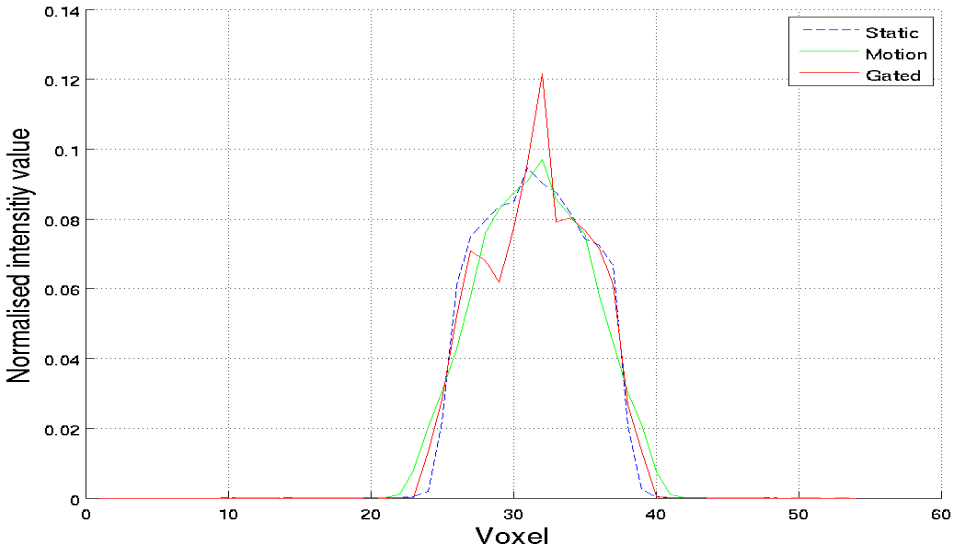

Fig. 4.1.20 Phantom motion amplitude = **1 cm** for Fig. 4.1.15, comparison of line profiles of static-, motion- and the gated images. The line profile of the gated image demonstrated a spatial resolution similar to the static phantom image.

Table. 4.1.
Comparison of FWHM of between the static, the motion and the gated by GSG for different motion amplitudes with 10 cm, 5 cm , 2 cm and 1 cm in Fig.4.1.17 ~ Fig.4.1.20. Difference of FWHM between the static and the gated demonstrate GSG improves the motion image.

Motion amplitude (cm)	**Motion states**	**FWHM voxels number**	**Distance from the static FWHM (voxel)**
10	Static	12	0
	Motion	22	10
	Gated	11	1
5	Static	12	0
	Motion	20	8
	Gated	11	1
2	Static	12	0
	Motion	9	3
	Gated	12	0
1	Static	12	0
	Motion	11	1
	Gated	12	0

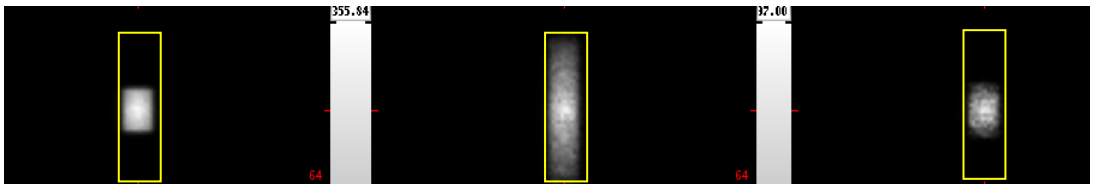

(a)Static simulation

(b) Motion simulation with 10cm amplitude

(c) Gated from motion by GSG

Fig. 4.1.21 Motion amplitude = **10 cm**, ROI is masked by yellow boxes in static, motion and gated images for EMR evaluation for gating improvement.

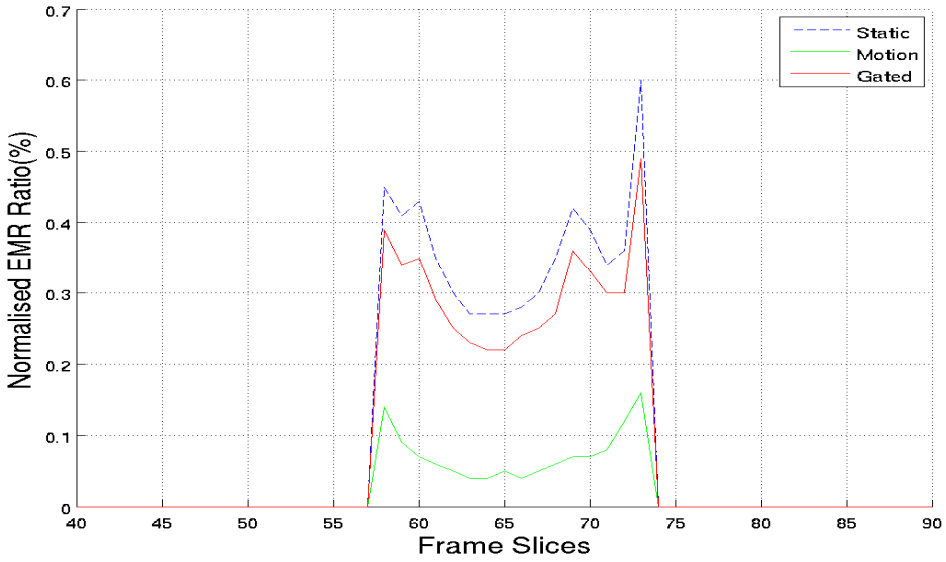

Fig. 4.1.22. Motion amplitude = **10 cm**, comparison of EMR values for slices of the static, the motion and the gated images in Fig.4.1.13.

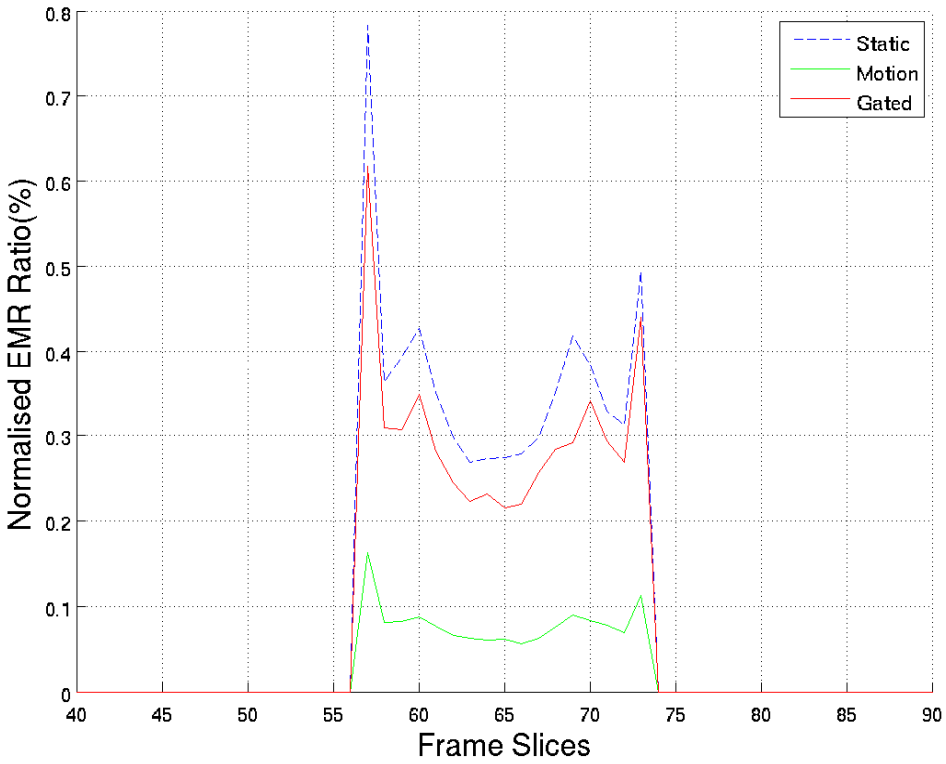

Fig. 4.1.23. Motion amplitude = **5 cm**, comparison of EMR values for slices of the static, the motion and the gated images in Fig.4.1.14.

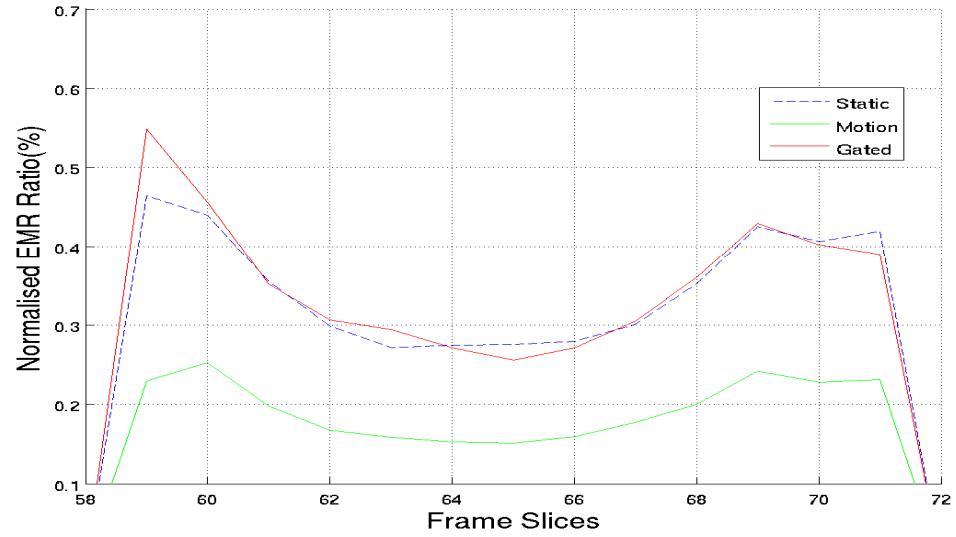

Fig. 4.1.24. Motion amplitude = **2 cm**, comparison of EMR values for slices of the static, the motion and the gated images in Fig.4.1.15.

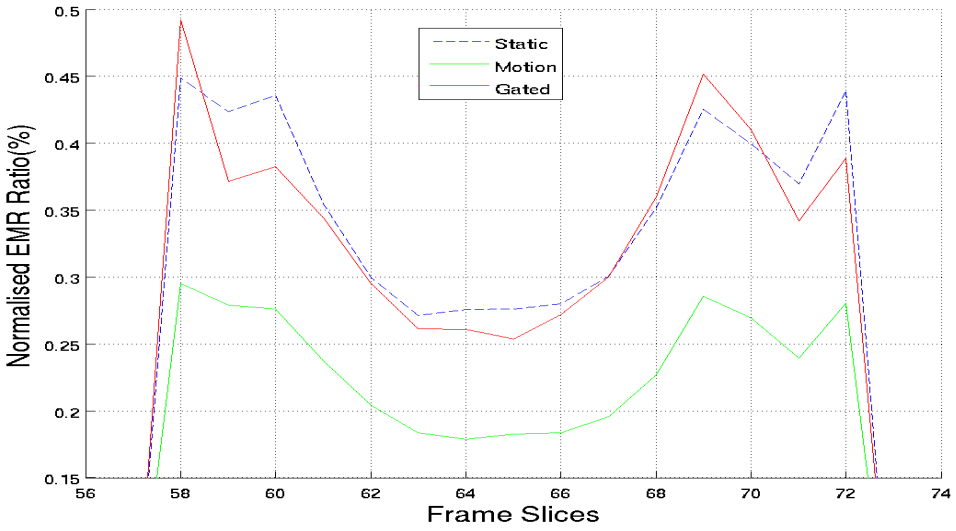

Fig. 4.1.25. Motion amplitude = **1 cm**, comparison of EMR values for slices of the static, the motion and the gated images in Fig.4.1.16.

4.1.3.3 Motion Correction

The use of gating techniques to eliminate motion effects may result in poor statistics for the reconstructed image. To solve this problem, COM and GSC methods were implemented for motion correction by applying a displacement transformation matrix correction to the sorted list-mode data event-by-event. Translating LOR events in frames to the position of the reference frame in terms of the displacements in the transformation matrix within the FOV as shown in Fig 3.25, a single motion-corrected dataset was obtained. The COM method is a common technique for respiratory motion correction as reviewed in Chapter 2.1.2. The displacement transformation matrix can be determined by calculating the axial component of the COM as described in section 3.5.

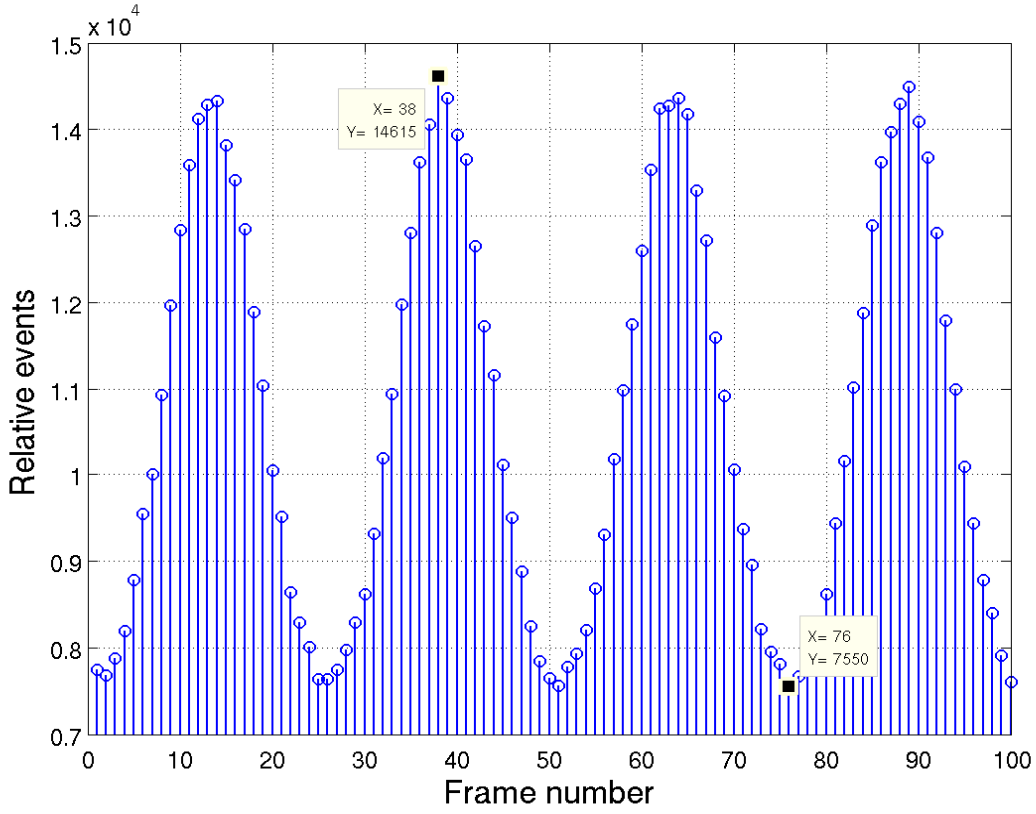

Fig. 4.1.26 Motion amplitude = 5 cm, simulation shows the frame with maximum event and the frame with minimum events.

The implementation of the motion correction by GSC is described in Chapter 3.5. Correction of the first 14 frames of the 5 cm motion amplitude case was described in detail to illustrate the implementation procedure of GSC. From the frame events plot (Fig. 4.1.5) with 5 cm amplitude, the maximum and minimum events corresponding to frames can be found in the sorted list-mode data as shown in Fig. 4.1.26, which are labelled as frame number 38 and 76 respectively. The frame labelled as 38 can be regarded as the reference frame, and that motion phase is located at the centre of FOV with the highest sensitivity value, while frame 76 with minimum events can be considered as the position phase of motion nearest the edge of the FOV with lowest sensitivity. As a result, the distance between frame 38 and frame 76 along z axis can be thought of as determining the motion amplitude which can be obtained by the COM method of calculating the displacement between two frames[69, 73]. For simulation studies, we do not need to estimate the motion amplitude because the motion amplitude is set in the phantom generation by using GATE or NCAT in all simulations, such as 5 cm motion amplitude for geometric phantom oscillation. However, the motion amplitude needs to be estimated in clinical studies by COM estimation since we do not know the motion amplitude in advance and so the simulation motion frame provides a means of validating the calibration of displacement versus change in count rate using COM

Following the estimation of motion amplitude, the transformation displacements to the reference frame can be determined in terms of Equation 3.3. For simple demonstration of application of GSC, only the first 14 frames (x =1 to x =14) were chosen with displacements computed relative to reference frames 38 and 76 as specified in Fig 4.1.27. The specific displacements in the transformation matrix calculated for each of 100 frames are plotted in Fig. 4.1.28. This shows the reference frame 38 with the maximum number of events has the minimum displacement value of 0 mm, while frame 76 with the minimum events has the maximum value of displacement of 50 mm towards the edge of the FOV.

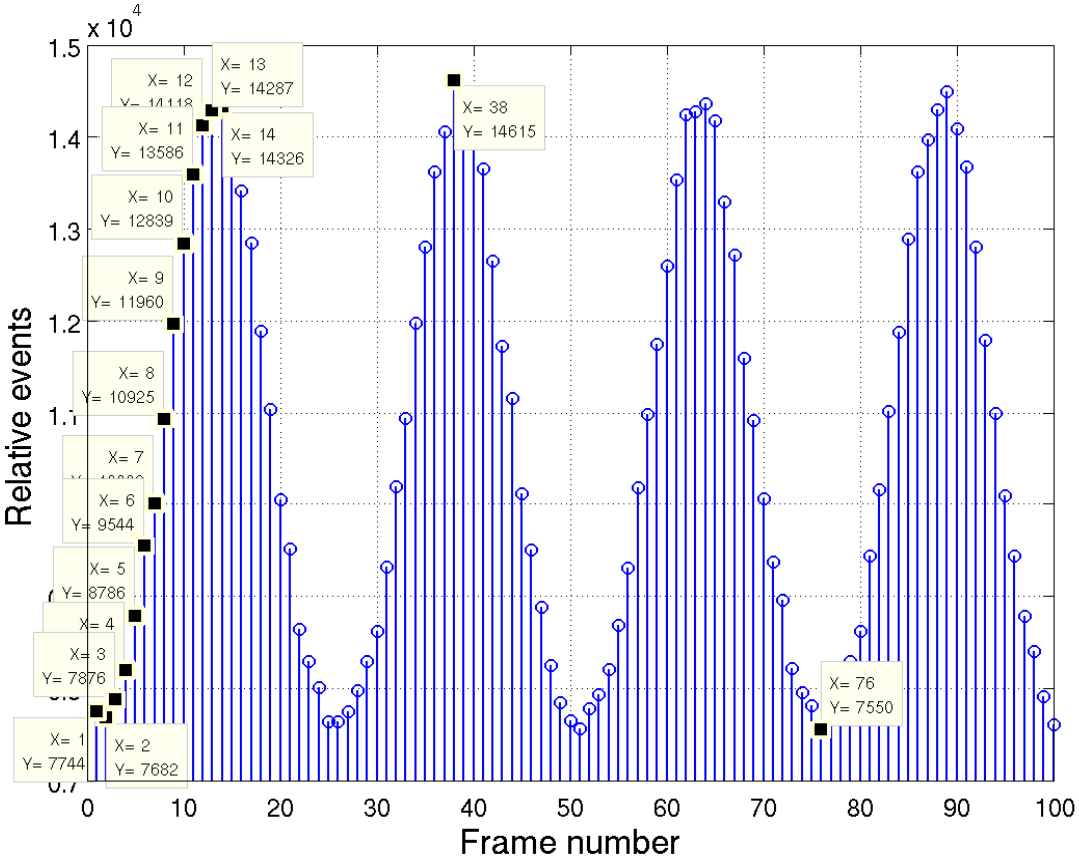

Fig. 4.1.27 Motion amplitude = 5 cm, simulation shows first 14 frames in motion cycles to be translated to the reference frame numbered 38.

After moving 14 frames to the reference frame 38, all translated frames were summed into one single frame and then reconstructed into an image as illustrated in Fig. 4.1.29(b). In order to compare the effect of the corrected by GSC to the non-corrected, the first 14 frames were also summed untranslated and reconstructed into an image as shown in Fig. 4.1.29(a). It is quite clear that the blurring at the edge of phantom is Fig. 4.1.29(a) due to motion. However, the blurring caused by motion is clearly corrected along the z axis by GSC as displayed in Fig. 4.1.29(b). In addition, comparison of the line profile curves from the uncorrected and the corrected images can be used to as a quantitative evaluation of the effect of the correction. It demonstrates that the quality of motion image (Fig 4.1.29(a)) was improved by the FWHM being reduced from 16 voxels to 9 voxels as displayed in Fig. 4.1.30, which means that the FWHM of the corrected image improves 7 voxels relative to the motion induced blurring of the phantom image along the axial direction. However, it needs to be noted that the corrected result has a much higher signal to noise ratio than the GSG (from a single respiratory phase) gated result shown in Fig 4.1.14. The GSC method not only decreases the blurring, but retains the high signal-to-noise ratio since all fist

14 frames were utilized to recover the blurring due to motion within the first 14 fames.

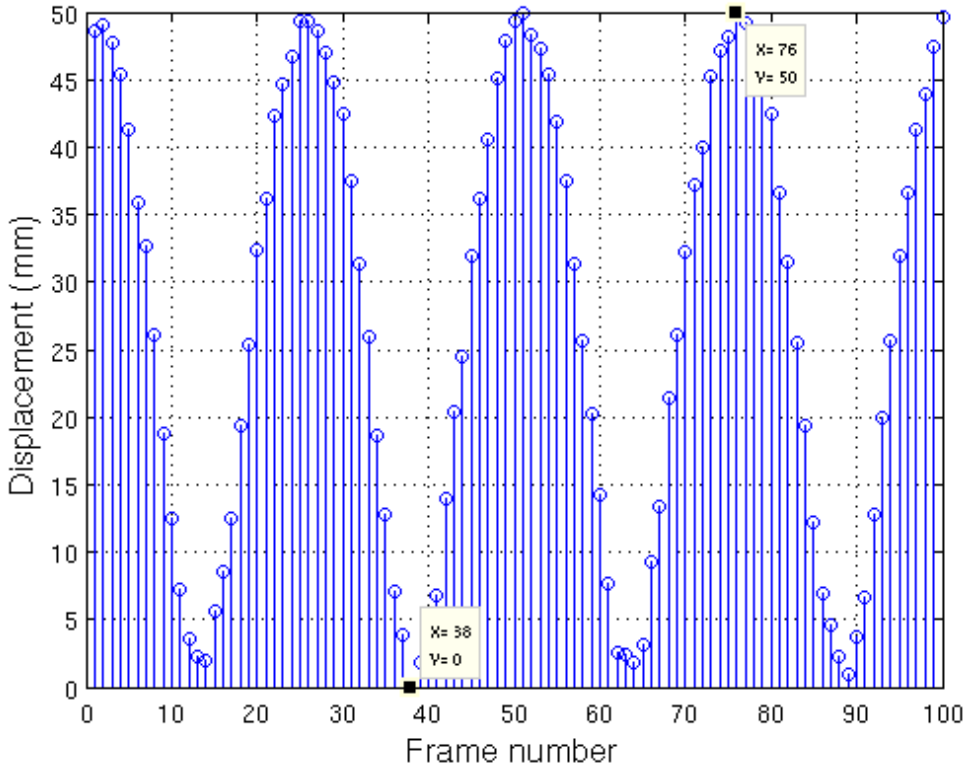

Fig. 4.1.28 Motion amplitude = 5 cm, simulation shows 100 frames versus displacements to be translated to the reference frame numbered 38 for correction.

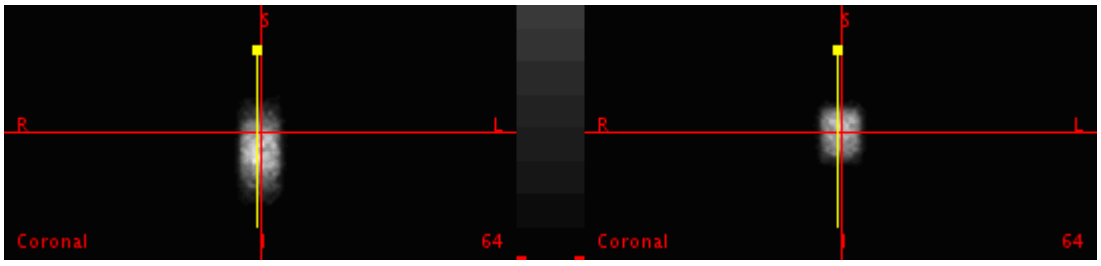

(a) Simulated oscillation of first 14 frames in coronal view.

(b) Corrected image of first 14 frames by GSC in coronal view.

Fig. 4.1.29 Motion amplitude = 5 cm, results from a simulation of a cylindrical phantom undergoing sinusoidal oscillation. First 14 frames motion were corrected by GSC.

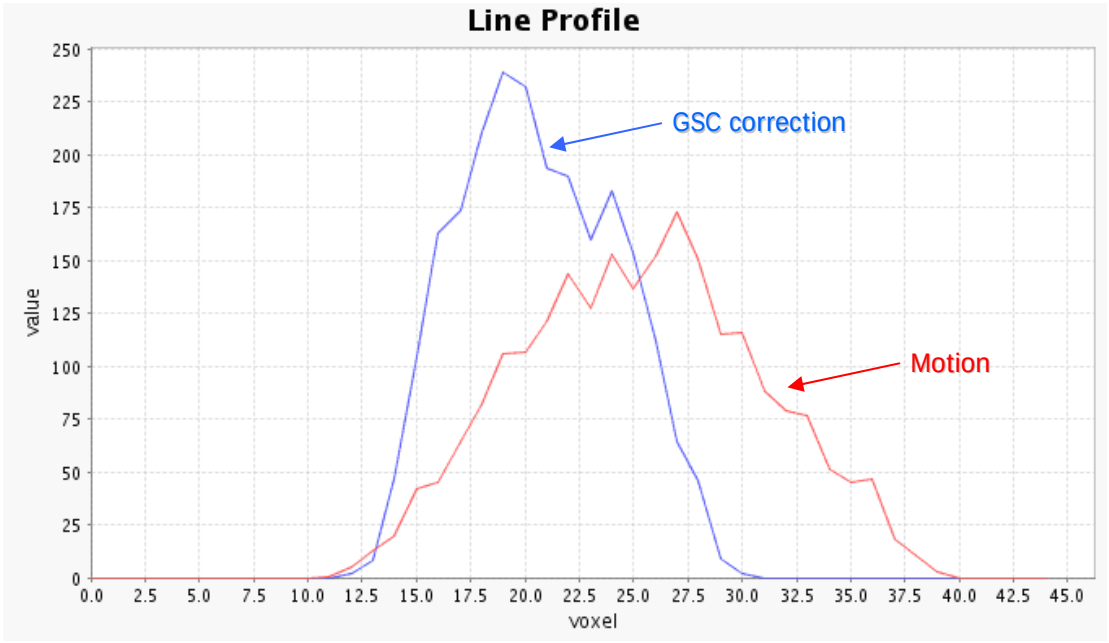

Fig. 4.1.30 Comparison of line profiles of the motion and the first 14 frames corrected-GSC reconstructed images for Fig 4.1.29, the line profile of the corrected-GSC image demonstrated motion deformation at edge of phantom was corrected by the FWHM reduced form 16 voxels to 9 voxels.

To correct all frames, the above procedure simply needs to be extended to translate every frame to the reference frame by displacement in the relevant transformation matrix, and then sum them and reconstruct the image. The results of correction by GSC using all 100 frames for motion amplitude with 10 cm, 5 cm, 2 cm and 1cm are illustrated in Fig. 4.1.31 ~ Fig. 4.1.34.

The corrected results are presented in two ways: GSC+Prior means utilising the known motion amplitude generated by GATE to correct motion, and GSC+COM means using the motion amplitude calculated by COM calibration to correct motion. The reconstructed images for the static, the un-corrected motion, the corrected by GSC+Prior and the corrected by GSC+COM, when viewed jointly, indicate an obvious improvement of the image quality by the GSC method in Fig. 4.1.31 ~ Fig. 4.1.34. The un-corrected motion reconstructed image (Fig. 4.1.31(b) ~ Fig. 4.1.34(b)) clearly shows that the edges of the simulated phantom were blurred due to the motion; while the motion corrected images show no such artifacts and have comparable contrast to the static reconstruction image. On the other hand, all results of the corrected images indicate less artifacts while maintaining higher signal to noise ratio compared with the results of the gated images displayed in section 4.1.3.2.

(a). Static (b). Summed

(c). Corrected by GSC + Prior (d). Corrected by GSC + COM

Fig. 4.1.31. Phantom motion amplitude = **10 cm**, simulated 100 frames sinusoidal oscillation were corrected by GSG + Prior known motion amplitude and GSC + COM estimation motion amplitude respectively. GSC + COM appears to 'over-correct' for large amplitudes

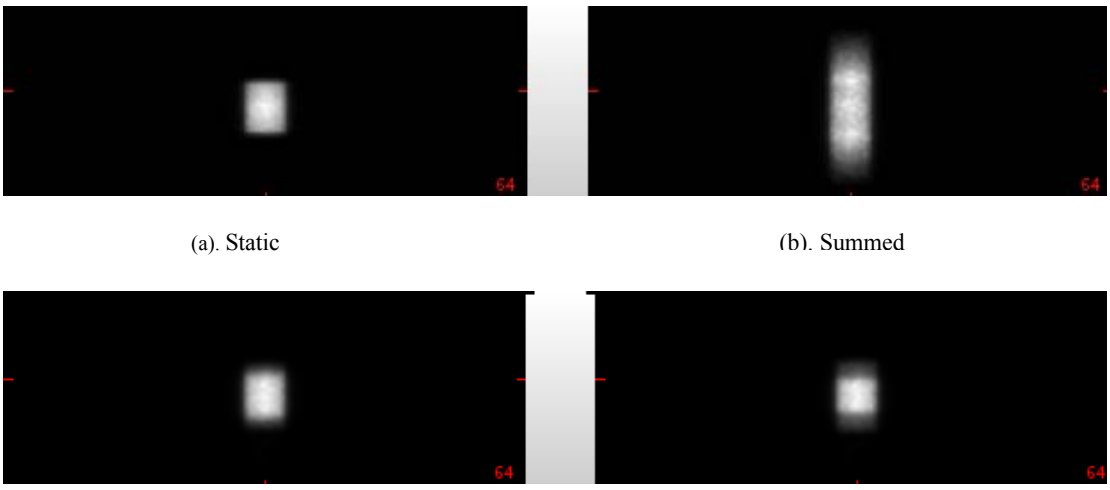

(a). Static (b). Summed

(c). Corrected by GSC + Prior (d). Corrected by GSC + COM

Fig. 4.1.32. Motion amplitude = **5 cm**, simulated 100 frames sinusoidal oscillation were corrected by GSG + Prior known motion amplitude and GSC + COM estimation motion amplitude respectively.

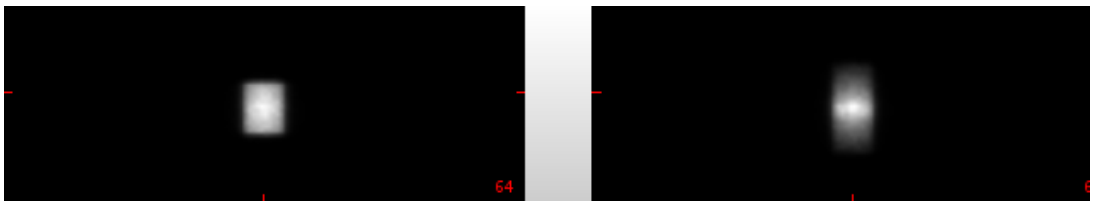

(a). Static (b). Summed

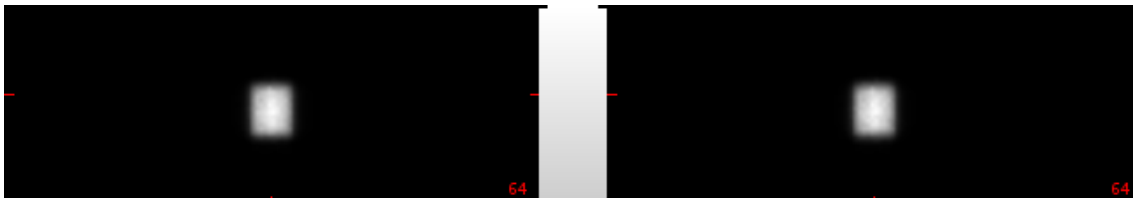

(c). Corrected by GSC + Prior (d). Corrected by GSC + COM

Fig. 4.1.33. Motion amplitude = **2 cm**, simulated 100 frames sinusoidal oscillation were corrected by GSG + Prior known motion amplitude and GSC + COM estimation motion amplitude respectively.

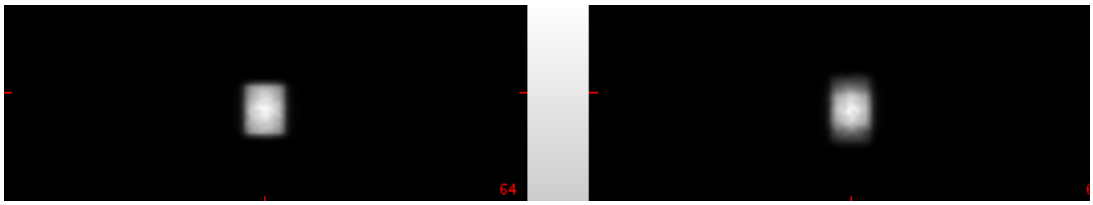

(a). Static (b). Summed

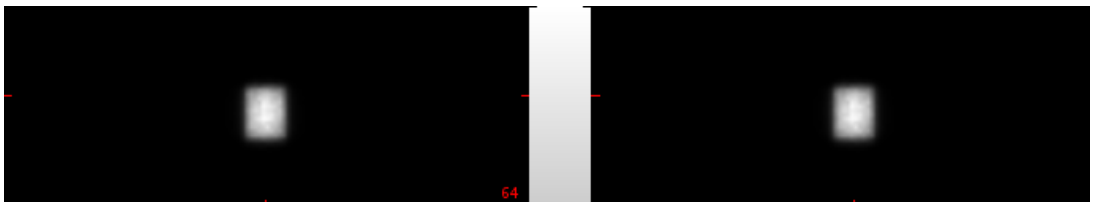

(c). Corrected by GSC + Prior (d). Corrected by GSC + COM

Fig. 4.1.34. Motion amplitude = **1 cm**, simulated 100 frames sinusoidal oscillation were corrected by GSG + Prior known motion amplitude and GSC + COM estimation motion amplitude respectively.

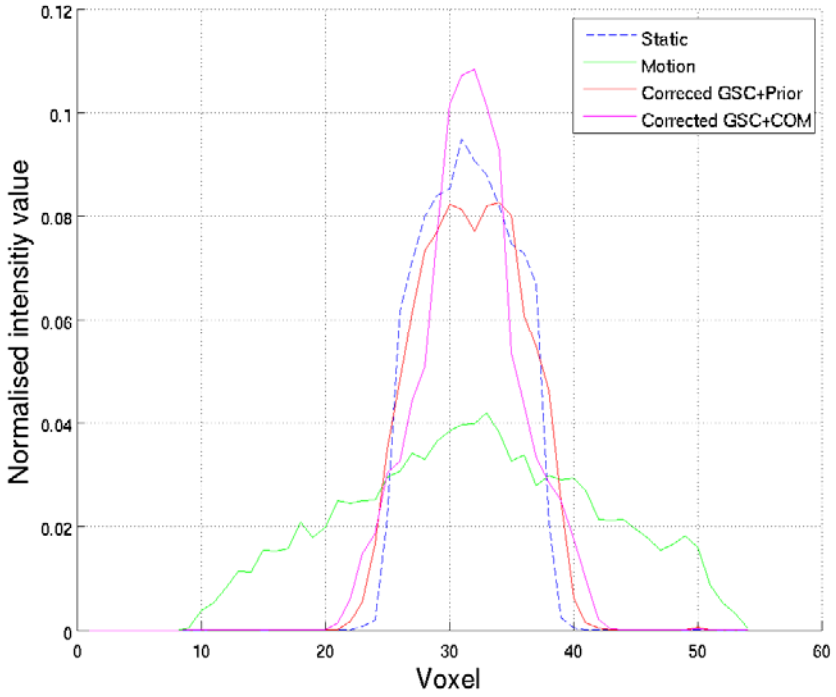

Fig. 4.1.35 Motion amplitude = **10 cm**, comparison of line profiles of the static, the motion and the corrected images for Fig. 4.1.31. The line profile of the corrected image demonstrated a spatial resolution similar to the static phantom image. GSC + COM appears to 'over-correct' for large amplitudes

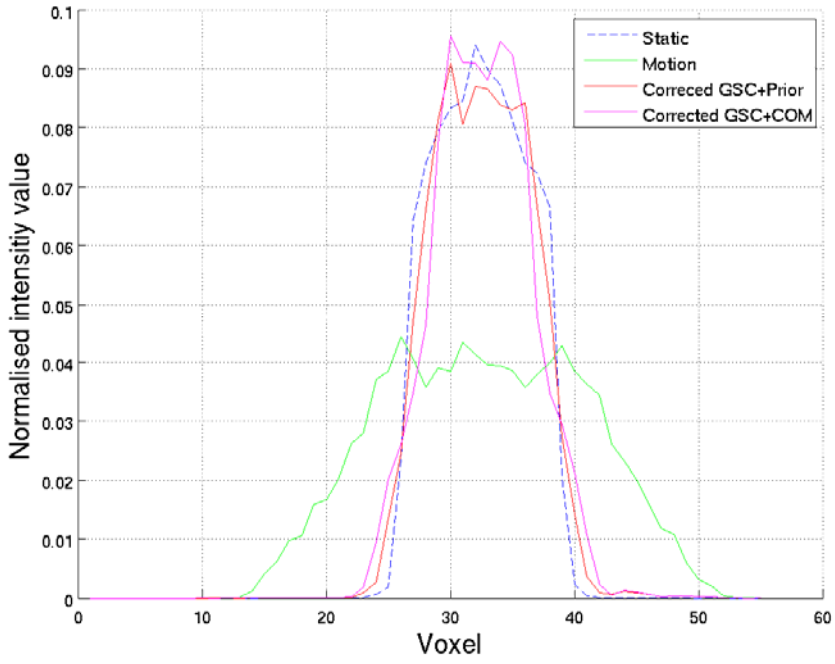

Fig. 4.1.36 Motion amplitude = **5 cm,** comparison of line profiles of the corrected-GSC + Prior and the corrected-GSC + COM reconstructed images for Fig. 4.1.32. The line profile of the corrected-GSC image demonstrated a uniform spatial resolution similar to the static phantom image.

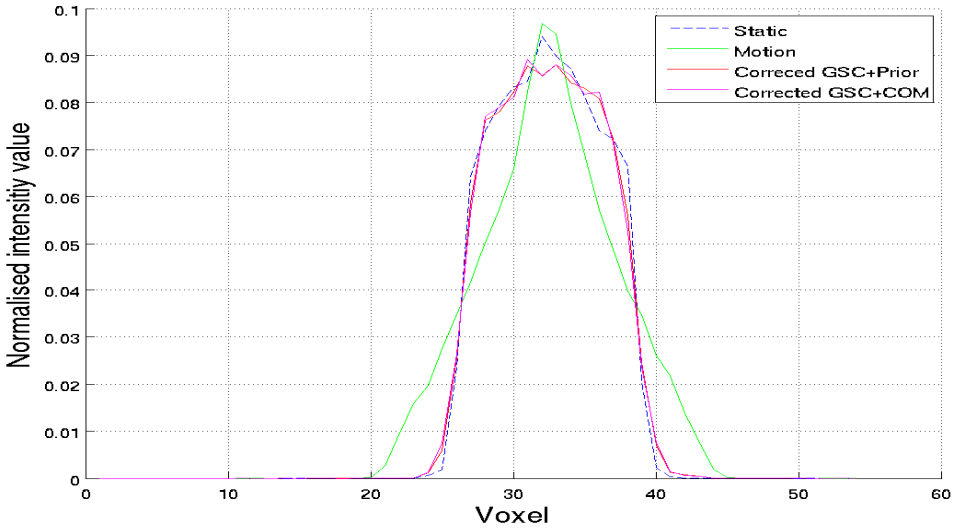

Fig. 4.1.37 Motion amplitude = **2 cm**, comparison of line profiles of the static, the motion and the corrected images for Fig. 4.1.33. The line profile of the corrected image demonstrated a spatial resolution similar to the static phantom image. GSC + Prior and GSC + COM appear identical correction for small amplitudes

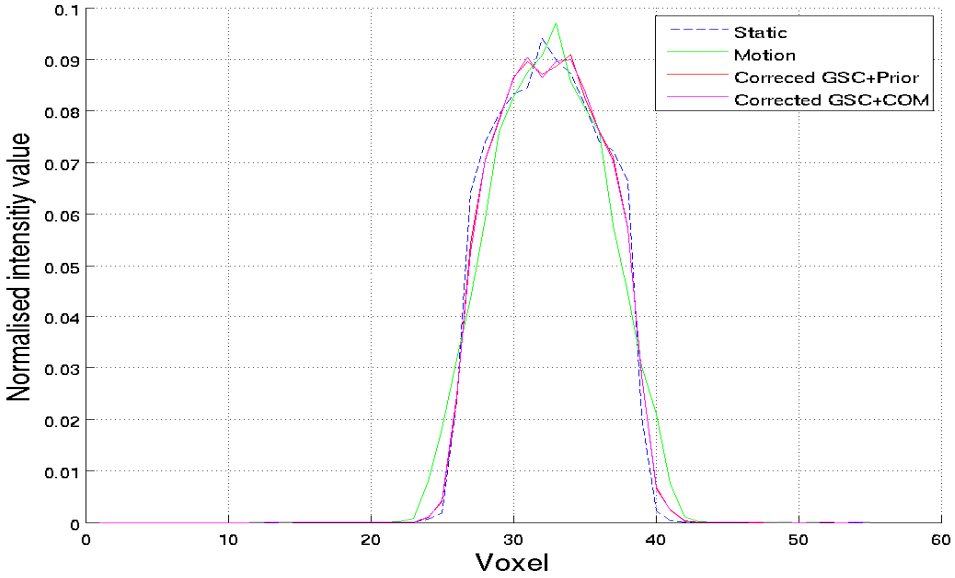

Fig. 4.1.38 Motion amplitude = **1 cm**, comparison of line profiles of the static, the motion and the corrected images for Fig. 4.1.34. The line profile of the corrected image demonstrated a spatial resolution similar to the static phantom image.

Table. 4.2.
Comparison of FWHM of between the static, the motion and the corrected images by GSC + Prior known amplitude and GSC + COM estimation amplitude for different motion amplitudes with 10 cm, 5 cm, 2 cm and 1 cm in Fig.4.1.35 ~ Fig.4.1.38. Distance of FWHM between the static and the corrected images demonstrate GSC improves the motion image in spatial resolution contrast.

Motion amplitude (cm)	**Motion states**	**FWHM voxels number**	**Distance to the static phantom (voxel)**
10	Static	12	0
	Motion	22	10
	Corrected by GSC+Prior	11	1
	Corrected by GSC+COM	8	4
5	Static	12	0
	Motion	20	8
	Corrected by GSC+Prior	11.5	0.5
	Corrected by GSC+COM	9	3
2	Static	12	0
	Motion	9	3
	Corrected by GSC+Prior	12	0
	Corrected by GSC+COM	12	0
1	Static	12	0
	Motion	11	1
	Corrected by GSC+Prior	12	0
	Corrected by GSC+COM	12	0

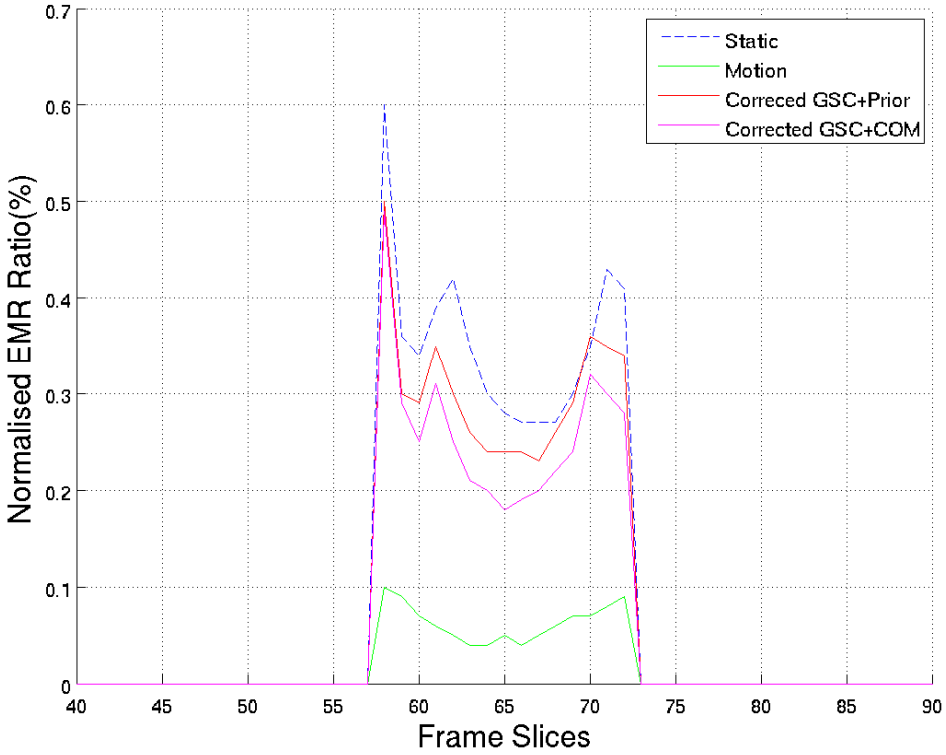

Fig. 4.1.39. Motion amplitude = **10 cm**, comparison of EMR slices values of the static, the motion and the gated images in Fig.4.1.33.

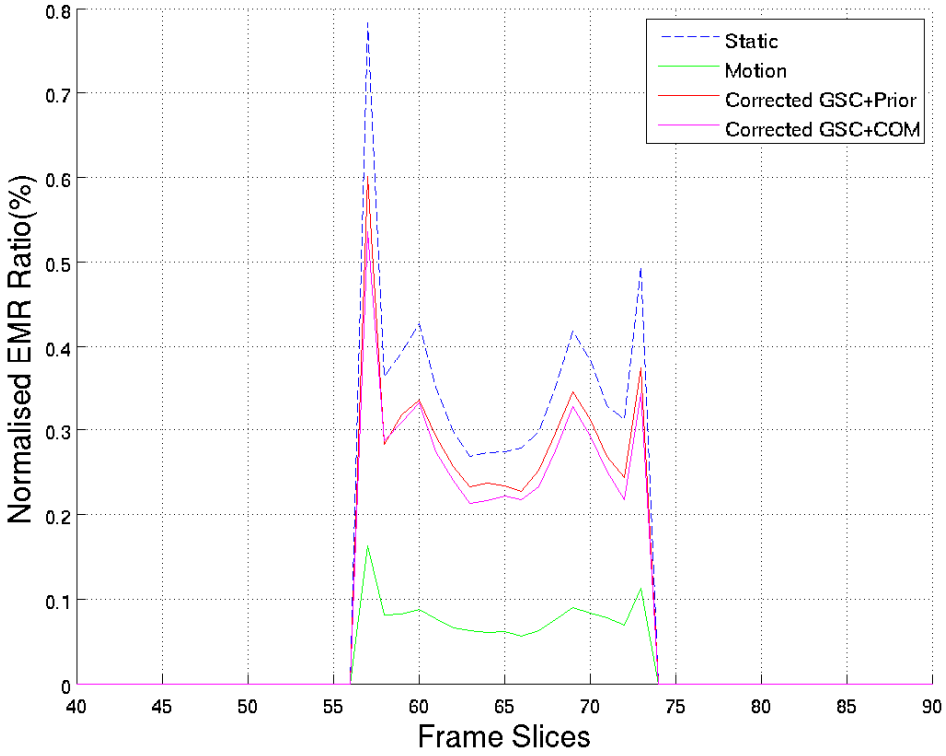

Fig. 4.1.40. Motion amplitude = **5 cm**, comparison of EMR slices values of the static, the motion and the gated images in Fig.4.1.34.

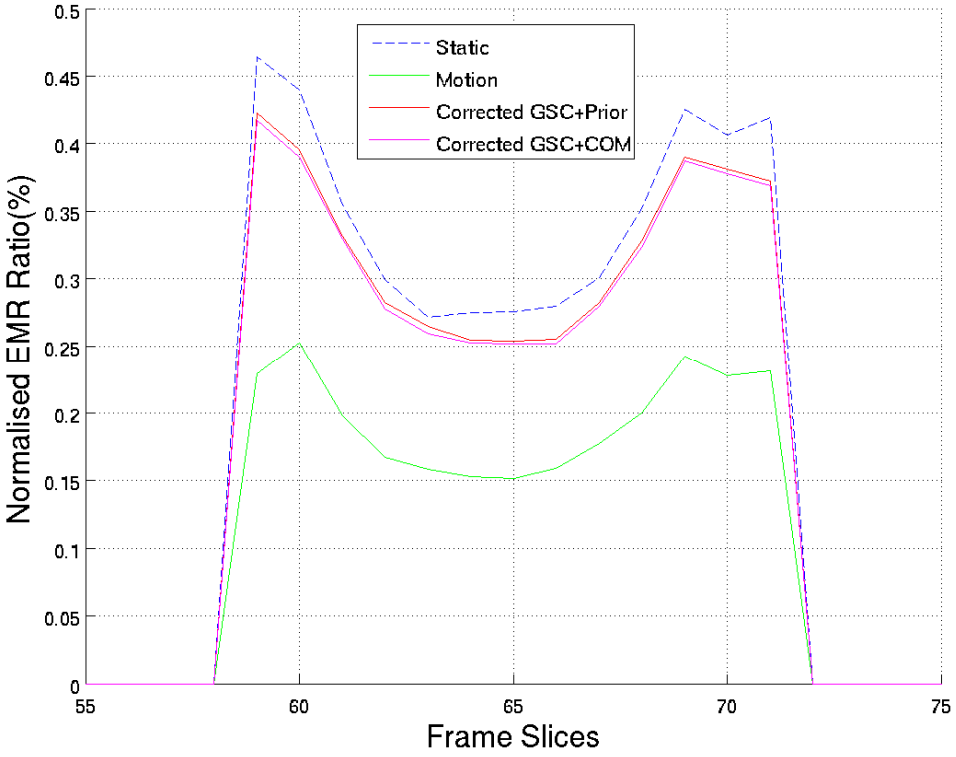

Fig. 4.1.41. Motion amplitude = **2 cm**, comparison of EMR slices values of the static, the motion and the gated images in Fig.4.1.35.

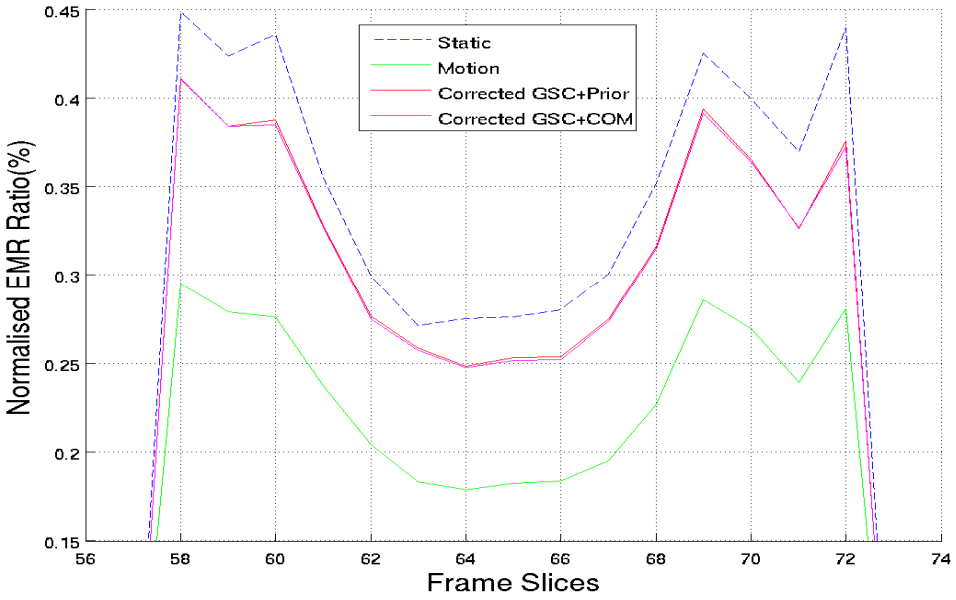

Fig. 4.1.42. Motion amplitude = **1 cm**, comparison of EMR slices values of the static, the motion and the gated images in Fig.4.1.36.

By visual evaluation, the corrected images by GSC+Prior (Fig. 4.1.31(c) ~ Fig. 4.1.34(c)) show the effect of motion correction is in good agreement with the static image. This correction effect can be concretely demonstrated by a comparison of the image line profiles ((Fig. 4.1.35 ~ Fig. 4.1.38) and the EMR matrix values (Fig. 4.1.39 ~ Fig. 4.1.42). FWHM values of the line profiles in Table 4.2 show that the GSC+Prior method most closely approaches the FWHM of the static image at all motion amplitudes. For the GSC+COM case, it is clearly seen that the quality of the corrected images decreases with increasing motion amplitude (Fig. 4.1.39(d) ~ Fig. 4.1.42(d)). The evidence can be found in quantitative evaluation by the image line profiles and the EMR matrix values as shown in Fig. 4.1.35 ~ Fig. 4.1.38 and Fig. 4.1.39 ~ Fig. 4.1.42. The corrected results from the GSC+COM case are almost the same as the GSC+Prior case when motion amplitude is 2 cm or 1 cm (FWHM distance values = 0); whereas the GSC+COM corrections become comparatively worse when the amplitude is 5 cm or 10 cm (FWHM distance values = 3, 4). The reason is because the motion amplitude estimated by COM derives from the actual image data. Fig 4.1.43 shows that the COM estimated amplitude values agree well with the known motion amplitudes under around 3 cm, while an apparent deviation of estimation can be seen when amplitudes increase over 3 cm.

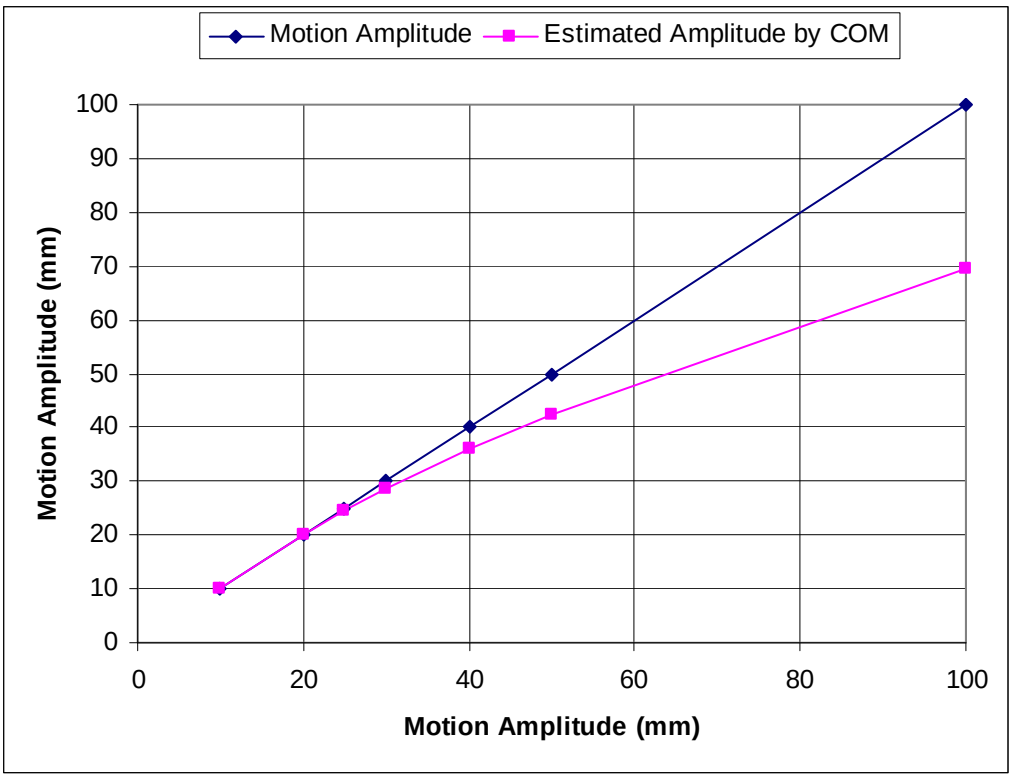

Fig. 4.1.43. Geometrical phantom motion amplitude estimated by COM. Comparison of real motion amplitudes with amplitudes estimated by COM, the estimated amplitude values show a good agreement with phantom motion under 3 cm.

The COM method under estimates the motion amplitude for large amplitude because some LORs are lost or un-measured due to phantom motion being too fast or passing out of the FOV as previously shown in Fig 2.6. In this circumstance, the COM correction is no longer accurate [70] as reviewed in Chapter 2.1.2.1. To fix this problem, Klein et al advised using masking techniques by selecting a volume of interest (VOI) method[73]. However, Bundschuh et al[74] applied COM techniques on patients to evaluate Klein's method, and pointed out the disadvantage of the COM method being the operator intervention required to process VOI.

For respiratory motion compensation, usually diaphragm motion amplitude is around 2 cm[21, 42]. Actually the respiratory motion amplitude estimated by the COM method may be taken as sufficient for respiratory motion of around 2 cm amplitude [69, 73, 74] because Fig 4.1.43 shows the COM method can obtain a good agreement under 3 cm amplitude.

4.1.4 Summary

A geometric phantom generated by using GATE was employed to simulate simple respiratory motion by a sinusoid oscillation. GSG, GSC [GSC+Prior and GSC+COM] were applied on the sorted list-mode data simulated by GATE. The gated and the corrected results demonstrate that GSG and GSC are able to gate and correct oscillatory motion. In addition, the GSC method for correction retains the high signal to noise ratio resulting in less motion induced artifacts without the statistical drawbacks of the gated image.

Respiratory motion is a non-rigid 3D motion, while the geometric phantom oscillation simulates rigid motion along the z axis. Therefore, simulation results of the geometric phantom provided the basis to proceed with a more complex, realistic simulation for validation of GSG and GSC.

4.2 Voxelised Simulation

4.2.1 Introduction

The voxelised phantom is able to simulate more detailed, realistic respiratory motion than the geometric phantom. The application of GSG and GSC to the voxelised phantom is the same as the application to the geometric phantom. In this research, the voxelised phantom was generated by using NCAT which provides a realistic and flexible model for defining the phantom in different respiratory phases [41]. The generated phantom was then imported into GATE [2] to simulate PET acquisition data which generated list-mode format data. The list-mode data stream was sorted into a sequence of frames, and then the GSG and GSC were tested on the sorted list-mode data.

4.2.2 Simulation Procedure

4.2.2.1 Phantom Generated by NCAT

Two types of voxelised phantom were generated by using NCAT for simulation of respiratory motion; with and without attenuation modelling. Three different lesions in different positions in the lungs, were investigated for the effect of gating and correction.

The NCAT simulation of the thorax was generated for 10 breathing cycles with each breathing cycle being 5 seconds, 2 cm motion amplitude. Using the NCAT phantom without attenuation modeling, 250 frames (200 msec), each of dimensions 64x64x64 with 5 mm cubic voxels were generated. Each of the generated frames may be regarded as corresponding to one particular respiratory motion phase. The distribution of radioactivity sources within the organs is detailed in Table 4.3.

To investigate the impact on the GSG and GSC methods of the non-uniform attenuation with three lesions of the thoracic-abdominal region, 80 dynamic frames (625 msec / frame) of attenuation coefficient maps in 10 breathing cycles, 2 cm motion amplitude were generated with NCAT. Each

frame was created as a 128x128x55 matrix with 3.125 mm cubic voxels. In addition, 15 mm, 12 mm and 10 mm diameters lesions were inserted in the lung-volume as illustrated in Table 4.4. Each of the emission frames and attenuation coefficient maps were then imported into GATE respectively. The activity concentration of the organs used in the simulation is documented in Table 4.5.

Table. 4.3
Simulation activity in the NCAT phantom with 64x64x64 matrix with 2 cm and 1.5 cm motion amplitude along z axis and y axis respectively

Organ	**Volume(ml)**	**Activity (kBq/ml)**
Lung	3212	2.3
Heart	822	12.6
Liver	1952	12.6
Kidneys	56	12.6
Spleen	279	12.6
Gall bladder	27	0.6
Stomach	361	0.6
Background	24346	0.6

Table. 4.4
Lesions in lung generated in the NCAT phantom with 128x128x55 matrix with

No	**Position**	**Lesion location(x, y, z)**	**Diameter (mm)**	**Activity ratio(lesion/background)**
1	Right lung	39,66,22	15	120
2	Left lung	81,64,36	12	120
3	Right lung	45,64,35	10	120

Table. 4.5
Simulation activity in the NCAT phantom with 128x128x55 matrix with 2 cm and 1.5 cm motion amplitude along z axis and y axis respectively

Organ	Volume(ml)	Activity (kBq/ml)
Lung	2820	2
Lesion1	2.3	12
Lesion2	1.3	12
Lesion3	0.8	12
Heart	737	7.5
Liver	961	7.5
Spleen	35	7.5
Kidneys	0.0	0.0
Gall bladder	0.0	0.0
Stomach	166	0.4
Background	14104	0.4

Respiratory motion simulated with the non-attenuation modelling using GATE and NCAT takes less computational time compared with that incorporating attenuation modeling. For example, with the simulation condition of a frame 128x128x55 with the activity of 12 MBq ^{18}F-FDG, the simulation with non-attenuation modelling required 8 hours computational time, whilst the simulation with attenuation modelling takes around 450 hours computation[67]. As a result of the computational burden of simulation, a strategy was adopted to simulate 250 shorter duration frames for non-attenuation modelling (64x64x64 matrix, 200 msec/frame, 250 frames, total time 500 hours). It consists of 250 frames for 10 breathing cycles, and can obtain a high temporal resolution of respiratory motion so as to investigate in detail the respiratory motion. Also its simulation is not time consuming due to non-attenuation modelling. In contrast, 80 frames with longer duration frames were used for attenuation modelling (128x128x55 matrix, 625 msec/frame, 80 frames, total time 14000 hours = 80 x 175 hours), since 10 breathing cycles containing 80 frames can reduce the duration of simulation. All simulations with and without attenuation modelling were carried out on the cluster super computer on the VPAC systems as mentioned in section 3.2.3.4.

4.2.2.2 Phantom Imported into GATE

The generated phantoms including the radioactivity frames, the attenuation frames and respiratory motion phases respectively were centred in the FOV of the PET scanner. For example, for simulation without attenuation modelling, each frame of 320 mm length was centred in the PET scanner of 180 mm length along the z-axis as a respiratory motion phase as shown in Fig. 4.2.1. The 250 frames generated by using NCAT were imported into GATE, and 250 individual simulations were executed.

4.2.2.3 Sort List-Mode Data

The sorted list-mode data of the voxelised phantom simulation is illustrated in Fig 4.2.2. It is different from the 'sort 'of list-mode data of the geometric phantom simulation that collected list-mode data by using GATE and binning it into a sequence of frames. The 'sort' of the voxelised phantom data is simply an import of each of the voxelised frames generated by NCAT into GATE to simulate each frame individually. Specifically, two types of voxelised phantom were acquired in list-mode data for simulation phantoms with and without attenuation modelling. These were sorted for validation of GSG and GSC. The sorted data for simulation with attenuation correction is comprised of 80 frames, each with a time interval of 625 msec and having matrix dimensions of 128 x 128 x 55, spanning 10 breathing cycles. The sorted data for simulation without attenuation correction is comprised of 250 frames, each with a time interval of 200msec and having matrix dimensions of 64x64x64, spanning 10 breathing cycles.

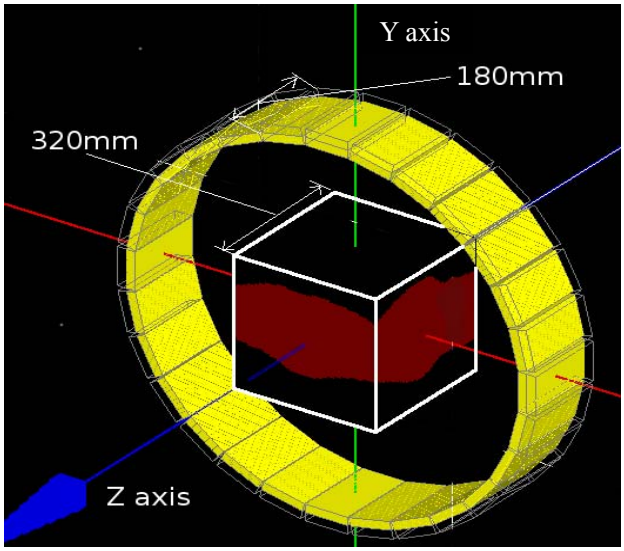

Fig. 4.2.1 GATE geometry visualization of the phantom represented by a 64x64x64 matrix with 320 mm edge-length and centred in the 180 mm axial FOV of the Allegro PET scanner.

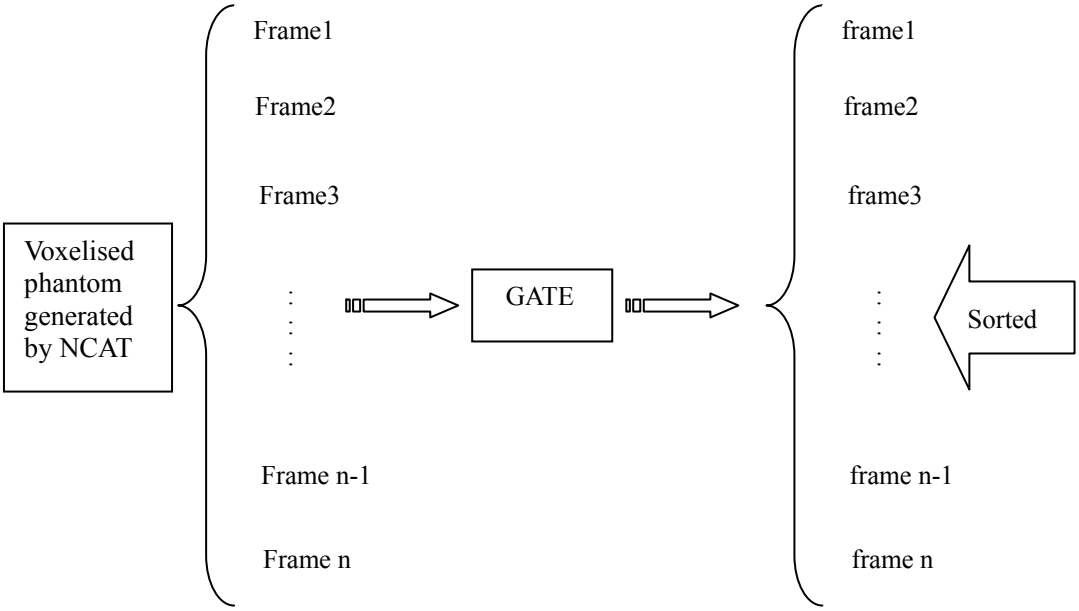

Fig. 4.2.2 Sort of list-mode data of voxelised phantom simulation into the sequence of frames. Voxelised phantom frames were generated by NCAT, and then respectively imported into GATE simulation to obtain frame events which can be regarded as the sorted frame.

4.2.2.4 Motion Gating and Correction

Following the sorting of list-mode data for the with and without attenuation modelling cases, GSG and GSC methods were applied to the sorted phantom frames data for respective validation. The single gated and corrected frame was reconstructed by PURE software[133] with and without attenuation correction respectively. The attenuation coefficient maps were generated by using NCAT.

4.2.3 Results and Discussion

4.2.3.1 Frame Events and Lung Volume Curves

The graph of frame events against frame number from the sorted list-mode data for validation of GSG and GSC by phantom for the case without attenuation modelling is illustrated in Fig 4.2.5. The graph of frame events against frame number for the case with attenuation modelling is illustrated in Fig 4.2.7. A graph of frame events against frame number for exactly the same parameters but without attenuation correction is illustrated in Fig 4.2.6 to demonstrate the difference made by attenuation correction.

There are broad similarities between the NCAT determined lung-volume (Fig 4.2.3 and Fig 4.2.4) and the simulated frame events. Fig 4.2.5(a) illustrates the distribution of frame events versus frame number for a phantom with frame matrix 64x64x64, with no attenuation modelling, over nine breathing cycles. However, there is a notable deviation from a symmetric sinusoidal character in this Fig 4.2.5(a). The statistical noise of events is a possible cause of this as each breathing cycle was sampled by 25 frames. This sampling regime provided for short frame duration times (200msec per frame), which enhances temporal resolution at the expense of increased statistical noise. Although this would suggest that a range of frames could be used to contribute to a given gate to reduce the statistical noise, only the peak frame count was used here to perform gating. The frames corresponding to the peak counts were chosen to gate the breathing

cycles at a single respiratory phase and are shown numbered in Fig. 4.2.5. On the other hand, Fig 4.2.6 and Fig 4.2.7 indicate the variation of event rate versus frame number for the frame matrix 128x128x55 with and without attenuation modelling over ten breathing cycles. They show smoother plots of frame events than Fig 4.2.5 has as they have a coarser temporal sampling regime of 8 frames per breathing cycle with the longer frame duration time (625msec per frame). One difference between Fig 4.2.6 and Fig 4.2.7 is that the plot of non-attenuation modelling is not as symmetric as the plot of attenuation modelling. The cause of this is due to non uniform distribution of activity sources in the phantoms resulting in the asymmetric plot, while attenuation modelling makes simulation of frame events collection more realistic and symmetric.

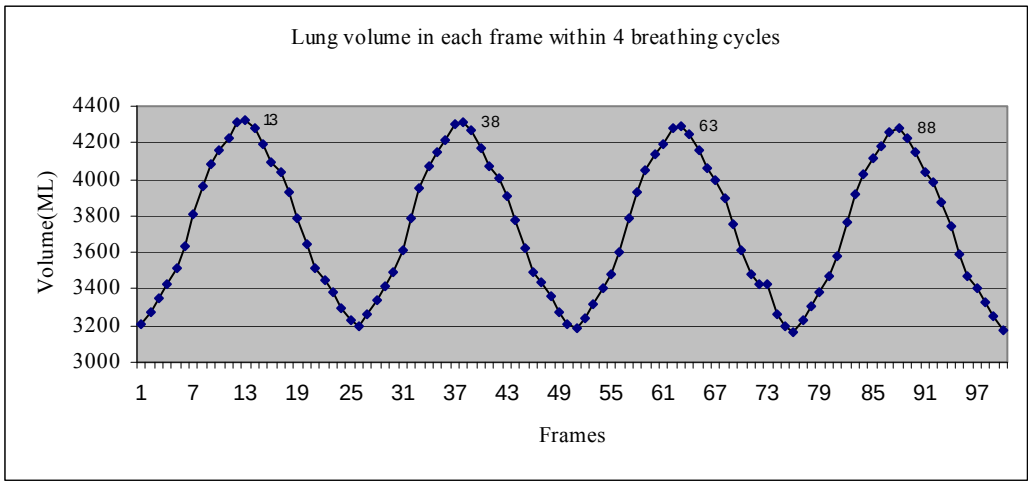

Fig 4.2.3 NCAT lung volume (mL) variation during four breathing

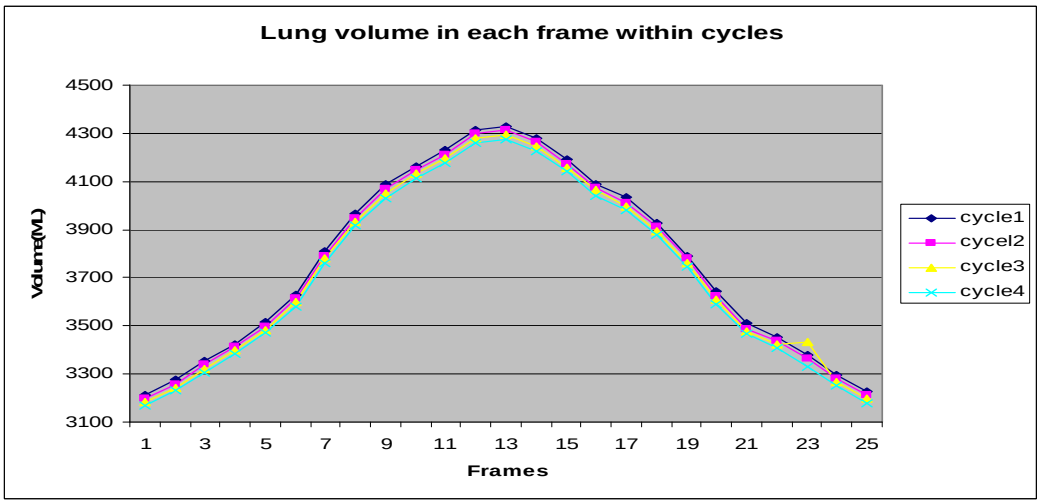

Fig 4.2.4 NCAT lung volume variation curves of during four breathing cycles are overlapped, which display a feature of sinusoidal curve.

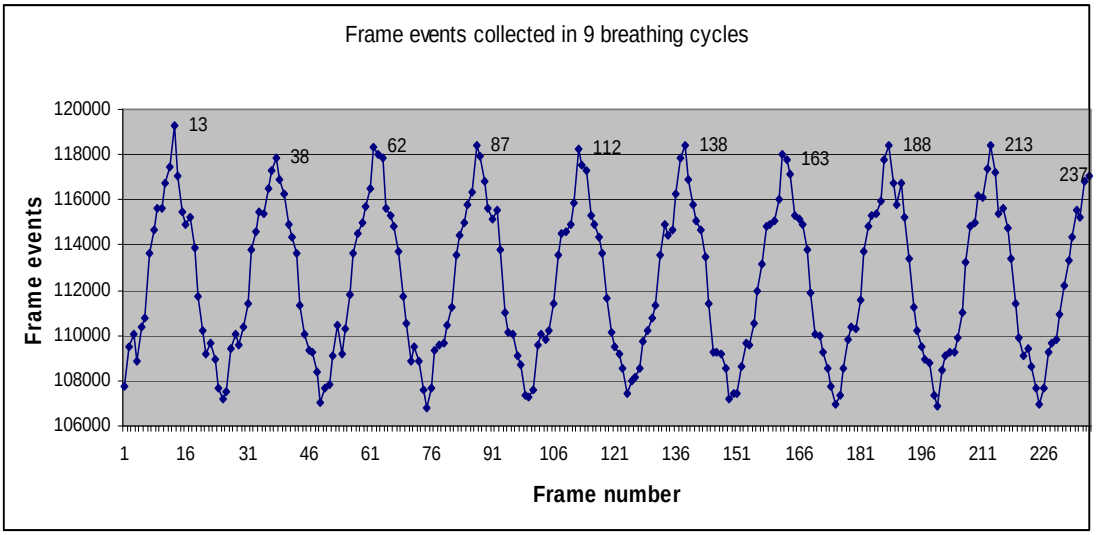

(a). Variation of frame counts in nine breathing cycles

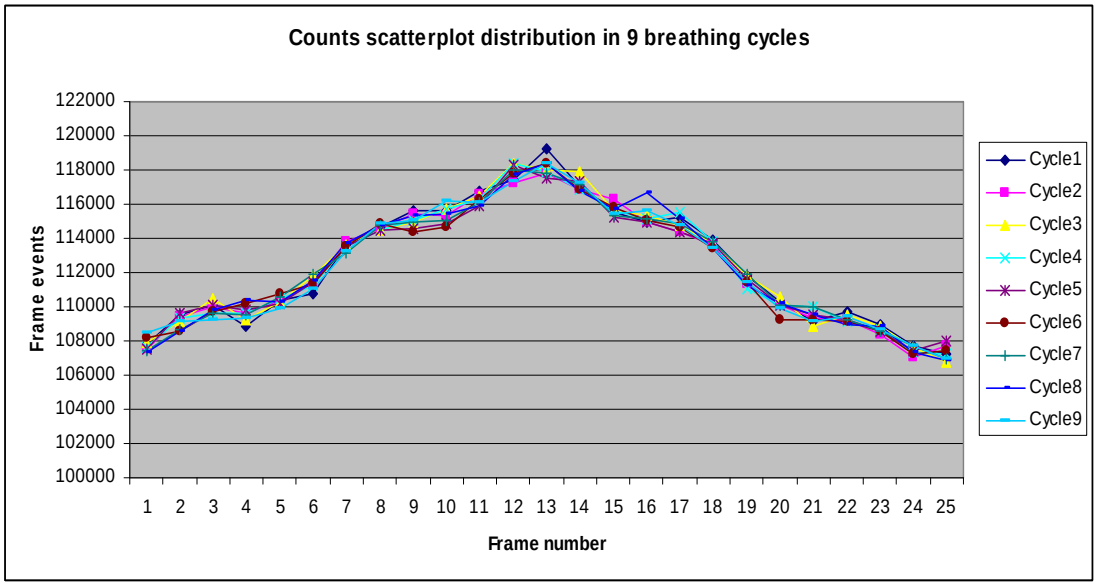

(b). Variation of frame counts overlapped in same position of nine breathing cycles. The shape of variation is similar with the change of lung volume as shown in Fig 4.2.4.

Fig 4.2.5. Count rate variation during breathing cycles for phantom 64x64x64 matrix, 200 msec per frame without attenuation modeling during nine breathing cycles as shown in (a) and (b) .

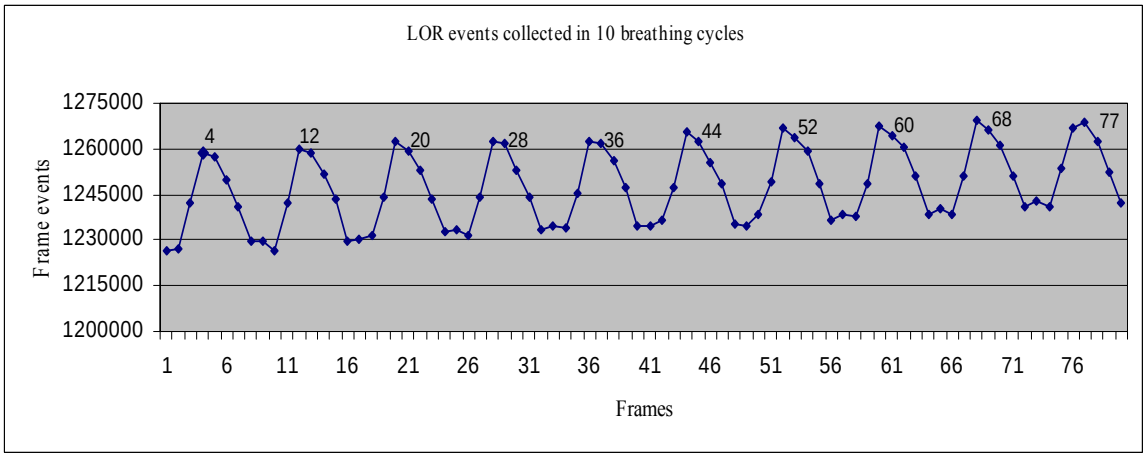

Fig 4.2.6 Event rate variation during breathing cycles for phantom 128x128x55 matrix, 625 msec per frame without attenuation modeling and a lesion modeling by NCAT phantom during 10 breathing cycles.

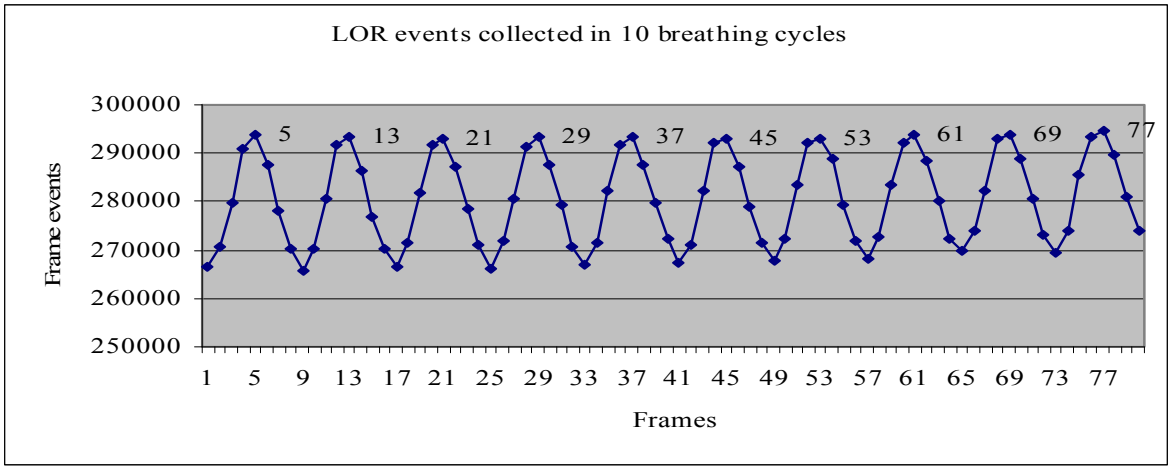

Fig 4.2.7 Count rate variation during breathing cycles for phantom 128x128x55 matrix , 625 msec per frame with attenuation modelling and a lesion by NCAT phantom during 10 breathing cycles.

4.2.3.2 Motion Gating with and without Attenuation Modeling

For the non-attenuation modelling simulation, Fig. 4.2.8 demonstrates the GSG method applied to respiratory motion by comparing reconstructed images in the sagittal and coronal view. The static image (Fig 4.2.8 (a) and (d)) and the summed images (Fig 4.2.8(b) and (e)) were generated from all 250 frames, and the gated images (Fig. 4.2.8(c) and (f)) with 10 frames. From these reconstructed images, the extent of respiratory motion is evident in the different positions of the base of the lung shown by the red line marked between Fig. 4.2.8 (a), (b), (c), (d), (e) and (f) respectively. To quantify the improvement of the gating by GSG, the line profile along the line marked on the image as a yellow line in Fig 4.2.8(d), (e) and (f) is used to compare the improved effect between the static, the summed and the gated case as illustrated in Fig 4.2.9. The summed profile curve shows a slow roll off of peak to valley in the boundary between lung and liver due to respiratory motion (Fig. 4.2.8(b) and (e)), while the gated line profile curve fits well with the static curve. Both curves increase quickly and then drop off sharply at peaks and valleys which means the intensity ratio between the image of the lung and liver is high near to the boundary. Therefore the gated image is improved with the visually well defined boundary between lung and liver as shown in Fig. 4.2.8 (c) and (f). In addition, the measure of improvement by the EMR method shows that the values of EMR of the gated and the static case are plotted over the summed image as illustrated in Fig 4.2.10, which indicates the overall image quality is improved after the gating by the GSG method.

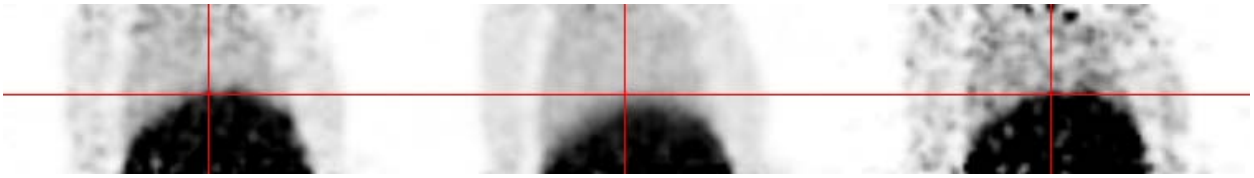

(a) Static image in sagittal view

(b) 250 frames summed image in sagittal view

(c) 10 frames gated image in sagittal view.

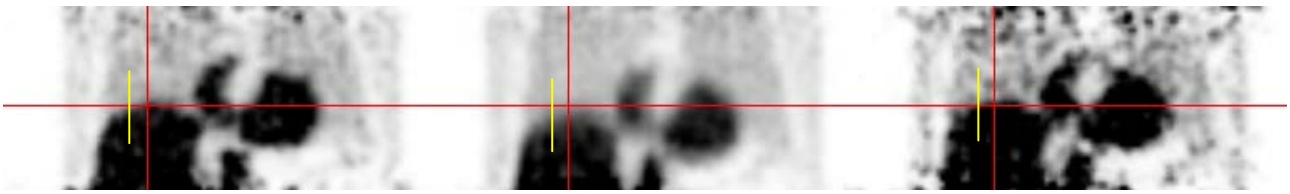

(d) Static image in coronal view.

(e) 250 frames summed in coronal view

(f) 10 fames gated in coronal view.

Fig. 4.2.8. Comparison of breathing summed and breathing gated reconstructed images for non-attenuation modeling. The red lines mark the same geometry in the summed and the gated images.

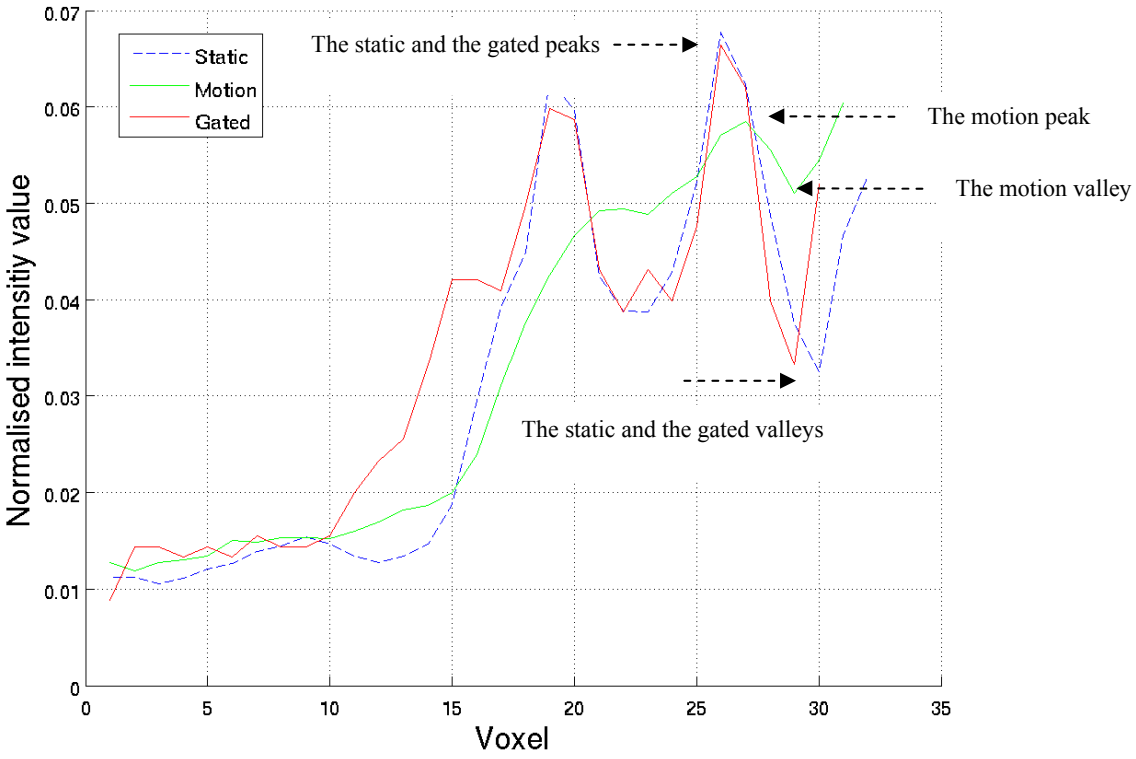

Fig. 4.2.9. Comparison of the normalized line profile from the static Fig 4.2.8(d), the summed Fig 4.2.8(e) and the gated Fig 4.2.8(f) reconstructed images as marked in yellow line in coronal view. The gated line profile demonstrates an improved spatial contrast.

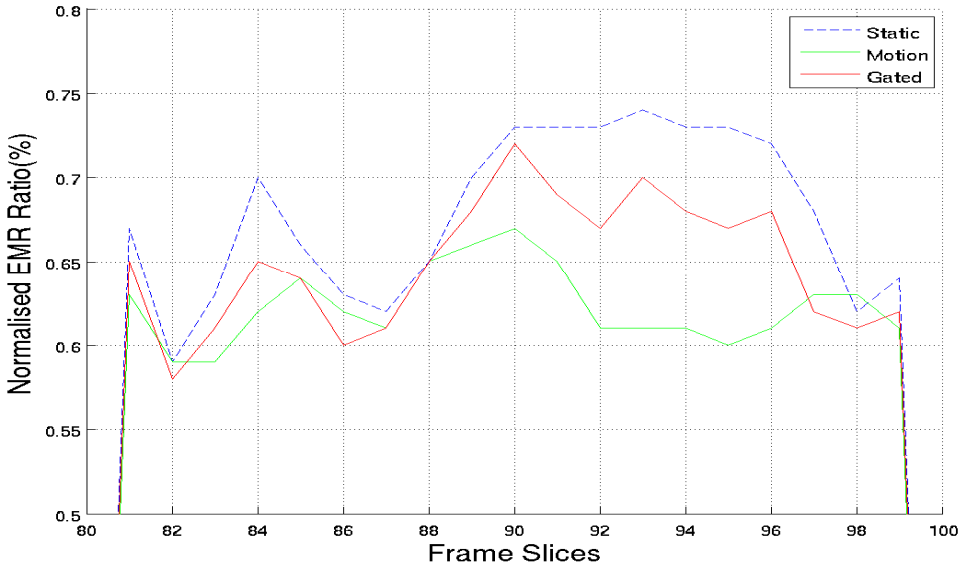

Fig. 4.2.10. Comparison of the normalized EMR values for the static, the summed and the gated in Fig 4.2.8, the gated EMR demonstrates an improved spatial contrast.

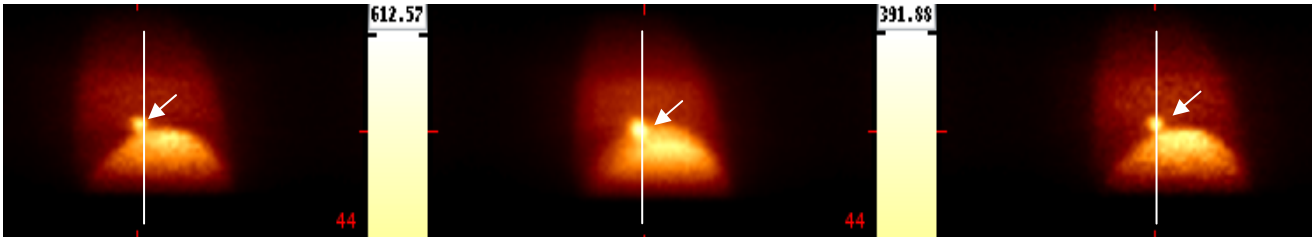

(a) Static phantom in sagittal view with 50 millions LORs collected.

(b) Summed 10 cycles with in sagittal view, 59 millions LORs collected.

(c) Gated 10 cycles with in sagittal view, 11 millions LORs collected.

Fig. 4.2.11. Motion gating at a single respiratory phase with a lesion and with non-attenuation modeling. A comparison of reconstructed images of the static, summed and the gated with a lesion in sagittal view respectively. The white arrows indicate that artifacts on lesion are clearly reduced by the GSG compared to the

In addition, the GSG method was applied to a non-attenuation modelled simulation. With a lesion, it was motion gated with peak counts frames labelled in the frame events curve as shown in Fig 4.2.6. The result of the gated summed frame was reconstructed into an image as shown in Fig 4.2.11 which demonstrates the lesion in the gated image (Fig. 4.2.11(c)) has good spatial resolution compared with the static image (Fig 4.2.11(a)) and the summed image (Fig. 4.2.11(b)). The image line profile indicates that the size of the lesion was reduced at FWHM from 5 voxels to 2.5 voxels as illustrated in Fig 4.2.12. EMR values of the lesion region shows the gated image better resolves the edge of the lesion compared with the summed as and comparably with the static as displayed in Fig 4.2.13.

On the other hand, for attenuation modelling, comparing the reconstructed images generated from the summed image in the transverse view (Fig. 4.2.14(a)) and sagittal plane view (Fig .4.2.14(b)) with the GSG gated image in the transverse view (Fig. 4.2.14(c)) and the sagittal plane view (Fig. 4.2.14(d)), the lung lesion shows a significant increase in spatial resolution in the transverse view and sagittal image plane views. Fig 4.2.14(e) shows evidence that the FWHM of the peak associated with the lesion was reduced from 8 voxels in the moving case to 4 voxels in the GSG gated case.

In the simulation incorporating attenuation effects, 20 million LOR events were collected for the summed breathing cycles over 50 seconds (10 breathing cycles), giving a coincidence count rate of 400 kcps. Gating at a single respiratory phase resulted in 2 million LOR events being collected.

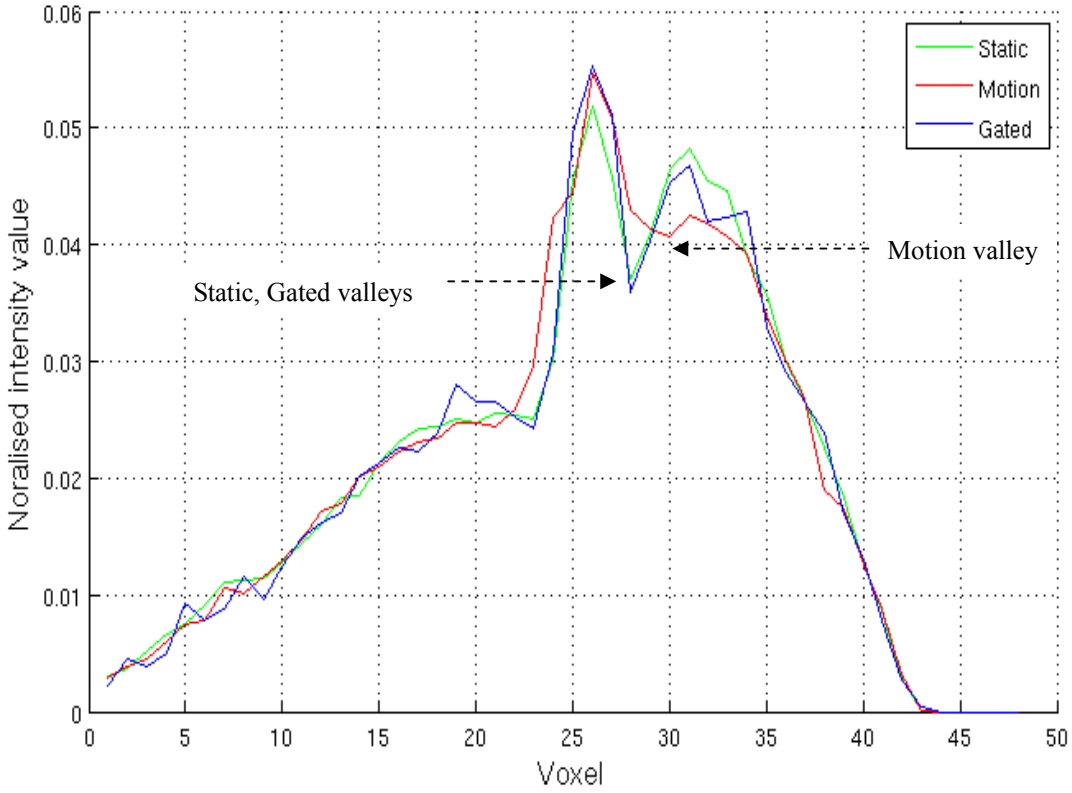

Fig. 4.2.12. Comparison of the normalized line profile for the static, the summed and the gated in Fig 4.2.11(a), (b) and (c) respectively, reconstructed images marked in white line demonstrate that the gated image has an improved spatial contrast.

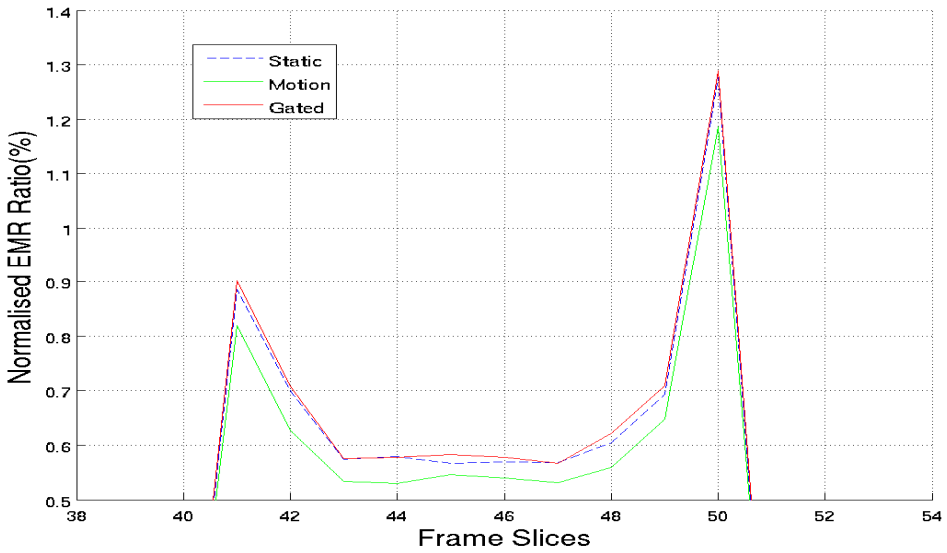

Fig. 4.2.13. Comparison of the normalized EMR values of the lesion region for the static, the summed and the gated in Fig 4.2.11, the gated EMR demonstrates an improved spatial contrast.

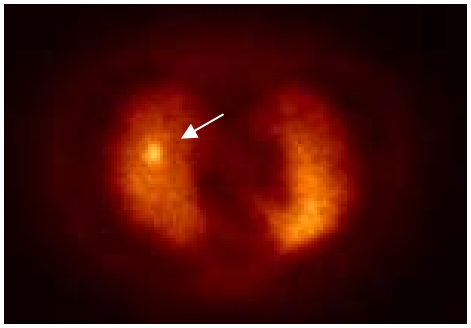

(a) Transverse view of summed 10 cycles

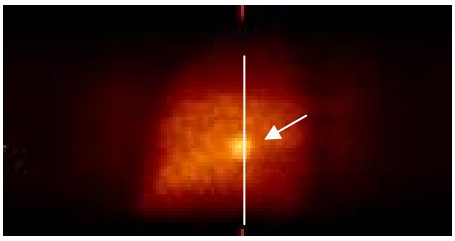

(b) Sagittal view of summed 10 cycles

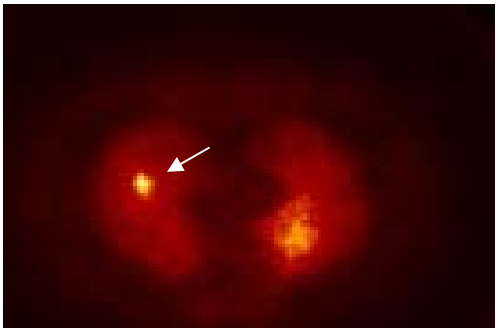

(c) Transverse view of gated images

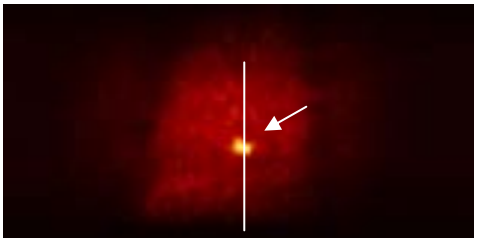

(d) Sagittal view of gated images

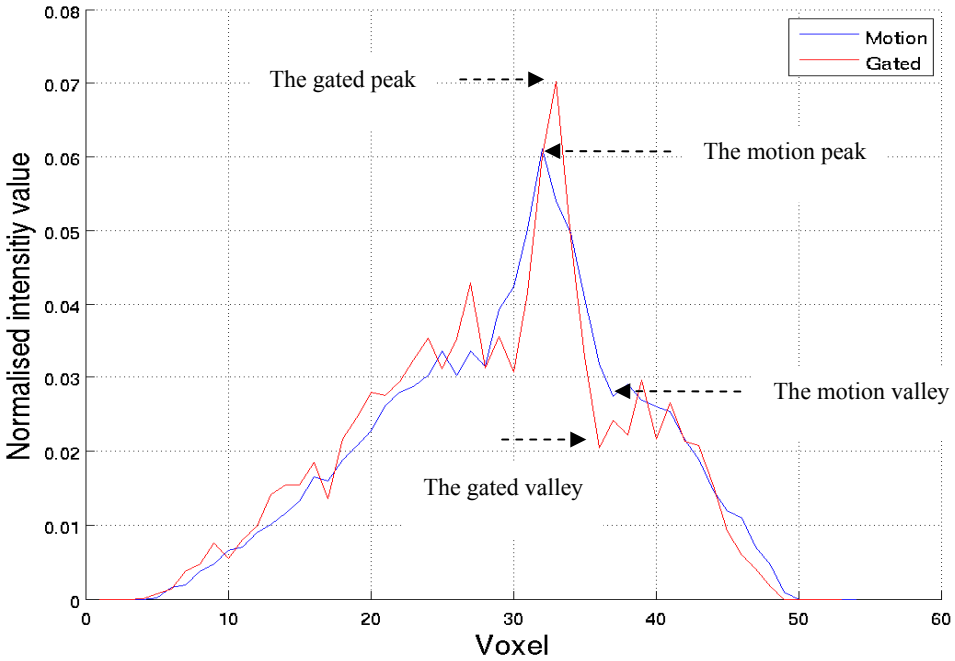

(e) Comparison of the line profile, the motion FWHM reduced from 8 voxels to 4 voxels of the gated, images marked in white lines demonstrate the gated image has an improved spatial contrast.

Fig. 4.2.14. Motion gating with attenuation modeling and a lesion. A comparison of reconstructed images of the summed and the gated in transverse and sagittal views (a) - (d) respectively and the line profile. The white arrows indicate that artifacts on lesion are clearly reduced by the proposed method GSG compared to the summed reconstruction.

4.2.3.3 Motion Correction

Based on the plot of frame events versus frame number as drawn in Fig 4.2.6, the GSC method is then applied to the sorted list-mode data, which is the same procedure as the previous application to the geometric phantom described in the section 4.1.3.3. 17 million LORs were collected with non-attenuation modelling within two breathing cycles consisting of 15 frames. Visual comparison of the static, the summed and the corrected images by GSC+Prior and GSC+COM, illustrated in Fig 4.2.15(b), shows that the size of lesion was reduced in the corrected image compared with the summed image (Fig 4.2.15(c) and Fig 4.2.15(d)). The improvement is demonstrated by the image line profiles as indicated in Fig 4.2.16 with the FWHM values detailed in Table 4.5. It is clearly seen that the FWHM of the lesion of the summed image of 6 voxels was reduced to 3.5 voxels for the corrected image. Additionally, both the GSC+Prior and GSC+COM methods have 1 voxel difference in FWHM to the static case which indicates the corrections are achieving spatial resolution close to that of the static case.

In the coronal plane view, Fig 4.2.15(f) shows clearly the lesion motion artifacts and the blurring of the boundary between lung and liver in the coronal plane of the summed image. With the implementation of the corrected by GSC+Prior and GSC+COM methods, a clear improvement of the boundary around the lesion between the lung and liver in terms of contrast is demonstrated in Fig 4.2.15(g) and (h). The EMR matrix values in the coronal view show the magnitude of the lesion edge EMR of the corrected images to be greater than that of the summed image. In addition, from Table 4.6 and EMR values, it is apparent that the quality of the GSC+Prior corrected and GSC+COM corrected images is almost same, the reason is that the motion amplitude estimated by COM method is close to the known amplitude of the NCAT phantom motion under 3 cm as shown in Fig 4.2.18, which is similar to the geometric phantom amplitude estimation as displayed in Fig 4.1.43.

The appearance of the two small lesions high in the lungs was not significantly improved by correction with GSC since the lesion motion compensation depends on lesion location and

size[32]. The two lesions placed at the upper lobe of lungs were of smaller size compared with the lesion located between lung and liver as specified in Table 4.4. Normally, the upper part of the lungs does not display motion as significant as the lower part of the lungs during respiration. Therefore the upper lesions were not improved by motion correction as much as the lower lesion. In addition, the upper lesions size (10mm, 12mm) was not as big as the lower lesion (15mm) as a result no significant improvement is observed as it suffers from significant partial volume effects[86]. This partial volume effect was partially reduced by considering a smaller voxels size in the reconstructed image.

4.2.4 Summary

A combination of GATE and NCAT to simulate a more realistic respiratory motion was used to validate GSG and GSC methods for motion gating and motion correction. The sorted frame events graphs have a similar sinusoid shape to the graph of lung volume change which is strong evidence that the change of frame events is associated with lung volume change. The simulation results with and without attenuation modelling demonstrate that GSG and GSC are able to respectively gate and correct respiratory motion along z axis.

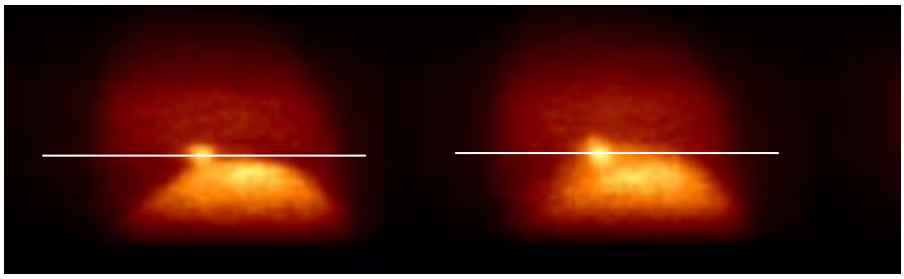

(a). Sagittal view of static

(b). Sagittal view of summed.

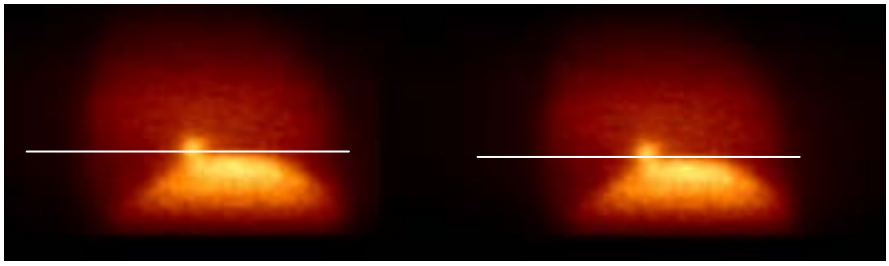

(c). Sagittal view of corrected with GSC+Prior

(d) . Sagittal view of corrected with GSC+COM

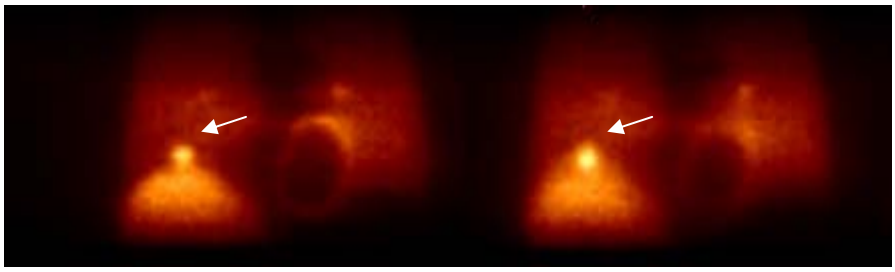

(e). Coronal view of static

(f). Coronal view of summed

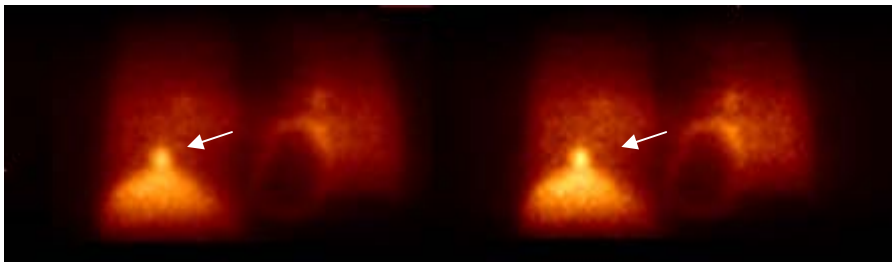

(g). Coronal view of corrected with GSC+Prior

(h). Coronal view of corrected with GSC+COM

Fig. 4.2.15. Motion correction with lesions and non-attenuation modeling. A comparison of reconstructed images of the summed and the corrected 15 frames in sagittal and coronal respectively. The white arrows indicate that the spatial resolution degradation on heart and lesion is reduced by GSC method compared to the summed reconstruction.

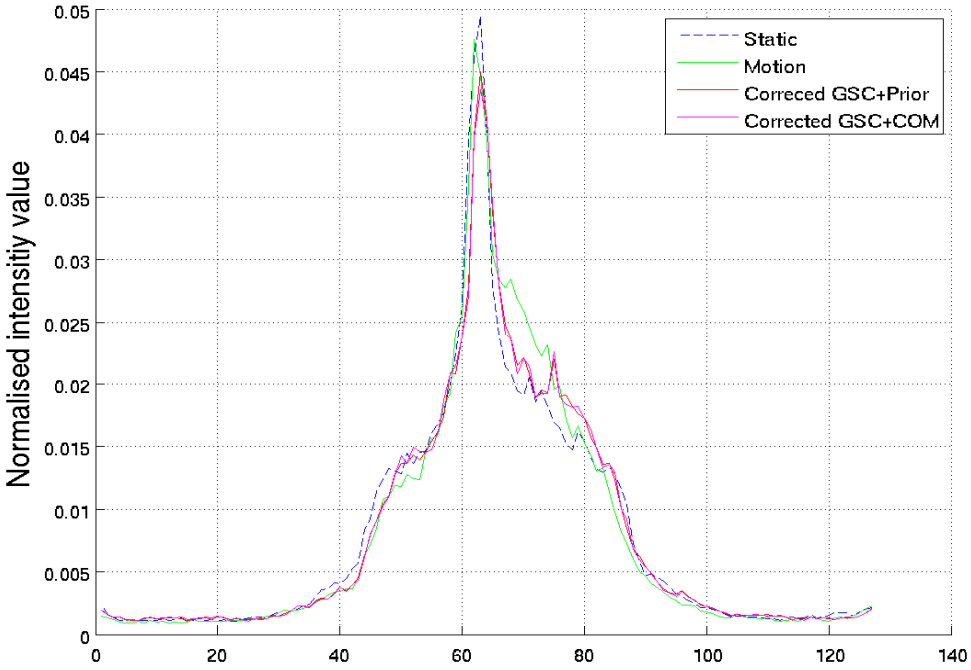

Fig. 4.2.16. Comparison of the normalized line profile from the static, the summed, the corrected by GSC+Prior and the corrected by GSC+COM in Fig 4.2.14 reconstructed images as marked in yellow line in sagittal view. The corrected line profile demonstrates an improved spatial contrast.

Table. 4.6.
Comparison of FWHM between the static, the motion and the corrected images by GSG for Fig.4.2.15, the corrected by GSC+Prior and GSC+COM image have the smallest difference, only 1 voxel from the static phantom.

Motion amplitude (cm)	**Motion states**	**FWHM voxels number**	**Difference to the static phantom (voxel)**
2	Static	2.5	0
	Motion	6	3.5
	Corrected by GSC+Prior	3.5	1
	Corrected by GSC+COM	3.5	1

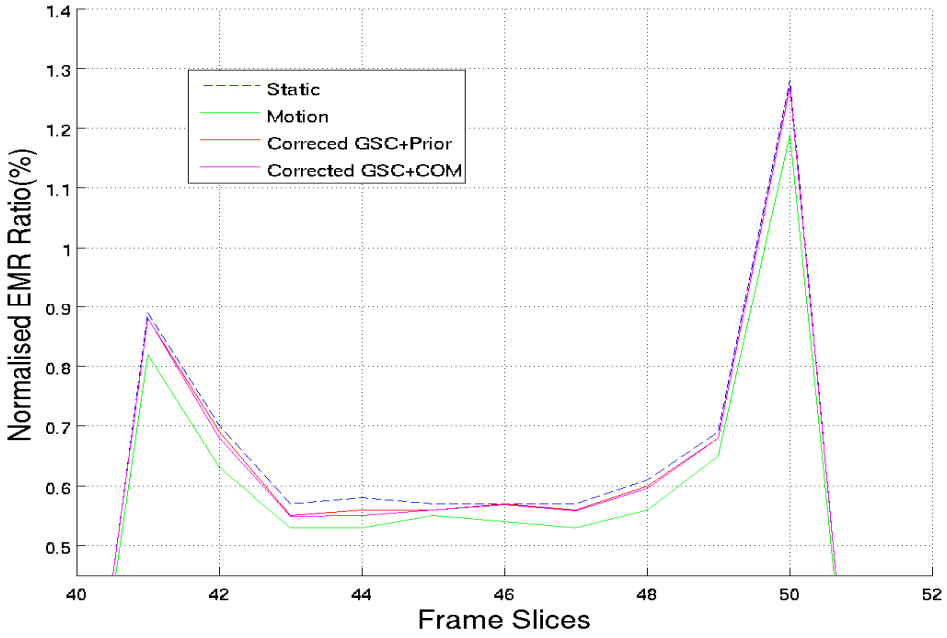

Fig. 4.2.17. Comparison of the normalized EMR values for the static, the summed and the gated in Fig 4.2.14, the gated EMR for GSC+Prior and GSC+COM demonstrate an improvement.

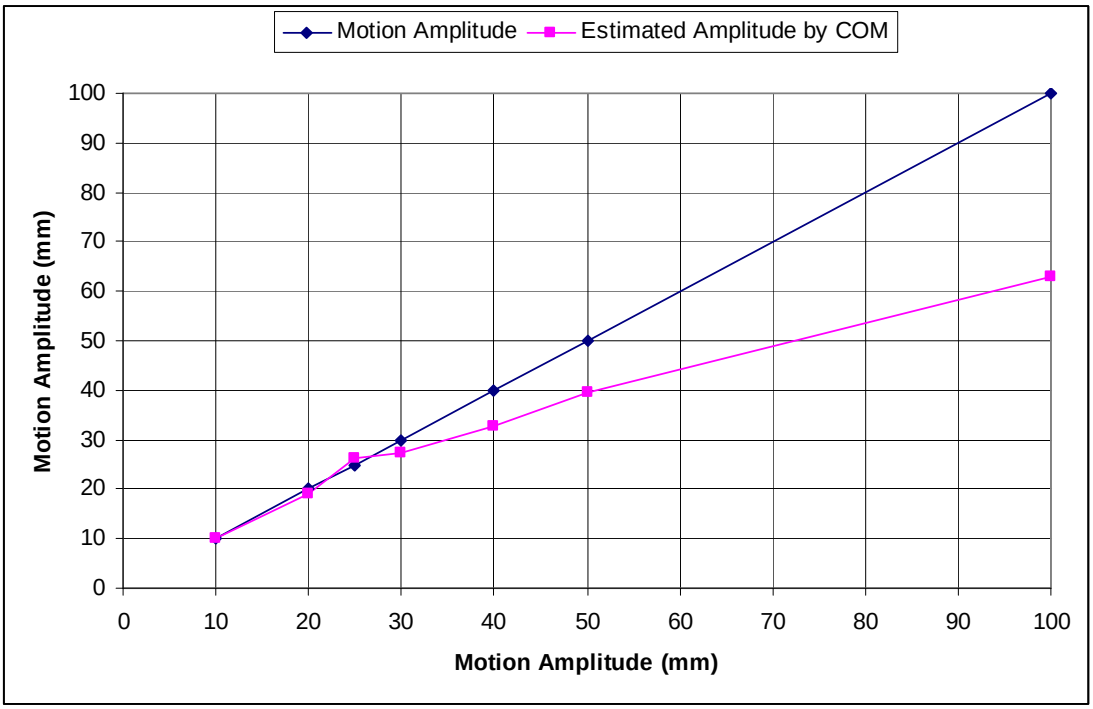

Fig. 4.2.18. NCAT phantom motion amplitude estimated by COM. Comparison of real motion amplitudes with amplitudes estimated by COM, the estimated amplitude values show a good agreement with phantom motion under 3 cm.

4.3 Clinical Validation

4.3.1 Introduction

The proposed GSG and GSC methods have been validated against phantom studies as described in Chapter 4.1 and Chapter 4.2. As a practical application of these methods, GSG and GSC need to be evaluated using clinical patient data including the cases with and without a tumour. For respiratory motion compensation in the clinical setting, the problem is more complex than phantom simulations since the respiratory cycle usually involves irregular breathing and other organ motion effects such as heart beating, liver or environmental background noise effect. As a result, the acquisition data contains a broad frequency spectrum which affects the implementation of motion compensation. In order to extract a respiratory motion signal from a real clinical study, the acquired list-mode stream data were sorted into dynamic frames and then band pass filtered in the frequency range of interest prior to GSG and GSC being applied for validation. It will be seen that clinical validation of GSG and GSC has one additional step of filtration for noise compared with the validation on the geometric and voxelised phantom, otherwise the procedure of validation is same.

4.3.2 Validation Procedure

4.3.2.1 Patient Scanned with and without-Tumor

Patients were scanned on Philips Allegro PET or Philips Gemini PET/CT for the purpose of validation of GSG or GSC respectively.

For the validation of GSG, a patient identified as P1 without a tumour was scanned on a Philips Allegro PET scanner once time. The patient was injected with 381.5 MBq ^{18}F-FDG and scanned

at 45 minutes post-injection with a standard clinical frame-mode protocol. Upon completion of the clinical scan, the patient was repositioned and scanned for a single bed position using a list-mode acquisition protocol. The list-mode scan consisted of a single 300 second, single-bed position (18cm/bed-position) emission scan from the lung to liver and was accompanied by a 23-sec transmission scan.

For the validation of GSC, the scanned collected data patient P1 from Allegro PET was used. Another dataset for a patient identified as P2 with a tumour identified in the lung region was collected on the Gemini PET/CT. As with P1 381.5 MBq ^{18}F-FDG was injected and the patient was scanned at 45 minutes post-injection with a standard frame -mode protocol. A 180 second list-mode stream of data was acquired at a single-bed position (18cm/bed-position) from the lung to liver.

4.3.2.2 Sorted List-Mode Data

The ‘sort’ of clinical list-mode data into dynamic frames is similar to the ‘sort’ of geometric simulation as specified in Fig 4.3.1. For the validation of GSG on the patient P1, the list-mode data was acquired and sorted into 1500 frames, 200 msec per frame. The graph of frame events versus frame number is illustrated in Fig. 4.3.2.

For the validation of GSC, the acquired list-mode data stream of P1 was sorted into 1000 frames with 300msec per frame. The list-mode data for P2 was sorted into 360 frames with 500msec per frame. The graph of frame events versus frame number for P2 is shown in Fig 4.3.3.

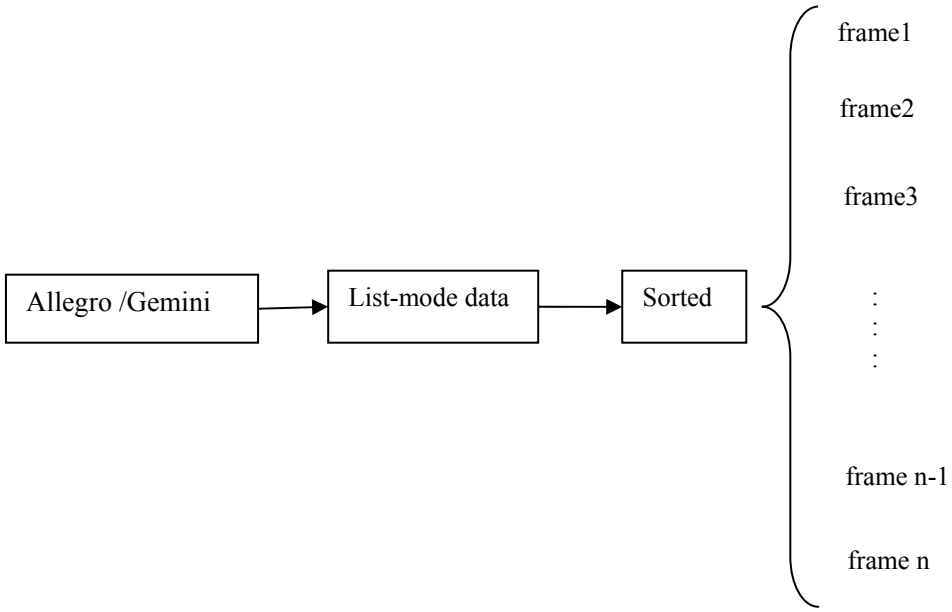

Fig. 4.3.1 Sort of List-mode data into the sequence of frames. List-mode data was acquired on Allegro/Gemini,and then was sorted into the sequence of frames with certain duration frame time.

4.3.2.3 Filter Noise in List-Mode Data

In a realistic situation, as there are more complex motion components resulting from irregular respiratory motion, cardiac motion and patient movement [135],a filter technique needs to be utilized prior to the application of GSG and GSC to the frame counts from the sorted list-mode data. To filter out signal components not related to respiratory motion, the temporal frame counts plot needs to be transferred into frequency domain to inspect what is the range of breathing cycle in the Power Spectral Distribution (PSD) of frame events so that the band-pass of filter required can be determined.

In the frequency domain, the frequency component of respiratory motion is clearly evident in the PSD figures as shown in Fig 4.3.4 and Fig 4.3.6. In order to allow robust phase detection, a band-pass filter was applied to the frame-event-rate versus time distribution emphasize the respiratory motion with 0.1Hz-0.3Hz and 0.2Hz -0.3Hz for P1 and P2 respectively as shown in

Fig 4.3.5 and Fig 4.3.7. Importantly, the data are filtered in the forward and reverse direction so as to the eliminate phase-shift effects induced by the filtering function.

4.3.2.4 Motion Gating and Correction

For motion gating, the GSG method was applied to the filtered list-mode data of P1. In this clinical study, the emission coincidence rate was 226 kcps, with 57 million prompt events collected within 300 seconds and resulting in 2 million gated events. The validation of motion correction (the GSC method) was tested on the sorted list-mode data of P1 and P2 respectively, with 34.6 million LORs collected within 180 seconds for P2.

In the reconstructed images, both GSG and GSC applied to patients were reconstructed by the PURE software. The attenuation correction by PURE was performed on P1 and P2 by using the water coefficient map as a uniform attenuation correction instead of a real attenuation correction, because the attenuation map file of PURE software package in its current format is not compatible with the transmission map format provided by Allegro/Gemini PET[133]. As a result of these limitations in PURE, the image quality of the reconstructed image provided by PURE will not be as good as the image quality reconstructed by Allegro/Gemini with attenuation correction by using transmission scans or the CT image. This thesis does, however, demonstrate the feasibility of the use of data-driven GSG and GSC to gate and correct respiratory motion in clinical studies.

4.3.3 Results and Discussion

4.3.3.1 Frame Events in Time Domain

The graphs of unfiltered frame events against frame number for P1 and P2 were plotted and displayed in Fig. 4.3.2 and Fig. 4.3.3 respectively. Comparing the two graphs, Fig 4.3.2 shows clear cyclic characteristics with 8 peaks over 40 seconds (8 breathing cycles) because the P1 is a patient without tumor. Patient P1's breathing seems to be more regular compared with patient P2

as illustrated in Fig 4.3.3. However, the two graphs obviously contain some noise making respiratory cycles ambiguous, but it can be seen that the frame events curves appear to track a cyclic waveform with a frequency close to the respiratory rate, therefore it is necessary to perform filtering on them.

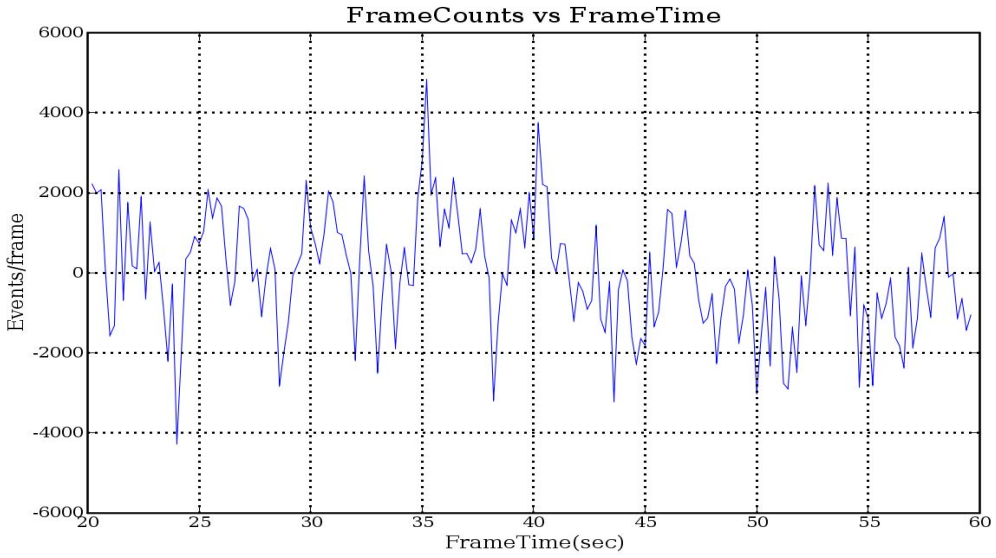

Fig. 4.3.2. Graph of mean value corrected frame events for a non-tumour patient numbered P1, LOR events of the measured raw frames per 0.2 sec from list-mode data. Baseline drift over 60 seconds is evident. The graph shows some peaks corresponding to 8 respiratory cycles.

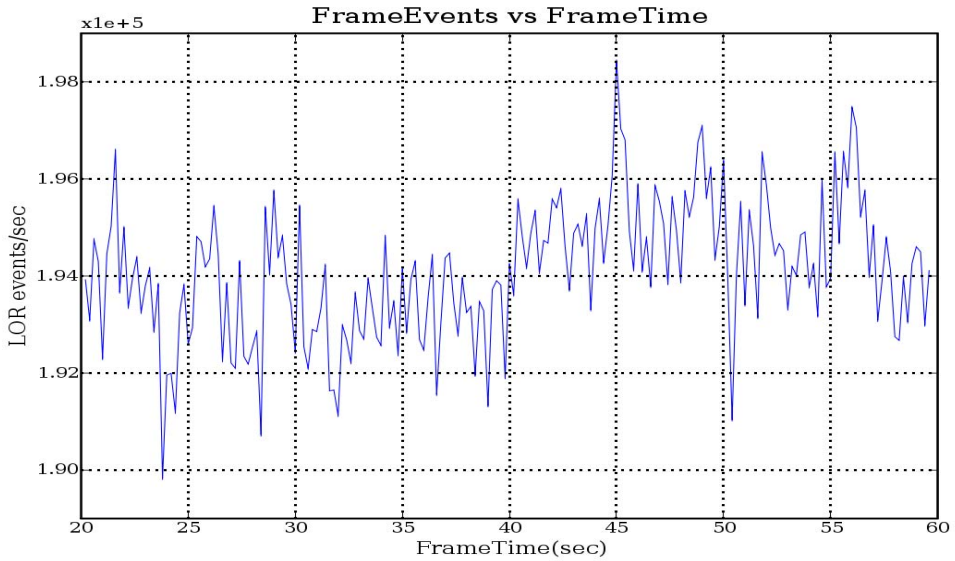

Fig. 4.3.3. The graph of frame events against frame number for tumour patient numbered P2, LOR events of the measured raw frames per 0.5 sec from list-mode data. Baseline drift over 60 seconds is evident. The graph shows some peaks corresponding to respiratory cycles.

4.3.3.2 Frame Events in Frequency Domain

In reality, the respiratory motion position, amplitude and period lengths vary with time and from patient to patient. This breath-to-breath and person-to-person variability and, in general, respiratory motion variability of additional frequency components may be attributed to various sources, such as heart beating, relative anatomic variations, and pulmonary activities[40]. It has also been shown that respiratory motion changes with age and is more regular in younger healthy adults [40]. As depicted in Fig. 4.3.2 and Fig. 4.3.3, the feature of breathing cycle, whilst clearly observable, is confounded by additional high- and low-frequency components. Computation of the spectrum using a Fast Fourier Transform (FFT) reveals the evidence of these additional terms in the PSD plot shown in Fig. 4.3.4 and Fig. 4.3.6 which contain a signal not only at the respiratory rate, but also a strong component due to the heartbeat. For example, Fig. 4.3.4 shows clearly the respiratory component in 0.16 – 0.2 Hz and additionally, a strong component due to the heartbeat in 0.75 – 1.16 Hz. Fig. 4.3.6 indicates the frequency component of respiratory motion at 0.25 Hz.

The noisy nature of the waveform is therefore due to statistical fluctuations as well as to translations of the heart during the cardiac contraction. The noise and the cardiac contraction generally occurs at a higher frequency than does the respiratory cycle, their effects on the sorted list-mode data may be reduced by using a band-pass filter. Assuming that the patient's tidal breathing cycle is around 5 seconds, in order to extract breathing frequency of LOR events of frames, the sorted data was filtered with a 2^{nd} order Butterworth filter for P1 with a band-pass of 0.10 to 0.30 Hz, a high band-stop of 0.05 and 0.40 Hz as illustrated in Fig. 4.3.5, which means that in frequency domain, respiratory motion frequency in range of 0.10 Hz ~ 0.30 Hz will be allowed to pass the filter, while high frequencies such as that of the heart beating or noise > 0.40 Hz or low frequency < 0.05 Hz will be attenuated by the filter. These smoothing operations reduce the high frequency components due to the cardiac cycle and noise, but retain a waveform more representative of respiratory motion.

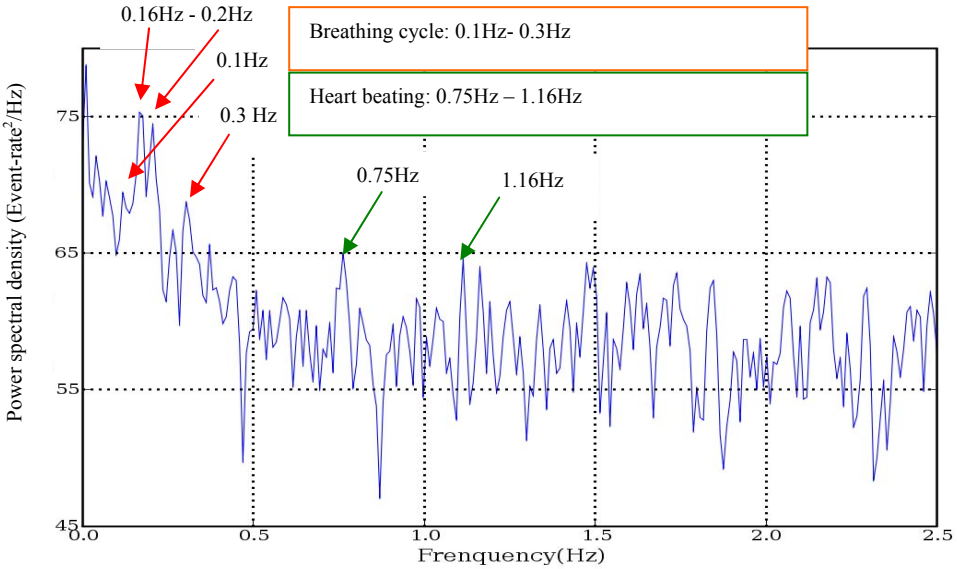

Fig. 4.3.4. The Power Spectral Distribution of frame event rate for the patient numbered P1 demonstrates several distinct frequencies, respiratory and cardiac features are indicated by red and green arrows respectively.

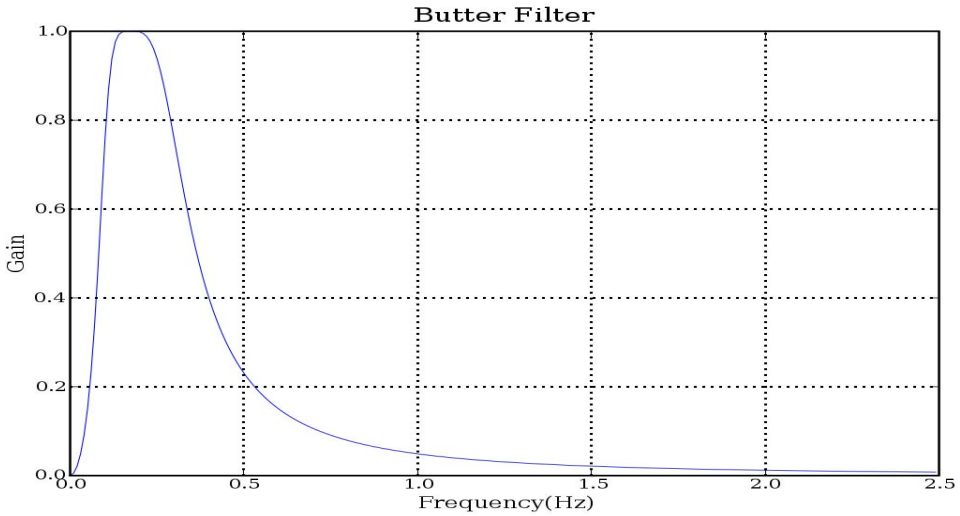

Fig. 4.3.5. Butterworth filter with a 2nd order for P1 and P2 with low band-pass 0.1Hz – 0.3 Hz.

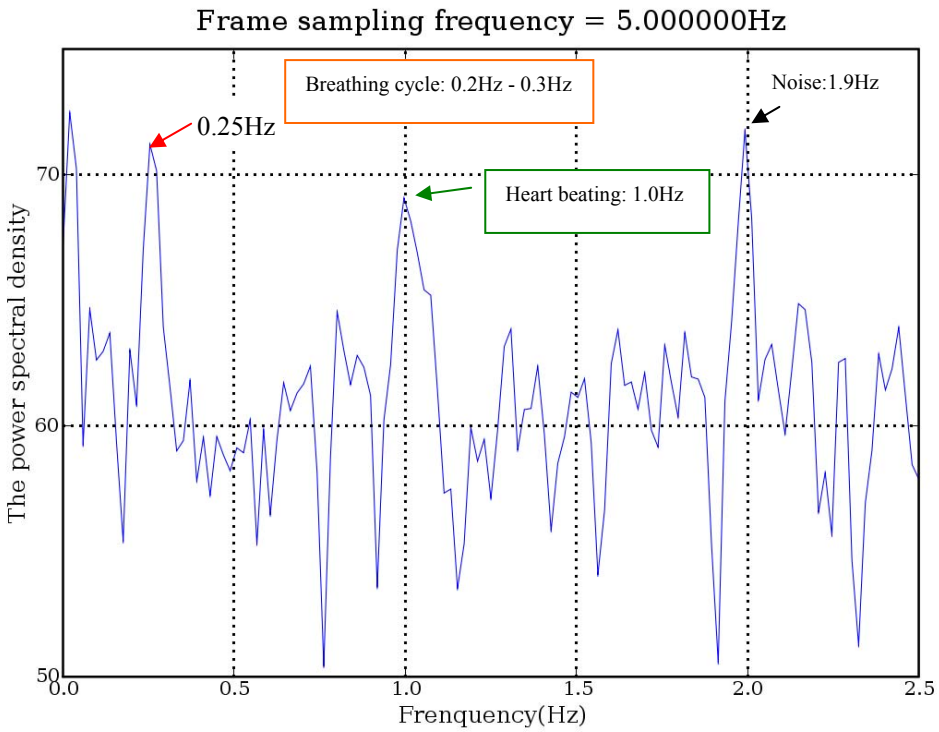

Fig. 4.3.6. The Power Spectral Distribution of Event Rate for P2 demonstrates several distinct frequencies; respiratory, cardiac and noise features are indicated by red, green and black arrows respectively.

4.3.3.3 Filtered Frame Events

Fig.4.3.7 and Fig. 4.3.9 show the results of the filtered frame events. It is clear that the filtered frame events not only fit well with the measured unfiltered frame events as illustrated in Fig. 4.3.8 and Fig. 4.3.10, but also that the noise is significantly reduced thereby allowing unambiguous extraction of the gating and correction phase. Despite the waveform being not completely a sinusoid curve due to irregularly breathing, we can see verification that the result of the filter operation is a waveform indicative of respiratory motion. Filtered curves demonstrate a cyclic change in frame-events throughout the study progression. From previous modelling and simulation, this is attributed to a change in axial position of the thoracic volume, relative to the scanner. With the methods of GSG and GSC investigated in the simulation studies, gating frames and correction of frames were determined from the filtered data. Frames corresponding to peak count rates on the filtered data were selected and then summed as a gated frame for the

reconstruction image.

For example, Fig 4.3.7 for P1 shows clear cyclic characteristics with 6 peaks over 60s seconds (8 breathing cycles). The phase of each cycle is then determined based on the peak of frame events 8 frams, and then summed as a gated frame for reconstruction.

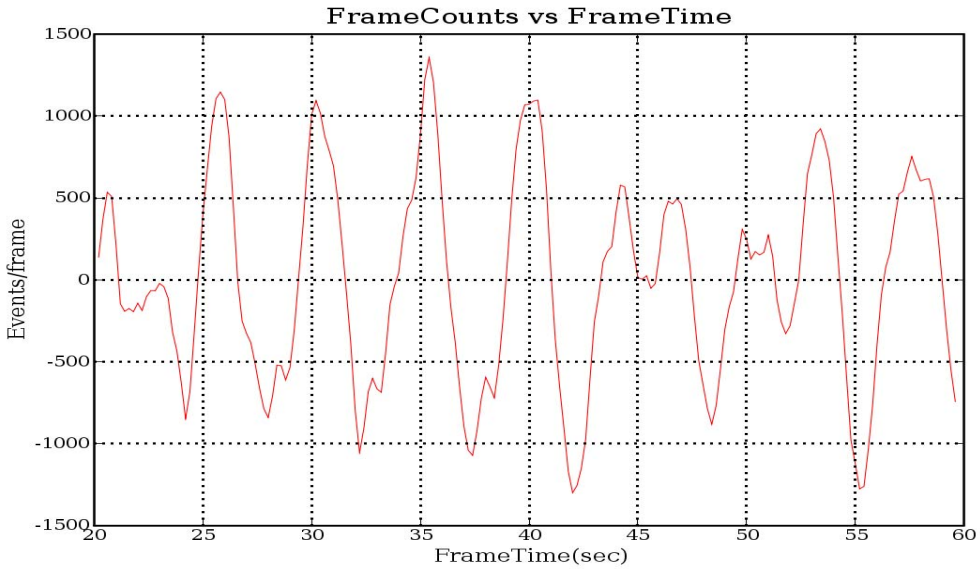

Fig. 4.3.7. Band pass filter of frame events (0.1 Hz – 0.3 Hz) for P1. The graph shows the filtered distribution with less high frequency contribution.

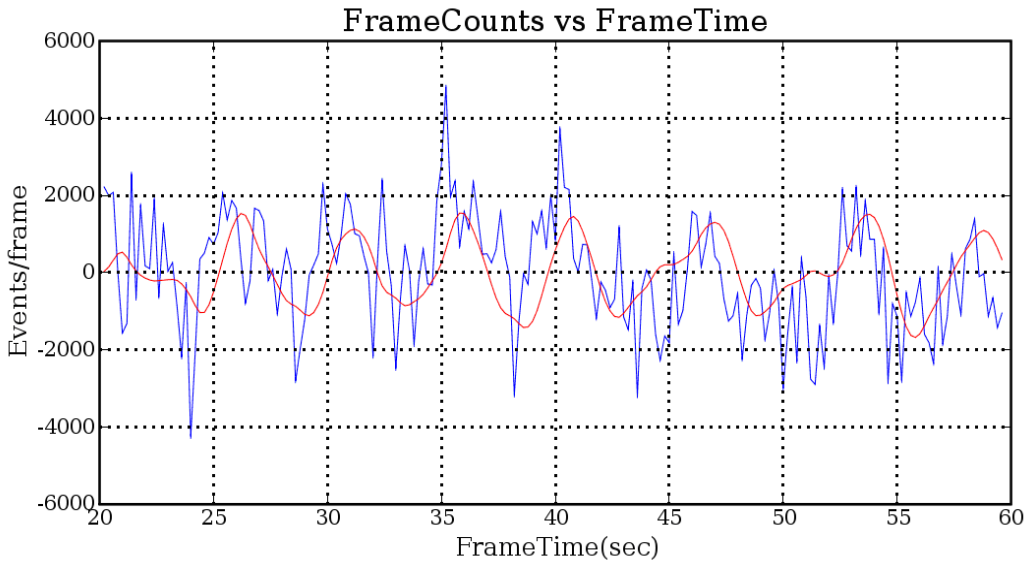

Fig. 4.3.8. Band pass filter of frame events graph for P1. The graph shows the filtered data in red as a representation of the respiratory motion component of the non-filtered in blue events per frame data. It is clear that the filtered frame events fit well with the measured unfiltered frame events.

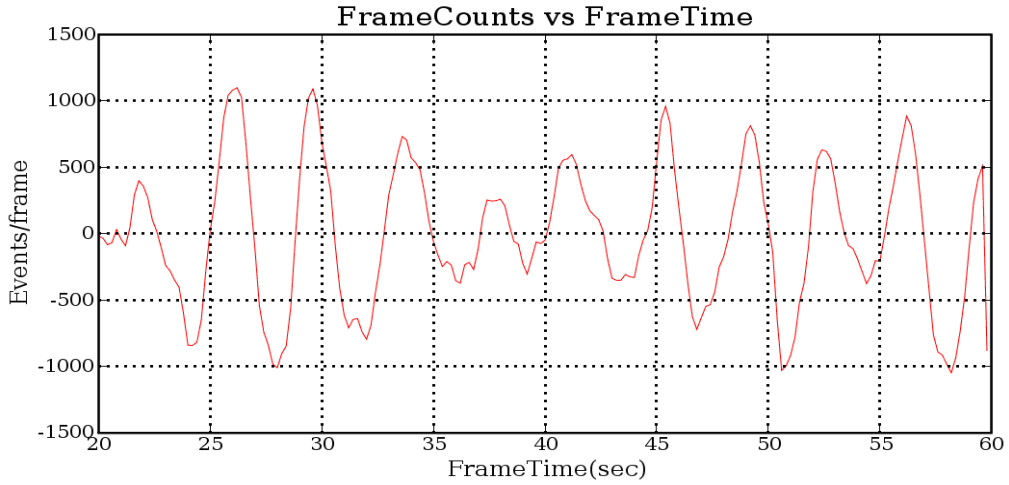

Fig. 4.3.9. Band pass filter of frame events (0.1 Hz – 0.3 Hz) for P2. The graph shows the filtered smoothly with less component of high frequency. It is clear that the filtered frame events fit well with the measured unfiltered frame events.

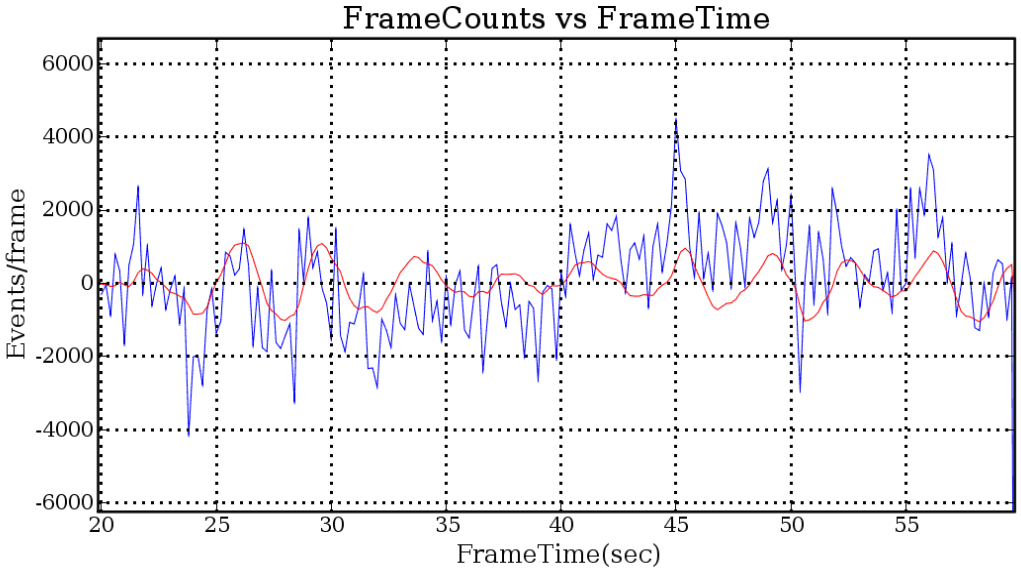

Fig. 4.3.10. Band pass filter of frame events for P2. The graph shows the filtered in red fits well the non-filtered in blue.

4.3.3.4 Motion Gating

A comparison of the summed image with 1500 frames (200 msec per frame) and the 46 gated-frame image obtained by the GSG method applied on non-tumour patient P1 is illustrated in Fig. 4.3.11(a) and (b). Despite the increased noise of the gated-frame image compared to the summed image Fig. 4.3.11(a) and (b), the gated-image has less motion artifact as illustrated in Fig. 4.3.11(b) which compares the z-axis line profile of the summed image and the gated image as shown in Fig.4.3.12. The gated profile demonstrates a higher peak-to-valley ratio and a fast roll off. which is evidence of gating improving spatial resolution compared to the image reconstructed without gating. In addition, in Fig 4.3.13 shows the gated EMR values of the liver-lung are higher than the summed EMR values, which means the edge between the liver and lung is better resolved after gating by the GSG method.

(a) Reconstructed image of the summed 1500 frames at sagittal

(b) Reconstructed image of the gated 46 frames at sagittal

Fig. 4.3.11. Comparison of reconstructed the summed and the gated for P1 by GSG at sagittal plane. Green lines indicate line profile.

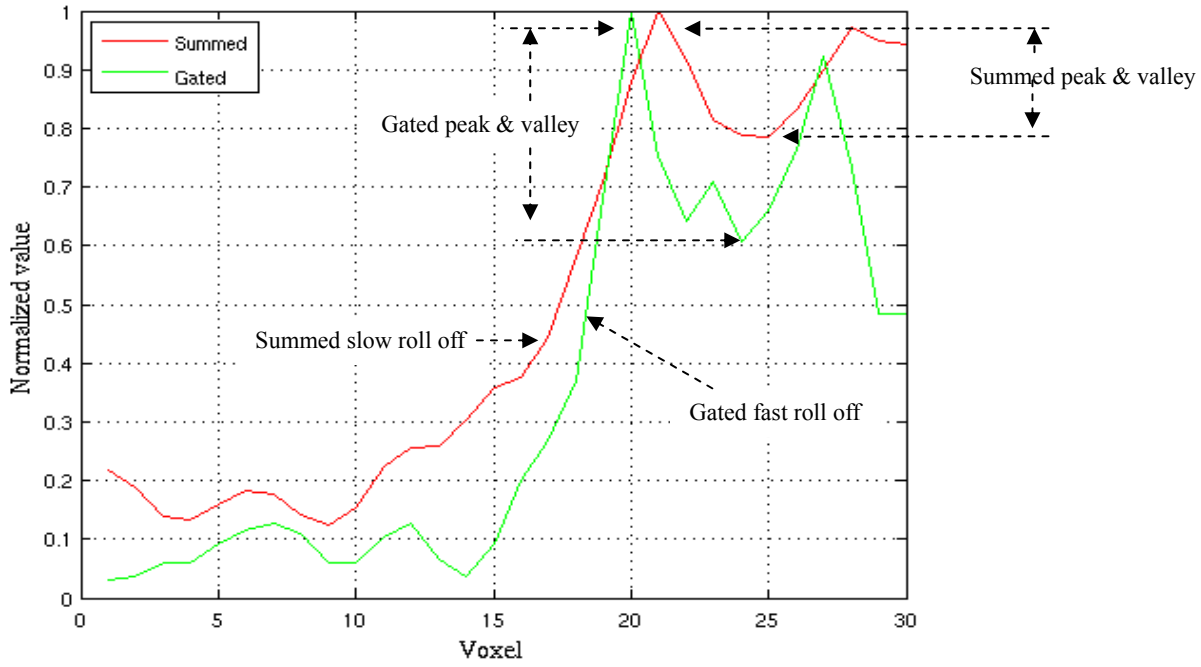

Fig. 4.3.12. Comparison of line profile from the summed Fig 4.3.11(a) and the gated Fig 4.3.11(b) reconstructed images for P1 in sagittal view. The gated line profile with a deeper valley and faster roll off than the summed demonstrates an improved spatial contrast.

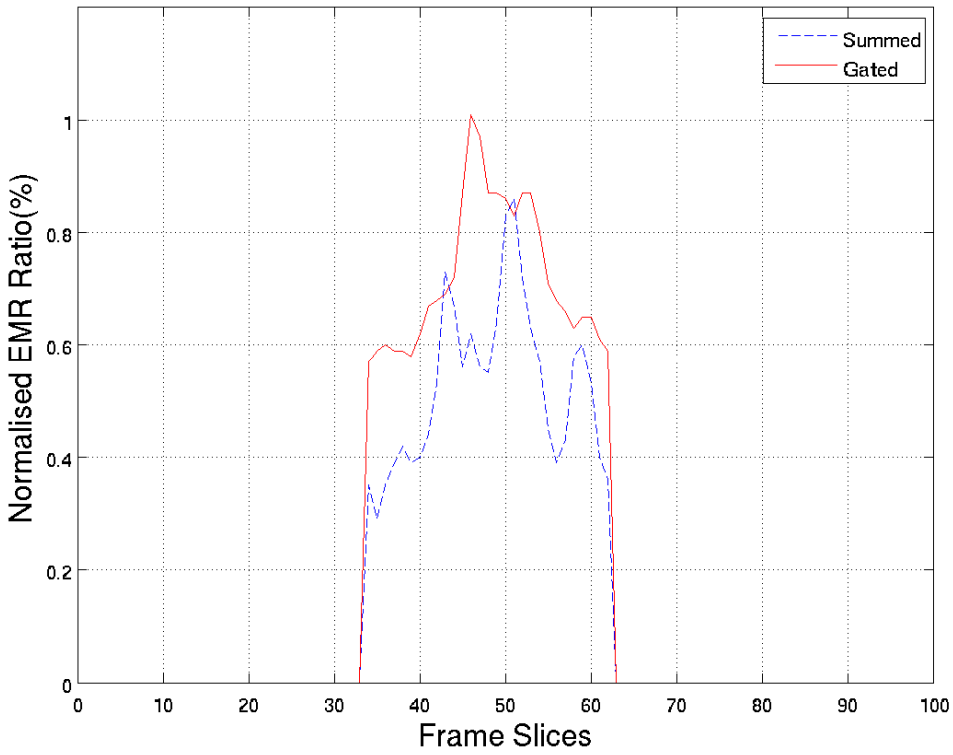

Fig. 4.3.13. Comparison of the normalized EMR values of the liver-lung region for the summed and the gated in Fig 4.3.11, the gated EMR values demonstrate an improved spatial contrast in the edge of lung and liver.

4.3.3.5 Motion Correction

The GSC+COM method described in section 3.5 and used for the simulation results in sections 4.1.3.3 and 4.2.3.3 for motion correction will be applied to the filtered clinical patient data with and without tumour. Since the respiratory motion amplitude is not known prior to correcting motion, it is necessary to estimate the motion amplitude by the COM method. This method has been demonstrated to be able to accurately estimate the respiratory motion under 3 cm amplitude according to the results presented in the sections 4.1 and 4.2, and in the literature on the COM method [69, 73, 74]. After estimation of motion amplitude for P1 and P2 by the COM method, axial displacements were determined for each respiratory phase. All frames were translated into the reference frame, and then summed as a corrected dataset for the reconstruction image.

The GSC+COM method was applied to patients P1 and P2 for validation of the motion correction. All the results of the summed and the corrected images were reconstructed by PURE with uniform water attenuation correction maps. The GSC+COM corrected result for the non-tumour P1 case is shown in Fig. 4.3.14 and Fig. 4.3.15. The summed image (Fig. 4.3.14(a)) displays more smoothing in the transverse view than the contrast corrected image (Fig. 4.3.14(b)) best seen at the edge of the lungs. Despite the effect of correction being not obvious visually as depicted in Fig. 4.3.14(b), the line profile of the reconstructed images do reflect some of the effects of the correction in spatial intensity between the summed and the corrected image as shown in Fig. 4.3.15. The summed image has 45 voxels at FWHM, while the corrected image has 41 voxels at FWHM. This reduction by four voxels in the FWHM by the GSC+COM method demonstrates the summed image quality being improved upon with the higher peak to valley ratio as shown in Fig 4.3.15. In addition, the corrected EMR ratio values indicate an increased magnitude in the edge of lungs as illustrated in Fig 4.3.16, which means the corrected edge of lungs is clearer than in the summed image.

Patient P2 with a tumour in the lung was corrected by GSC+COM as shown in Fig. 4.3.17 and Fig 4.3.18. In the comparison of the summed and the corrected images in the coronal view, the

respiratory bluring in the region of the tumour in the summed image (Fig. 4.3.17) has been clearly minimized in the GSC+COM image shown in Fig. 4.3.18. In addition, line profile of the summed and the corrected images as revealed in Fig 4.3.19 indicates that image quality was improved, as evidenced by the summed image with 7 voxels FWHM being reduced to 3 voxels at FWHM in the corrected image. A sharper imaging of the edge of the tumour was also demonstrated by the plot of EMR ratio values as indicated in Fig 4.3.20, which shows the corrected image EMR values being bigger than the summed image.

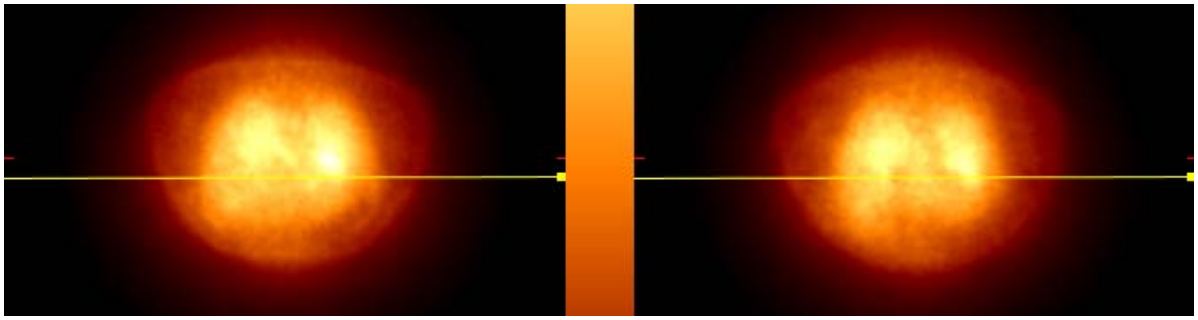

(a) Reconstructed image of the summed 1000 frames in transverse view.

(b) Reconstructed image of the corrected 1000 frames in transverse view.

Fig. 4.3.14. Comparison of the reconstructed summed (a) and corrected (b) images in transverse view for P1.

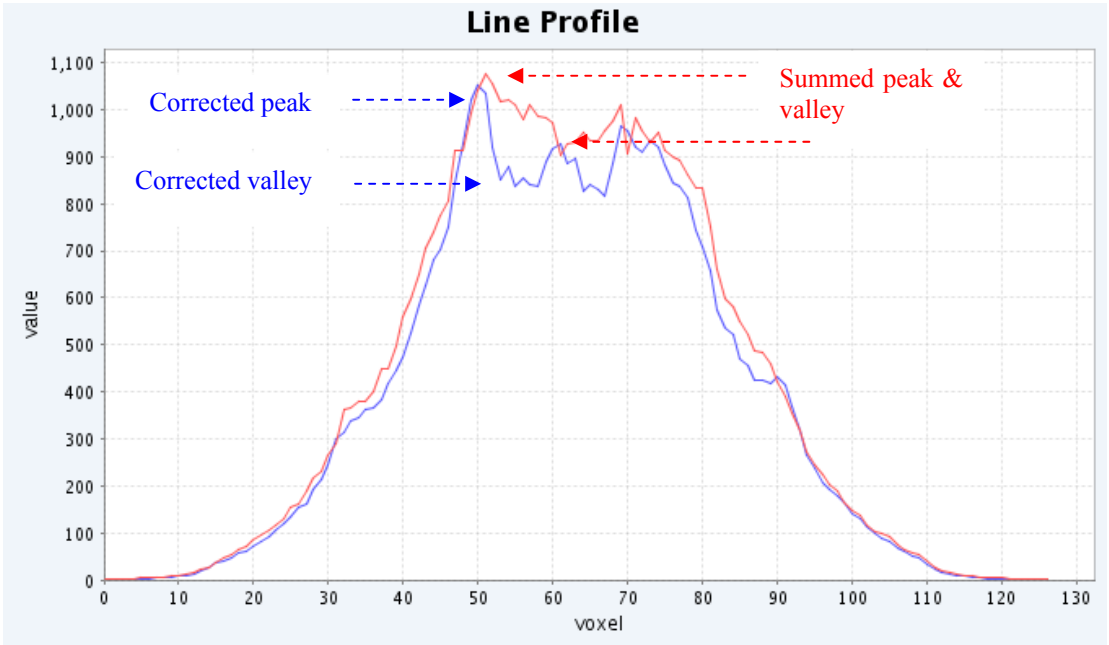

Fig. 4.3.15. Comparison of line profile from the summed Fig 4.3.14(a) and the corrected Fig 4.3.14(b) images at transverse view for P1. The gated line profile demonstrates an improved spatial contrast.

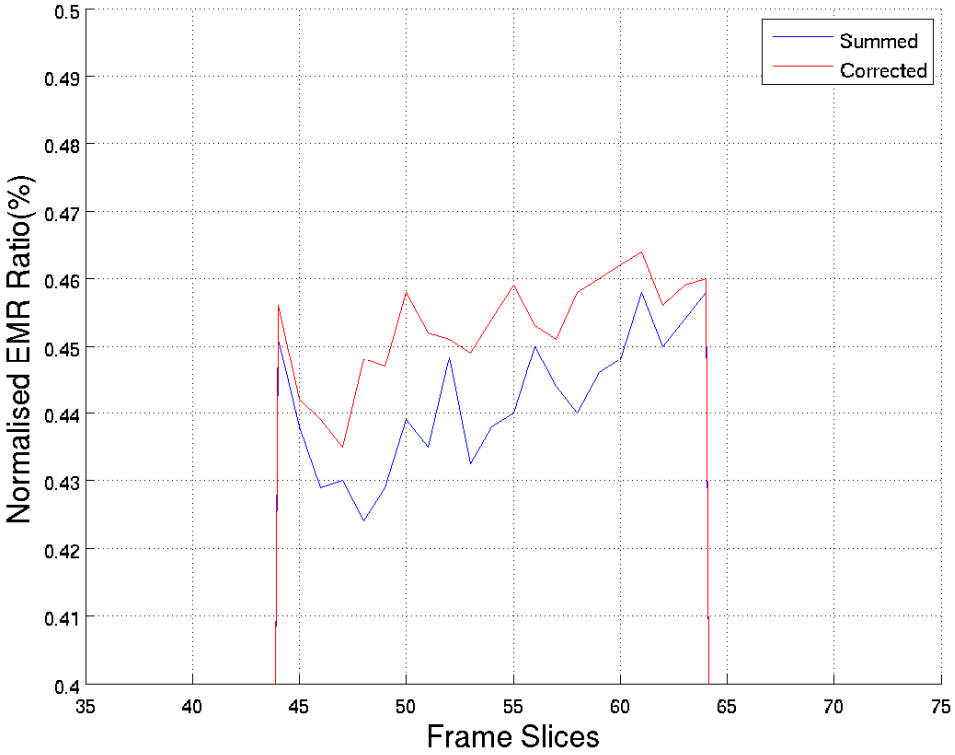

Fig. 4.3.16. Comparison of the normalized EMR values for the summed and the gated in Fig 4.3.14, the gated EMR demonstrate an improved spatial contrast.

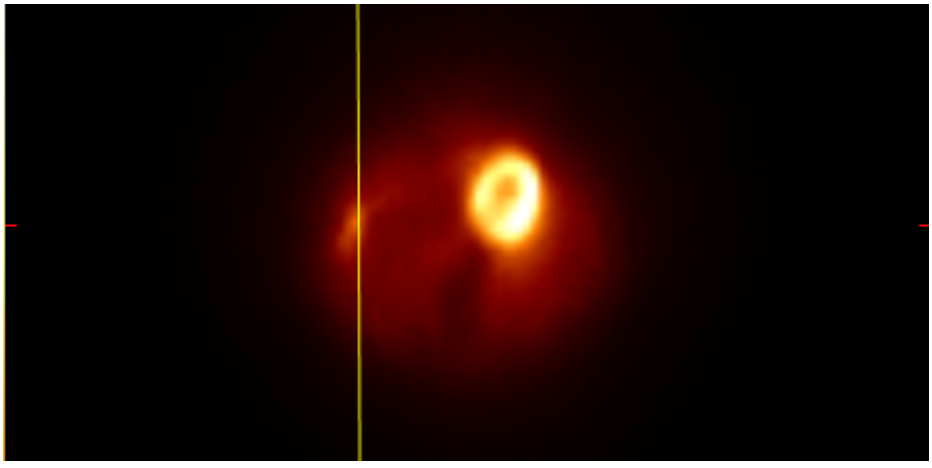

Fig. 4.3.17. The reconstructed summed 360 frames in transaxial view for P2.

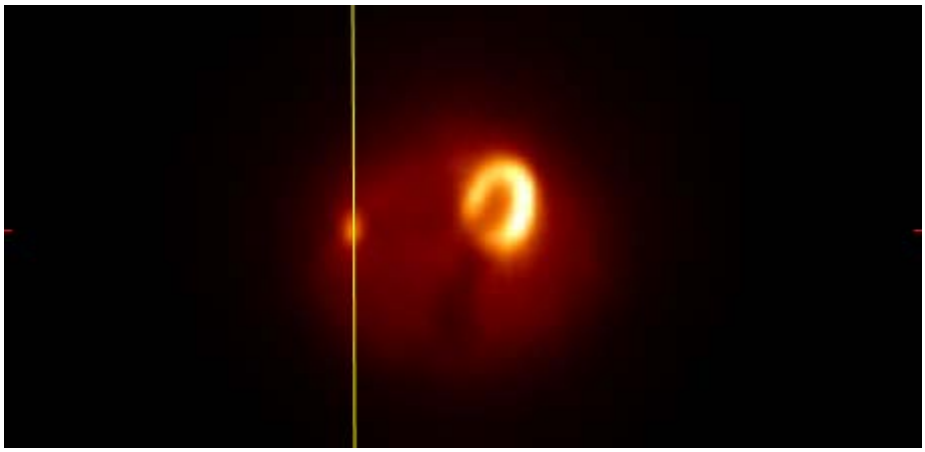

Fig. 4.3.18. The reconstructed corrected 360 frames in transaxial view for P2 by GSC+COM

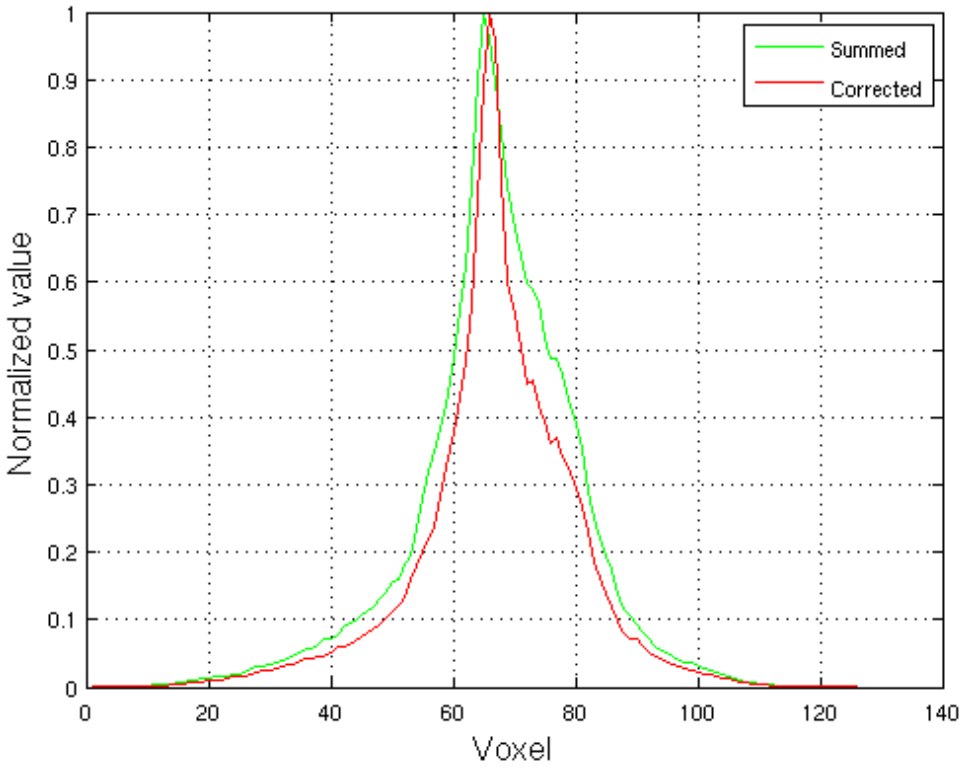

Fig. 4.3.19. Comparison of line profile from the summed Fig 4.3.17 and the corrected Fig 4.3.18 reconstructed images in coronal view for P2. The gated line profile demonstrates an improved spatial resolution.

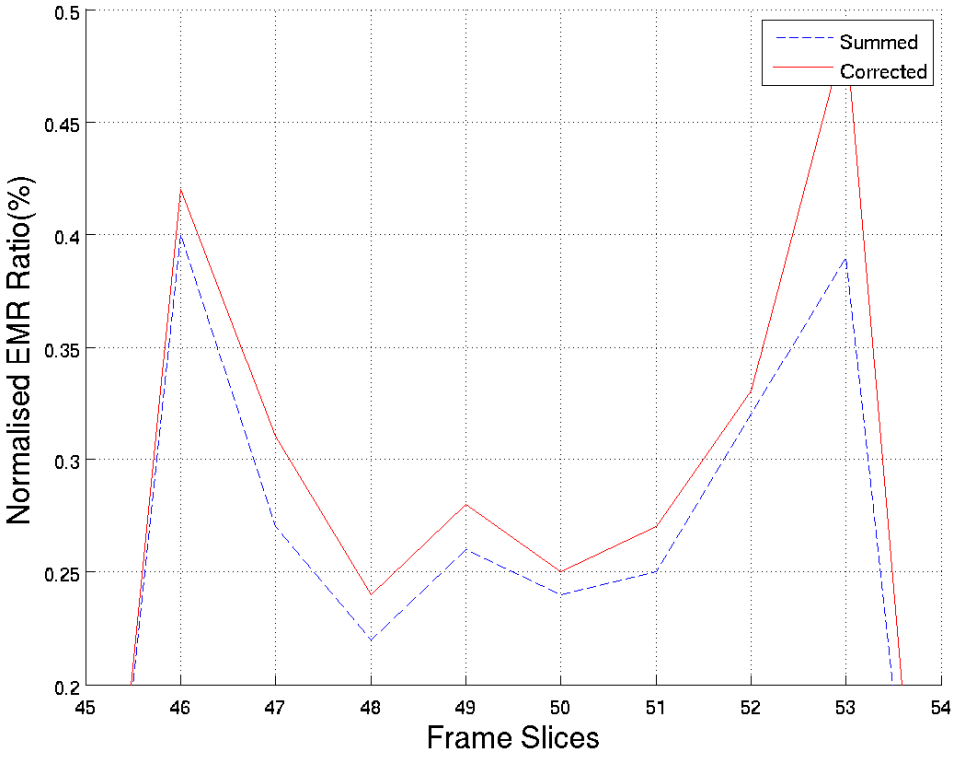

Fig. 4.3.20. Comparison of the normalized EMR values for the summed and the corrected in Fig 4.3.17 and Fig 4.3.18, the corrected EMR values demonstrate an improved in magnitude of edge.

4.3.4 Summary

Application of GSG and GSC to clinical studies is different from phantom studies due to irregular breathing and noise. As a result, the frame-event graphs plotted by clinical studies will be more complex than phantom studies, with many components in addition to respiratory motion being present in the sorted list-mode data. To extract respiratory cycles in the sorted list-mode data, LOR events of frames in time domain were transferred into frequency domain where the components of breathing cycle and noise may be highlighted in the distribution of PSD figures. Then the band-pass filter can be utilized to filter noise from the sorted list-mode data to selectively highlight respiratory motion effects.

GSG applied to a patient scan demonstrates that the gated image has less respiratory blurring than the summed image. GSC+COM was tested on two patient data sets, and the resulting

reconstructed images, the line profiles and EMR ratio values prove that the GSC+COM method is able to significantly improve the quality of image of respiratory motion.

CHAPTER

5

DISCUSSION AND CONCLUSION

5 Discussion and Conclusion

5.1 GEOMETRIC SENSITIVITY GATING 163

5.2 GEOMETRIC SENSITIVITY CORRECTION 165

5.3 STUDY LIMITATIONS AND FUTURE RESEARCH 167

5.3.1 Limitations of the methods 167

5.3.2 Further Research 172

5.4 CONCLUSION 172

5.5 MAIN CONTRIBUTIONS AND PUBLICATIONS 173

For the issue of the respiratory motion induced image degradation, a hypothesis was proposed in this thesis, which was that the non-uniform geometric sensitivity characteristic along the z axis of a 3D PET scanner could be used to detect and compensate for respiratory motion. In general, compensation for respiratory motion has two stages: gating and correction. According to the hypothesis, two specific proposals were made: GSG for the respiratory motion gating and GSC for the respiratory motion correction as described in Chapter 1.3. To test GSG and GSC, geometric and voxelised phantoms were generated by GATE and NCAT software packages respectively to simulate respiratory motion. Clinical patient data was collected, and then GSG and GSC were applied to the sorted list-mode data from both of the simulations and the clinical patient data.

This chapter evaluates the results of the validation of GSG and discusses the results of the GSC validation. The limitations of the GSG and GSC methods are identified and further development possibilities are then addressed, and concluding remarks are made.

5.1 Geometric Sensitivity Gating

Gating respiratory motion is the first step in compensating for respiratory motion. Many gating techniques have been developed as reviewed in Chapter 2. A novel data-driven method, GSG, was proposed in this thesis for respiratory motion gating. GSG was validated by simulations using geometric and voxelised phantoms and then applied to patient acquisitions.

It is posed that a variation in geometric sensitivity along the Z-axis in a 3D mode PET scanner can be utilized as a means of detecting respiratory motion. By detecting changes in the number of events per frame, a phase can be assigned to each frame which then allows a gating scheme to be implemented. Furthermore, by correcting for the motion of each phase to a reference phase, the entire data set can be utilized with the effects of motion reduced.

For the simulations of a geometric phantom with motion amplitude 10 cm, 5 cm, 2 cm and 1 cm, the temporal distribution of frame-events for static and motion phantoms are obviously different,

particularly as displayed in Fig 4.1.3 and Fig 4.1.4. The static phantom is consistent with a constant sensitivity while the motion phantom demonstrates a time-dependent sensitivity due to the change of geometric sensitivity value along the z axis, relative to the scanner. The geometric phantom described in Chapter 4.1 is only a one dimensional validation of GSG along the z axis rather than a 3D validation. However, it is a useful means to allow general evaluation and development of the GSG method.

As described in Chapter 4.2, simulations of a voxelised phantom were more realistic and complicated than the geometric simulations. A voxelised phantom with and without attenuation modelling was generated by using the NCAT software package. Voxelised simulations for respiratory motion can be regarded as 3D non-rigid motion. The plots of the change in number of frame events versus frame number as illustrated in Fig 4.2.5, Fig 4.2.6 and Fig 4.2.7, also indicate that the change of frame events is strongly position-dependent as a result of respiratory motion and the varying geometric sensitivity value along the z-axis.

With the clinical data study as described in Chapter 4.3, the graphs of frame events versus frame number were plotted as Fig 4.3.2 and Fig 4.3.3. Some cyclic characteristics of respiratory motion can be recognized from the graphs, but many other sources were present in, since clinical data produce more complex motion signatures resulting from irregular respiratory motion, cardiac motion and patient movement. If the sorted frames were transferred from the time domain to frequency domain to inspect the PSD, the range of respiratory motion is then clearly evident such as shown in Fig. 4.3.4 and Fig. 4.3.6. In order to allow robust respiratory phase detection, a band-pass filter was applied to emphasize the respiratory motion. The filtered graphs of frame events illustrate that the non-respiratory components are significant reduced, and clearer cyclic respiratory motion is observed thereby allowing extraction of the gating frames.

The frames for gating at a single respiratory phase were determined from plots of frame events versus the number of the frame. The gating frames of simulations and clinical studies correspond to the peak counts in each of the breathing cycles. Certainly, other frames may be chosen for gating, but the reason for picking the peak count frames is to get a relatively high single-to-noise

ratio in the reconstruction image as the frames contain maximum LOR numbers in each breathing cycle.

The gated summed single frame datasets were reconstructed into images of simulations and clinical studies as shown in sections 4.1.32, 4.2.32 and 4.3.3.4. Comparing the summed and the gated images, the degradation caused by the motion has been significantly reduced. For the geometric phantom with one dimensional motion, the blurring of the edge of the phantom due to oscillation has been visibly decreased. For the voxelised phantom with 3D motion, the boundary between lung and liver has become clearer, and the lesion is better resolved. For clinical studies, the dome-of-liver boundary is more clearly defined. The results of simulations and clinical studies presented in Chapter 4, demonstrate that the GSG data-driven method is able to be applied to the phantom simulations and clinical patient data.

In addition, it can be seen that an obvious increase in noise can be recognized in the gated images compared with the summed images. The noise results from the fundamental principle of the gating technique, which only makes use of a few of the available frames for gating. The GSG method is a gating technique, but developed with a novel idea. To solve the drawback of gating techniques that only apply to a single respiratory phase, another new method, GSC, was developed to correct respiratory motion by making use of all possible frames.

5.2 Geometric Sensitivity Correction

GSC utilises all frames to enhance signal-to-noise-ratio by transforming the frames to the reference respiratory phase. The estimation of transformation displacements was determined by changes in frame events relative to a reference by using the COM method. A calibration between change in frame events versus change in position was determined using the COM method. GSG and GSC have the same steps of requiring the sorted list-mode data and the plot of frame events, the only different step is that GSG uses the frame events changes for gating at a single respiratory phase, while GSC utilizes the changes to estimate the transformation along the z axis for all respiratory phase. GSC proposes a simple relationship between the change of frame events and

the displacement of respiratory phase as specified in Equation 3.3 in Chapter 3. It means that the transformation can be derived prior to image reconstruction rather than the transformation being estimated in the image space, which may avoid operator intervention. The further details are shown in Fig 3.29 in Chapter 3.

GSC was tested with simulations and clinical studies, in a similar way to the validation for the GSG method as described in Chapter 4. Simulations of geometric and voxelised phantoms were implemented for respiratory motion correction by using GATE and NCAT respectively, and two clinical patient data sets were obtained for the validation.

To simplify respiratory motion modelling, the oscillation of the geometric phantom may be regarded as an ideal simple respiratory motion along z axis. The oscillation can be used to study the transformation displacements determined for the respiratory motion. Although the oscillation is one dimensional motion, it is a cyclic motion along the z axis which can highlight two important features of respiratory motion: the periodicity of breathing and the motion along the craniocaudal direction. The results of the geometric phantom simulation demonstrate the displacements of oscillation do have a relationship with the change of frame events as illustrated in the Equation 3.3 of Chapter 3 and that these changes are detectable in clinical conditions. In addition, it can be seen that the signal to noise ratio in the corrected image has been enhanced relative to the gated image as shown by Fig 4.1.15 and Fig 4.1.33.

The GSC method was validated with the GSC+Prior method and the GSC+COM method. The GSC+Prior method exhibits a greater range of correction with motion amplitude from 10 cm to 1 cm compared with the correction of the GSC+COM method. Because GSC+Prior utilises the known phantom motion amplitude to correct motion, its accuracy of correction is perfect by definition and can be used as an indicator of the accuracy of the amplitude estimated by the COM method. This implies the accuracy of the GSC depends on the estimation of the motion amplitude. It has been shown that the accuracy of the amplitude estimated by the GSC+COM method is within statistical fluctuations of the true amplitude of the motion when the amplitude is under 3cm as shown in Fig 4.1.43 and Fig 4.2.18. Actually, the motion amplitude detection may be

implemented by many techniques as reviewed in Chapter 2, rather than only using COM method. The motivation for using the COM method in this thesis is that it is a data-driven method and therefore requires no hardware devices.

The results of the application of GSC for geometric phantom motion encouraged the extension of the method to the non-rigid motion simulated by the NCAT voxelised phantom. In comparison to the summed and the corrected images with and without attenuation, the motion artifacts surrounding the lesion were clearly diminished. This result demonstrates that GSC+Prior and GSC+COM can be applied to non-rigid respiratory motion to give an improved correction result.

To test the realistic clinical relevance of the GSC method ,the GSC+COM method was applied to the clinical data. It was necessary to filter the noise in the clinical sorted list-mode data prior to the application of the GSC+COM method. Two clinical patient data sets with and without a tumour were used to validate GSC+COM. The result of the application to the patient data indicates that the edge of the lungs in the corrected image is clearer than in the summed image due to the correction. Also, another correction result shows that the blurring of a tumour by respiratory motion in the lung was significantly reduced, compared with the summed image. These results demonstrate that the GSC+COM can be applied to both the phantom simulation and the clinical data, thereby recovering some of the image quality lost due to respiratory motion.

5.3 Study Limitations and Future Research

5.3.1 Limitations of the methods

The respiratory motion compensation technique developed in this thesis produces results which can significantly improve an image where respiratory motion artifacts or degradation are present. However, the technique is subject to limitations. In particular gating will be ineffective with non-3D mode PET scans, non-cyclic motion and radioactivity distributions for which the COM does not vary above statistical fluctuation throughout the full range of respiratory motion.

A comparison of sensitivity and axial position of 2D and 3D mode scanner shown in Fig 5.1[39].

It needs to be stated that the proposed GSG and GSC are based on the geometric sensitivity properties of 3D PET Scanners, which exhibit non-uniform (triangular) geometric sensitivity profile, not a uniform (trapezoidal) profile ast is the case for a 2D scanner (ignoring edge effects) or 3D with small ring differences such as rd = 11. If the PET scanner is operating in 2D mode, then the proposed method will not work properly due to a lack of change of frame counts. GSG may be inappropriate for 3D PET Scanners that do not accept all possible oblique LORs, for which the sensitivity profile has a central plateau. In addition, due to the variation of geometric sensitivity value being confined to the Z axis, the invariance of the geometric sensitivity with changes in position in the X and Y axis results in the GSG and GSC methods being insensitive to non-axial motion. Despite the reality that respiratory motion is 3D motion, the organ motion is largely in the axial direction, so the image quality can be significantly improved by correction along the Z axis only as the demonstrated by the results of simulations and clinical application in Chapter 4.

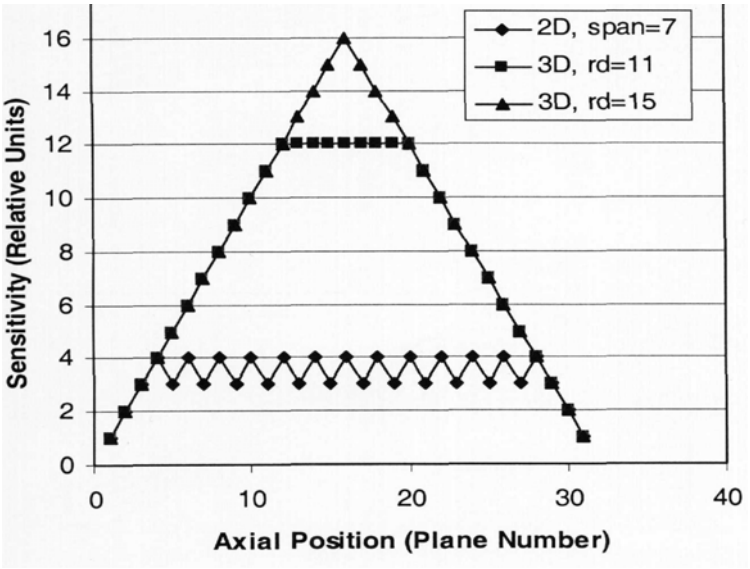

Fig. 5.1 Sensitivity and axial position for 16 rings scanner: 2D with span of 7 has low sensitivity; 3D with ring differences (rd) of 11 is central plateau sensitivity; 3D with ring differences of 15 is triangular sensitivity. GSG & GSC methods only can be applied to the 3D mode with rd = 15.

The application of GSG is limited to conditions of cyclic motion such as respiratory motion or heart beating, rather than non-repetitive motion, such as head movement or gross patient movement. The GSG takes those frames with the same level of frame events (such as peak events) from repetitive motion such as breathing cycles for gating. If the motion is non-repetitive, changes

in the number of frame events versus frame number will not be cyclic, therefore, no motion frames can be extracted to gate. However, this limitation of repetition does not apply to the GSC method as the correction transformation matrix of GSC is estimated from the change in the number of frame events without requiring the motion to be repetitive or cyclic. Equation 3.3 indicates the GSC method only involves motion amplitude and frame events.

In addition, the GSG and GSC will not work properly if the distribution of radiation does not vary above statistical fluctuation throughout the full range of respiratory motion. A specific example of this condition is shown in Fig 5.2 where the distribution of sources of radioactivity is strictly uniform within the FOV, and the motion of sources does not overrun the edge of the FOV or the transverse plane at the centre of FOV, the method will not work due to a lack of change in the total number of frame events. It can be seen that the sum of the sensitivity values does not change in the two states of motion as illustrated in Fig 5.2 (b) and Fig 5.2 (c). However, in reality, this situation is unlikely to occur as typically, an unbalanced distribution of radioactivity as shown in Fig 5.3(a) will be observed. In addition the motion of sources of radioactivity will cross over the edge of the FOV as shown in Fig 5.3(b), and/or the transverse plane at the centre of the FOV as shown in Fig 5.3(c)-(d). In these situations the method will be able to be applied as all results of simulations and clinical studies supported in this thesis.

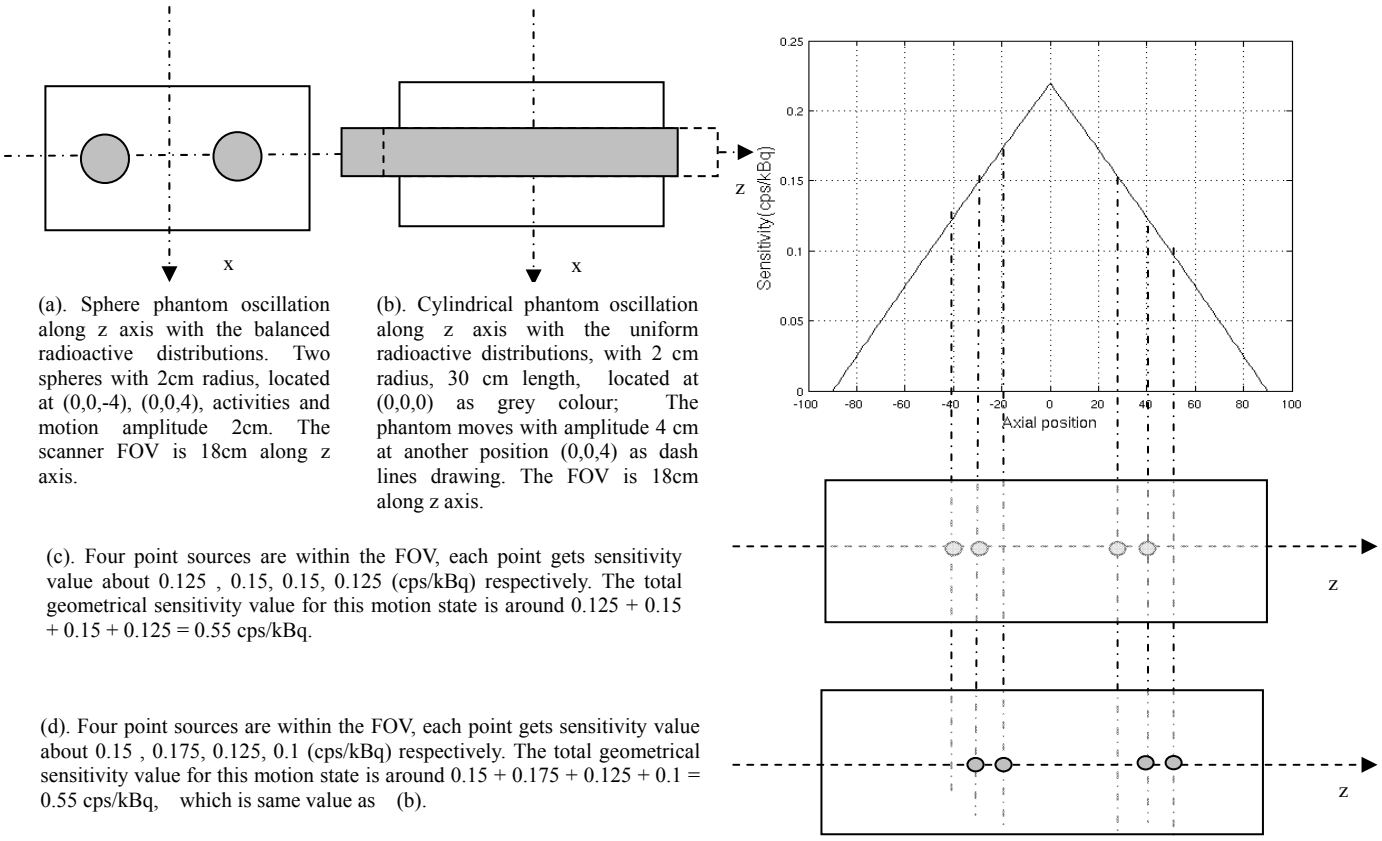

(a). Sphere phantom oscillation along z axis with the balanced radioactive distributions. Two spheres with 2cm radius, located at (0,0,-4), (0,0,4), activities and motion amplitude 2cm. The scanner FOV is 18cm along z axis.

(b). Cylindrical phantom oscillation along z axis with the uniform radioactive distributions, with 2 cm radius, 30 cm length, located at (0,0,0) as grey colour; The phantom moves with amplitude 4 cm at another position (0,0,4) as dash lines drawing. The FOV is 18cm along z axis.

(c). Four point sources are within the FOV, each point gets sensitivity value about 0.125 , 0.15, 0.15, 0.125 (cps/kBq) respectively. The total geometrical sensitivity value for this motion state is around 0.125 + 0.15 + 0.15 + 0.125 = 0.55 cps/kBq.

(d). Four point sources are within the FOV, each point gets sensitivity value about 0.15 , 0.175, 0.125, 0.1 (cps/kBq) respectively. The total geometrical sensitivity value for this motion state is around 0.15 + 0.175 + 0.125 + 0.1 = 0.55 cps/kBq, which is same value as (b).

Fig.5.2. Variation of sensitivity value of the motion of the balanced uniform radioactivity distribution along z axis within the FOV of 3D scanners as shown in (a) and (b). For example, each sphere contains two point sources in (a). Comparison of the states of motion between (c) and (d), sensitivity value in (c) is same as (d), it means that radioactivity sources move between the edge of the FOV and the transverse plane at the centre of the FOV, the sensitivity efficiency does not change such as different two motion states (c) and (d). As a result, the proposed method can not be applied to this balanced uniform radioactivity distribution.

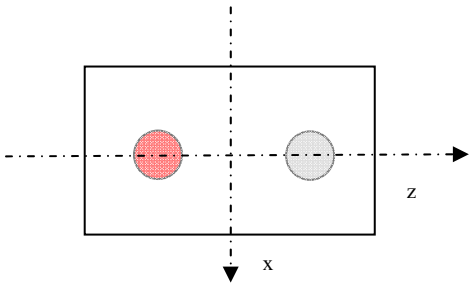

(a). Two sphere phantoms oscillation along z axis with an unbalanced radioactive distributions.

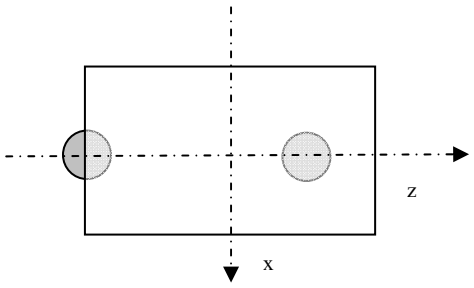

(b). Two sphere phantoms oscillation along z axis, one phantom overruns the edge of the FOV.

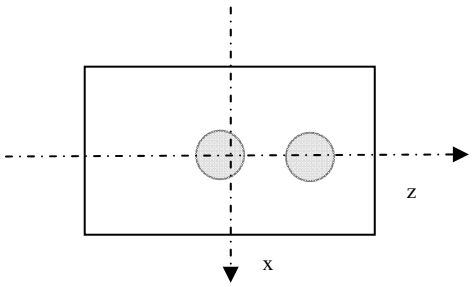

(c). Two sphere phantoms oscillation along z axis, one phantom overruns the transverse plane at the centre of the FOV.

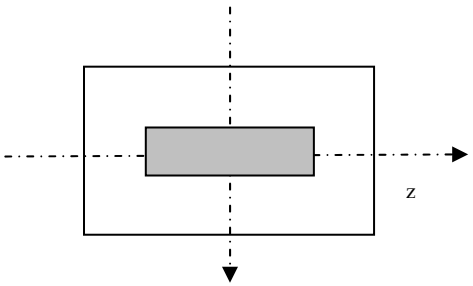

(d). Cylindrical phantom oscillation along z axis, overruns the transverse plane at the centre of the FOV.

Fig. 5.3 Total sensitivity value will be varying in any one of situations above with phantom oscillations along z axis in 3D scanner (a) – (d). As a result, the number of LORs detected in frames will change. Therefore the GSG and GSC methods can be applied.

5.3.2 Further Research

At present, the GSC method corrects respiratory motion along the Z axis direction only rather than in all three dimensions Even so, the result of the correction presented is significant. Motion in the X and Y motion directions, and to some extent elastic motion terms needs to be incorporated into the transformation matrix for respiratory motion compensation at the next stage of research.

5.4 Conclusion

Respiratory motion can significantly degrade the quality of the reconstructed images in PET imaging. In this thesis, the GSG and the GSC were proposed for respiratory motion gating and correction respectively in terms of the geometric sensitivity properties of a 3D mode PET scanner acquiring in list-mode. The GSG and the GSC were tested by phantom simulations and clinical studies. All results of simulations and clinical studies demonstrate that the GSG and the GSC methods are able to improve the quality of image of respiratory motion in PET imaging.

Compared with existing techniques for respiratory motion compensation, the major advantages of the GSG and the GSC are:

- No additional hardware device is required;
- They only use list-mode data and are non-invasive;
- There is no acquisition burden;
- There is no additional patient preparation required;
- There is no additional time required for clinical setup;

5.5 Main Contributions and Publications

To deal with the respiratory motion issue, this thesis proposed two novel methods, the GSG and the GSC, that utilise geometric sensitivity properties of 3D PET imaging to compensate respiratory motion. The thesis contributions are:

- A proposed new method for respiratory motion correction with geometric sensitivity gating (GSG) of data from a single respiratory phase that was validated by the use of simulations and clinical studies.
- A proposed new method for respiratory motion correction with geometric sensitivity correction (GSC) of data from all respiratory phases that was validated by simulations and clinical studies.

The following is a list of publications and published abstracts arising form this research work.

1. J. He, G. O'Keefe, S. Gong, T. Saunder, G. Jones, A. Scott, and M, Geso "A Novel Method for Respiratory Motion Gated with Geometrical Sensitivity of the Scanner in 3D PET ", IEEE Transactions on Nuclear Science (In Press). It can be seen in Appendix E.
2. J. He, G. O'Keefe, G. Jones, T. Saunder, S. Gong, M. Geso, and A. Scott, "Investigation of Respiratory Motion Gating with Geometric Sensitivity in Allegro PET", *Proceedings of* the IEEE 2007 Nuclear Science Symposium, Medical Imaging Conference, Honolulu, Hawaii, USA, October, 2007.
3. J. He, G. O'Keefe, G. Jones, T. Saunder, S. Gong, M. Geso, and A. Scott, " Non-invasive Approach for Respiratory Motion Gating in PET: Digital Phantom Evaluation", Abstract, *Proceedings of* the EPSM – ABEC (Engineering and Physical Sciences in Medicine and The Australian Biomedical Engineering Conference) 2007 Conference 'Advancing Professionalism', Western Australia, October, 2007.
4. J. He, G. O'Keefe, G. Jones, T. Saunder, S. Gong, M. Geso, and A. Scott, "Evaluation of Geometric Sensitivity for Respiratory Motion Gating by GATE and NCAT Simulation", *Proceedings of* the 29th Annual International Conference of the IEEE Engineering in Medicine and Biology Society, Lyon, France, August, 2007.

5. J. He, G. O'Keefe, G. Jones, T. Saunder, S. Gong, M. Geso, and A. Scott, “Simulation of Respiratory Motion Gating Using GATE and NCAT”, Medical Physics, Vol. 34, pp. 2362-2362, 2007.
6. J. He, G. O'Keefe, G. Jones, T. Saunder, S. Gong, M. Geso, and A. Scott, "Application of GATE and NCAT to Respiratory Motion Gating: A Simulation Study”, Abstract, *Proceedings of* the 37th Australian and New Zealand Society of Nuclear Medicine Annual Scientific Meeting, Adelaide, April, 2007.
7. J. He, G. O'Keefe, G. Jones, T. Saunder, S. Gong, M. Geso, and A. Scott, "Application of GATE and NCAT to Respiratory Motion Simulation in Allegro PET", *Proceedings of* the IEEE 2006 Nuclear Science Symposium, Medical Imaging Conference, San Diego, California, USA, 2006.
8. J. He, G. O'Keefe, G. Jones, T. Saunder, S. Gong, M. Geso, and A. Scott, "Simulation of Respiratory Motion Using GATE", Abstract, *Proceedings of* the 9th Congress of the World Federation of Nuclear Medicine & Biology, COEX Seoul, Korea, 2006.
9. J. He, G. O'Keefe, G. Jones, T. Saunder, S. Gong, M. Geso, and A. Scott, " Application of GATE and NCAT to Respiratory Motion Simulation in Allegro PET ”, Abstract, *Proceedings of* the 36th Australian and New Zealand Society of Nuclear Medicine Annual Scientific Meeting, Perth, 2006.

APPENDICES

Appendices

APPENDIX A GATE MACROS OF PHILLIPS ALLEGRO PET SCANNER SIMULATION 176

APPENDIX B GATE MACROS OF GEOMETRIC PHANTOM AND SOURCE MOTION..... 180

APPENDIX C GATE MACROS OF VOXELISED PHANTOM AND SOURCE 182

APPENDIX D NCAT PHANTOM GENERATION PARAMETERS 184

APPENDIX E PUBLICATION IN IEEE TRANSACTIONS ON NUCLEAR SCIENCE (IN PRESS) 191

Appendix A GATE macros of Phillips Allegro PET scanner simulation

```
/control/verbose 0

#     V I S U A L I S A T I O N

#/control/execute visualisation.mac

#         W O R L D
/gate/world/geometry/setXLength 1.5 m
/gate/world/geometry/setYLength 1.5 m
/gate/world/geometry/setZLength 1.5 m
/gate/world/setMaterial Air

#         D E T E C T O R
/gate/world/daughters/name cylindricalPET
/gate/world/daughters/insert cylinder
/gate/cylindricalPET/setMaterial Air
/gate/cylindricalPET/geometry/setRmax 52. cm
/gate/cylindricalPET/geometry/setRmin 28. cm
/gate/cylindricalPET/geometry/setHeight 24.02 cm
/gate/cylindricalPET/vis/forceWireframe

#         S H I E L D I N G
/gate/cylindricalPET/daughters/name Shielding
/gate/cylindricalPET/daughters/insert cylinder
/gate/Shielding/setMaterial Lead
/gate/Shielding/geometry/setRmax 46.132 cm
/gate/Shielding/geometry/setRmin 28. cm
/gate/Shielding/geometry/setHeight 2.86 cm
/gate/Shielding/vis/forceSolid
/gate/Shielding/vis/forceWireframe
/gate/Shielding/vis/setColor white

#         R E P E A T     S H I E L D I N G
/gate/Shielding/repeaters/insert linear
/gate/Shielding/linear/setRepeatNumber 2
/gate/Shielding/linear/setRepeatVector 0. 0. 21.16 cm



#         D E T E C T O R   =   R S E C T O R
/gate/cylindricalPET/daughters/name rsector
/gate/cylindricalPET/daughters/insert box
/gate/rsector/geometry/setXLength 40 mm
/gate/rsector/geometry/setYLength 94.5 mm
/gate/rsector/geometry/setZLength 18.3 cm
/gate/rsector/setMaterial Glass
/gate/rsector/placement/setTranslation    45.2 0 0 cm
/gate/rsector/vis/forceWireframe

#         M O D U L E
/gate/rsector/daughters/name module
/gate/rsector/daughters/insert box
/gate/module/geometry/setXLength 20. mm
/gate/module/geometry/setYLength 94.5 mm
/gate/module/geometry/setZLength 18.3 cm
/gate/module/setMaterial PTFE
/gate/module/placement/setTranslation    -10. 0 0 mm
/gate/module/vis/forceWireframe

#          C R Y S T A L
```

```
/gate/module/daughters/name crystal
/gate/module/daughters/insert box
/gate/crystal/geometry/setXLength 20. mm
/gate/crystal/geometry/setYLength 4 mm
/gate/crystal/geometry/setZLength 6 mm
/gate/crystal/setMaterial GSO
/gate/crystal/placement/setTranslation 0 0 0 mm

#        L A Y E R      G S O
/gate/crystal/daughters/name GSO
/gate/crystal/daughters/insert box
/gate/GSO/geometry/setXLength 20. mm
/gate/GSO/geometry/setYLength 4 mm
/gate/GSO/geometry/setZLength 6 mm
/gate/GSO/placement/setTranslation 0 0 0 mm
/gate/GSO/setMaterial GSO

#   R E P E T I T I O N       C R I S T A L
/gate/crystal/repeaters/insert cubicArray
/gate/crystal/cubicArray/setRepeatNumberX 1
/gate/crystal/cubicArray/setRepeatNumberY 22
/gate/crystal/cubicArray/setRepeatNumberZ 29
/gate/crystal/cubicArray/setRepeatVector 0. 4.3 6.3 mm

#   R E P E T I T I O N       R S E C T O R
/gate/rsector/repeaters/insert ring
/gate/rsector/ring/setRepeatNumber 28

# P H A N T O M

# The phantom must model the attenuation geometry

/control/execute phantom.mac

#      A T T A C H       S Y S T E M
/gate/systems/cylindricalPET/rsector/attach rsector
/gate/systems/cylindricalPET/module/attach module
/gate/systems/cylindricalPET/crystal/attach crystal
/gate/systems/cylindricalPET/layer0/attach GSO

#      A T T A C H       L A Y E R    SD
/gate/GSO/attachCrystalSD
/gate/rsector/attachPhantomSD
/gate/module/attachPhantomSD


#            P H Y S I C S
#/gate/physics/gamma/selectRayleigh lowenergy
#/gate/physics/gamma/selectPhotoelectric lowenergy
#/gate/physics/gamma/selectCompton lowenergy


/gate/physics/gamma/selectRayleigh inactive
/gate/physics/gamma/selectPhotoelectric standard
#/gate/physics/gamma/selectCompton lowenergy
/gate/physics/gamma/selectCompton standard #########


#            I N A C T I V E       S E C O N D A R Y      E L E C T R O N S
/gate/physics/setElectronCut 30.01 cm

#            I N A C T I V E       X - R A Y S
/gate/physics/setXRayCut 1. GeV
```

```
/gate/physics/setDeltaRayCut 1. GeV
/gate/physics/verbose 0

#            I N I T I A L I Z E
/gate/systems/cylindricalPET/verbose 0
/gate/geometry/enableAutoUpdate
/run/initialize

#            S O U R C E
/control/execute source.mac

#     D I G I T I Z E R
/gate/digitiser/Singles/insert adder
/gate/digitiser/Singles/insert readout
/gate/digitiser/Singles/readout/setDepth 1
/gate/digitiser/Singles/insert blurring
/gate/digitiser/Singles/blurring/setResolution 0.15
/gate/digitiser/Singles/blurring/setEnergyOfReference 511. keV

/gate/digitiser/Singles/insert deadtime
/gate/digitiser/Singles/deadtime/setDeadTime 210. ns
/gate/digitiser/Singles/deadtime/setMode paralysable
/gate/digitiser/Singles/deadtime/chooseDTVolume module

/gate/digitiser/Singles/insert timeResolution
/gate/digitiser/Singles/timeResolution/setTimeResolution 3. ns
/gate/digitiser/Singles/timeResolution/verbose 0

/gate/digitiser/Singles/insert thresholder
/gate/digitiser/Singles/thresholder/setThreshold 0.435 MeV
/gate/digitiser/Singles/insert upholder
/gate/digitiser/Singles/upholder/setUphold 0.587 MeV

#     C O I N C I      S O R T E R
/gate/digitiser/Coincidences/setWindow 6.5 ns
/gate/digitiser/Coincidences/minSectorDifference 7


#     V E R B O S I T Y
/control/verbose 0
/grdm/verbose 0
/run/verbose 0
/event/verbose 0
/tracking/verbose 0
/gate/application/verbose 0
/gate/generator/verbose 0
/gate/stacking/verbose 0
/gate/event/verbose 0
/gate/source/verbose 0

#  C H A N G E      T H E      S E E D (1)   O R     N O T (0)
/gate/output/root/setSaveRndmFlag 1

#     O U T P U T
/gate/output/verbose 0
/gate/output/lmf1/disable
#/gate/output/ascii/setFileName gate_hoffman_att
/gate/output/ascii/setOutFileHitsFlag 0
/gate/output/ascii/setOutFileSinglesFlag 0
/gate/output/ascii/setOutFileCoincidencesFlag 1
#/gate/output/root/setFileName gate_hoffman_att
/gate/output/root/setRootHitFlag 0
/gate/output/root/setRootSinglesFlag 0
```

```
/gate/output/root/setRootCoincidencesFlag 0
/gate/output/root/setRootSinglesBlurringFlag 0
/gate/output/root/setRootSinglesDeadtimeFlag 0
/gate/output/root/setRootNtupleFlag 0

#      S T A R T
/gate/application/setTimeSlice         1      s
/gate/application/setTimeStart         0.    s
/gate/application/setTimeStop          1      s
/gate/application/startDAQ
exit
```

Appendix B GATE macros of geometric phantom and source motion

 # This is for phantom motion

Modified by Jianfeng He –20060120

Movements of the phantom

```
/gate/world/daughters/name phantom
/gate/world/daughters/insert cylinder
/gate/phantom/setMaterial Water
/gate/phantom/vis/setColor green
/gate/phantom/geometry/setRmax 5.0 cm
/gate/phantom/geometry/setHeight 10. cm
/gate/phantom/attachPhantomSD


/gate/phantom/moves/insert osc-trans
/gate/phantom/osc-trans/setAmplitude 10. 0. 0. cm
/gate/phantom/osc-trans/setFrequency 50 Hz
/gate/phantom/osc-trans/setPeriod 1 s
/gate/phantom/osc-trans/setPhase 90 deg

/gate/timing/setTime 0 s
/gate/timing/setTime 1 s
/gate/timing/setTime 2 s
/gate/timing/setTime 3 s
/gate/timing/setTime 4 s
/gate/timing/setTime 5 s
/gate/timing/setTime 6 s
/gate/timing/setTime 7 s
/gate/timing/setTime 8 s
/gate/timing/setTime 9 s
/gate/timing/setTime 10 s
```

 # This is for motion sources

```
#                G A M M A
# Define the shape/dimensions of the large sourcecontainer that should contain the full trajectory of the moving source

/gate/source/addSource SourceConfinement
/gate/source/SourceConfinement/gps/type Volume
/gate/source/SourceConfinement/gps/shape Cylinder
/gate/source/SourceConfinement/gps/radius 5. cm
/gate/source/SourceConfinement/gps/halfz 15. cm

/gate/source/SourceConfinement/gps/centre 0. 0. 0. cm
#/gate/SourceConfinement/vis/setColor blue

/gate/source/SourceConfinement/setType backtoback
/gate/source/SourceConfinement/gps/particle gamma
/gate/source/SourceConfinement/setForcedUnstableFlag true
/gate/source/SourceConfinement/setForcedHalfLife 6586.2 s
/gate/source/SourceConfinement/gps/energytype Mono
/gate/source/SourceConfinement/gps/monoenergy 0.511 MeV
#/gate/source/SourceConfinement/setActivity 3700000. Bq
/gate/source/SourceConfinement/setActivity 30000. Bq

/gate/source/SourceConfinement/gps/angtype iso
/gate/source/SourceConfinement/gps/mintheta 0. deg
/gate/source/SourceConfinement/gps/maxtheta 180. deg
/gate/source/SourceConfinement/gps/minphi 0. deg
/gate/source/SourceConfinement/gps/maxphi 360. deg
/gate/source/SourceConfinement/gps/confine movsource
/gate/source/list
```

Appendix C GATE macros of voxelised phantom and source

```
#   This macro has been modified by:
#       Jianfeng He based on Frederic Lamarre's macro
#
#V O X E L I Z E D  M A T R I X  NCAT  P H A N T O M


/gate/world/daughters/name hof_brain
/gate/world/daughters/insert parameterizedBoxMatrix
/gate/hof_brain/geometry/insertReader interfile
/gate/hof_brain/interfileReader/insertTranslator range
#/gate/hof_brain/interfileReader/rangeTranslator/readTable range.dat
/gate/hof_brain/interfileReader/rangeTranslator/readTable range_vox.dat

/gate/hof_brain/interfileReader/rangeTranslator/describe 1
/gate/hof_brain/interfileReader/readFile test.h33
/gate/hof_brain/placement/setTranslation    0. 0. 0. mm
/gate/hof_brain/placement/setRotationAxis 1 0 0
/gate/hof_brain/placement/setRotationAngle 0 deg
/gate/hof_brain/attachVoxelPhantomSD
#/gate/hof_brain/addOutput doseOutput
#/gate/output/doseOutput/saveUncertainty true
#/gate/output/doseOutput/setFileName hof_brain_paraDose.bin

/gate/hof_brain/attachPhantomSD



#   This macro has been modified by Jianfeng He based on Frederic Lamarre's macro
#
#V O X E L  S O U R C E  B A S E D  O N  T H E  NCAT  P H A N T O M

/gate/source/addSource voxel_brain voxel
########### Range translator
/gate/source/voxel_brain/reader/insert interfile
########### Range translator
#/gate/source/voxel_brain/interfileReader/translator/insert range
#/gate/source/voxel_brain/interfileReader/rangeTranslator/readTable activityRange.dat
#/gate/source/voxel_brain/interfileReader/rangeTranslator/describe 1

###########    Linear translator: All numbers directly #into activities
/gate/source/voxel_brain/interfileReader/translator/insert linear
/gate/source/voxel_brain/interfileReader/linearTranslator/setScale 10.50 Bq

/gate/source/voxel_brain/interfileReader/readFile test.h33
#/gate/source/voxel_brain/interfileReader/readFile lung_lesn.h33

/gate/source/voxel_brain/setType backtoback
/gate/source/voxel_brain/gps/particle gamma
/gate/source/voxel_brain/setForcedUnstableFlag true
/gate/source/voxel_brain/setForcedHalfLife 6586.2 s
/gate/source/voxel_brain/gps/energytype Mono
/gate/source/voxel_brain/gps/monoenergy 0.511 MeV
/gate/source/voxel_brain/setPosition -160. -160. -160.mm # 64*64*64;0.5mm

/gate/source/voxel_brain/gps/confine NULL
/gate/source/voxel_brain/gps/angtype iso
/gate/source/voxel_brain/dump 1
```

```
/gate/source/list

#
# The head of image file: test.h33
#

!name of data file := test.bin
!number of images := 64
!matrix size [1] := 64
!matrix size [2] := 64
!number format := unsigned integer
scaling factor (mm/pixel) [1] := +5.000000e+00
scaling factor (mm/pixel) [2] := +5.000000e+00
slice thickness (pixels) := +5.000000e+00
!END OF INTERFILE :=
```

Appendix D NCAT phantom generation parameters

This is a general parameter file for the DYNAMIC NCAT phantom, version d2.0.
Not all the parameters are used in any individual program. Unused parameters are read in, but simply ignored by program THE ORDER OF THE PARAMETERS IS IMPORTANT

1 : activity_phantom_each_frame (1=save phantom to file, 0=don't save)
1 : attenuation_coeff_phantom_each_frame (1=save phantom to file, 0=don't save)
1 : activity_phantom_average (1=save , 0=don't save) see NOTE 0
1 : attenuation_coeff_phantom_average (1=save, 0=don't save) see NOTE 0

2 : motion_option (0=beating heart only, 1=respiratory motion only, 2=both motions) see NOTE 1

2 : output_period (SECS) (if <= 0, then output_period=time_per_frame*output_frames)
0.2 : time_per_frame (SECS) (**IGNORED unless output_period<=0**)
10 : output_frames (# of output time frames)

1 : hrt_period (SECS) (length of beating heart cycle; normal = 1s) see NOTE 2
0.0 : hrt_start_phase_index (range=0 to 1; ED=0, ES=0.4) see NOTE 2
5 : resp_period (SECS) (length of respiratory cycle; normal breathing = 5s) see NOTE 2
0.0 : resp_start_phase_index (range=0 to 1, full exhale=0, full inhale=0.455) see NOTE 2
2.0 : max_diaphragm_motion (extent in cm's of diaphragm motion; normal breathing = 2 cm) see NOTE 3
1.2 : max_AP_expansion (extent in cm's of the AP expansion of the chest; normal breathing = 1.2 cm) see NOTE 3

35.2 : body_long_axis (sets body transverse axis - scales only body outline) (visible male = 35.2 cm)
26.7 : body_short_axis (sets body AP axis - scales only body outline) (visible male = 26.7 cm)
41.7 : body_height (sets height of torso - scales only body outline) (visible male = 41.7 cm)

30.0 : rib_long_axis (sets ribcage transverse axis - scales everything and repositions the heart to adjust to the scaling) (visible male = 30.0 cm)
22.7 : rib_short_axis (sets ribcage AP axis - scales everything and repositions the heart to adjust to the scaling) (visible male = 22.7 cm)
37.3 : rib_height (sets height of ribcage - scales everything and repositions the heart to adjust to the scaling) (visible male = 37.3 cm)

0.5 : thickness of large intestine wall (cm)
36.0 : rectum_long_axis (sets diameter of rectum transverse axis; visible male = 36 cm)
49.0 : rectum_short_axis (sets rectum AP axis diameter; visible male = 49.0 cm)
4 : location of air in the large intestine and rectum see NOTE 4

1.0 : hrt_scale (scales heart in 3D - 1.0 is visible male) (Can use this to alter the heart or the following, but not both)
9.43 : hrt_lv_length (sets the length of the LV - entire heart is scaled with the LV) (NCAT heart = 9.43 cm)
2.97 : hrt_lv_radius (sets the ave. radius of the LV - entire heart is scaled with the radius) (NCAT heart = 2.97 cm)

1 : breast_type (0=supine, 1=prone)
0 : which_breast (0 = none, 1 = both, 2 = right only, 3=left only)
18.2 : breast_long_axis (sets the breasts lateral dimension) (PRONE normal = 15.1 cm, SUPINE normal = 18.2 cm)
7.0 : breast_short_axis (sets the breasts antero-posterior dimension) (PRONE normal = 7.0 cm, SUPINE = 4.0 cm)
14.0 : breast_height (sets the breasts height) (PRONE normal = 14.0 cm, SUPINE normal = 14.9 cm)
4.6 : theta angle of the breasts (angle the breasts are tilted transversely (sideways) from the centre of the chest (PRONE normal = 4.6, SUPINE NORMAL = 40.0)
0.0 : phi angle of the breasts (angle the breasts are tilted up (+) or down (-) (PRONE normal = 0, SUPINE normal = -20.0)

3.4 : height of right_diaphragm/liver dome (visible human = 3.4 cm)
1.9 : height of left diaphragm dome (visible human = 1.9 cm)

0.1 : intv in cm (thickness of body tissue around the heart and liver)

0.5 : pixel width (cm); see NOTE 5
0.5 : slice width (cm); see NOTE 5
64 : array size see NOTE 6
1 : subvoxel_index (=1,2,3,4 -> 1,8,27,64 subvoxels/voxel, respectively)
85 : start_slice; see NOTE 7
148 : end_slice; see NOTE 7

-90 : zy_rotation (beta) in deg. (-90); see NOTE 8
-20. : xz_rotation (phi) in deg. (-20); see NOTE 8
-50. : yx_rotation (psi) in deg. (-50); see NOTE 8
0.0 : x translation in cm ; see NOTE 8
0.0 : y translation in cm ; see NOTE 8
0.0 : z translation in cm ; see NOTE 8
1 : apical_thinning (1 = present, otherwise not present) /*parameter is ignored*/
0.0 : valve thickness in cm (0= no valve); cannot be a negative value /*parameter is ignored*/
0.3 : av_step(cm): step width for smooth change between Atr & Ven (0=none) /*parameter is ignored*/
0 : total_rotation (deg); /*parameter is ignored*/

0 : activity units (1= scale by voxel volume; 0= don't scale) NOTE 9

SEE NOTE 9 FOR INFORMATION ON SETTING ORGAN ACTIVITIES - activities can be fixed or determined by user defined time-activity curves
---
0 : myoLV_time_curve (1= activity determined by a time-activity curve; 0= fixed activity)
75 : hrt_myoLV_act - fixed activity in left ventricle myocardium if above option is 0
sample_act.txt : myoLV_act_filename - name of file containing time-activity curve for LV myocardium
---
0 : myoRV_time_curve (1= activity determined by a time-activity curve; 0= fixed activity)
75 : hrt_myoRV_act - activity in right ventricle myocardium
sample_act.txt : myoRV_act_filename - name of file containing time-activity curve for RV myocardium
---
0 : myoLA_time_curve (1= activity determined by a time-activity curve; 0= fixed activity)
75 : hrt_myoLA_act - activity in left atrium myocardium
sample_act.txt : myoLA_act_filename - name of file containing time-activity curve for LA myocardium
---
0 : myoRA_time_curve (1= activity determined by a time-activity curve; 0= fixed activity)
75 : hrt_myoRA_act - activity in right atrium myocardium
sample_act.txt : myoRA_act_filename - name of file containing time-activity curve for RA myocardium
---
0 : bldplLV_time_curve (1= activity determined by a time-activity curve; 0= fixed activity)
75 : hrt_bldplLV_act - activity in left ventricle chamber (blood pool)
sample_act.txt : bldplLV_act_filename - name of file containing time-activity curve for LV blood pool
---
0 : bldplRV_time_curve (1= activity determined by a time-activity curve; 0= fixed activity)
75 : hrt_bldplRV_act - activity in right ventricle chamber (blood pool)
sample_act.txt : bldplRV_act_filename - name of file containing time-activity curve for RV blood pool
---
0 : bldplLA_time_curve (1= activity determined by a time-activity curve; 0= fixed activity)
75 : hrt_bldplLA_act - activity in left atria chamber (blood pool)
sample_act.txt : bldplLA_act_filename - name of file containing time-activity curve for LA blood pool

---
0 : bldplRA_time_curve (1= activity determined by a time-activity curve; 0= fixed activity)
75 : hrt_bldplRA_act - activity in right atria chamber (blood pool)
sample_act.txt : bldplRA_act_filename - name of file containing time-activity curve for RA blood pool
---
0 : body_time_curve (1= activity determined by a time-activity curve; 0= fixed activity)
10 : body_activity (background activity) ;
sample_act.txt : body_act_filename - name of file containing time-activity curve for body
---
0 : liver_time_curve (1= activity determined by a time-activity curve; 0= fixed activity)
75.0 : liver_activity;
sample_act.txt : liver_act_filename - name of file containing time-activity curve for liver
---
0 : gall_bladder_time_curve (1= activity determined by a time-activity curve; 0= fixed activity)
2 : gall_bladder_activity;
sample_act.txt : gall_bladder_act_filename - name of file containing time-activity curve for gall bladder
---
0 : lung_time_curve (1= activity determined by a time-activity curve; 0= fixed activity)
20 : lung_activity;
sample_act.txt : lung_act_filename - name of file containing time-activity curve for lungs
---
0 : st_wall_time_curve (1= activity determined by a time-activity curve; 0= fixed activity)
2 : st_wall_activity; (stomach wall)
sample_act.txt : st_wall_act_filename - name of file containing time-activity curve for stomach wall
---
0 : st_cnts_time_curve (1= activity determined by a time-activity curve; 0= fixed activity)
2 : st_cnts_activity; (stomach contents)
sample_act.txt : st_cnts_act_filename - name of file containing time-activity curve for stomach contents
---
0 : kidney_time_curve (1= activity determined by a time-activity curve; 0= fixed activity)
75 : kidney_activity;
sample_act.txt : kidney_act_filename - name of file containing time-activity curve for kidneys
---
0 : spleen_time_curve (1= activity determined by a time-activity curve; 0= fixed activity)
75 : spleen_activity;
sample_act.txt : spleen_act_filename - name of file containing time-activity curve for spleen
---
0 : rib_time_curve (1= activity determined by a time-activity curve; 0= fixed activity)
2 : rib_activity;
sample_act.txt : rib_act_filename - name of file containing time-activity curve for ribs
---
0 : spine_head_time_curve (1= activity determined by a time-activity curve; 0= fixed activity)
2 : spine_head_activity;
sample_act.txt : spine_head_act_filename - name of file containing time-activity curve for spine
---
0 : spine_process_time_curve (1= activity determined by a time-activity curve; 0= fixed activity)
2 : spine_process_activity;
sample_act.txt : spine_preocess_act_filename - name of file containing time-activity curve for spine
---
0 : pelvis_time_curve (1= activity determined by a time-activity curve; 0= fixed activity)
2 : pelvis_activity;
sample_act.txt : pelvis_act_filename - name of file containing time-activity curve for pelvis bone
---
0 : bone_cartilage_time_curve (1= activity determined by a time-activity curve; 0= fixed activity)
2 : bone_cartilage_activity;
sample_act.txt : bone_cartilage_act_filename - name of file containing time-activity curve for bone cartilage

---
0 : artery_time_curve (1= activity determined by a time-activity curve; 0= fixed activity)
2 : artery_activity;
sample_act.txt : artery_act_filename - name of file containing time-activity curve for arteries
---
0 : vein_time_curve (1= activity determined by a time-activity curve; 0= fixed activity)
2 : vein_activity;
sample_act.txt : vein_act_filename - name of file containing time-activity curve for veins
---
1 : bladder_time_curve (1= activity determined by a time-activity curve; 0= fixed activity)
2 : bladder_activity;
sample_act.txt : bladder_act_filename - name of file containing time-activity curve for bladder
---
0 : prostate_time_curve (1= activity determined by a time-activity curve; 0= fixed activity)
2 : prostate_activity;
sample_act.txt : prostate_act_filename - name of file containing time-activity curve for prostate
---
0 : ascending_large_intest_time_curve (1= activity determined by a time-activity curve; 0= fixed activity)
2 : ascending_large_intest_activity;
sample_act.txt : ascending_large_intest_act_filename - name of file containing time-activity curve for ascending l. intest.
---
0 : transcending_large_intest_time_curve (1= activity determined by a time-activity curve; 0= fixed activity)
2 : transcending_large_intest_activity;
sample_act.txt : transcending_large_intest_act_filename - name of file containing time-activity curve for transc. l. intest.
---
0 : descending_large_intest_time_curve (1= activity determined by a time-activity curve; 0= fixed activity)
2 : desc_large_intest_activity;
sample_act.txt : desc_large_intest_act_filename - name of file containing time-activity curve for desc. l. intest.
---
0 : small_intest_time_curve (1= activity determined by a time-activity curve; 0= fixed activity)
2 : small_intest_activity;
sample_act.txt : small_intest_act_filename - name of file containing time-activity curve for small intestine
---
0 : rectum_time_curve (1= activity determined by a time-activity curve; 0= fixed activity)
2 : rectum_activity;
sample_act.txt : rectum_act_filename - name of file containing time-activity curve for rectum
---
0 : seminal_vessicles_time_curve (1= activity determined by a time-activity curve; 0= fixed activity)
2 : sem_vess_activity;
sample_act.txt : sem_vess_act_filename - name of file containing time-activity curve for sem. ves.
---
0 : vas_deferens_time_curve (1= activity determined by a time-activity curve; 0= fixed activity)
2 : vas_def_activity;
sample_act.txt : vas_def_act_filename - name of file containing time-activity curve for vas def.
---
0 : testicular_time_curve (1= activity determined by a time-activity curve; 0= fixed activity)
2 : testicular_activity;
sample_act.txt : testicular_act_filename - name of file containing time-activity curve for test.

2.0 : ascending large intestine air activity;
2.0 : transverse large intestine air activity;
2.0 : descending large intestine air activity;
2.0 : small intestine air activity;

2.0 : rectum air activity;
2.0 : ureter activity;
2.0 : urethra activity;
2.0 : lymph normal activity;
2.0 : lymph abnormal activity;
511. : radionuclide energy in keV (range 1-1000 keV) ; for attn. map only

NOTES:

NOTE 0: The average phantom is the average ONLY OF THOSE FRAMES GENERATED. That is, if you specify that only 2 frames be generated, then the average phantom is just the average of those 2 frames.

****
** FOR A GOOD AVERAGE, generate at least 8-16 frames per 1 complete heart
** cycle and/or per 1 complete respiratory cycle.
****

NOTE 1 : Heart motion refers to heart BEATING or contraction, while resp. motion refers to organ motion due to breathing. Note that the entire heart is translated or rotated due to resp. motion, even if it is not contracting.
** IF motion_option=1 , THE HEART WILL MOVE (TRANSLATE) BUT NOT BEAT.****

NOTE 2 : Users sets the length and starting phase of both the heart and respiratory cycles. NORMAL values for length of heart beat and respiratory are cycles are 1 sec. and 5 secs., respectively,
BUT THESE CAN VARY AMONG PATIENTS and will increase if the patient is under stress.

An index value between 0 and 1 is used the specify the starting phase of the heart or resp cycles. IF NO MOTION IS SPECIFIED THEN THE STARTING PHASE IS USED AS THE SINGLE PHASE AT WHICH THE PHANTOM IS GENERATED. (see documentation for more details).

NOTE 3 : These NORMAL values are for normal tidal breathing.
** Modeling a deep inhale may require higher values. **

The AP_expansion parameter controls the anteroposterior diameter of the ribcage, body, and lungs. The ribs rotate upward to expand the chest cavity by the amount indicated by the AP_expansion parameter. The lungs and body move with the expanding ribs. There is maximum amount by which the AP diameter can expand, due to the size of the ribs (some expansions are impossible geometricly.) If the user specifies too great an expansion, the program will terminate with an error message.

The diaphragm motion controls the motion of the liver, the left diaphragm, the heart, stomach, and spleen. The liver is set to move forward during inspiration an amount equal to the AP expansion of the chest. The liver moves back to its original position during expiration. The liver is also set to move up/down with the diaphragm. The heart moves with the liver. The stomach and spleen also move with the liver but at a reduced extent.

NOTE 4:

- rotation parameters determine
  initial orientation of beating (dynamic) heart LV long axis
  see the subroutine CALC_DYN_HEART_ROT_MATRIX for details
- zy_rotation : axis rotates toward axis (about x-axis) by beta
  xz_rotation : axis rotates toward axis (about y-axis) by phi
  yx_rotation : axis rotates toward axis (about z-axis) by psi

- Based on patient data, the mean and SD heart orientations are:
  zy_rot = -110 degrees (no patient data for this rotation)
  xz_rot = 23 + 10 deg.
  yx_rot = -52 + 11 deg.

NOTE 5 : if option 1 is chosen, the values of the activity specified in
this parameter file are scaled by the voxel volume
FOR EXAMPLE:
1) body_activity = 1.0 and unit option equal 1
=> phantom will output the value 1.0*(pixel_width)^3 in body voxel OR
2) body_activity = 1.0 and unit option equal 0
=> phantom will output the value 1 in body voxels

NOTE 6: The activity of the organs in the phantom can be set to be fixed, or they can be set according to a user-defined time-activity curve. If the option flag for an organ is set to 0, the activity of the organ is static for the entire simulation. The fixed value is set by the organ_act parameter. The parameter asking for the time-activity curve filename
is then ignored. If the option flag for an organ is set to 1, the activity for the organ is determined by a user-defined time-activity curve; the parameter for the fixed activity value for the organ (organ_act) is ignored. The program then requires the name of the text file that contains the time-activity curve. The text file for the time-activity curve should be setup as shown in the sample file "sample_act.txt".

This file creates a lesion in the NCAT phantom in either the lungs or liver:

0 : Organ to place lesion inside (0 = right lung, 1 = left lung, 2 = liver)
39, 66, 22 : (x,y,z) location to place lesion (pixels) See NOTE 1
15.0 : Diameter of lesion (mm)
---
0 : lesn_time_curve (1= activity determined by a time-activity curve; 0= fixed activity) SEE NOTE 2
120.0 : lesn_activity - Activity ratio of the lesion
sample_act.txt : lesn_act_filename - name of file containing time-activity curve for lesion SEE NOTE 2

NOTE 1: Initial location of the lesion within the organ. Location is specified in pixel values. If the specified location is not in the specified organ, the program will report an error.

0 : Organ to place lesion inside (0 = right lung, 1 = left lung, 2 = liver)
45,64,35 : (x,y,z) location to place lesion (pixels) See NOTE 1
10.0 : Diameter of lesion (mm)

0 : Organ to place lesion inside (0 = right lung, 1 = left lung, 2 = liver)
39,66,22 : (x,y,z) location to place lesion (pixels) See NOTE 1
15.0 : Diameter of lesion (mm)

1 : Organ to place lesion inside (0 = right lung, 1 = left lung, 2 = liver)
81,64,36 : (x,y,z) location to place lesion (pixels) See NOTE 1
12.0

NOTE 2: The activity of the lesion in the phantom can be set to be fixed, or it can be set according to a user-defined time-activity curve. If the option flag is set to 0, the activity of the lesion is static for the entire simulation. The fixed value is set by the lesn_activity parameter. The parameter asking for the time-activity curve filename is then ignored. If the option flag is set to 1, the activity for the lesion is determined by a user-defined time-activity curve; the parameter for the fixed activity value for the lesion (lesn_activity) is ignored. The program then requires the name of the text file that contains the time-activity curve. The text file for the time-activity curve should be setup as shown in the sample file "sample_act.txt".

Motion vectors inside the lungs and liver can be output to text files using the program resp_vectors. The text files contain the motion of the points from the previous time frame to the current frame. For example, the text file "vector_1_2.txt" would contain the motion of the points from time frame 1 to time frame 2. The file "vector_2_3.txt" would contain the motion between frames 2 and 3. The vectors are output in pixel units.

Appendix E Publication in IEEE Transactions on Nuclear Science (In press)

REFERENCES

References

[1] P. E. Valk, D. Delbeke, D. L. Bailey, D. W. Townsend, and M. N. Maisey, *Positron Emission Tomography : Clinical Practice*: Springer-Verlag London Ltd, 2005.

[2] D. W. Townsend, J. P. J. Carney, J. T. Yap, and N. C. Hall, "PET/CT Today and Tomorrow," *The Journal of Nuclear Medicine*, vol. 45, pp. 4S-14S, 2004.

[3] J. Thibaud, "L'annihilation des positrons au contact de la matiere et la radiation qiu en resulte," *Les Comptes Rendus de l'Académie des Sciences*, vol. 197, pp. 1629−32, 1933.

[4] F. Joliot, "Preuve experimental de l'annihilation des elections positifs," *Les Comptes Rendus de l'Académie des Sciences*, vol. 197, 1933.

[5] F. Wrenn, M. Good, and P. Handler, "The use of positron emitting radioisotopes for the localization of brain tumors," *Science*, vol. 113, pp. 527−7, 1951.

[6] N. A. Dyson, "The annihilation coincidence method of localizing positron-emitting isotopes, and a comparison with parallel counting," *Physics in Medicine and Biology*, vol. 4, pp. 376−90, 1960.

[7] P. V. Harper, K. A. Lathrop, H. Krizek, N. Lembares, V. Stark, and P. B. Hoffer, "Clincial feasibility of myocardial imaging with $^{13}NH_3$," *The Journal of Nuclear Medicine*, vol. 13, pp. 278−80, 1972.

[8] G. N. Hounsfield, "Computerized transverse axial scanning(tomography): Part 1. Description of system," *The British Journal of Radiology*, vol. 46, pp. 1016−22, 1973.

[9] D. A. Chesler, "Positron tomography and three-dimensional reconstruction technique," *Tomographic Imaging in Nuclear Medicine*, pp. 176−83, 1973.

[10] M. E. Phelps, E. J. Hoffman, N. A. Mullani, and M. Ter-Pogossian, "Application of annihilation coincidence detection to transaxial reconstruction tomography," *The Journal of Nuclear Medicine*, vol. 16, pp. 210-24, 1975.

[11] D. W. Townsend, T. J. Spinks, T. Jones, A. Geissbuhler, M. Defrise, M. C. Gilardi, and e. al, "Three dimensional reconstruction for a multi-ring camera," *IEEE Transactions on Nuclear Science*, vol. 36, pp. 1056-65, 1989.

[12] T. J. Spinks, T. Jones, M. C. Gilardi, and J. D. Heather, "Physical performance of the latest generation of commercial positron scanners," *IEEE Transactions on Nuclear Science*, vol. 35, pp. 721-5, 1988.

[13] D. W. Townsend, "Advances in PET imaging from physics to physician," 2005.

[14] B. Yaremko, T. Riauka, D. Robinson, R. Murray, A. Alexander, A. McEwan, and W. Roa, "Thresholding in PET images of static and moving targets," *Physics in Medicine and Biology*, vol. 50, pp. 5969-5982, 2005.

[15] M. Schwaiger, S. Ziegler, and S. G. Nekolla, "PET/CT: Challenge for Nuclear Cardiology," *The Journal of Nuclear Medicine*, vol. 46, pp. 1664-1678, 2005.

[16] K. C. McCall and R. Jeraj, "Dual-component model of respiratory motion based on the periodic autoregressive moving average(periodic ARMA) method," *Physics in Medicine and Biology*, vol. 52, pp. 3455−3466, 2007.

[17] C. Caldwell, K. Mah, C. Yee, Y. C. Ung, C. E. Danjoux, M. J. Balogh, S. N. Ganguli, and L. E. Ehrlich, "Observer variation in contouring gross tuor volume in patients with poorly defined non-small cell lung tumors on CT: teh impact of 18FDG-Hybrid PET fusion," *International Journal of Radiation Oncology, Biology, Physics.*, vol. 51, pp. 923−34, 2001.

[18] C. Caldwell, K. Mah, M. Skinner, and C. E. Danjoux, "Can PET provide the 3D extent of tumor motion for individualized internal target volumes? A phantom study of the limitations of CT and the promise of PET," *International Journal of Radiation Oncology, Biology, Physics.*, vol. 55, pp. 1381−93, 2003.

[19] D. Visvikis, F. Lamare, P. Bruyant, N. Boussion, and C. C. L. Rest, "Respiratory motion in positron emission tomography for oncology applications: Problems and solutions," *Nuclear Instruments and Methods in Physics Research*, vol. 569, pp. 453-457, 2006.

[20] K. M. Langen and D. T. Jones, "Organ motion and its management," *International Journal of Radiation Oncology, Biology, Physics.*, vol. 50, pp. 265-78, 2001.

[21] Y. Seppenwoolde, H. Shirato, K. Kitamura, S. Shimizu, M. V. Herk, J. V. Lebesque, and K. Miyaska, "Precise and Real-Time Measurement of 3D Tumor Motion in Lung Due to Breathing and Heartbeat, Measured During Radiotheray," *International Journal of Radiation Oncology, Biology, Physics.*, vol. 53, pp. 822-834, 2002.

[22] P. E. Kinahan, D. W. Townsend, and D. Sahin, "Attenuation correction for a combined 3D PET/CT scanner," *Medical Physics*, vol. 25, pp. 2046-2053, 1998.

[23] Y. Nakamoto, B. B. Chin, C. Cohade, M. Osama, M. Tatsumi, and R. L. Wahl, "PET/CT: artifacts caused by bowel motion," *Nuclear Medicine Communications*, vol. 22, pp. 221-225, 2004.

[24] W. Sureshbabu and O. Mawlawi, "PET/CT Imaging Artifacts," *Journal of Nuclear Medicine Technology*, vol. 33, pp. 156-161, 2005.

[25] M. M. Osman, C. Cohade, Y. Nakamoto, L. T. Marshall, J. P. Leal, and R. L. Wahl, "Clinically Significant Inaccurate Localization of Lesions with PET/CT: Frequency in 300 Patients," *The Journal of Nuclear Medicine*, vol. 44, pp. 204-243, 2003.

[26] Y. E. Erdi, S. A. Nehmeh, T. Pan, and A. Pevsner, "The CT Motion Quantitation of Lung Lesions and Its Impact on PET-Measured SUVs," *Journal of Nuclear Medicine*, vol. 45, pp. 1287-1292, 2004.

[27] T. Beyer, G. Antoch, T. Blodgett, L. F. Freudenberg, T. Akhurst, and S. Murller, "Dual-modelity pet/ct imaging: teh effect of respiratory motion on combined image quality in clinical oncology," *European Journal of Nuclear Medicine and Molecular Imaging*, vol. 30, pp. 588-596, 2003.

[28] C. Cohade, M. Osman, L. T. Marsh, and R. L. Wahl, "PET-CT: accuracy of pet and ct spatial registration of lung lesions," *European Journal of Nuclear Medicine and Molecular Imaging*, vol. 30, pp. 721−726, 2003.

[29] M. M. Osman, C. Cohade, Y. Nakamoto, and R. L. Wahl, "Respiratory Motion Artifacts on PET Emission Images Obtained Using Attenuation Correction on PET-CT," *European Journal of Nuclear Medicine and Molecular Imaging*, vol. 30, pp. 603-606, 2003.

[30] J. Hanley, M. M. Debois, and D. Mah, "Deep inspiration breathhold technique for lung tumors: The potential value of target immobilization and reduced lung density in dose escalation," *International Journal of Radiation Oncology Biology Physics*, vol. 45, pp. 603-611, 1999.

[31] J. B. A. Maintz and M. A. Viergever, "An Overview of Medical Image Registration Methods," *Medical Image Analysis*, vol. 2, pp. 1-36, 1998.

[32] F. Lamare, M. J. L. Carbayo, T. Cresson, G. Kontaxakis, J. Savean, C. C. L. Rest, A. J. Reader, and D. Visvikis, "List-mode-based Reconstruction for Respiratory Motion Correction in PET Using Non-rigid Body Transformations," *Physics in Medicine and Biology*, vol. 52, pp. 5187−5204, 2007.

[33] P. J. Markiewicz, A. J. Reader, M. Tamal, J. Julyan, and D. L. Hasting, "An advanced analytic method incorporating the geometrical properties of scanner and radiation emissions into the system model for the true component of 3D PET data," *IEEE Nuclear Science Symposium Conference Record, 2005.*, vol. 4, pp. 2310-2314, 2005.

[34] W. Wang and J. A. Kolthamrner, "4-D Geometric Sensitivity for Multi-headed Planar Detector PET Systems," *IEEE Nuclear Science Symposium Conference Record ,2001.*, vol. 2, pp. 1104−1108, 2001.

[35] T. Makela, P. Clarysse, O. Sipila, N. Pauna, C. P. Q, K. T, and I. E. Magnin, "A Review of Cardiac Image Registration Methods," *IEEE Transactions on Medical Imaging*, vol. 21, pp. 1011-1021, 2002.

[36] M. E. Phelps, *PET Molecular Imaging and Its Biological Applications*. New York: Springer-Verlag, 2004.

[37] G. Tarantola, F. Zito, and P. Gerundini, "PET Instrumentation and Reconstruction Algorithms in Whole-Body Applications," *The Journal of Nuclear Medicine*, vol. 44, pp. 756-769, 2003.

[38] J. O. Graeme, "Advanced Nuclear Medicine Medical Physics：PET scanner designs, Normalisation, Artifacts," in *RMIT University - 2005, Lecture 2 – Semester 2*. Melbourne, 2005, pp. 44.

[39] F. H. Fahey, "Data Acquisition in PET Imaging," *Journal of Nuclear Medicine Technology*, vol. 30, pp. 39-49, 2002.

[40] J. B. West, *Respiratory Physiology --the essentials 5th Edition*: Williams & Wilkins, 1995.

[41] W. P. Segars, "Development of A New Dynamic NURBS-Based Cardiac-Torso(NCAT) Phantom," in *Biomedical Engineering and Department of Radiology*: Ph.D dissertation, The University of North Carolina http://www.bme.unc.edu/~wsegars/segars_NCAT_dis.pdf, 2001, pp. 221.

[42] P. H. Weiss, J. M. Baker, and E. J. Potchen, "Assessment of hepatic respiratory excursion," *Journal of Nuclear Medicine*, vol. 13, pp. 733-735, 1972.

[43] K. M. Langen and D. T. L. Jones, "Organ Motion and Its Management," *International Journal of Radiation Oncology, Biology, Physics.*, vol. 50, pp. 265-278, 2001.

[44] M. V. Green, J. Seidel, S. D. Stein, T. E. Eedder, K. M. kempner, C. Kertzman, and T. A. Zeffiron, "Head movement in normal subjects during stimulated PET brain imaging with and

without head restraint," *Journal of Nuclear Medicine*, vol. 35, pp. 1538-1546, 1994.

[45] W. Birkfellner, F. Watzinger, F. Wanschitz, G. Enislidis, C. Kollmann, D. Rafolt, R. Nowothny, R. Ewers, and H. Bergmann, "Selective measurement of white matter and gray matter diffusion trace values in normal human brain," *Medical Physics*, vol. 25, pp. 2237-2241, 1998.

[46] J. B. Hummel, M. R. Bax, M. L. Figl, Y. Kang, C. M. Jr, W. W. birkfellner, H. Bergmann, and R. Shahidi, "Design and application of an assessment protocal for electromagnetic tracking systems," *Medical Physics*, vol. 32, pp. 2371-2379, 2005.

[47] S. R. Goldstein, M. E. Daube-Witherspoon, M. V. Green, and A. Eidsath, "A Head Motion Measurement System Suitable for Emission Computed Tomography," *IEEE Transactions on Medical Imaging*, vol. 16, pp. 17-27, 1997.

[48] W. F. Jones, "Real-time Event Stream Correction for Patient Motion in Clinical 3-D PET," *IEEE Transactions on Nuclear Science Conferences*, pp. 2062-2064, 2002.

[49] P. P. Bruyant, M. A. Gennert, C. Seckert, D. Beach, J. D. Morgenstern, N. Kumar, S. Nadella, and M. A. King, "A Robust Visual Tracking System for Patient Motion Detection in SPECT: Hardware Solutions," *IEEE Transactions on Nuclear Science*, vol. 52, pp. 1288-1294, 2005.

[50] H. Ue, H. Haneishi, H. Iwanaga, and K. suga, "Nonlinear Motion Correction of Respiratory-Gated Lung SPECT Images," *IEEE Transactions on Medical Imaging*, vol. 25, pp. 486-495, 2006.

[51] S. A. Nehmeh, Y. E. Erdi, C. C. Ling, K. E. Rosenzweig, O. D. Squire, L. E. Braban, E. Ford, K. Sidhu, G. S. Mageras, S. M. Larson, and J. L. Humn, "Effect of respiratory gating on reducing lung motion artifacts in PET imaging of lung cancer," *Medical Physics*, vol. 29, pp. 366-371, 2002.

[52] S. A. Nehmeh, Y. E. Erdi, T. Pan, A. Pevsner, K. E. Rosenzweig, E. York, G. S. Mageras, H. Schoder, P. Vernon, O. Squire, H. Mostafavi, S. M. Larson, and J. L. Humn, "Four-dimensional(4D) PET/CT imaging of the thorax," *Medical Physics*, vol. 31, pp. 3179-3186, 2004.

[53] R. R. Fulton, S. R. Meikle, S. Elberl, J. Pfeiffer, C. J. Constable, and M. J. Fulhan, "Correction for Head Movement in Positron Emission Tomograph Using an Optical Motion-Tracking System," *IEEE Transactions on Nuclear Science*, vol. 49, pp. 116-123, 2002.

[54] B. J. Lopersti, A. Russo, W. F. Jones, T. Fisher, D.G. Crouch, D. E. Altenburger, and D. W. Townsend, "Implementation and Performance of an Optical Motion Tracking System for High Resolution Brain PET Imaging," *IEEE Transactions on Nuclear Science*, vol. 46, pp. 2059-2067, 1999.

[55] H. Watable, K. Koshino, P. M. Bloomfield, R. R. Fulton, and H. Iida, "Development of motion correction technique for PET study using optical tracking system," *International Congress Series*, vol. 1265, pp. 31-38, 2004.

[56] L. Tellmann, R. R. Fulton, K. Bente, I. Stangier, O. Winz, U. Just, H. Herzog, and U. K. Pietrzyk, "Motion Correction of Head Movement in PET: Realisztion for Routine Usage," presented at IEEE Transactions on Nuclear Science Symposium Conference, 2004.

[57] S. A. Nehmeh, Y. E. Erdi, K. E. Rosenzweig, H. Schoder, S. M. Larson, O. D. Squire, and J. L. Humm, "Reduction of Respiratory Motion Artifacts in PET Imaging of Lung Cancer by Respiratory Correlated Dynamic PET: Methodology and Comparison with Respiratory Gated PET," *Journal of Nuclear Medicine*, vol. 44, pp. 1644-1648, 2003.

[58] K. Koshino, N. Kawachi, T. Yayashi, H. Watable, S. Hasegawa, J. Hatazawa, and H. Iida, "Effects of motion correction on quantification of myocardial blood flow with 15O-H2O PET," presented at Proceedings of the International Workshop on Quantitation in Biomedical Imaging with PET and MRI, Osaka, Japan, 2004.

[59] S. A. Nehmeh, Y. E. Erdi, C. C. Ling, K. E. Rosenzweig, H. Schoder, S. M. Larson, H. A. Macapinlac, O. D. Squire, and J. L. Humn, "Effect of Respiratory Gating on Quantifying PET Images of Lung Cancer," *Journal of Nuclear Medicine*, vol. 43, pp. 876-881, 2002.

[60] T. Kleshneva, J. Muzik, and M. Alber, "An algorithm for automatic determination of the respiratory phases in four-dimensional computed tomography," *Physics in Medicine and Biology*, vol. 51, pp. N269-276, 2006.

[61] L. Livieratos, L. stegger, P. M. Bloomfield, K. Schafers, D. L. Bailey, and P. G. Camici, "Rigid-Body Transformation of List-Mode Projection Data For Respiratory Motion Correction in Cardiac PET," *Physics in Medicine and Biology*, vol. 50, pp. 3313-3322, 2005.

[62] H. D. Kubo and B. C. Hill, "Respiration gated radiotherapy treatment: a technical study," *Physics in Medicine and Biology*, vol. 41, pp. 83-91, 1996.

[63] T. Zhang, H. Keller, M. J. O'Brien, T. R. Mackie, and B. Paliwal, "Applicatin of the spirometer in respiratory gated radiotherapy," *Medical Physics*, vol. 30, pp. 3165-3171, 2003.

[64] L. Boucher, S. Rodrigue, R. Lecomte, and F. Benard, "Respiratory Gating for 3-Dimensional PET of the Thorax: Feasiblity and Initial Results," *The Journal of Nuclear Medicine*, vol. 45, pp. 214-219, 2004.

[65] K. P. Schafers, M. Dawood, and N. Lang, "Motion correction in PET/CT," *Nuklearmedizin*, vol. 5a(suppl), pp. S46-S50, 2005.

[66] R. L. Eisner, T. Noever, and D. Nowak, "Use of cross-correlation function to detect patient motion during SPECT imaging," *Journal of Nuclear Medicine*, vol. 28, pp. 97-101, 1987.

[67] J. He, G. O'Keefe, G. Jones, T. Saunder, S. Gong, M. Geso, and A. Scott, "Application of GATE and NCAT to Respiratory Motion Simulation in Allegro PET," presented at IEEE 2006 Nuclear Science Symposium, Medical Imaging Conference, San Diego, California, USA, 2006.

[68] Wikipedia, "Center of Mass," Wikipedia, The Free Encyclopedia, 2007, pp. http:/en.wikipedia.org/wiki/Center_of_mass.

[69] P. P. Bruyant, M. A. King, and P. H. Pretorius, "Correction of the respiratory motion of the heart by tracking of the center of mass of thresholded projections: a simulation study using the dynamic MCAT phantom," *IEEE Transactions on Nuclear Science*, vol. 49, pp. 2159 - 2166, 2002.

[70] P. Schmidlin, "Development and Comparison of Computer Methods for Organ Motion Correction in Scintigraphy," *Physics in Medicine and Biology*, vol. 20, pp. 465-476, 1975.

[71] B. E. Oppenheim, "A method using a digital computer for reducing respiratory artifacts on liver scans made with a camera," *The Journal of Nuclear Medicine*, vol. 12, pp. 625-628, 1971.

[72] N. H. Baimel and M. J. Bronskill, "Optimization of analog-circuit motion correction for liver scintigraphy," *The Journal of Nuclear Medicine*, vol. 19, pp. 1059-1066, 1978.

[73] G. J. Klein, B. W. Reutter, T. F. Budinger, and R. H. Huesman, "Fine-Scale Motion Detection Using Intrinsic List Mode PET Information," presented at Proceedings of the 2001 IEEE Workshop on Mathematical Methods in Biomedical Image Analysis, 2001.

[74] R. A. Bundschuh, A. Martinez-Moeller, M. Essler, M. J. Martinez, S. G. Nekolla, S. I. Ziegler, and M. Schwaiger, "Postacquisition Detection of Tumor Motion in the Lung Upper Abdomen Using List-Mode PET Data: A Feasibility Study," *The Journal of Nuclear Medicine*, vol. 48, pp. 758-763, 2007.

[75] W. Foundation, "Center of Mass," vol. 13 May 2008: Wikimedia Foundation, Inc., 2007, pp. http:/en.wikipedia.org/wiki/Center_of_mass.

[76] W. Lu and T. R. Mackie, "Tomographic motion detection and correction directly in sinogram space," *Physics in Medicine and Biology*, vol. 47, pp. 1267-1284, 2002.

[77] A. Z. Kyme, B. F. Hutton, R. L. Hatton, D. W. Skerrett, and L. R. Barnden, "Practical Aspects of a Data-Driven Motion Correction Approach for Brain SPECT," *IEEE Transactions on Medical Imaging*, vol. 22, pp. 722-729, 2003.

[78] A. M. Passalaqua and R. Narayanaswamy, "Patient motion correction of SPECT images: dual scan approach," *IEEE Nuclear Science Symposium and Medical Imaging Conference , 1994., 1994 IEEE Conference Record*, vol. 3, pp. 1270-1274, 1994.

[79] C. Pellot-Barakat, M. Ivanovic, A. Herment, K. Erlandsson, and D. K. Shelton, "Detection of motion in hybrid PET/SPECT imaging based on the correlation of partial sinograms," *IEEE Transactions on Medical Imaging*, vol. 20, pp. 1072-1083, 2001.

[80] J. A. Cooper, P. H. Neumann, and McCandless, "Detection of patient movement during myocardial perfusion imaging," *The Journal of Nuclear Medicine*, vol. 34, pp. 1341-1348, 1993.

[81] P. Schleyer, "Respiratory Motion Correction in Nuclear Medicine Imaging," in *Department of Electrical & Electronic Engineering The University of Melbourne*. Melbourne: The University of Melbounrne, 2003.

[82] D. Visvikis, O. Barret, T. Fryer, A. Turzo, F. Lamare, C. C. L. Rest, and Y. Bizais, "A posteriori respiratory motion gating of dynamic PET images," *IEEE Nuclear Science Symposium and Medical Imaging Conference Record.*, 2004.

[83] F. S. Salinas, "Spatial Normalization: A Survey of Current Methods," http://ric.uthscsa.edu/personalpages/lancaste/DI2_Projects_2004/FS_Project.pdf., 2004, pp. 1-9.

[84] J. Kybic and M. Unser, "Fast Parametric Elastic Iamge Registration," *IEEE Transactions on Imaging Processing*, vol. 12, pp. 1427-1442, 2003.

[85] S. K. Woo, H. Watable, C. Y, K. M. Kim, C. C. Park, P. M. Bloomfield, and H. Iida, "Sinogram-Based Motion Correction of PET Images Using Optical Motion Tracking System and List-Mode Data Acquisition," *IEEE Transactions on Nuclear Science*, vol. 51, pp. 782-788, 2004.

[86] F. Lamare, T. Cresson, J. Savean, C. C. L. Rest, A. J. Reader, and D. Visvikis, "Respiratory

motion correction for PET oncology applications using affine transformation of list mode data," *Physics in Medicine and Biology*, vol. 52, pp. 121-140, 2007.

[87] F. Lamare, T. Cresson, J. Savean, C. C.-L. Rest, A. Turzo, Y. Bizais, and A. J. Reader, "Affine transformation of list mode data for respiratory motion in PET," *IEEE Nuclear Science Symposium Conference Record.*, vol. 5, pp. 3151-3155, 2004.

[88] F. Qiao, T. Pan, J. W. C. Jr, and O. R. Mawlawi, "A motion-incorporated reconstruction method for gated PET studies," *Physics in Medicine and Biology*, vol. 51, pp. 3769-3783, 2006.

[89] D. J. W. Kim, B. R. Murray, R. Halperin, and W. H. Y. Roa, "Held-breath self-gating technique for radiotherapy of non-small-cell lung cancer: A feasibility study," *International Journal of Radiation Oncology, Biology, Physics.*, vol. 49, pp. 43-9, 2001.

[90] C. D. Biancia, E. Yorke, G. Mageras, P. Giraud, K. Rosenzweig, H. Amols, and C. Ling, "Comparison of two breathing levels for gated intensity modulated radiation therapy (IMRT) of lung cancer," *Medical Physics*, vol. 30, 2003.

[91] E. A. Barnes, B. R. Murray, D. M. Robinson, L. J. Underwood, J. Hanson, and W. H. Y. Roa, "Dosimetric evaluation of lung tumour immobilization using breath hold at deep inspiration," *International Journal of Radiation Oncology, Biology, Physics.*, vol. 50, 2001.

[92] H. D. Mah, K. E. Rosenzweig, E. B. Yorke, C. C. Ling, S. A.Leibel, and G. Mageras, "Technical aspects of the deep inspiration breath-hold technique in the treatment of thoracic cancer," *International Journal of Radiation Oncology, Biology, Physics.*, vol. 48, pp. 1175-85, 2000.

[93] B. Feng, P. P. Bruyant, P. H. Pretorius, R. D. Beach, H. C. Gifford, J. Dey, M. A. Gennert, and M. A. King, "Estimation of the Rigid-Body Motion From Three-Dimensional Images Using a Generalized Center-of-Mass Points Approach," *IEEE Transactions on Nuclear Science*, vol. 53, pp. 2712-2718, 2006.

[94] W. J. Geckle, T. L. Frank, J. M. Links, and L. C. Becker, "Correction for patient motion in SPECT: application to exercise thallium-201 cardiac imaging," *The Journal of Nuclear Medicine*, vol. 29, pp. 441-450, 1988.

[95] G. Germano, T. Chua, P. Kavanagh, H. Kiat, and D. S. Berman, "Detection and correction of patient motion in dynamic and static myocardial SPECT using a multi-detector camera," *The Journal of Nuclear Medicine*, vol. 34, pp. 1349-1355, 1993.

[96] M. K. O'Connor, K. M. Kanal, M. W. Gebhard, and P. J. Rossman, "Comparison of Four Motion Correction Techniques in SPEC Imaging of the Heart: A Cardiac Phantom Study," *The Journal of Nuclear Medicine*, vol. 39, pp. 2027-2034, 1998.

[97] G. J. Klein, B. W. Reutter, and R. H. Huesman, "Data-driven respiratory gating in list mode cardiac PET," *The Journal of Nuclear Medicine*, vol. 40, pp. 113p, 1999.

[98] D. S. Lalush and B. M. W. Tsui`, "A priori motion models for four-dimensional reconstruction in gated cardiac SPECT," *IEEE Nuclear Science Symposium Conference Record.*, vol. 3, pp. 1923-1930, 1996.

[99] D. R. Gilland, B. A. Mair, J. E. Bowsher, and R. J. Jaszczak, "Simultaneous reconstruction and motion estimation for gated cardiac," *IEEE Transactions on Nuclear Science*, vol. 49, pp. 2344-2353, 2002.

[100] Z. Cao, D. R. gilland, B. A. Mair, and R. J. Jaszczak, "Three-dimensional motion estimation with image reconstruction for gated cardiac ECT," *IEEE Transactions on Nuclear Science*, vol. 50, pp. 384-352, 2003.

[101] D. R. Gilland, B. A. Mair, and J. Sun, "Joint 4D reconstruction and motion estimatioin in gated cardiac ECT," *Proc. Int. Meeting on Fully Three-Dimensional Image Reconstruction in Radiology and Nuclear Medicine, Utah, USA*, pp. 303-309, 2005.

[102] E. Gravier and Y. Yang, "Motion-compensated reconstruction of tomographic image sequences," *IEEE Transactions on Nuclear Science*, vol. 52, pp. 51-57, 2005.

[103] J. Qi and R. H. Huesman, "List Mode Reconstrunction For PET With Motion Compensation:A Simulation Study," *IEEE Int. Symp. biological Imaging*, pp. 413-416, 2002.

[104] M. W. Jacobson and J. A. Fessler, "Joint Estimation of Image and deformation Parametrs in Motion Corrected PET," *IEEE Nuclear Science Symposium and Medical Imaging Conference Record*, vol. 5, pp. 3290-3294, 2003.

[105] M. W. Jacobson and J. A. Fessier, "Joint estimation of respiratory motion and activity in 4D PET using CT side information," *Macro to Nano, 3rd IEEE International Symposium on Biomedical Imaging*, pp. 275-278, 2006.

[106] F. Lamare, M. J. L. Carbayo, G. Kontaxakis, A. Santos, A. Turzo, Y. Bizais, C. C. L. Rest, and D. Visvikis, "Incorporation of Elastic Transformations in List-Mode Based Reconstruction for Respiratory Motion Correction in PET," *IEEE Nuclear Science Symposium and Medical Imaging Conference Record.*, pp. M03-247, 2005.

[107] F. Lamare, M. J. Ledesma-Carbayo, A. J. Reader, O. Mawlawi, G. Kontaxakis, A. Santos, C.

C.-L. Rest, and D. Visvikis, "Respiratory Motion Correction in 4D PET/CT: Comparison of Implementation Methodologies for Incorporation of Elastic Transformations in the Reconstruction System Matrix," *IEEE Nuclear Science Symposium Conference Record*, 2006.

[108] A. Rahmim, P. M. Bloomfield, S. Houle, M. Lenox, C. Michel, K. R. Buckley, T. J. Ruth, and S. V, "Motion Compensation in Histogram-Mode and List-Mode EM Reconstructions: Beyond the Event-Driven Approach," *IEEE Transactions on Nuclear Science*, vol. 51, 2004.

[109] G. J. Klein, B. W. Reutter, and R. H. Huesman, "4D Affine Registration Models for Resspiratory-Gated PET," *IEEE Transactions on Nuclear Science*, vol. 15, pp. 41-45, 2001.

[110] M. Dawood, X. Jiang, N. Lang, O. Schober, and K. P. Schafers, "Lung Motion Correction of Respiratory Gated 3d PET-CT Images," in *European Journal of Nuclear Medicine and Molecular Imaging*, vol. 32, 2005.

[111] Y. J. He, A. Cai, and J. A. Sun, "Incremental Backprojection Algorithm: Modification of the Searching Flow Scheme and Utilization of the Relationship Among Projection Views," *IEEE Transactions on Medical Imaging*, vol. 12, pp. 555-559, 1993.

[112] M. J. Ledesma-Carbayo, J. Kybic, M. Desco, A. Santos, M. Suhling, P. Hunziker, and M. Unser, "Spatio-temporal nonrigid registration for ultrasound cardiac motoni estimation," *IEEE Transactions on Medical Imaging*, vol. 24, pp. 1113-1126, 2005.

[113] R. Shekhar, V. Walimbe, S. Raja, V. Zagrodsky, M. Kanvinde, G. Wu, and B. Bybel, "Automated 3-Dimensional Elastic registration of Whole-body PET and CT from Separate or Combined Scanners," *The Journal of Nuclear Medicine*, vol. 46, pp. 1488, 2005.

[114] P. J. Slomka, D. Dey, C. Przetak, U. E. Aladl, and R. P. Baum, "Automated 3-dimensional registration of stand-alone(18)F-FDG whole-body PET with CT," *The Journal of Nuclear Medicine*, vol. 44, pp. 1156, 2003.

[115] A. Gottschalk, P. V. Harper, F. F. Jimenez, and J. P. Petasnick, "Quantification of teh respiratory scanning with the rectilinear focused colliatro scanner an the gamma scintillation camera," *The Journal of Nuclear Medicine*, vol. 7, pp. 243-251, 1966.

[116] F. S. Salinas, "Spatial Normalization: A Survey of Current Methods," pp. 1-9.

[117] J. Kybic and M. Unser, "Fast Parametric Elastic Iamge Registration," *IEEE Transactions on Imaging Processing*, vol. 12, pp. 1427-1442, 2003.

[118] M. Wu, O. Carmichael, P. Lopez-Garcia, C. S. Carter, and H. J. Aizenstein, "Quantitative comparison of AIR, SPM, and the fully deformation model for atlas-based segmentation of fucnctional and structural MR images," *Human Brain Mapping*, vol. 27, pp. 747-754, 2005.

[119] T. Makela, P. Clarysse, O. Sipila, N. Pauna, C. P. Q, K. T, and I. E. Magnin, "A Review of Cardiac Image Registration Methods," *IEEE Transactions on Medical Imaging*, vol. 21, pp. 1011-1021, 2002.

[120] A. F. Bielajew, "Fundamentals of the Monte Carlo method for neutral and charged particle transport," 2000.

[121] S. Jan, G. Santin, D. Strul, S.Staelens, K. Assie, D. Autret, S. Avner, R. Barbier, M. Bardies, P. M. Bloomfield, D. Brasse, V. Breton, P. Bruyndonckx, I. Buvat, A. F. Chatziioannou, Y. Choi, and e. al, *GATE Users Guide: GATE-Geant4 Application for Tomographic Emission: a simulation toolkit for PET and SPECT*: http://www.lphe.epfl.ch/GATE/, 2006.

[122] P. M. Systems, "Allegro User's Manual: Amanual describing how to use the Allegro Imaging System," in *DOC-USERMAN-ALLEGRO-ENG, REV B*: Philips Medical Systems, 2002, pp. 1-260.

[123] F. Lamare, A. Turzo, Y. Bizais, C. Cheze, L. Rest, and D. Visvikis, "Validation of a Monte Carlo simulation of the Philips Allegro/GEMINI PET systems using GATE," *Physics in Medicine and Biology*, vol. 51, pp. 943-962, 2006.

[124] J. He, G. O'Keefe, G. Jones, T. Saunder, S. Gong, M. Geso, and A. Scott, "Application of GATE and NCAT to Respiratory Motion Simulation in Allegro PET," presented at Australian and New Zealand Society of Nuclear Medicine 36th Annual Scientific Meeting, Perth, Western Australia, 2006.

[125] S. Jan, G. Santin, D. Strul, S.Staelens, K. Assie, D. Autret, S. Avner, R. Barbier, M. Bardies, P. M. Bloomfield, D. Brasse, V. Breton, P. Bruyndonckx, I. Buvat, A. F. Chatziioannou, Y. Choi, and e. al, "GATE: a simulation toolkit for PET and SPECT," *Physics in Medicine and Biology*, vol. 49, 2004.

[126] J. He, G. O'Keefe, G. Jones, T. Saunder, S. Gong, M. Geso, and A. Scott, "Simulation of respiratory motion using GATE," presented at 9th Congress of the World Federation of Nuclear Medicine & Biology, COEX Seoul, Korea, 2006.

[127] H. Zaidi and C. Morel, "Eidolon: A Monte Carlo Simulator for Multi-ring 3D PET Scanners," PARAPET, Geneva University Hospital Division of Nuclear Medincie, Switzerland 1999.

[128] P. Segars, "4D NURBS-BASED CARDIAC-TORSO (NCAT) PHANTOM," http://www.bme.unc.edu/~wsegars/, 2002.

[129] R. Brun and F. Rademakers, "Root an Object-Oriented Data Analysis Framework: Users

Guide 4.04." http://root.cern.ch/root/doc/RootDoc.html, 2005, pp. 1-393.

[130] P. M. Systems, "MOSAIC Animal PET Imaging System User's Manual," Philps Medical Systems (Cleveland), Inc, 2004.

[131] G. O'Keefe, "Dynamic Acquisition Performance with the Philips Allegro PET scanner," presented at Australian and New Zealand Society of Nuclear Medicine 34th Annual Scientific Meeting, Melbourne, Victoria, Australia, 2005.

[132] A. J. Reader, S. Ally, F. Bakatselos, R. Manavaki, R. J. Walledge, A. P. Jeavons, P. J. Julyan, S. Zhao, D. L. Hastings, and J. Zweit, "One-Pass List-Mode EM Algorithm for High-Resolution 3-D PET Image Reconstruction Into Large Arrays," *IEEE Transactions on Nuclear Science*, vol. 49, pp. 693-699, 2002.

[133] R. Brinks, "PURE: a list-mode reconstruction application." Aachen: Philips Medical Systems Research, 2006.

[134] R. Siddon, "Fast calculation of the exact radiological path for a three-dimensional CT array," *Medical Physics*, vol. 12, pp. 252–5, 1986.

[135] S. A. Nehmeh, Y. E. Erdi, C. C. Ling, K. E. Rosenzweig, H. Schoder, S. M. Larson, H. A. Macapinlac, O. D. Squire, and J. L. Humn, "Effect of Respiratory Gating on Quantifying PET Images of Lung Cancer," *Journal of Nuclear Medicine*, vol. 43, pp. 876-881, 2002.